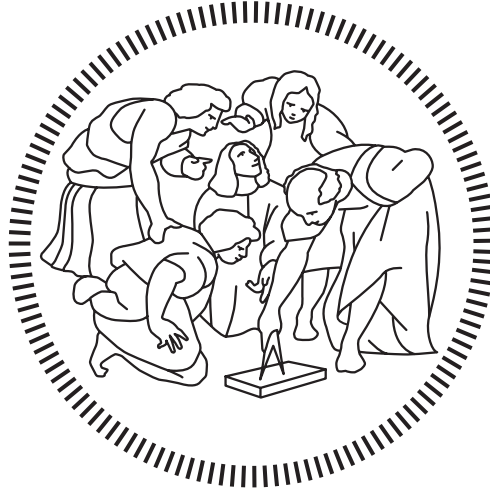


Politecnico di Milano

SCHOOL OF INDUSTRIAL AND INFORMATION ENGINEERING
Master of Science – Aeronautical Engineering



**AeroSwitch project:
Proof of concept of a Distributed Electric Propulsion
aircraft enforcing flight symmetry control**

Supervisor

Prof. Lorenzo TRAINELLI

Co-Supervisors

Prof. Carlo E.D. RIBOLDI

Prof. Alberto L.M. ROLANDO

Candidates

Davide PASQUALI – 920249

Matteo TOMBOLINI – 919893

Ringraziamenti

Chi si iscrive al Corso di Laurea in Ingegneria Aeronautica sa di immettersi su un percorso tanto stimolante quanto impegnativo. Tuttavia, nessuno poteva prevedere che a degli studenti potesse essere data l'opportunità di depositare un brevetto e coronare il progetto AeroSwitch con il volo di un velivolo, seppur radiocomandato. Questo sogno è stato realizzato grazie al prezioso contributo di tante persone, cui va tutto il nostro riconoscimento.

In primo luogo vogliamo ricordare i professori Trainelli, Riboldi e Rolando che ci hanno supportato in questo percorso. Sono accomunati dall'amare il proprio lavoro, che è soprattutto frutto di passione, e rappresentano paradigmi diversi del modello di insegnante che ogni studente spera di incontrare lungo il proprio cammino. Averli visti entusiasti come il giorno del primo volo dell'aeromodello ci riempirà per sempre il cuore.

All'inizio di questo lavoro di tesi abbiamo avuto la fortuna che ci venisse affidato uno spazio nel laboratorio dipartimentale. Abbiamo fatto noi stessi il trasloco del materiale e attrezzato la nuova postazione. Forse anche per questo abbiamo iniziato a sentire questo luogo come la nostra seconda casa. In verità, il merito va soprattutto a tutto il personale che ci ha accolto. Oltre al supporto tecnico che prontamente ci avete offerto, ci avete regalato il sorriso ogni giorno. Ricorderemo sempre le burle reciproche con il Paolo Rubini, le mattinate trascorse a saldare con Sandro Mottironi, gli insegnamenti di vita di Antonio Ravenna e Silvio Ferragina e l'affettuosità di Daniela Rigamonti. Menzione d'onore spetta a Donato Grassi e Luca Riccobene. Ci avete fatto capire che la realtà non può essere piegata al desiderio, ma comunque vale la pena perseguirla. Questa e altre vostre perle di saggezza/comicità hanno allietato il nostro lavoro in galleria del vento.

Se siamo stati fuori dal laboratorio, è perché eravamo a volare (sembra ancora strano poterlo dire!). Abbiamo avuto la fortuna di essere ospitati dal Gruppo Modellisti Sportivi di Ceriano Laghetto, a cui va tutta la nostra gratitudine, in particolare a Elio e Francesco per l'interesse profuso nei nostri confronti e in quello che abbiamo realizzato. In questi mesi abbiamo anche avuto la fortuna e l'onore di partecipare al programma di accelerazione per progetti innovativi, *Switch2Product*. Grazie al prezioso contributo di Paola Bagnoli e Fatima Zahra Mokrane, ci stiamo avvicinando alla finalizzazione di un business plan per la concretizzazione del nostro progetto in un percorso imprenditoriale.

Desideriamo poi condividere la riconoscenza e l'affetto verso tutti gli amici che hanno condiviso con noi momenti bellissimi, o talvolta negativi, ma altrettanto formativi in questi anni di università. Grazie Cami, che hai condiviso con noi il tuo sorriso in ogni giornata della nostra tesi, così come Ele, Max, Marcone, Leo e Teo avete fatto in questi anni.

In questo elenco non abbiamo citato volontariamente gli altri membri del team, Sayan e Andrea. C'è poco da parlare, ogni giorno fa commuovere pensare a cosa sia diventata la nostra amicizia, ormai siamo come fratelli. All'inizio di questo percorso nessuno avrebbe mai immaginato quante gioie sarebbero arrivate. Non desideriamo altro che continuare a percorrere la strada intrapresa, insieme.

E come possiamo non ringraziare gli amici che, anche al di fuori del Politecnico, ci hanno sempre sostenuto in tutti questi anni? Fra i tantissimi, Davide vorrebbe ricordare in particolare Luca, Riccardo, Alberto e Francesco; Matteo invece desidera ringraziare Thomas, Riccardo, Federico e Andrea.

Per concludere, ringraziamo di cuore le nostre famiglie. Siamo due ragazzi molto diversi, però ci accomunano molte caratteristiche, come l'interesse viscerale per l'aviazione o qualsiasi campo afferente, passioni coltivate grazie ai vostri sacrifici e la vostra costante motivazione. Siete stati inoltre la nostra salvezza nei momenti di difficoltà, credendo in noi e accompagnandoci al conseguimento di un traguardo tanto aspirato come la laurea magistrale. Siete i primi artefici dei nostri risultati e speriamo di potervi ancora tanto rendere orgogliosi di noi.

Abstract

Current master's thesis focuses on the demonstration of the feasibility of single-engine in-flight simulation with a multi-engine electric aircraft, in both normal and emergency operational condition. This work aims to validate the concept developed by Team AeroSwitch in response to AIAA 2020 Graduate Team Aircraft Design Competition and culminated in a recent patent submission. The thesis achieves the goal of developing a scaled demonstrator of the concept introduced above by designing, assembling, and testing a radio-controlled (RC) aircraft model provided with the AeroSwitch technology. Intended for electrically propelled fixed-wing aircraft, it exploits differential thrust of an even number of electric motors placed on the wing leading edges to reproduce propeller effects typical of a single-engine and deal with failures of one or more electric motors, regaining flight symmetry. Beneficial effects on safety and cost of operations are the main drivers of this concept, based on an instance of a Distributed Electric Propulsion (DEP) architecture. Flight test activities have been carried out for all relevant flying modes. Single-engine in-flight simulation reflected the behavior of a real General Aviation aircraft, according to the data collected during a flight test activity carried out on a Cruiser Aircraft *PS-28*, applying properly conceived flight test techniques to isolate propeller effects. These can be summarized as a generation of sideslip, along with a slight turn rate and a bank angle variation, that require corrective action by the pilot. The condition of One Electric Motor Inoperative (OEMI) can be safely faced as well, imposing a specific setpoint to each of the residual electric motors through the control unit properly conceived, so that overall thrust symmetry is regained. Besides, the in-flight simulation of multi-engine One Engine Inoperative (OEI) condition has also been carried out. This is obtained shutting down one or more electric motors, without applying any throttle remapping contrary to OEMI cases. In an effort to exploit the potential of the current realization, thrust asymmetry was also enforced to verify feasibility of flat turns and coordinated turns with propulsive yaw control. Besides, the scale model flight testing investigates the effects of DEP, highlighting its influence on aerodynamic performance, with a remarkable increase in lift coefficient at high angle of attack.

Keywords: General Aviation, Distributed Electric Propulsion, Propulsive Control, One Engine Inoperative, Single-engine, Multi-engine, Flight Testing, AeroSwitch, Sideslip, Electric Aircraft, Hybrid Aircraft, Unmanned Air Vehicle, Propeller effects.

Sommario

Il presente lavoro di tesi magistrale è incentrato sulla dimostrazione della fattibilità della simulazione in volo del comportamento di un velivolo monomotore utilizzando un velivolo plurimotore elettrico, sia in condizioni operative normali sia di emergenza. Questo lavoro mira alla validazione del concetto sviluppato dal Team AeroSwitch in risposta alla competizione di progetto di velivolo indetta dalla AIAA nel 2020, culminato nel recente deposito di un brevetto. La tesi raggiunge l'obiettivo di sviluppare un dimostratore in scala dell'idea, progettando, assemblando e testando un velivolo radiocomandato dotato della tecnologia AeroSwitch. Destinata ad aeromobili ad ala fissa e propulsione elettrica, sfrutta la spinta differenziale di un numero pari di motori elettrici posti sul bordo d'attacco dell'ala per riprodurre gli effetti propulsivi tipici di un monomotore e far fronte alle avarie di uno o più motori elettrici, ripristinando il volo simmetrico. Gli effetti benefici sulla sicurezza e sul costo delle operazioni sono i principali motori di questo progetto, basato sulla realizzazione concreta di un'architettura che applica la propulsione elettrica distribuita (DEP). Sono state svolte attività sperimentali in volo per tutte le modalità più rilevanti. La simulazione della modalità di volo monomotore riflette il comportamento di un vero velivolo di Aviazione Generale, secondo i dati raccolti durante l'attività di test svolta su un Cruiser Aircraft *PS-28*, applicando tecniche opportunamente concepite per isolare gli effetti dell'elica. Questi possono essere riassunti come una generazione di un angolo di derapata, insieme ad una leggera velocità di virata ed una variazione dell'angolo di rollio, che richiedono un'azione correttiva da parte del pilota. Anche la condizione di un motore elettrico inoperativo (OEMI) può essere affrontata in sicurezza, imponendo uno specifico valore di manetta a ciascuno dei motori elettrici ancora operativi attraverso la centralina appositamente realizzata, in modo da garantire la simmetria di spinta complessiva. Inoltre, è stata eseguita anche la simulazione in volo della condizione tipica di un plurimotore con un motore inoperativo (OEI). Quest'ultima si ottiene spegnendo uno o più motori elettrici, senza applicare alcuna legge di controllo differente ai motori, contrariamente ai casi OEMI. Nel tentativo di sfruttare il potenziale dell'attuale realizzazione, è stato anche sfruttato il controllo dell'asimmetria di spinta per verificare la fattibilità di virate piatte e virate coordinate con il controllo dell'imbardata grazie all'uso dei soli motori. Inoltre, la sperimentazione in volo sul modello in scala è servita ad indagare gli effetti della propulsione distribuita, evidenziandone l'influenza sulle prestazioni aerodinamiche con un notevole aumento del coefficiente di portanza ad alto angolo d'attacco.

Parole chiave: Aviazione Generale, Propulsione elettrica distribuita, Controllo in imbardata, Motore inoperativo, Monomotore, Plurimotore, Sperimentazione in volo, AeroSwitch, Derapata, Aereo elettrico, Aereo ibrido-elettrico, Aereo non pilotato, Effetti propulsivi.

Extended Abstract

Current master's thesis focuses on the demonstration of the feasibility of single-engine in-flight simulation with a multi-engine electric aircraft, in both normal and emergency operational conditions. This work aims to validate the concept developed by Team AeroSwitch in response to AIAA 2020 Graduate Team Aircraft Design Competition and culminated in a recent patent submission. The proposed aircraft, *Trybrid*, is a multi-engine hybrid electric aircraft. It exploits the differential thrust of an even number of electric motors placed on the wing leading edges to reproduce propeller effects typical of a single-engine at high power settings. Conversely, differential thrust can also be applied to deal with failures of one or more electric motors, regaining flight symmetry. Beneficial effects on safety and cost of operations are the main drivers of this concept, based on an instance of a Distributed Electric Propulsion (DEP) architecture that is now spurring a booming interest in all aircraft categories.

The thesis achieves the goal of developing a scaled demonstrator of the concept introduced above by designing, assembling, and testing a radio-controlled (RC) aircraft model provided with the AeroSwitch technology. The RC model, christened the *SwitchMaster*, exhibits the same configuration as the *Trybrid*, with six electric motors blowing on the wing. These are regulated by the control unit specifically designed for this purpose, the Multi-Motor Management Unit (*M3U*). Flight test activities have been carried out for all relevant flying modes. Single-engine in-flight simulation reflected the behavior of a real General Aviation aircraft, according to the data collected during a flight test activity carried out on a Cruiser Aircraft *PS-28*, applying properly conceived flight test techniques to isolate propeller effects. These can be summarized as a generation of a sideslip, along with a slight turn rate and a bank angle variation, that require appropriate corrective action by the pilot. The same effects are obtained on the *SwitchMaster* by imposing a different setpoint to the external electric motors, scaling the effects through a regulation knob.

Other tested modes were the conditions of One Electric Motor Inoperative (OEMI), in all possible failure modes. The strategy implemented to face this emergency conditions consists of imposing a specific setpoint to each of the residual electric motors through the *M3U*, so that overall thrust symmetry is regained, maximizing available power. In this way, a single-engine rated pilot could safely fly the aircraft equipped with this propulsive system even in case of failure of one electric motor. Besides, the in-flight simulation of multi-engine One Engine Inoperative (OEI) condition has also been carried out. This is obtained shutting down one or more electric motors, without applying any throttle remapping as in OEMI cases. In this way the pilot is required to apply the prescribed procedure to keep straight and level flight, in accordance with foreseen workload.

In an effort to exploit the potential of the current realization, propulsive yaw control was preliminary experimented. The strategy implemented is again based on the thrust asymmetry developed for single-engine simulation, but scaled in magnitude as to fit the purpose. Flat turns can be completed, as well as coordinated turns in which thrust asymmetry is used in place of rudder deflection. The results achieved by this thesis are hopefully just the beginning of a flourishing research path, exploiting the potential of electric propulsion and DEP.

Contents

Ringraziamenti

Abstract	i
Sommario	iii
Extended Abstract	v
List of Figures	xi
List of Tables	xv
List of symbols and acronyms	xvii
1 Introduction and motivation	1
1.1 Teamwork description	2
1.2 Structure of the thesis	3
2 Technological context	5
2.1 Electric propulsion	5
2.1.1 Batteries	5
2.1.2 Electric motors	6
2.1.3 Inverter	7
2.2 Hybrid-electric propulsion	7
2.3 Distributed Electric Propulsion	8
2.4 State of the art	9
2.4.1 Aircraft on the market	10
2.4.2 Ongoing projects	11
3 Single-engine and multi-engine behavior	13
3.1 Single-engine aircraft sideslip angle generation	13
3.1.1 Effects of propeller spinning on yaw axis	13
3.1.2 Effects of propeller spinning on pitch axis	18
3.1.3 Effects of propeller spinning on roll axis	18
3.2 Investigation on multi-engine aircraft One Engine Inoperative condition	18
3.2.1 Twin-engine airplanes with counter-rotating propellers	21
4 AeroSwitch concept	23
4.1 Genesis of the concept	23
4.1.1 <i>Trybrid</i> overview	23
4.2 Design requirements and concept development	24

4.2.1	Pilot interface	26
4.2.2	Single-engine mode	27
4.2.3	Multi-engine mode	30
4.2.4	Turbine simulation	31
4.2.5	Comfort enhancer	31
4.3	Concept effectiveness	31
5	Preliminary investigation	33
5.1	Definition of axes and angles	33
5.1.1	Sign conventions	34
5.2	Sideslip angle estimation	34
5.2.1	INS method	34
5.2.2	MAG method	35
5.3	Correction for the effect of the wind	35
5.3.1	AGARD method	36
5.3.2	Sideslip-reset method	37
5.4	Beta-testing	38
5.5	Computer flight simulator	38
5.5.1	Validation of methods for sideslip angle estimation	39
5.6	Preliminary flight test activity	41
5.6.1	Test aircraft	41
5.6.2	Test instrumentation	43
5.6.3	Test range	44
5.6.4	Test objectives and schedule	44
5.6.5	Test execution	45
5.7	Flight test data analysis	46
5.7.1	Effect of wind	47
5.7.2	Propeller effect analysis	50
6	Scaled demonstrator	55
6.1	Purpose	55
6.2	Design and component selection	55
6.3	Modifications	58
6.3.1	Motor support design and testing	58
6.4	Model construction	63
6.5	Systems architecture	65
6.5.1	Onboard power distribution	66
6.5.2	Electronic speed controllers	67
6.6	Flight Management Unit configuration	68
6.6.1	FMU flight modes	71
6.7	Radio configuration	72
7	Multi-Motor Management Unit	75
7.1	System description	75
7.2	On-board integration	78
7.3	Working modes	79
7.3.1	Outline	79
7.3.2	Safety modes	81
7.3.3	Multi-Engine normal	82
7.3.4	Single-Engine normal	84

7.3.5	Single-Engine One Electric Motor Inoperative	89
7.3.6	Multi-Engine One Engine Inoperative	94
7.3.7	Propulsive yawing control mode	98
8	Preliminary testing	101
8.1	Bench and ground testing	101
8.1.1	Propulsive unit bench testing	101
8.1.2	Propulsive unit wind tunnel testing	102
8.1.3	Wing wind tunnel testing	106
8.1.4	Ground, hardware and fail mode testing	114
8.2	Computer flight simulator testing	115
8.3	Familiarization flights	116
9	Flight testing	121
9.1	Test campaign planning	121
9.2	Data acquisition and FTI	123
9.3	General considerations	124
9.3.1	Concept validation	124
9.3.2	Aircraft characterization	125
9.4	Multi-Engine normal conditions	126
9.5	Single-Engine normal condition	129
9.6	One Electric Motor Inoperative conditions	133
9.6.1	Motor #1 inoperative	134
9.6.2	Motor #2 inoperative	136
9.6.3	Motor #3 inoperative	137
9.7	One Engine Inoperative conditions	139
9.7.1	Three motors inoperative	139
9.7.2	100% knob	141
9.7.3	Motor #3 out	142
9.7.4	Motor #2 out	143
9.7.5	Motor #1 out	144
9.7.6	Motors #1 & #3 out	146
9.8	Aerodynamics and flight dynamics characterization	147
9.9	Yaw control	150
9.9.1	Flat turn with thrust asymmetry	150
9.9.2	Turn coordination with thrust asymmetry	151
9.10	Analysis of FTT differences between a GA aircraft and a RC aircraft	155
10	Conclusion	157
10.1	Future developments	158
A	System architecture requirement specifications	165
A.1	Scope	165
A.2	Equipment and components	165
A.2.1	TX-RX radio control	165
A.2.2	Autopilot	165
A.2.3	Electric motors	166
A.2.4	Propellers	166
A.2.5	Electronic speed controllers	166
A.2.6	<i>M3U</i>	166

A.2.7	Ground station	167
A.3	Operating modes	167
A.3.1	All engines operative (Normal) Multi-Engine mode	167
A.3.2	(Emergency) Multi-Engine mode with three electric motors inoperative on the same side	167
A.3.3	All engines operative (Normal) Single-Engine mode	167
A.3.4	(Emergency) Single-Engine mode with One Electric Motor Inoperative (OEMI)	168
A.3.5	All engines operative (Normal) Single-Engine mode - Alternative . . .	168
A.3.6	Safe mode	168
B	Pixhawk FMU tuned parameters	169
C	Pixhawk FTI sensors	171
D	Zubax Myxa ESC tuned parameters	173
E	Preliminary flight test activity planning	175
E.1	Test aircraft	175
E.1.1	Flight controls and landing gear	176
E.1.2	Avionic and Systems	176
E.1.3	Engine and propeller	178
E.1.4	Mass and balance	179
E.2	Test instrumentation	180
E.2.1	Aircraft native instrumentation	180
E.2.2	Smartphone application	180
E.3	Test range	181
E.4	Limitations	183
E.4.1	Weather limitations	183
E.4.2	Aircraft limitations	183
E.5	Test objectives and schedule	183
E.6	Flight test cards	184

List of Figures

1.1	Team AeroSwitch logo	1
1.2	Team AeroSwitch ready for the RC airplane maiden flight	2
2.1	Pipistrel <i>E-811-268MVL</i> C engine	7
2.2	NASA <i>X-57 Maxwell</i>	8
2.3	Effect of blowing on NASA <i>X-57 Maxwell</i> aerodynamic performance	9
2.4	Pipistrel <i>Alpha Electro</i>	10
2.5	Pipistrel <i>Velis Electro</i>	10
2.6	Rolls-Royce <i>Spirit of Innovation</i>	11
2.7	Tecnam <i>H3PS</i> specs	12
2.8	H2Fly <i>HY4</i>	12
3.1	Propeller spiraling slipstream effect	14
3.2	Propeller asymmetrical thrust effect	15
3.3	Propeller torque effect	16
3.4	Propeller gyroscopic effect	17
3.5	Twin-engine airplane in OEI condition	20
4.1	Serial hybrid-electric architectural schematic example	23
4.2	Rendering of <i>Trybrid</i>	24
4.3	<i>Trybrid</i> propulsive system architectural schematics	24
4.4	<i>EPMS</i> unit feedback loop example	25
4.5	<i>EPMS</i> unit connections	26
4.6	Working logic for SE mode - Normal Situation	27
4.7	Application example for the case of One Electric Motor Inoperative in SE mode	28
4.8	Application example for the case of <i>EPMS</i> fail	28
4.9	Working logic for SE mode - Emergency Situation	29
4.10	Working logic for ME mode in normal situation	30
4.11	Working logic for ME mode in emergency situation	30
5.1	Definitions of axes and aerodynamic angles	33
5.2	Flowchart for the estimation of SSA	37
5.3	Comparison of INS and MAG methods	40
5.4	Wind correction verification	40
5.5	Time history of simulator trial with constant wind	41
5.6	<i>PS-28</i> 3-view representation	42
5.7	<i>PS-28</i> test aircraft	42
5.8	Speed components and values derived from latitude, longitude, altitude	47
5.9	Speed through composition of components	47
5.10	Wind intensity and direction estimation	48

5.11	Wind intensity and direction estimation with different time resolution	49
5.12	Systematic discrepancy between heading and track angles	49
5.13	Sideslip offset (test point Ms2)	50
5.14	Main test constant speed trial Mv2	51
5.15	Main test constant altitude trial Mh1	52
6.1	Legacy Aviation <i>Turbo BushMaster</i> CAD representation	56
6.2	Selected motor datasheet	57
6.3	Wing 3-view drawing	58
6.4	Wing CAD model	58
6.5	Preliminary evaluation of different kind of motors support	59
6.6	Motor support CAD model	60
6.7	Freshly printed motor and ESC panels	61
6.8	Motor support static load test	62
6.9	Zubax <i>Myxa A2</i> electronic speed controller with and without heat sink	62
6.10	Wing with motor supports and with the complete propulsion set	63
6.11	Sectioned CAD rendering of dummy spinner and Pitot probe assembly	63
6.12	Different phases of aircraft build-up	64
6.13	Propulsive architecture notation	65
6.14	Aircraft electrical system architecture	66
6.15	Top and bottom rendered view of Zubax <i>Myxa</i> ESC	68
6.16	Wind tunnel Pitot calibration	69
6.17	Results of wind tunnel Pitot probe calibration	69
6.18	<i>SwitchMaster</i> internal arrangement	70
6.19	<i>Taranis X9D PLUS</i> radio switches arrangement	72
6.20	Radio control map and its effect	73
7.1	<i>M3U</i> board and connections	75
7.2	Architecture of the <i>M3U</i> board	76
7.3	Block scheme of the <i>M3U</i> command chain	78
7.4	Onboard CAN bus network configuration	78
7.5	<i>M3U</i> working modes tree	80
7.6	<i>M3U</i> control law for the multi-engine normal working mode	82
7.7	Output simulation for the multi-engine normal working mode (RPM control)	83
7.8	Output simulation for the multi-engine normal working mode (current control)	84
7.9	SE simulation on the <i>Trybrid</i>	85
7.10	<i>M3U</i> control law for the single-engine normal working mode (knob at 100%)	86
7.11	Output simulation for the single-engine normal working mode (knob at 100%)	87
7.12	<i>M3U</i> single-engine normal mode (knob at 20%)	88
7.13	Curve approximating the results of propulsive unit wind tunnel testing	90
7.14	Motor #6 control law for <i>SE-OEMI-M2</i> mode	90
7.15	Motors setpoint curves for OEMI modes	92
7.16	Pilot input vs. overall output for OEMI modes	93
7.17	<i>M3U</i> control law for the multi-engine OEI working mode	94
7.18	Output simulation for the multi-engine OEI working mode (RPM control)	95
7.19	Yawing moment coefficient comparison between the TBM and two GA ME airplanes	96
7.20	Output simulation for the reviewed multi-engine OEI mode (motor #3 failure)	97
7.21	<i>M3U</i> input-output relationship for propulsive yawing control	98
7.22	Pilot input vs. overall output for propulsive yawing control	99

8.1	<i>Kucher</i> visualization of most though ESC temperature test, at trial end . . .	102
8.2	Typical lithium battery discharge characteristic	103
8.3	Wind tunnel testing propulsive system setup	103
8.4	Main output of propulsive system wind tunnel testing	104
8.5	Thrust results with a SSA of 20 deg	105
8.6	Thrust scaling with wind speed	106
8.7	Wind tunnel testing of the aircraft wing	107
8.8	Standard wing ($C_L - \alpha$) curve	107
8.9	Standard wing drag polar curve	108
8.10	Blown wing wind tunnel testing results, $V_\infty = 15$ m/s	109
8.11	Blown wing wind tunnel testing results, $V_\infty = 20$ m/s	110
8.12	Blown wing wind tunnel polar plot with uncertainty bars at different motors setpoints, $V_\infty = 20$ m/s	111
8.13	Blown wing wind tunnel testing results in single-engine configuration, $V_\infty =$ 15 m/s	112
8.14	Blown wing wind tunnel testing results in multi-engine OEMI configuration, $V_\infty = 15$ m/s	113
8.15	A view on one ESC installation	114
8.16	The SwitchMaster in <i>X-Plane 11</i>	115
8.17	Photographs from the <i>SwitchMaster</i> maiden flight	117
8.18	Illustrative time history of landing technique	119
9.1	Multi-engine normal, constant speed trial MAS = 12.5 m/s	127
9.2	Multi-engine normal, constant speed trial MAS = 16 m/s	127
9.3	Multi-engine normal, constant altitude trial MAS = 10 m/s	128
9.4	Multi-engine normal, constant altitude trial MAS = 12.5 m/s	128
9.5	Single-engine normal, constant speed trial (MAS = 10 m/s, knob = 14%) . .	130
9.6	Single-engine normal, constant speed trial (MAS = 12 m/s, knob = 11%) . .	130
9.7	Single-engine normal, constant speed trial (MAS = 14 m/s, knob = 21%) . .	131
9.8	Single-engine normal, constant altitude trial (MAS = 10 m/s, knob = 19%) .	131
9.9	Single-engine normal, constant altitude trial (MAS = 12 m/s, knob = 9%) . .	132
9.10	Single-engine normal, constant altitude trial (MAS = 14 m/s, knob = 14%) .	132
9.11	M1/M6 inoperative, constant speed trial	135
9.12	M1/M6 inoperative, constant altitude trial	135
9.13	M2 inoperative, constant speed trial	136
9.14	M2 inoperative, constant altitude trial	137
9.15	M3 inoperative, constant speed trial	138
9.16	M3 inoperative, constant altitude trial	138
9.17	3 EMs inoperative - effect of controls on track angle	140
9.18	3 EMs inoperative - other quantities of interest	140
9.19	100% knob setting - effect of controls on track angle	141
9.20	100% knob setting - other quantities of interest	141
9.21	EM3 inoperative - effect of controls on track angle	142
9.22	EM3 inoperative - other quantities of interest	143
9.23	EM #2 inoperative - effect of controls on track angle	143
9.24	EM #2 inoperative - other quantities of interest	144
9.25	EM #1 inoperative - effect of controls on track angle	145
9.26	EM #1 inoperative - other quantities of interest	145
9.27	EM #1 & EM #3 inoperative - effect of controls on track angle	146
9.28	EM #1 & EM #3 inoperative - other quantities of interest	146

9.29	Electric motors mechanical efficiency and propulsive efficiency	148
9.30	C_L - α of trim shots test	148
9.31	Polar curves of trim shots test	149
9.32	Trajectory in flat turn	150
9.33	Time histories of flat turn	151
9.34	Non-coordinated turn	152
9.35	Turn coordinated with the rudder	152
9.36	Time histories of controls in thrust-coordinated turn with 40% gain	153
9.37	Effect of thrust-coordinated turn on parameters of interest with 40% gain	153
9.38	Time histories of controls in thrust-coordinated turn with 80% gain	154
9.39	Effect of thrust-coordinated turn on parameters of interest with 80% gain	154
E.1	<i>PS-28</i> 3-view representation	175
E.2	<i>PS-28</i> test aircraft	176
E.3	Dynon <i>SkyView HDX</i> system connections	177
E.4	Dynon <i>SkyView HDX</i> PFD example view	177
E.5	<i>Rotax 912 ULS S2</i> power curve in standard conditions	178
E.6	<i>Rotax 912 ULS S2</i> power curve variation with altitude	179
E.7	<i>PS-28</i> center of balance representation	179
E.8	ICAO visual approach chart with test zone highlighted	182
E.9	Preliminary test flight test card (constant speed)	185
E.10	Main test flight test card (constant speed)	185

List of Tables

2.1	Battery specific energy	6
2.2	NASA <i>X-57 Maxwell</i> specs	8
2.3	Pipistrel <i>Alpha Electro</i> specs	10
2.4	Pipistrel <i>Velis Electro</i> specs	10
2.5	Rolls-Royce <i>Spirit of Innovation</i> specs	11
2.6	Tecnam <i>H3PS</i>	12
2.7	H2Fly <i>HY4</i> specs	12
4.1	Trim solution for several flight conditions for SE simulation	31
5.1	Sign convention table	34
5.2	Results of wind reconstruction methods	40
5.3	<i>PS-28</i> main parameters (from POH)	42
5.4	Dynon <i>SkyView HDX</i> exportable parameters of interest	43
5.5	<i>AndroSensors</i> parameter outputs	44
5.6	Planned flight mission sequence	44
5.7	Test points for preliminary trials	45
5.8	Test points for the main trials	46
5.9	Account of test points for propeller effect characterization	52
6.1	<i>TBM</i> main parameters	56
6.2	Buying list	56
6.3	Motor support and wing static load trial	61
6.4	Limit control surface deflection and corresponding RC input	70
6.5	<i>Taranis X9D PLUS</i> radio switches function assignment	72
6.6	<i>Taranis X9D PLUS</i> radio channel assignment	73
7.1	<i>M3U</i> firmware release history	80
7.2	<i>M3U</i> jumpers configuration	81
9.1	Test campaign summary	122
9.2	Log data fields and sampling rate	123
9.3	Effect of knob and trim speed on flight symmetry in constant speed FTT	129
9.4	Effect of knob and trim speed on flight symmetry in constant altitude FTT	129
9.5	Account of sideslip variation in OEMI testing	137
9.6	Configurations for OEI simulation	139
9.7	Results of OEI simulation testing	147
9.8	High AOA trim shots in full flap configuration	149
9.9	Body angular rates determination	149
B.1	<i>Pixhawk 4</i> FMU modified parameters	169

C.1	Internal FMU sensors	171
C.2	External FMU sensors	171
D.1	<i>Zubax Myxa</i> ESC modified parameters	173
E.1	<i>PS-28</i> main parameters (from POH)	176
E.2	<i>Rotax 912 ULS S2</i> main parameters	178
E.3	Masses of <i>PS-28</i>	179
E.4	Dynon <i>SkyView HDX</i> exportable parameters of interest	180
E.5	<i>AndroSensors</i> parameter outputs	181
E.6	<i>PS-28</i> speed limitations	183
E.7	<i>Rotax 912</i> limitations	183
E.8	Pre-flight loading table	184
E.9	Planned flight mission sequence	184

List of symbols and acronyms

Symbols

Symbol	Definition	Unit
α	Angle of attack	deg
β	Sideslip angle	deg
χ	Track angle	deg
δ	Magnetic heading	deg
$\delta_a, \delta_e, \delta_f, \delta_r$	Aileron, elevator, flap, rudder deflection	deg
δ_{knob}	Asymmetry percentage (knob on the radio)	[-]
δ_{t_i}	Output throttle to the i-th propulsive unit	[-]
δ_{tot}	Pilot input throttle	[-]
$\dot{\psi}$	Turn rate	deg /s
η_m	Mechanical efficiency	[-]
η_P	Propulsive efficiency	[-]
$\hat{\gamma}$	Flight path angle	deg
$\hat{\psi}$	Non-dimensional turn rate	[-]
$\mathcal{L}, \mathcal{M}, \mathcal{N}$	Roll, pitch, yaw moment components	N m
\mathbf{C}	Rotation matrix	
Φ	Bank angle	deg
ψ	Azimuth angle	deg
ψ_w	Direction from which the wind is blowing	deg
θ	Pitch angle	deg
\mathbf{V}	Velocity vector	
ξ	Track angle	deg
b	Wing span	m
D	Drag	N
d	Magnetic declination	deg
g	Gravitational acceleration	m/s
h	Altitude	m, ft
J	Propeller advance ratio	[-]
L	Lift	N
n	Engine revolutions	RPM
P	Power	W
p, q, r	Roll, pitch, yaw angular rates	rad/s
T	Thrust	N
u, v, w	Velocity vector body components	m/s
V	Velocity	m/s, kn
V_A	Maneuvering speed	kn
V_w	Atmospheric wind speed	kn

V_{MC}	Minimum control speed	kn
V_{NE}	Never exceed speed	kn
V_{NO}	Normal operating speed	kn
V_{S1}	Stall speed in clean configuration	kn

Super/subscripts

Symbol	Definition
∞	Undisturbed
\mathcal{B}	Body frame
\mathcal{S}	Stability frame
\mathcal{W}	Wind frame
\mathcal{E}	Earth frame
D	Down
E	East
N	North
P	Port
S	Starboard
W	Wind

Abbreviations and acronyms

<i>CAN</i>	Control Area Network
<i>EPMS</i>	Energy and Propulsion Management System
<i>M3U</i>	Multi-Motor Management Unit
AGL	Above Ground Level
AHRS	Attitude & Heading Reference System
AIAA	American Institute of Aeronautics and Astronautics
AMSL	Above Mean Sea Level
AOA	Angle of Attack
ASA	Acrylonitrile Styrene Acrylate
BP	Battery Pack
CAD	Computer Aided Design
CAS	Calibrated AirSpeed
CFD	Computational Fluid Dynamics
CG	Center of Gravity
CHT	Cylinder Head Temperature
CPU	Central Processing Unit
CS	Certification Specifications
DEP	Distributed Electric Propulsion
EASA	European union Aviation Safety Agency
ECEF	Earth-Centered-Earth-Fixed
EFIS	Electronic Flight Instrument System
EGT	Exhaust Gas Temperature
EM	Electric Motor
ESC	Electronic Speed Controller
FAA	Federal Aviation Administration
FAR	Federal Aviation Regulations
FIR	Flight Information Region
FL	Flight Level
FMU	Flight Management Unit
FOH	First-Order Hold
FT	Flight Test
FTE	Flight Test Engineer
FTI	Flight Test Instrumentation
FTP	Flight Test Pilot
FTT	Flight Test Technique
GA	General Aviation
GND	GrouND
GNSS	Global Navigation Satellite System
GPS	Global Positioning System
GS	Ground Speed
HUMS	Health and Usage Monitoring System
IAS	Indicated AirSpeed
ICAO	International Civil Aviation Organization
ICE	Internal Combustion Engine
INS	Inertial Navigation System
IPC	Inter-Process Communication
LAD	Level-Acceleration-Decelerations
LED	Light-Emitting Diode

LQR	Linear-Quadratic Regulator
MAC	Mean Aerodynamic Chord
MAG	MAGnetic
MAS	Measured AirSpeed
MAVLink	Micro Air Vehicle Link
MCU	Micro-Controller Unit
ME	Multi-Engine
MEMS	Micro Electro-Mechanical Systems
METAR	METeorological Aerodrome Reports
MFD	Multi-Function Display
MTOM	Maximum Take-Off Mass
NASA	National Aeronautics and Space Administration
ND	Not Determined
NED	North-East-Down
NOTAM	NOTice to AirMen
OAT	Outside Air Temperature
OEI	One Engine Inoperative
OEMI	One Electric Motor Inoperative
PDB	Power Distribution Board
PFD	Primary Flight Display
PGS	Power Generation System
PIC	Pilot In Command
PID	Proportional-Integrative-Derivative (regulator)
POH	Pilot Operating Handbook
PPL	Private Pilot License
PWM	Pulse-Width Modulation
RAM	Random-Access Memory
RC	Radio-Controlled
RPM	Round Per Minute
SD	Secure Digital
SE	Single-Engine
SoC	State of Charge
SSA	SideSlip Angle
TAS	True AirSpeed
TBM	Turbo BushMaster
THR	Throttle
TRL	Technology Readiness Level
UART	Universal Asynchronous Receiver-Transmitter
UAV	Unmanned Air Vehicle
UBEC	Universal Battery Elimination Circuit
USB	Universal Serial Bus
VFR	Visual Flight Rules

Chapter 1

Introduction and motivation

In conjunction with the course of "Aircraft Design" A.Y. 2019-2020, held by professors Lorenzo Trainelli and Carlo E.D. Riboldi, the AeroSwitch team, made of Lorenzo Alberti, Davide Pasquali, Andrea Santeramo and Matteo Tombolini, signed up for the 2020 American Institute of Aeronautics and Astronautics (AIAA) Aircraft Design competition for graduate students [1]. The project was delivered in May 2020 with a paper entitled *Trybrid - a new concept for General Aviation trainer*. It featured a novel aircraft concept that allows to fly an airplane both as a multi-engine one and as a single-engine one, thanks to propulsive electric motors and a dedicated control unit and system architecture. A patent application is pending for the proposed system.

In August 2020 the team was notified to have been awarded the first place in the competition, a really remarkable honor. At the same time, starting from June 2020, the team took part in the *Switch2Product* innovation challenge, promoted by Politecnico di Milano, Deloitte and PoliHub [2]. The purpose of the challenge was to support participants to enter into the business world exploiting their innovative solutions and products, also providing legal, administrative and bureaucratic support. Passing preliminary phases and preparing a final investor pitch, the team was selected in December 2020 to access the "acceleration program", in which the team should lay the foundations for the future product developments.

These two experiences and the Italian patent submission greatly involved team and professors in the challenge of bringing such novel aircraft concept to the real world, in the General Aviation (GA) airplane market. It is a really challenging objective, that involves a great amount of resources. Therefore, the planned path from zero to the GA market is articulated into stages. The first one is the proof-of-concept of the patented idea, made with a radio controlled airplane for simplicity and affordability. Then, a partnership with an aircraft manufacturer should allow to retrofit an existing airplane with the proposed system, in order to realize a full-working prototype and to test it in flight, before starting the production phase. Certification of such a novel airplane concept will be difficult and complicated, but safety level increment should be the key to achieve it.



AERO SWITCH

Fig. 1.1: Team AeroSwitch logo

1.1 Teamwork description

In the illustrated framework, the work to be done was centered on the first part of the path-to-market: retrofitting a commercial radio controlled airplane in order to demonstrate the system working principle (therefore increasing the TRL from 2 to 6). Being too complex to be completed by an individual person in an acceptable amount of time, the work has been distributed among the four members of the team, presented in Figure 1.2. Extensive support and guidance was offered by professors Lorenzo Trainelli, Carlo E. D. Riboldi, Maurizio Boffadossi and Alberto L. M. Rolando. In particular, Prof. Rolando developed the full hardware and software of the control unit that enables the propulsive control, as illustrated later in this work.

The complete process leading to the operational implementation of the AeroSwitch concept on a scaled flying demonstrator was shared among team-mates as detailed in the following.

- **Lorenzo Alberti** [3] was assigned the development of a high-fidelity airplane model on the commercial flight simulator suite *X-Plane 11*. The airplane should be as close as possible to the real flying radio-controlled airplane, for what concerns geometry, aerodynamics, flight dynamics, controllability and system simulation. The purpose of the flight simulator is to investigate the novel aircraft concept flight mechanics and dynamic response before flying the real one. It serves to better develop the control unit laws and to forecast the airplane behavior and, especially, potential bad habits, both for flight safety and for better phenomena comprehension. After the simulation is validated with real flight data, it also served as test-bench for hazardous or impractical tests.
- **Davide Pasquali** and **Matteo Tombolini**, authors of current thesis work, focused on the realization and flight testing of the radio-controlled airplane model demonstrating the AeroSwitch concept.
- **Andrea Santeramo** [4] had the leading role in aerodynamic investigation. The main topic was Distributed Electric Propulsion (DEP), both in nominal framework and when coupled with differential thrust actuation. Results of wind tunnel testing of the singular propulsive unit and of the wing were compared with numerical software simulations. The effect of blowing induced by propellers was thus isolated, in the very same configuration of the flying airplane. Last part of the work regarded the analysis of flight test data.

It is worth-mentioning that, even if the work is here presented as subdivided into three theses, the whole process of interest was carried out as a team. Every team member worked on every topic and aspects, actively collaborating the one with the other.



Fig. 1.2: Team AeroSwitch ready for the RC airplane maiden flight

1.2 Structure of the thesis

The structure of present thesis well reflects the chronological order of the work. Chapter 2 describes the technological context of electric propulsion. The theoretical outline that will act as the background of the entire dissertation is reported in Chapter 3. In particular, single-engine and multi-engine flight characteristics in both normal and emergency operational conditions are described. In response, in Chapter 4 the AeroSwitch concept is introduced and explained, with direct reference to the patent submission form.

A flight test activity on a Cruiser Aircraft *PS-28* was carried out. Its planning and execution are reported in Chapter 5, along with the methods followed to estimate sideslip angle, being the most important parameter to characterize flight symmetry. Such investigation aimed to understand the influence of propeller effects, to define a guideline for deliverables of single-engine in-flight simulation on the scale demonstrator. The realization of this latter is extensively covered in Chapter 6, along with components tuning and modifications.

Due to lack of suitable products on the market, a control unit, namely Multi-Motor Management Unit (*M3U*), has been developed from scratch to independently control each motor. This is presented and illustrated in Chapter 7, which also includes practical considerations related to scale model design and realization.

As will be shown in Chapter 6, integration and testing of different components and systems require an extensive effort. Luckily, the path to the maiden flight of the scale model was almost clear of obstacles, with the main tasks accomplished reported in Chapter 8. Once this whole set of preliminary testing activities were completed, it was possible to carry out the FT campaign intended to demonstrate most relevant flight modes of the scale model. Chapter 9 describes the execution of the tests and reports flight data analysis.

In the last chapter, the assessment of the performed work is presented, with particular emphasis on validation of AeroSwitch concept. These considerations are directly related to the possible future developments, to exploit the potential of the current realization.

Chapter 2

Technological context

2.1 Electric propulsion

Electric and hybrid propulsion systems have received a great deal of attention in recent years in various branches of transportation, including aviation. The main driver is the great overall flexibility of this technology, with potential enhancement of performance, reliability and safety. Moreover, pure-electric aircraft promise significant benefits for air quality, as the pollutants emitted on the fuel combustion process are avoided. Hybrid-electric aircraft may similarly help improve local air quality impacts of aviation due to its lower fuel burn.

Electric propulsion may also result in lower aircraft noise levels, since electric engines will not have some of the noise sources associated with piston engines. The lower noise levels associated with electric aircraft may facilitate their use in densely populated areas.

The main limit to the usability of the electric alternative for propulsion has been bound to the limits of energy storage systems, i.e. batteries. Until recently, batteries did not offer sufficient energy-to-mass and energy-to-volume densities [5] to be accommodated on-board an aircraft without a relevant negative impact on payload or aircraft size. Today, as a result of many research efforts towards the improvement of such performance indexes, it is possible to design and fly an electrically propelled aircraft. This is testified by some existing examples, both prototypical and production models in the categories of ultra-light and General Aviation [6].

Among the factors limiting the diffusion of the existing electric aircraft is their relatively high production cost, which will be only recursively lowered by the spreading of this technology, through know-how consolidation and scale economy effects. Also the cold perception by the potential customers plays a role in the lingering diffusion of such systems. Especially private pilots and flight training organization tend to be very cautious with respect to radically new technologies and prototype aircraft, when it comes to risking a relevant capital (as emerged from a market survey, described in [7]). Also on the side of researchers and designers, the tendency to treat electric aircraft as prototypes is testified by the lack of literature illustrating a common framework for the preliminary design of such aircraft, which in most cases are obtained through a modification of existing machines, originally gliders or ICE-propelled designs. This is the case of many state of the art exemplars, some of which are reported in Section 2.4.

2.1.1 Batteries

Batteries are now the biggest bottleneck in the development of hybrid/electric airplanes. Limits in specific energy, safety and durability make a real challenge for an aircraft designer. Three mature battery technologies satisfy these requirements: Lead-based, Nickel-based and

Lithium-based. Table 2.1 reports the reference specific energy available on the market now for each technology [8]. Comparing the values, it is clear that Lithium-based batteries have the highest one, which confirms why this is the most, if not the only, adopted technology.

Technology	Energy density [W h/kg]
Lead-based	50
Nickel-based	80
Lithium-based	200

Tab. 2.1: Battery specific energy

There are many possible realizations of Lithium batteries, which differ from the internal chemistry. Best trade-off between safety and performance is offered by Nickel Cobalt Aluminum (NCA) and Nickel Manganese Cobalt (NMC) technologies. NCA batteries have the highest specific energy in the Lithium-ion paramount: they can have over 260 W h/kg. However, NMC batteries are not far from this value, and have longer durability, up to 2000 life cycles [9], while limit for NCA batteries is 1500 [8] and common realizations reach only 500 cycles.

2.1.2 Electric motors

Regardless of the final architecture of the power-train for the aircraft, another key component is given by electric drives: in recent years the electrification of automobiles pushed the industry towards more powerful or more compact high-reliability motors to be compliant with market growth. There are many types of electric motor. For aircraft propulsion applications the most usual choice is that of alternate current (AC), axial-flux, synchronous, permanent magnet, brushless motors.

The main characteristics of interest for selecting a motor in a preliminary hybrid-electric powertrain design are the power-to-weight ratio and operating rotational speed. At the current technological level, a reasonable power-to-weight ratio value for an electric motor is between 6 – 8 kW/kg [10], which entails a smaller size and lower weight of the electric motor with respect to internal combustion engines (ICE) with the same power output. This feature allows to place electric motors where internal combustion engines simply do not fit, for instance in the wings, like mostly typical for distributed propulsion architectures.

Electric motors are attractive for aviation also for operational reasons. Thanks to the lower number of moving parts, electric motors are easier to service and maintain and less exposed to component failures than internal combustion engines. They usually operate in a lower temperature range, and for this reason there is no need for a warm-up phase. By constitution, an electric motor may act as an electric generator receiving mechanical power from outside. On aircraft, this makes energy recuperation easier in phases of the flight with low demanded propulsive power.

For what concerns performance, efficiency of an electric motor in converting stored energy into mechanical energy is much higher by constitution. Performance is not affected by altitude and it is possible to exploit the benefit of electric motors to provide non-continuous power for some minutes, if well cooled. For example, the electric motor enforced on hybrid-electric aircraft under development Pipistrel *Panthera* can reach a 53% overrating [11].

Pipistrel is also the first developer of type certified electric liquid-cooled engine, the *E-811-268MVLC*. It provides 57.6 kW (77 hp) of peak power and 49.2 kW (66 hp) of maximum continuous power (16.67% overrating). It combines a liquid-cooled electric motor and a liquid-cooled power controller. This explains why it is type certified as a engine, rather than

a motor. By the way, the propulsion motor is an axial flux synchronous permanent magnet electric motor. Lighter and more compact, these motors are also more powerful than radial flux motors, making them ideal for their application in aviation. The associated controller converts direct current (DC) from the batteries to alternating current (AC) for the motor. The controller receives torque command via *CAN* bus and adjusts the motor current input accordingly through the engine high voltage AC bus.

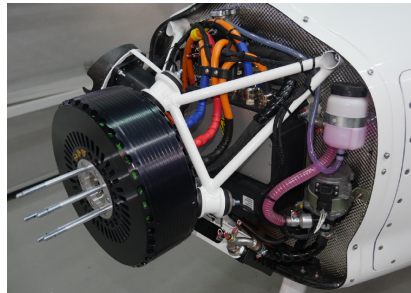


Fig. 2.1: Pipistrel *E-811-268MVLC* engine [12]

2.1.3 Inverter

As previously highlighted, most electric motors for aviation work with alternate current (AC), and electric generators produce AC power. On the contrary, batteries (or fuel cells) invariably work with direct current (DC). Hence inverters - converting DC power to AC and viceversa - are needed to make power connection between the corresponding modules.

Inverters are very critical components in terms of temperature limitations. Currently inverters can operate only up to a temperature of 60-70°C. By the way, this value is consistent with the limitations of the inverter installed on the scale demonstrator, as discussed in Section 6.5.2. In order to avoid overheating, a suitable cooling system should be included in the design of the power system.

Inverters are typically made of different components, including transistors, capacitors, filters, temperature sensors, etc. Among the several types of inverters available on the market, those adopted more typically in the automotive and aeronautical field are based on Silicon IGBTs (Insulate Gate Bipolar Transistors). Another more expensive but still viable alternative is the Silicon carbide (SiC) IGBT technology, providing higher efficiency thanks to the higher switching frequency and less stringent temperature limits.

2.2 Hybrid-electric propulsion

Hybrid-electric propulsion is the compromise which seems to be the connection between yesterday's and tomorrow's powertrain, assuring noise and greenhouse abatement close to airports area while assuring good range performance. A further degree of freedom is the architecture. Possible realizations include:

- **Series** hybrid: an electric motor drives the propeller, powered either by a battery, fuel cell or a generator fed by a thermal engine; a power converter, equipped with a proper power control unit delivers the proper electric current to the motor.
- **Parallel** hybrid: the propeller is driven by an electric motor, powered by batteries, and by an internal combustion engine (ICE) coupled on the same axis.

- **Series-Parallel** hybrid: the user is driven by an electric motor, powered either by a battery or a generator, and by ICE; the two lines are connected by a generator, making this solution more complex and heavy.

In an ICE-based hybrid-electric aircraft, the power generation module may consist of the ICE itself, connected in series to an electric generator. Before being added up to the DC power coming from the batteries, the AC power from the generator will be converted by an inverter.

A DC-DC converter is usually needed to reduce the DC voltage of the power flow from the generator and batteries before feeding it to the avionic system. In a fuel-cell-based hybrid-electric aircraft a DC-DC converter may be needed to match the voltages of the battery and fuel-cell, since these elements might operate at largely different voltage levels.

Series architecture has the advantages of assuring ICE is always operating at its maximum efficiency RPM and not requiring complex control system and mechanical transmission. If compared with parallel architecture, overall efficiency suffers at high speed and a further drawback is that electric motor(s) and battery pack(s) must be sized for maximum power, increasing weight, volume and costs. What instead must be emphasized is that series architecture is compatible with DEP, which brings in advantages as wing blowing, with a consistent maximum lift coefficient increment, but also drag increment due to higher dynamic pressure and wake interference.

2.3 Distributed Electric Propulsion

Hybrid-electric and pure-electric propulsion allows to make the thrust to be distributed over a large number of electric motors (EMs) distributed along the entire wingspan. This solution is known as Distributed Electric Propulsion (DEP).

In recent years, NASA has been studying the development of designs based on electric propulsion and DEP. This technology exploits the different characteristics of EMs compared to traditional ICEs, in particular the reduced dimensions and weights. These advantages open up new scenarios for aircraft designers: in this way, it is possible to place the EMs in order to integrate the propulsion system within the airframe.

The current scope of NASA is to design an aircraft to demonstrate the benefits of DEP [13]: a meaningful example, NASA *X-57 Maxwell*, is shown in Figure 2.2. *X-57 Maxwell* project is the heart of the Scalable Convergent Electric Propulsion and Operations Research (SCEPTOR) program, whose goal is to obtain a 350% to 500% more efficient aircraft in cruise. It has been decided to adopt the fuselage of the Tecnam *P2006T* and build a high aspect ratio wing that employs 2 tip motors and 12 smaller ones active only during the terminal phases of flight as high-lift devices (in cruise blades are folded).



Fig. 2.2: NASA *X-57 Maxwell* [14]

Aircraft	NASA <i>X-57 Maxwell</i>
Type	Pure-electric aircraft
Seats	4
Energy storage	Batteries
Propulsion	14 electric motors
Top speed	150 kn
Endurance	60 min
Range	160 km

Tab. 2.2: NASA *X-57 Maxwell* specs [14]

This system has the task of providing the required lift at low speeds. In fact, the high-lift system consists of a single hinge point slotted flap and high-lift propellers. These latter act by increasing the dynamic pressure on the wing section within the propeller slipstreams, which increases the total lift produced.

As of 2021, NASA *X-57* has not yet completed its maiden flight. Nevertheless, it is possible to predict its aerodynamic performance through CFD simulations. The comparison of blown and unblown configurations of the NASA *X-57 Maxwell* aircraft is reported in Figure 2.3 [15], [16].

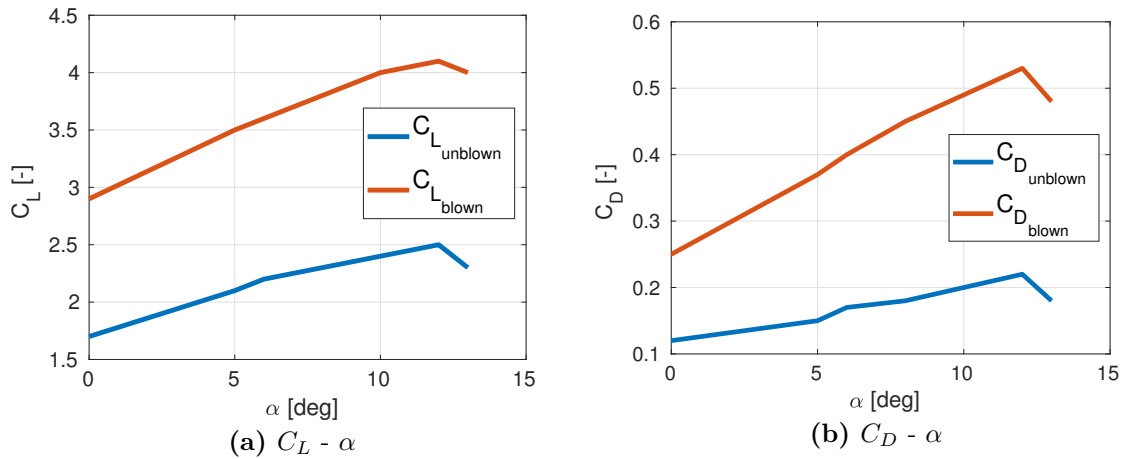


Fig. 2.3: Effect of blowing on NASA *X-57 Maxwell* aerodynamic performance

Results show how big is the increment achieved in lift, which can be exploited for example to shorten take-off run and generally achieve better low speed power-on handling qualities.

Another presumable benefit of DEP is the installation drag reduction. Engine nacelles and pylons introduce propulsion installation drag, comprised of friction, interference, and wave drag. Engine installations embedded in the fuselage surface may save wetted area equivalent to nearly half of a typical podded nacelle.

As a downside, the increase in drag coefficient experienced in Figure 2.3b is remarkable too, due to the added lift-induced drag. This performance degradation could be actually compensated by the reduction of wing surface that can be allowed by high-lift augmentation enhanced by DEP. Direct consequences would be lower wetted wing area and thus viscous drag. Of course this benefit is better exploited on other categories rather than General Aviation, namely commercial liners and military transport aircraft. Conversely, higher wing loading could affect handling, and make a GA trainer less suitable for a student pilot. As a side note, added drag could be minimized maximizing spacing of electric motors, reducing propellers diameter and adopting wingtip-propellers.

2.4 State of the art

A list of GA aircraft using the previously described technologies is now presented. A main distinction is considered between aircraft already available on the market, and projects still in progress. The selection reported is intended to cover the general framework of pure-electric and hybrid-electric GA aircraft.

2.4.1 Aircraft on the market

Two aircraft will be considered:

1. Pipistrel *Alpha Electro*, ultralight pure-electric aircraft;
2. Pipistrel *Velis Electro*, certified pure-electric aircraft;

Pipistrel *Alpha Electro*

Pipistrel *Alpha Electro* [17] is a two-seat ultra-light electric trainer. It has short take-off distance, powerful 1000+ fpm climb capability and an endurance of one hour plus a 30-minute reserve. It meets microlight and ASTM LSA requirements, as well as standards for electric propulsion systems.

The 60+ kW electric motor only weighs 20 kg and is more powerful than the popular Rotax *912* series, typically used on microlights and LSAs. The 21 kWh battery pack is dual-redundant and designed to be either quickly replaceable within minutes or charged in less than one hour.



Fig. 2.4: Pipistrel *Alpha Electro* [17]

Aircraft	Pipistrel <i>Alpha Electro</i>
Type	Pure-electric ultralight
Seats	2
Energy storage	Batteries
Propulsion	60 kW EM
Top speed	105 kn
Endurance	90 min
Range	150 km

Tab. 2.3: Pipistrel *Alpha Electro* specs [17]

Pipistrel *Velis Electro*

Velis Electro [18] is a pure-electric derivative of the proven *Virus SW 121*. It is the world's first electric powered airplane to receive a Type Certificate, issued by EASA. It is equipped with the previously mentioned Pipistrel type certified electric liquid-cooled engine *E-811-268MVLC*, providing 57.6 kW (77 hp) of peak power and 49.2 kW (66 hp) of maximum continuous power.



Fig. 2.5: Pipistrel *Velis Electro* [18]

Aircraft	Pipistrel <i>Velis Electro</i>
Type	Pure-electric CS-VLA
Seats	2
Energy storage	Batteries
Propulsion	57.6 kW EM
Top speed	98 kn
Endurance	60 min
Range	100 km

Tab. 2.4: Pipistrel *Velis Electro* specs [18]

Featuring noise levels of only 60 dB, *Velis Electro* is considerably quieter than other aircraft of the category (Cessna *172* for example can reach 90 dB [19]). Its powertrain is entirely liquid-cooled, including the batteries, and demonstrated the ability to withstand

faults, battery thermal runaway events, and crash loads as part of the certification process. The reduced number of moving parts dramatically decreases maintenance costs and the risk of malfunctions is further minimized thanks to its built-in continuous health-monitoring system. This enhanced reliability allows the *Velis Electro* to have more than double the lifespan of powertrain elements in comparison to the previous generation of electric airplanes.

Battery system includes two Pipistrel battery packs connected in parallel, installed in a redundant 2-unit arrangement, total nominal capacity 24.8 kWh. One battery pack is located in the nose of the airplane and the second behind the cabin. This ensures redundancy of the power source: in case of battery failure, the malfunctioning battery would get automatically disconnected from the system. A single battery is capable of standalone operation and has enough power capability to support climbing and continuation of flight.

The liquid-cooling system consists of a radiator and two electrically driven pumps installed in series, located behind the rear battery pack. An air inlet for the radiator is located on left side of the fuselage, and the warm air leaves the fuselage at the bottom. Two high power axial fans are installed behind the radiator in order to allow battery cooling during charging.

Unlike a start-up procedure of a conventionally powered airplane, the *Velis Electro* is powered-up by four switches and requires no warm-up time before take-off.

2.4.2 Ongoing projects

Similarly to previously described DEP demonstrator NASA *X-57*, each of the outlined technologies is under development with great investments from industries and institutions. Many European union founded projects are willing to contribute to greener aviation and the result is the great ferment in the field. Among the several projects ongoing, it is possible to identify a great variety of objectives, proven by the different exemplars outlined below.

Rolls-Royce *ACCEL*

The objective of Rolls-Royce is to build the world's fastest all-electric aircraft. In particular, target speed for 2021 is 260 kn, to beat the record previously set by a Siemens powered *Extra 330*. The program started from the retrofit of *Nemesis NXT* air racer, to develop the pure-electric *Spirit of Innovation*. Battery pack is made of six thousands cells that can provide up to 320 km of range. Propulsive unit is made of three coupled electric motors manufactured by YASA, capable of 370 kW, and a specifically developed engine control unit. The project is founded with UK Government participation and its aim is to develop technology and know-how on a one-off airplane, to pave the way to full-scale production [20].



Fig. 2.6: Rolls-Royce *Spirit of Innovation* [20]

Aircraft	Roll-Royce <i>Spirit of Innovation</i>
Type	Pure-electric racer
Seats	1
Energy storage	Batteries
Propulsion	3 EMs for combined 370 kW
Top speed	260 kn
Endurance	180 min
Range	320 km

Tab. 2.5: Rolls-Royce *Spirit of Innovation* specs [20]

Tecnam *H3PS*

Tecnam is developing the *H3PS* in partnership with Rotax and Rolls-Royce (which stands for High Power High-Scalability Hybrid powertrain). It is an hybrid-electric aircraft based on Tecnam *P-2010*. Contrarily to previously mentioned Pipistrel *Panthera*, which enforces series architecture, the *H3PS* is a valid exemplar of parallel hybrid-electric aircraft. It will be the result of European union *Horizon 2020* co-financed project [21, 22]. A 30kW electric motor is combined with an internal combustion capable of 105 kW, in spite of the original 134 kW engine of *P-2010*.



Tab. 2.6: Tecnam *H3PS* [21]

Aircraft	Tecnam <i>H3PS</i>
Type	Hybrid-electric aircraft
Seats	4
Energy storage	Batteries + fuel
Propulsion	30 kW EM + 105 kW ICE
Top speed	ND
Endurance	ND
Range	ND

Fig. 2.7: Tecnam *H3PS* specs[22]

H2fly *HY4*

Hybrid hydrogen-electric powertrain demonstration has one of its forerunner in the *MAHEPA* consortium [10], with the partnership of DLR (and its spinoff) H2Fly, Pipistrel, the University of Ulm, and Hydrogenics. As of today, their collaboration has produced *HY4*, the first four-seat aircraft with hydrogen electric powertrain. The twin-fuselage design of *HY4* is based on the Pipistrel *Taurus G4* aircraft. Each fuselage, with space for two passengers, is connected by a mid-wing section integrating the propulsion unit. The propeller is placed in front of the propulsion unit, whereas a low-temperature hydrogen fuel-cell is placed behind the propulsion unit. Its latest version flew in November 2020. With a renovated and optimized fuel-cell system technology, it has a declared range of 1500 km.



Fig. 2.8: H2Fly *HY4* [23]

Aircraft	H2Fly <i>HY4</i>
Type	Hybrid-electric aircraft
Seats	4
Energy storage	Batteries + Fuel cells
Propulsion	80 kW electric motor
Top speed	108 kn
Endurance	ND
Range	1500 km

Tab. 2.7: H2Fly *HY4* specs [23]

Chapter 3

Single-engine and multi-engine behavior

3.1 Single-engine aircraft sideslip angle generation

In order to precisely simulate the behavior of a single-engine propeller-driven airplane in flight, it is necessary to investigate how the propeller itself influences the flight conduction. Propeller effects on aircraft motion can be separated between effects on yaw, pitch and roll axis. These effects are so significant, that the designer must consider them in the development of a new airplane.

Main effect is on yaw axis, whereas influence on roll and pitch is less perceptible from the pilot's perspective. This explains why the following dissertation (based on [24, 25]) focuses on the yaw dynamics, but also outlines the other effects.

3.1.1 Effects of propeller spinning on yaw axis

Propellers of most of the single-engine aircraft on the market spin in the clockwise direction as viewed from the rear, inducing a left-turning tendency. It is difficult to model the propeller-generated yawing moment, as it depends on many factors (i.e. engine thrust and speed, airspeed, propeller geometry, fuselage and tail geometric characteristic, attitude, center of gravity location, etc.). It appears as a unique phenomenon to the pilot, who is trained to counteract it with the rudder in the different flight phases (namely, running the propeller at high RPM introduces effects not present when in idle). However, from a physical point of view, it is possible to distinguish the independent contributions to yawing moment generation: spiraling slipstream, asymmetrical thrust (also called "P-factor"), torque and gyroscopic precession.

Spiraling slipstream

A typical single-engine aircraft features a standard propeller whose rotation is clockwise, as seen from the pilot. The high-speed rotation of an aircraft propeller gives a spiraling motion to the slipstream. At high propeller speeds and low forward speed (as in take-off and approach to power-on stall), this spiraling rotation is very compact and exerts a strong side-ward force on the aircraft vertical tail surface and fuselage. When this spiraling slipstream strikes the vertical fin, it causes a yawing moment about the aircraft vertical axis. The more compact the spiral, the more prominent this force is. As the forward speed increases, however, the spiral elongates and becomes less effective. The corkscrew flow of the slipstream also causes a rolling moment around the longitudinal axis.

The corkscrew shaped blade tip vortex is sketched in Figure 3.1 as it encloses the fuselage of the airplane, which is the majority behind the center of gravity, and the vertical tail. Impacting them, the vortex generates a side force which results in a yawing moment. The tip vortex is caused by the pressure differential between the forward (low pressure) and rearward (high pressure) sides of the propeller. This pressure differential causes air on the back side of the propeller to flow toward the tip, while the opposite happens on the forward face. The opposite radial flow directions on the two sides cause the formation of this vortex at the tip, exactly as it does on a regular wing. The vortex is indicative of the downwash left by the propeller blade. The downwash component, which is perpendicular to the wake left by the propeller blade, changes its angle of attack, generating additional lift on it in the process.

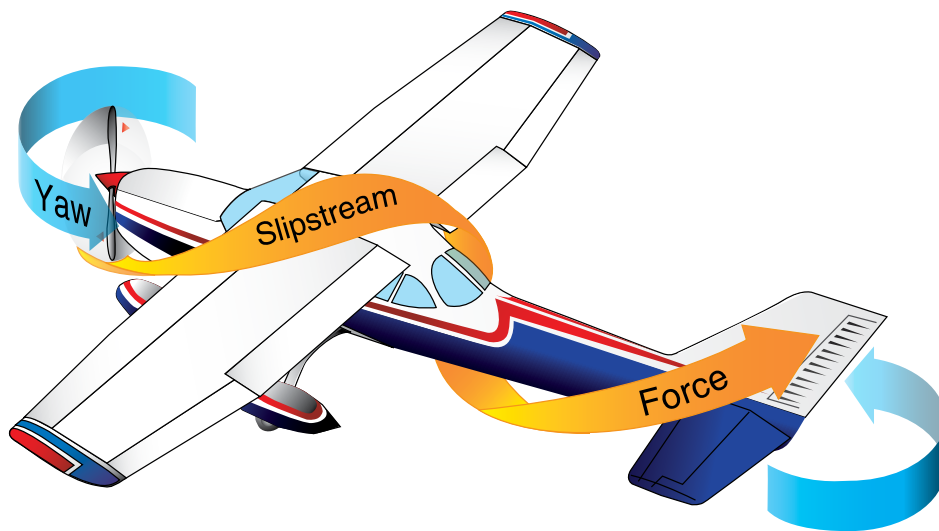


Fig. 3.1: Propeller spiraling slipstream effect [25]

The resulting yawing moment for this aircraft (assuming a clockwise propeller rotation) tends to move the nose to the left. It can be suppressed by a rudder deflected so that trailing edge goes right (step on the right pedal), generating an opposing lift on the vertical tail. The magnitude of the yawing moment depends on engine power, speed of rotation, and the airspeed of the aircraft.

Asymmetrical thrust

When an aircraft is flying with a high AOA, the incoming airflow is not orthogonal to the blade disk. Therefore, the velocity of the incoming airflow, as seen by the downward and upward moving blade, is the result of the vector sum of the velocity of the propeller blade in its plane of rotation and the velocity of the air passing horizontally through the propeller disc. With the aircraft being flown at positive AOAs, the right (viewed from the rear) or downswinging blade is passing through an area where overall velocity is greater than that affecting the left or upswinging blade. Since the propeller blade is an airfoil, increased velocity means increased lift. The downswinging blade has more lift and tends to pull (yaw) the aircraft nose to the left.

This effect is often called "P-factor", where P stands for propeller. It might be easier to visualize considering the propeller shaft mounted perpendicular to the ground (like a helicopter). With the air moving horizontally across this vertically mounted propeller, the blade proceeding forward into the flow of air has a higher airspeed than the blade retreating. Thus, the blade proceeding into the horizontal airflow is creating more lift, or thrust, moving

the center of thrust toward that blade. On a single-engine aircraft with a clockwise spinning propeller, it moves the center of thrust to the right of the propeller disc area, causing a yawing moment toward the left, around the vertical axis.

This unbalanced thrust becomes proportionately smaller and continues getting smaller until it reaches the value of zero when the propeller shaft is exactly horizontal in relation to the moving air. The magnitude of this effect is greater with increasing horsepower, propeller size, and pitch.

At high power, a tractor configuration will experience a destabilizing moment that will tend to increase the azimuth angle. Rudder input is required to correct it, but the designer should guarantee that the yawed condition can be exacerbated also if the pilot is not sufficiently responsive. In particular, the directional stability derivative C_{N_β} should be large enough. When the pilot steps on the right rudder pedal, the counteracting moment is quadratic with the airspeed of the aircraft. However, the asymmetric moment may not necessarily be as low since it is highly dependent on the radial velocity of the propeller, which depends on the RPM. This highlights a potentially critical flight condition for the aircraft at high power, low airspeed, high AOA, which is typical for an initial climb after take-off or during a bailed landing maneuver. A graphical representation of this effect is depicted in Figure 3.2.

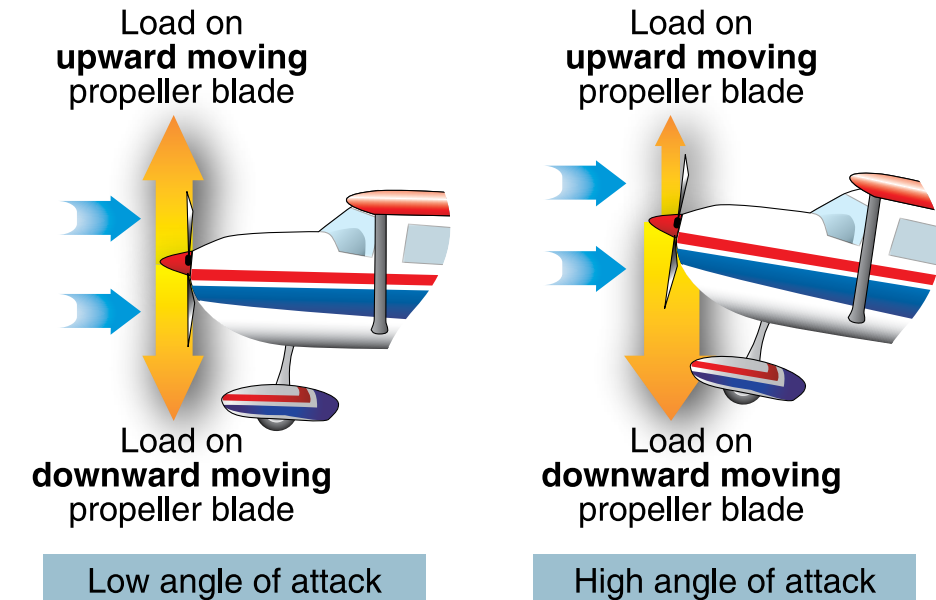


Fig. 3.2: Propeller asymmetrical thrust effect [25]

Torque

Internal engine parts and propeller are revolving in one direction due to the generation of a torque. At the same time, a reaction torque is applied to the aircraft, according to Newton's *Third Law of Physics*. When the aircraft is airborne, it tends to make the aircraft roll. Since aileron deflection may be required to overcome torque, the asymmetrical aileron drag results in additional yaw variation and thus requires more rudder deflection.

To compensate for roll tendency, old aircraft were typically rigged in a manner to create more lift on the wing that is being forced downward. Modern aircraft are designed with the engine offset to counteract this effect of torque. Generally, the compensating factors are permanently set so that they act at cruising speed, since most of the aircraft operating time is at that speed. However, aileron trim tabs permit further adjustment for other speeds.

When the aircraft wheels are on the ground during the take-off roll, an additional turning moment around the vertical axis is induced by torque reaction. As the left side of the aircraft is being forced down by torque reaction, more weight is being placed on the left tire of main landing gear. This results in more ground friction, or drag, on the left tire than on the right, causing a further turning moment to the left. The magnitude of this moment is dependent on many variables. Some of these are: size and horsepower of engine, size of propeller and engine speed, size of the aircraft and condition of the ground surface. This yawing moment on the take-off roll is corrected by the pilot's proper use of the rudder or rudder trim. The torque effect is represented in Figure 3.3.

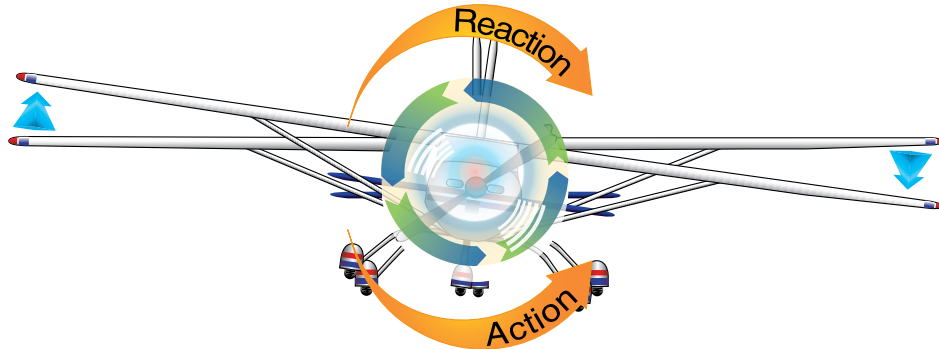


Fig. 3.3: Propeller torque effect [25]

Angular momentum and gyroscopic effects

All practical applications of the gyroscope are based upon two fundamental properties of gyroscopic action: rigidity in space and precession. The one of interest for this discussion is precession. Precession is the resulting action, or deflection, of a spinning rotor when a deflecting force is applied to its rim. When a force is applied, the resulting force takes effect 90 deg ahead of the force, thus in the direction of rotation vector. The rotating propeller of an airplane makes a very good gyroscope and thus has similar properties. As the motion takes place, gyroscopic precession induces restoring moments, trying to keep the propeller in the original orientation. As soon as the rotation ceases, so will those moments. Gyroscopic precession will only affect an airplane while it is changing attitude, and this can be hard to separate from asymmetrical thrust which also starts producing a yawing or pitching moment, as soon as the aircraft starts to rotate in pitch or yaw.

This effect has always been associated with tailwheel-type aircraft and most often occurs when the tail is being raised during the take-off roll. This change in pitch attitude has the same effect as applying a force to the top of the plane of rotation of the propeller. The resultant force acting 90 deg ahead causes a yawing moment to the left around the vertical axis, as depicted in Figure 3.4. The magnitude of this moment depends on several variables, one of which is the abruptness with which the tail is raised (amount of the force applied).

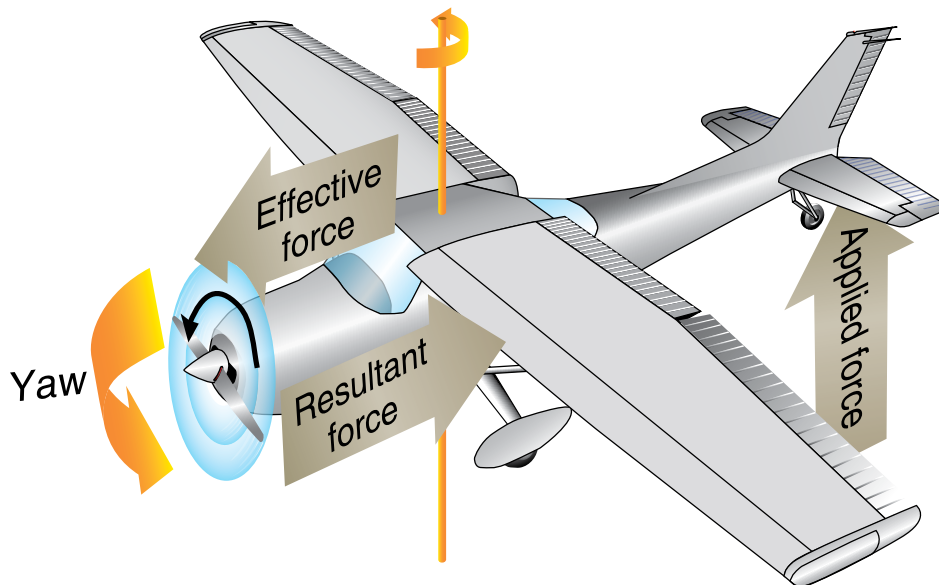


Fig. 3.4: Propeller gyroscopic effect [25]

More in general, any force applied to any point of the rim of the propeller plane of rotation will generate a gyroscopic moment. Depending on where the force is applied, the airplane is caused to yaw left or right, to pitch up or down, or a combination of pitching and yawing. It can be said that, as a result of gyroscopic action, any yawing around the vertical axis results in a pitching moment, and any pitching around the lateral axis results in a yawing moment. To correct for the effect of gyroscopic action, it is necessary for the pilot to properly use elevator and rudder to prevent undesired pitching and yawing.

Rigging

Proper rigging of the thrust-line can reduce trim drag and increase control authority in a relatively narrow band of the aircraft flight envelope, or change stability in another. Because of the number of factors involved, it is impossible to provide guidelines to select the proper angles, and some requirements for control are directly in contrast with the desire for reduced trim drag.

Commonly, a single-engine propeller-driven aircraft is not symmetric, as it could appear looking at it. Two main corrections for the generated (overall, sum of the discussed contributions) yawing moment are applied on almost every airplane of the category: non-centered thrust line and aerodynamic asymmetry. The thrust line is commonly tilted-down and leftward of a couple of degree (dependently on the airframe and engine) to counteract the already illustrated effects. Moreover, aerodynamic asymmetry is produced with a slightly cambered vertical tail airfoil or a small angle of incidence of it, a fixed trim tab on the rudder or other side-force generating devices. These devices are fixed and produce a force proportional to dynamic pressure: therefore, they are tuned to let the aircraft fly symmetrically in cruise, as this is the most typical condition.

When applying full throttle, the pilot should act the rudder on one side to keep the airplane flying in straight line, whereas on the other side when idling. As a confirmation of this, fighter planes of Second World War era exhibit large vertical tail and rudder, to counteract the effects of powerful engines acting on a small airframe.

3.1.2 Effects of propeller spinning on pitch axis

Propeller spinning can also act on pitch axis dynamics. In particular, propeller axial force generates a pitching moment about the aircraft center of gravity, depending on the arm between vertical location of thrust line and vertical center of gravity location. Unfortunately, the determination of the normal force is not a simple task, as it depends on the blade geometry, engine speed, airspeed, and angle of attack of the airplane.

The CG of the tractor configuration is aft of the propeller. Consequently, the normal force will destabilize the aircraft (introducing a nose pitch-up contribution). However, if the propeller is aft of the CG, as in the case of most pusher aircraft, the effect is opposite or stabilizing (nose pitch-down contribution).

Another possible contribution to pitch moment generation is due to the increase of dynamic pressure on the tail, as a result of power increment. The action of the spiraling slipstream may strike the horizontal stabilizer and cause a pitching moment, similar to the yawing moments previously outlined. For most airplanes though, the influence of the wing downwash on the horizontal stabilizer is so great that any action of the spiraling slipstream on the horizontal stabilizer is lost in the airflow and the effect is negligible.

Finally, a sideslip may also cause a pitching moment, usually nose-down in tractor airplanes. Tilting the thrust axis so that it points downwards one or two degrees (such that the thrust tries to rotate the aircraft nose down) makes a significant increase in the stability of the aircraft when it is at high power and low speed. However, this results in a certain amount of trim drag at high speeds.

3.1.3 Effects of propeller spinning on roll axis

The majority of the aspects concerning interaction between propeller rotation and roll induced rotations have already been discussed. To sum up:

- Sideslip may induce a rolling moment with power-on because the slipstream strikes more wing.
- Engine torque may contribute to a rolling moment depending on the size of the engine and propeller in relation to the aircraft.
- Spiraling slipstream may contribute to a rolling moment if it alters the direction of the airflow over the wing.

3.2 Investigation on multi-engine aircraft One Engine Inoperative condition

Most of General Aviation multi-engine airplanes are twin-engine. With both engines operative, sideslip is eliminated due to perfect thrust symmetry. The condition of zero sideslip, also known as coordinated flight, is confirmed by the ball of the turn coordinator instrument being centered.

When an engine fails, thrust is no more symmetrically distributed with respect to the longitudinal axis, and the aircraft enters the so-called One Engine Inoperative (OEI) flight condition. The following dissertation is intended to describe this scenario and the way to deal with it, according to [24, 25].

In a conventional multi-engine airplane, typically a twin-engine, the two thrust units are located on the wings, therefore far from the aircraft center of gravity. An exception are aircraft in push-pull configuration (like the Cessna *Model 377 Skymaster*), for which following

considerations do not apply. When an engine fails, the remaining engine produces a thrust force generates a yawing moment. Also a roll moment is produced, due to the asymmetry of the lift in each wing, with a greater lift generated by the wing with the operating engine. Roll moment arm is significantly smaller than the one related to yaw, namely the distance between thrust line and center of gravity. Moreover, the dead engine produces an extra drag item generated by the windmilling propeller, which should be feathered.

In addition to the thrust asymmetry, also the P-factor introduced in Section 3.1 has serious implications to multi-engine propeller aircraft. To explain this effect, consider a twin-engine aircraft with both engines operating normally and both propellers rotating clockwise as seen from the cockpit. Due to asymmetry effects, the point of application of thrust of each propeller is at the right of the rotation axis. Therefore, the arm of the two resultant thrust vectors is different, with the right engine acting over a distance which is larger than that of the left engine. Indeed, a relatively small moment is generated about the center of gravity and must be reacted through a small rudder deflection or by trimming the airplane nose right, using the rudder trim in an attempt to center the Turn and Bank indicator ball. Some aircraft feature a yaw string attached in front of the windscreen, that provides the pilot with additional help by allowing him to visually assess the severity of the yaw.

An hazardous situation the pilot must be trained to face is OEI configuration. If the airplane is slowed down below a certain airspeed, control authority is lost and the rudder will be incapable of opposing the yaw. This airspeed is called minimum control airspeed, denoted by V_{MC} . If the airspeed falls below this airspeed, the aircraft will roll upside-down, possibly causing an inverted spin, if not impacting the ground first. At any rate, it is a likely fatal scenario. As a consequence, it is imperative the pilot always maintains sufficient airspeed, and slows down only after having reduced power in a dive. The minimum control airspeed is usually higher than the airplane stalling speed and take-off rotation should never be performed until this speed has been exceeded.

Now consider the scenario in which the left engine fails. In this configuration, the left engine is assumed to be the critical one, because a greater moment is generated compared to the mirror case of failure of right engine. In other words, an inoperative left engine is the most problematic condition between the two. The asymmetric thrust generates a massive moment that forces the aircraft to yaw toward the dead engine. This may be intensified by windmilling of the propeller in idle, with an associated increase in drag. This may be reduced by feathering the propeller, as typically enhanced on most of twin-engine aircraft.

The standard emergency procedure the pilot must implement is to eliminate the yaw by stepping on the rudder pedal on the same side as the functional engine. Simultaneously, the aircraft must be banked between 2 deg and 5 deg to the still operating engine ("raise the dead"), to balance the sideforce induced by rudder deflection through sideways lift component. When used together in the proper combination (as displayed in Figure 3.5), these two corrective actions assure zero sideslip and best climb performance. Once trim is established, the pilot will feather the idling propeller.

Pilots are trained to identify the side of the dead engine by stepping on the rudder pedals. In fact, the pedal on the same side as the dead engine is softer. This is due to the floating tendency of the rudder, and leads to the mnemonic: *"dead foot, dead engine"*.

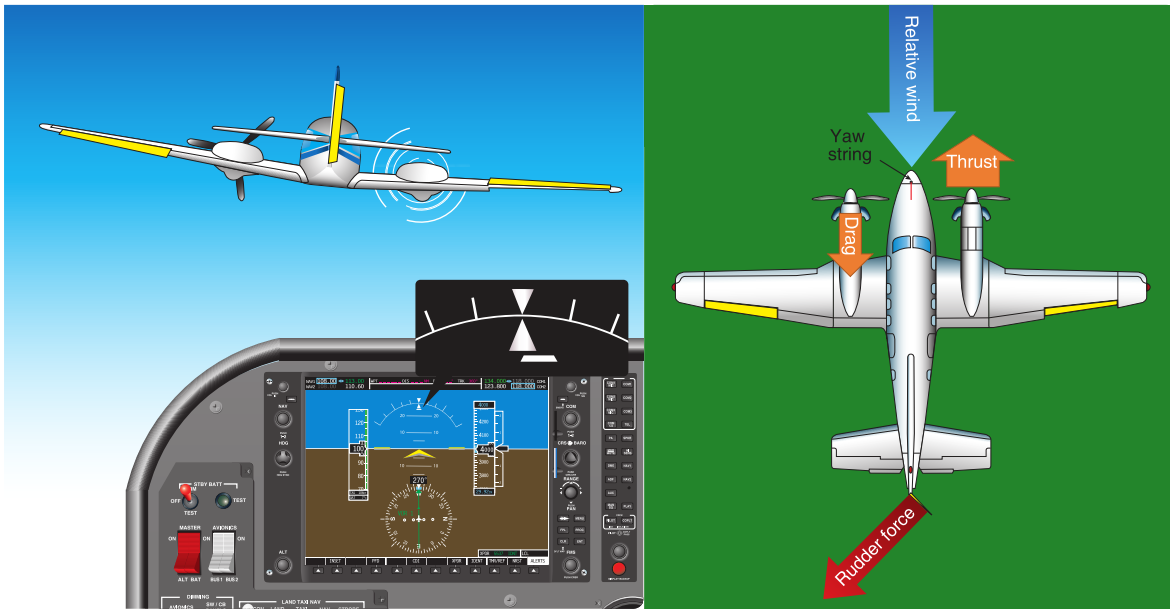


Fig. 3.5: Twin-engine airplane in OEI condition [25]

In a multi-engine airplane with an inoperative engine, the centered ball is no longer the indicator of zero sideslip, due to the inherent roll angle. Therefore, in OEI condition, the ball is approximately one-third to one-half the possible excursion on the same side of the operative engine. The only possible indication of zero sideslip could come from the yaw string, otherwise minimization of sideslip is a matter of placing the airplane at a predetermined bank angle and ball position.

The precise condition of zero sideslip (bank angle and ball position) varies slightly from model to model and with available power and airspeed. If the airplane is not equipped with counter-rotating propellers, it also varies slightly with the engine failed due to P-factor. If the engines are further apart, the moment of thrust will be larger, so the rudder will have to produce larger force to counteract it and the bank will have to be higher to counteract the rudder force. The further aft the rudder is, the less force it needs to produce to yield the same moment and therefore less bank will be needed. The zero sideslip ball position for straight flight is also the zero sideslip position for turning flight. As a rule of thumb, in order to achieve the maximum rate-of-climb in the OEI configuration a bank angle of 2 deg is recommended if the non-critical engine fails, and 3 deg if the critical engine fails. If the bank angle is exaggerated, the rate-of-climb could easily be detrimentally affected and could prevent the aircraft from maintaining altitude. The extreme case of a bank angle in excess of 5 deg almost certainly results in a loss of altitude for underpowered twin-engine aircraft.

In OEI flight at low altitudes and airspeeds, such as the initial climb after take-off, pilots must operate the airplane so as to guard against the three major accident factors: loss of directional control, loss of performance, and loss of flying speed. All have equal potential to be lethal.

To discuss the effect of engine power on the performance of a generic twin-engine piston aircraft, consider the *Piper PA-23 Apache*. In normal operation, the aircraft climbs 1478 fpm at sea level and reaches maximum 173 kn calibrated airspeed. Upon losing an engine, the best rate of climb will drop to 239 fpm and its maximum airspeed to 97 kn. A drag increase associated with maintaining a constant heading with OEI greatly impacts on performance. The problem with this turn of events is that the low rate of climb does not leave room for mistakes. In light of the low-power sensitivity, an inexperienced or frantic pilot may easily

maneuver the airplane off the peak conditions, causing it to lose altitude.

3.2.1 Twin-engine airplanes with counter-rotating propellers

The OEI condition can be slightly mitigated by installing a combination of right engine and propeller rotating counter-clockwise (more in general, opposite to that of the left engine). This way, there is no critical engine. Interestingly, an examination of aviation history reveals counter-rotating configuration is actually rarely applied. Albeit safer, its primary drawback is that production is more expensive, as it must feature two engines and propellers that are dissimilar because they rotate in opposite directions. This downside could be mitigated with the adoption of electric motors: a brushless electric motor can spin clockwise or counter-clockwise with the same performance without any productive difference. This way, only propellers would be different.

Operating a conventional twin-engine with counter-rotating propellers results in greater expenses, as engine parts are no longer interchangeable. Conversely, the designer should size the control system and surfaces to handle the critical engine in case of propellers rotating in the same direction. Among the produced aircraft, Piper *PA-31*, *PA-34 Seneca*, Beechcraft *Model 76 Duchess*, and Diamond *DA-42 Twinstar*, all feature counter-rotating piston engines. On the contrary, it is interesting that large airplanes typically do not feature propellers that rotate in opposite direction. This is an example of a design choice that focuses on reducing maintenance costs in lieu of piloting ease in emergency condition.

Chapter 4

AeroSwitch concept

4.1 Genesis of the concept

AIAA 2020 Graduate Team Aircraft Design Competition request for proposal [26] required a two-aircraft trainer family, one single-engine and one multi-engine, with maximum parts commonality. Therefore, the objective was to achieve 100% commonality between the two aircraft, namely design and build just one exemplar that fits both category and can train pilots either for single-engine or multi-engine rating.

4.1.1 *Trybrid* overview

Proposed aircraft was the *Trybrid* [7], a serial hybrid-electric aircraft (an example of the architecture is shown in Figure 4.1) with 6 electric motors distributed on the wings, sized to perform the required missions.

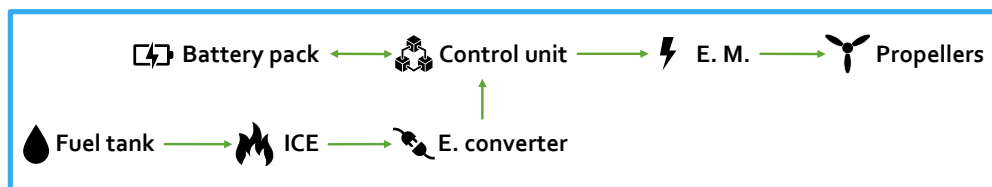


Fig. 4.1: Serial hybrid-electric architectural schematic example

It exploits the hybrid-electric propulsion to overcome the dualism between single-engine and multi-engine aircraft. Technically multi-engine, it is also flyable as a single-engine under all respects (including typical flight characteristics and handling qualities) by a single-engine rated pilot. Furthermore, it is capable of flying even at 160 knots true airspeed and up to FL230 in full instrument meteorological condition. It is equipped with anti-ice system and autopilot, while hybrid propulsion guarantees a hourly cost well below its competitors. Finally, *Trybrid* can be easily converted to pure-electric propulsion, conveniently trading off range performance with higher comforts standards and lower operating costs.

A graphical representation of *Trybrid* is shown in Figure 4.2.



Fig. 4.2: Rendering of *Trybrid*

The AeroSwitch concept, developed to fulfill the design requests, led to the application of an Italian patent [27] (currently pending) and the participation in *Switch2Product* innovation challenge. The developed idea is extensively described in next sections (several figures are directly taken from the submitted document).

4.2 Design requirements and concept development

General Aviation is made up of single-engine and multi-engine aircraft. A ME typically have higher performance, but above all is safer than a SE thanks to the lower probability of total power loss. Anyway, these are more expensive to operate and maintain, and this is reflected in the fact only 9% of propeller-driven GA airplane was twin-engine in 2018 [28], despite being safer. Being able to combine SE and ME advantages into one singular concept, it could be a potential success.

The AeroSwitch concept consists of the in-flight simulation of SE behavior. In this framework, an even number of electric motors are placed symmetrically with respect to the longitudinal axis and SE or ME flight modes are obtained via software and hardware implementation. Electric motors on the left and right side spin in the opposite direction. It must be avoided that a SE rated pilot or student pilot finds himself into an asymmetric thrust condition, which would be extremely dangerous.

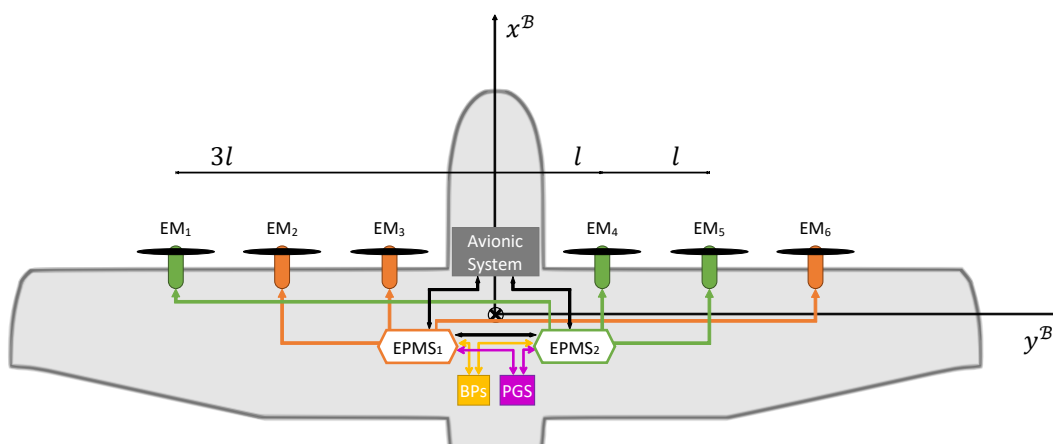


Fig. 4.3: *Trybrid* propulsive system architectural schematics

In the patent application, different configurations of motors were considered, while in developing the *Trybrid*, the one with 6 EMs was selected. The system exploits the benefit of electric motors to provide up to 150% non-continuous power for some minutes, if well cooled [11].

To forestall the event of asymmetric flight with a single-engine pilot rated on-board, a specific system logic and redundancy of the electric motors management is developed, as outlined in Figure 4.3. Battery packs and PGS are managed by two distinct Energy and Propulsion Management System (*EPMS*), collaborating and communicating one each other and with the avionic suite. The *EPMS*s are responsible for feeding EMs and for the entire power and energetic management, charge or discharge of BPs, PGS management and 6 independent electric motor throttling regulations. One *EPMS* is responsible for 3 electric motors, placed so that their equivalent moment is zero, as described by Equation (4.1):

$$\begin{cases} \sum_{i=1}^6 \mathcal{N}_{CG}^{EM_i} = 0 \\ \mathcal{N}_{CG}^{EM_1} = \mathcal{N}_{CG}^{EM_4} + \mathcal{N}_{CG}^{EM_5} \quad \wedge \quad \mathcal{N}_{CG}^{EM_2} + \mathcal{N}_{CG}^{EM_3} = \mathcal{N}_{CG}^{EM_6} \end{cases} \quad (4.1)$$

Even in case of failure of one *EPMS*, 50% of continuous power is still available and capable of granting symmetric flight. Moreover, by enforcing non-continuous power, previous percentage can rise to 75%.

In this specific architecture, the two *EPMS* units are not in a redundant configuration, but in a cooperant one. This strategy is lighter, simpler, cheaper and still represents a safe solution in case of one *EPMS* failure, as residual thrust is sufficient to satisfy climb prescriptions from FAA FAR-23 and EASA CS-23 specification [29].

*EPMS*s embed a small inertial unit with MEMS (Micro Electro-Mechanical Systems). Their accuracy and reliability are enough for the purpose, as they are used to keep sideslip angle β equal to zero when needed.

An example of feedback control logic is presented in Figure 4.4. This logic can be implemented via a PID or LQR controller.

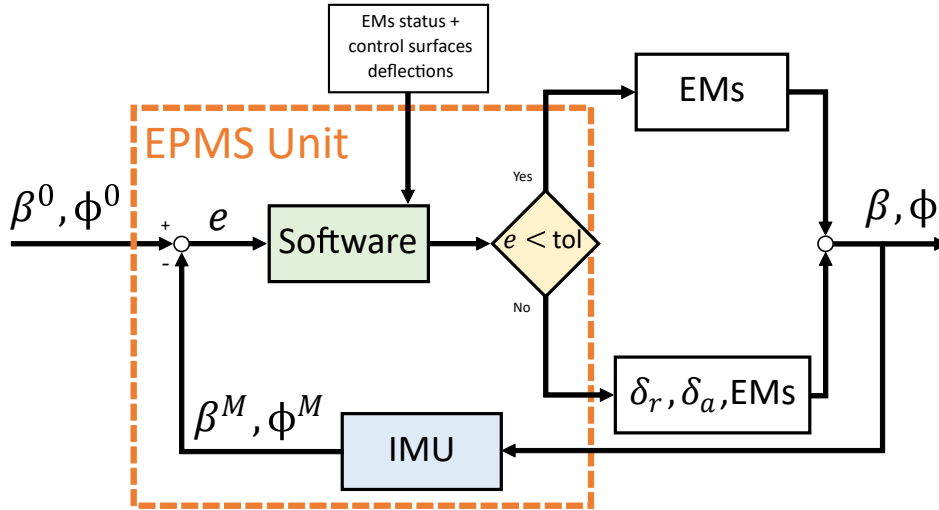


Fig. 4.4: *EPMS* unit feedback loop example

Propeller design could take advantage of electric propulsion being foldable. Thanks to foldable propellers, the system can switch-off pairs of EMs, depending on power required at the moment. This leads to a drag reduction in cruise and to employ remaining EMs at higher efficiency. Propellers can close at slow rotational speed, as blades remain open thanks to centrifugal force, hence motor controllers can simply impose to stop rotation for blade closure.

*EPMS*s are responsible for failure identification and management. Potential malfunctions are:

- communication lost with avionic suite or other *EPMS* unit;

- one motor struck or malfunctioning, or a propeller broken, or electrical connection lost, identifiable comparing electric current normally needed with the actual one;
- battery pack malfunctioning or PGS failure or sub-optimal functioning.

EPMSs must identify the situation, take the right corrective action and communicate it to the pilot. The units also include a Health and Usage Monitoring System (HUMS) for BPs, PGS, EMs and electrical systems, which records abnormal parameter values. This whole integrated system increases the overall safety level. Chance of full power loss is really unlikely compared to conventional aircraft, especially SE ones, and must be the result of multiple failures. This aspect is certainly a driver over certification restriction.

EPMS schematic interconnection is outlined in Figure 4.5.

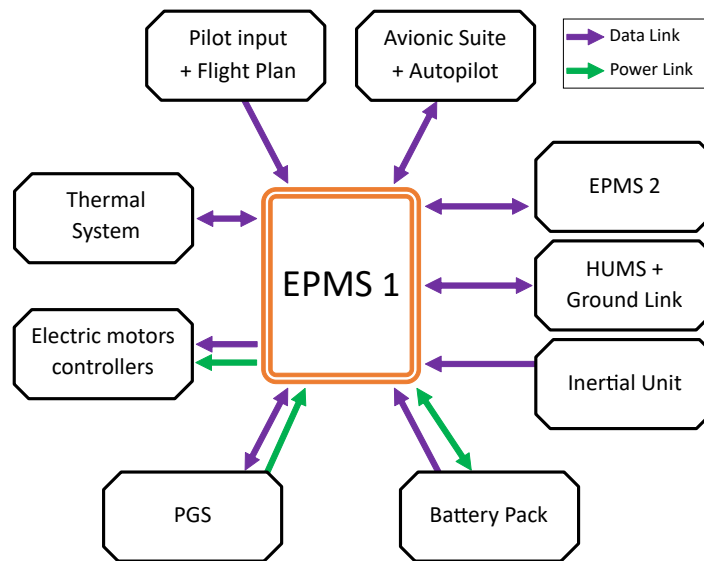


Fig. 4.5: *EPMS* unit connections

4.2.1 Pilot interface

The PIC can switch between SE or ME mode via the MFD only on ground before starting operations. PFD must show the selected mode all the time in a clear and unmistakable way. Moreover, the pilot can choose the preferred energetic strategy for the mission, or leave the decision to *EPMSs*. PFD and MFD show fictitious parameters based on the selected flight mode, for instance manifold pressure for one or two engines, one or two propellers RPM and so on.

Each propulsive side has its own thrust lever and they are normally joined together. Their position will not be directly related to the rotational speed of electric motors, but to the needed power, in percentage of the total available. They will also account for non-continuous power adjustment.

During training, flight instructor will assist the student pilot formation via MFD. Failures can be injected so that the student response could be tested. An emergency "Panic Button" on-board could give authority to the system to exit from an accidental spin, acting motors with differentiated thrust.

4.2.2 Single-engine mode

As outlined in Chapter 3, the main difference between SE and ME aircraft is that single-engine aircraft is not symmetric. Propeller rotation induces a slipstream on aircraft fuselage and tail, that creates a yawing moment, shown in terms of sideslip angle β . The airframe is built non-symmetric in order to compensate this effect in cruising regimes, while in low-power or high-power regimes pilot have to act on rudder to keep β close to zero. β angles developed in this way are small, and not a particular issue for pilots of any experience. This behavior is simulated by *EPMSs* acting differently on one of the outboard motors, for instance asking 95% of power instead of 100% when adding power. In descent *EPMSs* could close 5 propellers out of 6. Differential power ratios have to be tested in flight test campaign. An example of SE configuration working logic is reported in Figure 4.6.

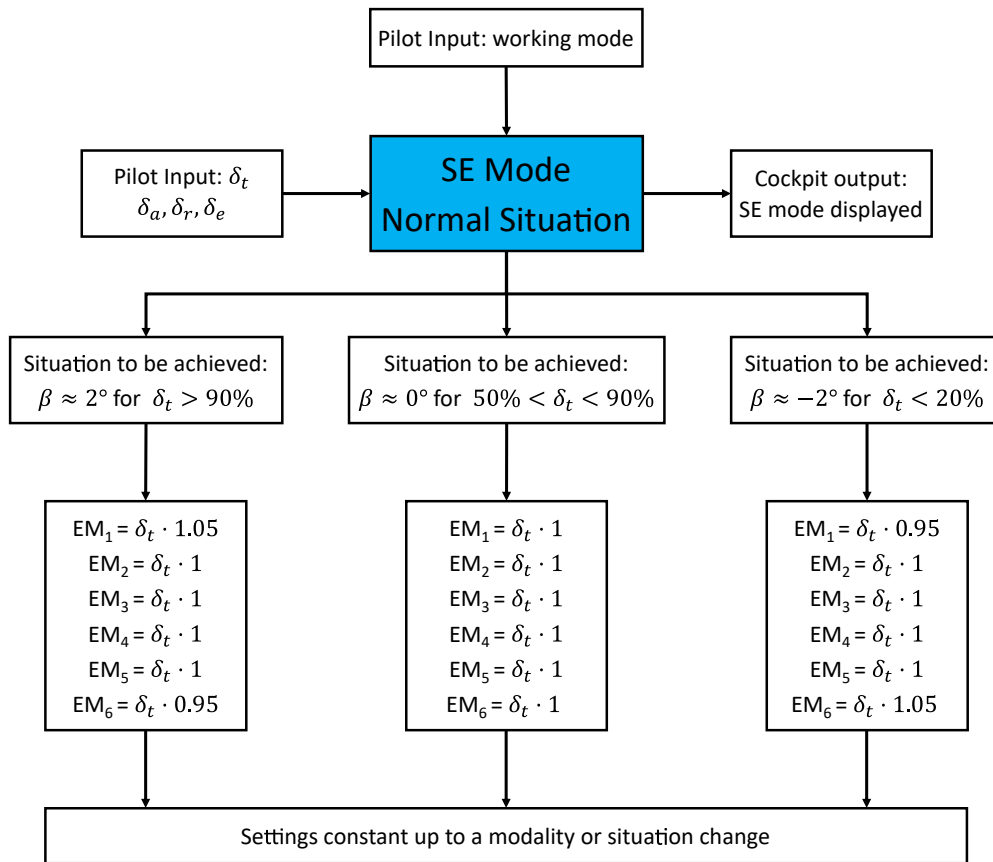


Fig. 4.6: Working logic for SE mode - Normal Situation

Thrust levers are by default locked together. In case of a differential setting, *EPMSs* will consider the major demanding one.

Gyroscopic effect due to propeller rotation of a single-engine airplane could be even simulated acting differently on the electric motors when maneuvering. Furthermore, normal reciprocating engine working mode can be simulated, introducing a loss of available power with increasing altitude or a different power supply curve.

Emergency Situation

In a multi-engine framework, a One Engine Inoperative (OEI) condition is an emergency situation in which one engine fails and remaining one(s) generate a yawing moment due to the

asymmetric thrust condition. This situation is hazardous, and ME-rated pilots are trained to handle it. The asymmetric condition is way bigger than the one generated by propeller spinning on a SE airplane. A SE-rated pilot is not trained to deal with OEI, therefore it is not admissible to fly in an OEI situation with a single-engine rated pilot or student pilot.

Potential threats for the SE mode are:

- Motor failure, propeller failure, bird-strike: these three situations share the same output, namely thrust asymmetry. *EPMSs* will handle this collecting data from the embedded inertial platform, managing power supplied to each motor to keep zero sideslip. In case this is not enough (motors are at their critical temperature or power value, or all three motors on one side are inoperative) *EPMSs* will also command autopilot rudder and ailerons to prevent sideslip. This could also work for a minor structural damage resulting in an asymmetric drag. An application example is reported in Figure 4.7.

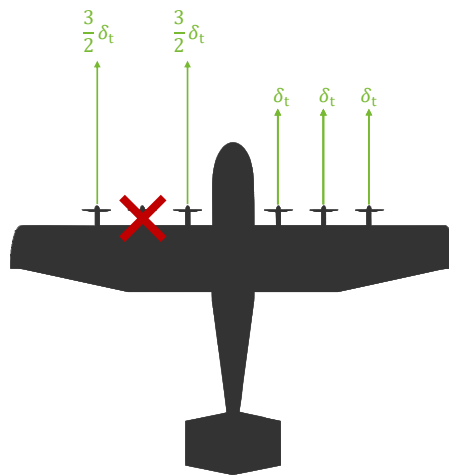


Fig. 4.7: Application example for the case of One Electric Motor Inoperative in SE mode

- One *EPMS* failure: this only affects maximum power available, because, as previously stated, one thrust line can sustain symmetric flight; this is shown in Figure 4.8.

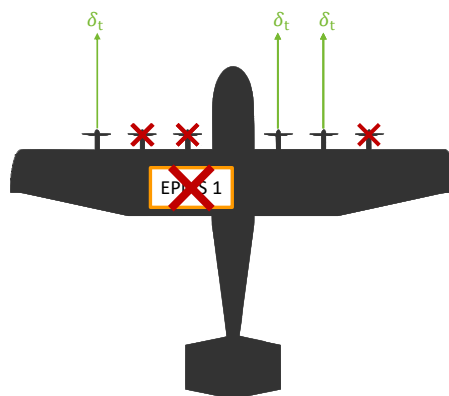


Fig. 4.8: Application example for the case of *EPMS* fail

- Hardware or software *EPMS* malfunction: the single *EPMS* enters in a downgraded working logic. The same thrust percentage is applied to each EM. Alternatively, it is automatically switched off, leaving total control to the other unit.

- Minor structural damage: in case of a minor damage, an asymmetric drag could derive. This would be corrected by the EPMSs as mentioned above.

For every situation, acoustic and graphical alerts will warn the pilot to assure situational awareness. A logic scheme for emergency situation in SE mode is outlined in Figure 4.9.

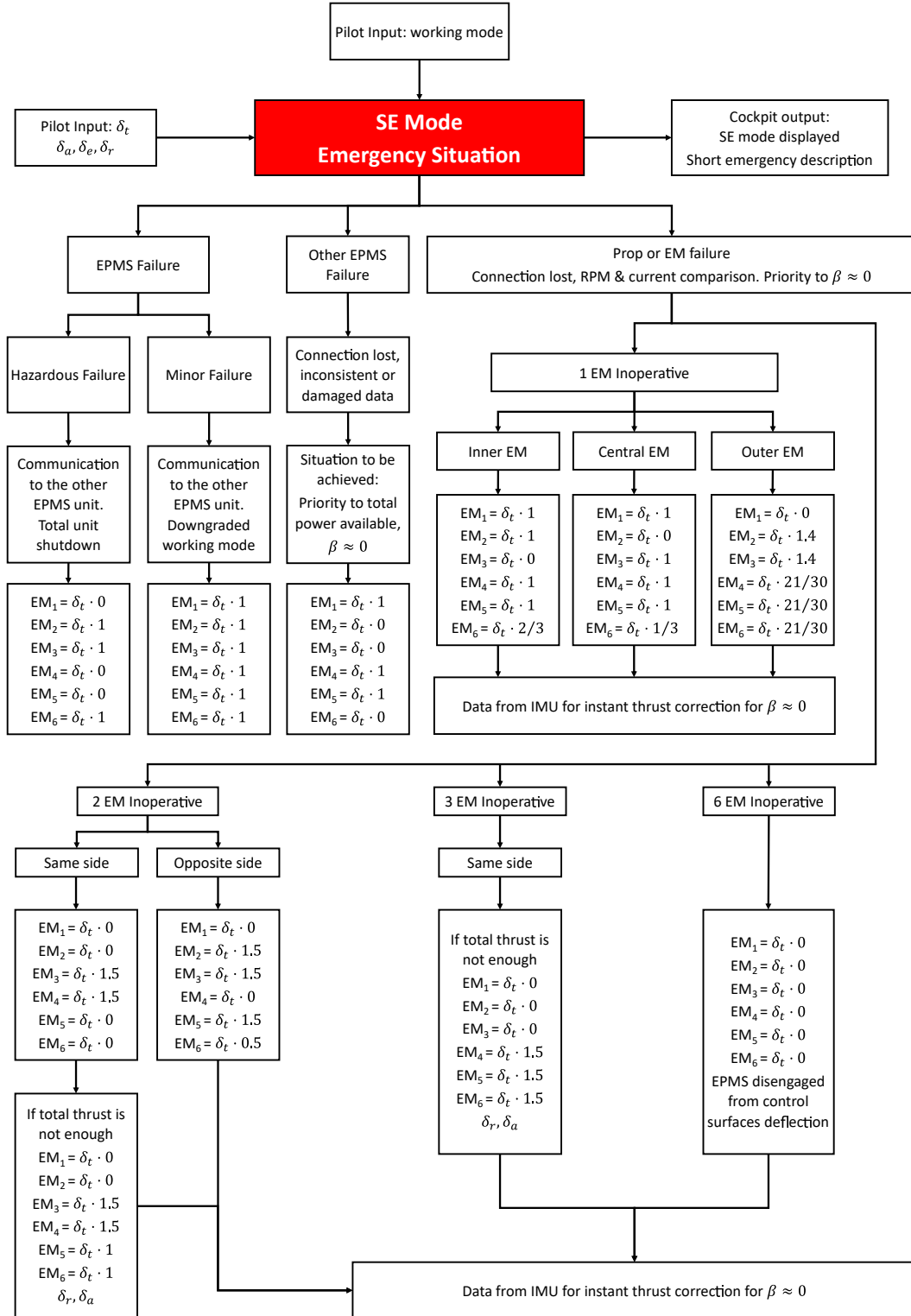


Fig. 4.9: Working logic for SE mode - Emergency Situation

4.2.3 Multi-engine mode

Multi-engine configuration works in a much simpler fashion, as there is no need to simulate unwanted propulsive effects as for SE mode. Thrust levers can be unlocked and used independently, for training or other purposes. PIC has the complete authority on aircraft behavior.

A multi-engine rated PIC must be capable of handling asymmetric thrust due to motor failure. Nevertheless, pilot workload in emergency has a significant impact on safety. The same strategy for SE emergency situation is adopted, unless the pilot explicitly decides to bypass it.

Logic for normal and emergency operations are respectively explained by figures 4.10 and 4.11.

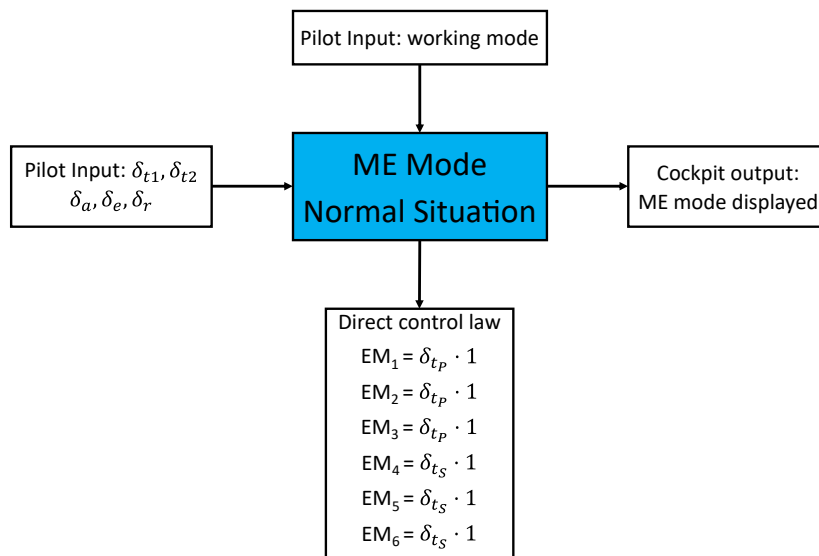


Fig. 4.10: Working logic for ME mode in normal situation

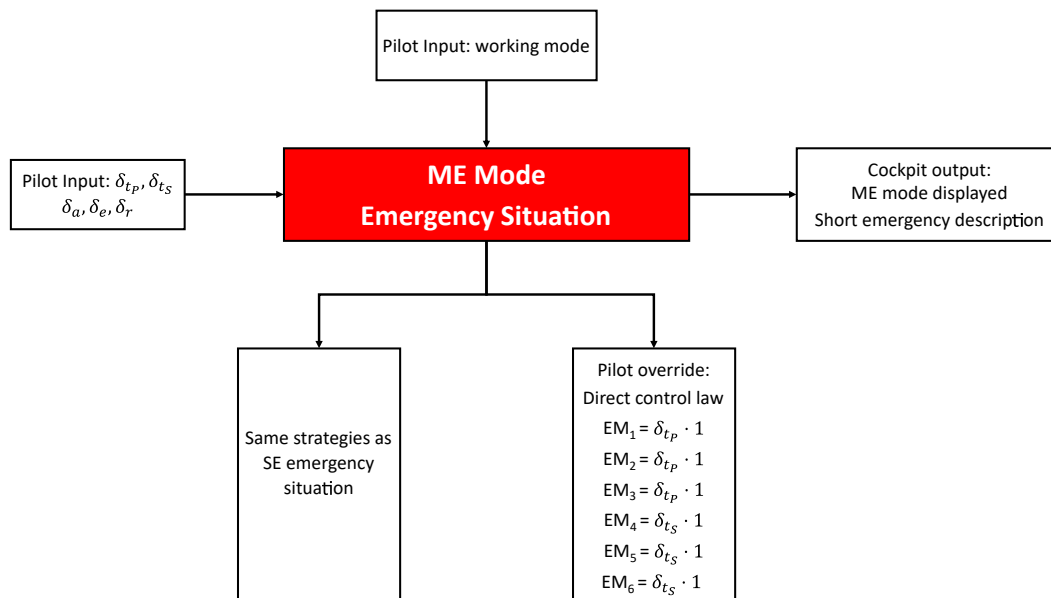


Fig. 4.11: Working logic for ME mode in emergency situation

4.2.4 Turbine simulation

It is also possible for both switch modes to simulate turbine engine behavior. This primarily accounts for engine spool-up time, forcing student pilots to make high-RPM approach. Secondly, virtual turbine engine parameters should be displayed on PFD and MFD. This mode could also simulate speedbrakes with differential but symmetrical use of the electric motors, up to the limit of reverting some motor spinning direction.

4.2.5 Comfort enhancer

For every working configuration, a comfort enhancement mode is available. This will employ *EPMSs* to suppress Dutch-Roll mode and provide automatic turn coordination with differential electric motors actuation, and to reduce noise and vibrations as far as feasible.

4.3 Concept effectiveness

Equilibrium equations can be enforced to determine differential power required for SE simulation and resultant flight attitude. Simulation scope was to prove the conceived system let the aircraft behave as expected in SE mode. Some characteristic working conditions are reported in Table 4.1, combining values of airspeed and differential propeller thrust.

CAS [kn]	Differential thrust	α [deg]	β [deg]	δ_r [deg]	δ_a [deg]
100 kn	10%	4.38	0.74	-0.98	-0.06
100 kn	25%	4.38	1.86	-2.46	-0.17
68 kn	10%	11.55	1.83	-2.42	-0.16
132 kn	10%	2.25	2.25	-0.56	-0.04

Tab. 4.1: Trim solution for several flight conditions for SE simulation

The asymmetry needed to generate the yawing moment can be produced acting on a singular motor (10% less power on motor #1) or on two (-5% on motor #1 and +5% on #6). The latter allows to reach full nominal thrust.

Sideslip angle induced with SE simulation strongly depends on airspeed and the overall behavior perfectly reflects that of real single-engine aircraft in all aspects. For example, with a 10% thrust disequilibrium at low speed SSA is greater than at high speed. Induced roll angle, and consequently required aileron deflection, is one order of magnitude smaller than induced azimuth angle variation, while longitudinal dynamics is not affected by thrust disequilibrium, until total supplied power is constant. This overall behavior perfectly reflects that of real single-engine aircraft.

Chapter 5

Preliminary investigation

5.1 Definition of axes and angles

The aerodynamic forces and moments on an aircraft are produced by the relative motion with respect to the air and depend on the orientation of the aircraft with respect to the airflow. Therefore, it is necessary to define two different coordinate systems: body-axes and wind-axes.

In accordance with most common notation [30], the body coordinate system centered in aircraft center of mass has its x-axis parallel to the fuselage reference line and its z-axis in the aircraft plane of symmetry. Applying a left-handed rotation around the body y-axis through angle of attack α , an intermediate coordinate system is obtained: stability-axes. The wind coordinate system is obtained from the stability-axes system by a rotation around the z-axis that aligns the wind x-axis directly into the relative wind: the angle of rotation is exactly sideslip angle β . Angle of attack and sideslip angle are also referred to as aerodynamic angles, whose sign convention is graphically depicted in Figure 5.1.

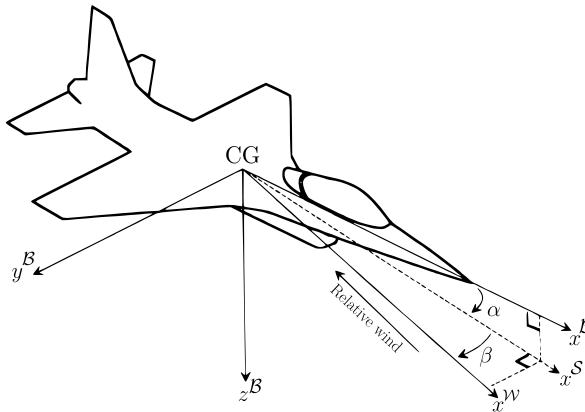


Fig. 5.1: Definitions of axes and aerodynamic angles

Being aircraft velocity vector in body components $\mathbf{V}_{CG}^B = \{u \ v \ w\}^T$, sideslip angle may be obtained from Eq. (5.1),

$$\sin \beta = \frac{v}{V} \quad , \quad (5.1)$$

where $V = |\mathbf{V}_{CG}^B|$.

Body coordinate system can be visualized performing a sequence of rotations to Earth local reference frame (apex \mathcal{E}). Adopting North-East-Down (NED) convention, the sequence of rotation to get body frame is:

1. right-handed rotation about z-axis, or positive ψ (azimuth)
2. right-handed rotation about the new y-axis, or positive θ (pitch)
3. right-handed rotation about the new x-axis, or positive Φ (bank)

Defining $\mathbf{C}_{\mathcal{B}/\mathcal{E}}$ as the rotation matrix that transforms the coordinate of the velocity vector from NED system to body system,

$$\mathbf{V}^{\mathcal{B}} = \mathbf{C}_{\mathcal{B}/\mathcal{E}} \mathbf{V}^{\mathcal{E}} \quad . \quad (5.2)$$

Rotation matrix eventually assumes the expression reported in Eq. (5.3),

$$\mathbf{C}_{\mathcal{B}/\mathcal{E}} = \begin{bmatrix} \cos \theta \cos \psi & \cos \theta \sin \psi & -\sin \theta \\ -\cos \Phi \sin \psi + \sin \theta \sin \Phi \cos \psi & \sin \theta \sin \Phi \sin \psi + \cos \Phi \cos \psi & \cos \theta \sin \Phi \\ \sin \theta \cos \Phi \cos \psi + \sin \Phi \sin \psi & \sin \theta \cos \Phi \sin \psi - \sin \Phi \cos \psi & \cos \theta \cos \Phi \end{bmatrix} \quad . \quad (5.3)$$

5.1.1 Sign conventions

For avoidance of any doubt, sign conventions of parameters such as deflection of control surfaces is reported in Table 5.1, to be consistent in the whole document.

Parameter	Positive sign convention
β	Right wing leading into sideslip
Φ, θ, ψ	Right-hand rule
δ_a	Right aileron trailing edge down (left turn)
δ_e	Elevator trailing edge down
δ_f	Downward deflection
δ_r	Rudder trailing edge deflected towards left wing Left pedal

Tab. 5.1: Sign convention table

5.2 Sideslip angle estimation

Sideslip angle could be measured using a Pivoted-vane sensor, externally mounted. One of the main problems is that the measurement of the sideslip angle at the place of installation of the sensor sometimes significantly differs from actual values. In addition, the accuracy of a typical mechanical sensor is small. Besides, sometimes there is not enough room to fit a typical sensor as in the case of the aircraft scale model used as demonstrator for AeroSwitch concept.

Therefore, it was necessary to rely on methods for estimation of sideslip angle through the measurements of other parameters. These approaches are described in sections 5.2.1 and 5.2.2, whose validation is discussed in Section 5.5.1.

5.2.1 INS method

The method here reported is taken from [31]. The main assumption on which it is based is the absence of wind, meaning speed relative to the ground matches true airspeed. Speed components in NED system are measured by a GNSS receiver and converted through matrix

transformation into body system components, provided that attitude and heading angles are known through an Inertial Navigation System (INS). This can be exploited by an inexpensive AHRS (Attitude & Heading Reference System).

The process of determination of the sideslip angle is based on the measurement of $V_N, V_E, V_D, \theta, \Phi, \psi$, so that Eq. (5.4) can be adopted,

$$\begin{pmatrix} u \\ v \\ w \end{pmatrix} = \mathbf{C}_{\mathcal{B}/\mathcal{E}} \begin{pmatrix} V_N \\ V_E \\ V_D \end{pmatrix} , \quad (5.4)$$

enforcing rotation matrix reported in Eq. (5.3).

Once velocity components in body system are retrieved, sideslip angle estimation is straightforward enforcing Eq. (5.1). The only disadvantage of this method can be the dependence from a GNSS receiver, which provides a relatively slow delivery of components of linear speed (usually every 1 s), and is prone to momentary interruptions in communication with space-based segment.

5.2.2 MAG method

An alternative method to derive sideslip angle is via comparison of track angle, obtained from GNSS velocity measurement, with true heading angle. This latter could be delivered by the INS, being ψ itself. Alternatively, and more conveniently, it can be derived from the readings of a magnetometer. In fact, the reconstructed vector points to the local magnetic North, thus delivers magnetic heading ψ_{MAG} . It is then necessary to apply calibration, accounting for magnetic declination d (depending on position on Earth's surface and changing over time) and deviation δ (error induced by nearby metallic objects), to refer the measurement to true North. Compass heading conversion is applied through Eq. (5.5),

$$\psi = \psi_{MAG} + \delta + d \quad . \quad (5.5)$$

As long as wind is absent, since it would otherwise introduce drift, sideslip angle is just the difference between track angle and true heading, with conventions in accordance to what was discussed in Section 5.1. Track angle χ is the angle between North and East components of velocity vector on horizontal plane, V_N and V_E , thus could be derived enforcing Eq. (5.6),

$$\chi = \tan^{-1} \left(\frac{V_E}{V_N} \right) \quad . \quad (5.6)$$

There is no other obstacle for determination of sideslip angle:

$$\beta = \chi - \psi \quad . \quad (5.7)$$

5.3 Correction for the effect of the wind

Sideslip angle describes the orientation of the aircraft longitudinal axis with respect to the airspeed vector. The presence of the wind is responsible for the incongruity between true airspeed and the value of velocity returned by GNSS receiver. True airspeed must be derived from air data: TAS is obtained from impact pressure measured by Pitot-static probe, static pressure available from static port and temperature delivered by OAT sensor.

The following dissertation is based on the assumption that wind has no vertical component. This simplification is typically legit, since vertical winds are short-lived and inconsistent. It implies only horizontal components are compensated, meaning the objective of this method is

to determine wind components V_{W_N} and V_{W_E} (local North and East to be consistent with GNSS data, given in NED frame). Once these have been estimated, the air mass velocities must be transformed in the body axis via the rotation matrix:

$$\begin{Bmatrix} \hat{u} \\ \hat{v} \\ \hat{w} \end{Bmatrix} = \mathbf{C}_{B/\mathcal{E}} \begin{Bmatrix} V_N - V_{W_N} \\ V_E - V_{W_E} \\ V_D \end{Bmatrix} . \quad (5.8)$$

Sideslip angle estimation applies the same equations of the case with no wind. Equation (5.1) is still valid, enforcing \hat{u} , \hat{v} and \hat{w} , corrected for wind:

$$\sin \hat{\beta} = \frac{\hat{v}}{\sqrt{\hat{u}^2 + \hat{v}^2 + \hat{w}^2}} . \quad (5.9)$$

Wind estimation could be used to correct the value of track angle as estimated by the approach discussed in Section 5.2.2:

$$\hat{\chi} = \tan^{-1} \left(\frac{V_E - V_{W_E}}{V_N - V_{W_N}} \right) , \quad (5.10)$$

from which,

$$\hat{\beta} = \hat{\chi} - \psi . \quad (5.11)$$

In conclusion, several approaches have been followed to select suitable values for wind speed component V_{W_N} and V_{W_E} , reported in the following sections. From these variables it is possible to derive wind intensity V_W and the direction from which it is blowing ψ_W , easily comparable with measurements of weather ground stations.

5.3.1 AGARD method

AGARD (Advisory Group for Aerospace Research and Development) proposed a method for computation of wind speed and direction, exploiting error minimization between combination of true airspeed and wind speed and the measured ground speed [31]. According to this method, North and East wind components are the ones that minimize the sum of the squares of the residual errors between measured true airspeed and its reconstruction from GNSS velocity components, over a defined period of time, namely:

$$ERR_i := \sum_{j=i-I}^{i+I} \left[V_j^2 - (V_{N_j} - V_{W_N})^2 - (V_{E_j} - V_{W_E})^2 - V_{D_j}^2 \right]^2 . \quad (5.12)$$

Values for V_{W_N} and V_{W_E} are chosen to minimize this error, which will occur when the following partial derivative equations are equal to zero:

$$\begin{cases} \frac{\partial ERR_i}{\partial V_{W_N}} = \sum_{j=i-I}^{i+I} \left[V_j^2 - (V_{N_j} - V_{W_N})^2 - (V_{E_j} - V_{W_E})^2 - V_{D_j}^2 \right]^2 (V_{N_j} - V_{W_N}) = 0 \\ \frac{\partial ERR_i}{\partial V_{W_E}} = \sum_{j=i-I}^{i+I} \left[V_j^2 - (V_{N_j} - V_{W_N})^2 - (V_{E_j} - V_{W_E})^2 - V_{D_j}^2 \right]^2 (V_{E_j} - V_{W_E}) = 0 \end{cases} . \quad (5.13)$$

These two equations for the two unknowns V_{W_N} and V_{W_E} can be easily solved numerically through Newton-Raphson method (assembling Jacobian with finite differences), minimizing the error at each i -th instant of time, considering a suitable number I of samples before and after. This is possible as long as the analysis is performed offline, whereas real time application of the method would need to leverage only previous samples.

5.3.2 Sideslip-reset method

The method previously described for the determination of intensity and direction of wind is accurate as long as the conditions do not change much at a local scale. Conversely, in case of gusts this method is no longer effective and thus delivers erroneous estimations, which translate into sideslip angle different from zero at trim. This undesired behavior emerged from the real aircraft flight test activity and paved the way to the need for an alternative method for wind estimation. The other suggestion was that the flight test aircraft native instrumentation provided itself an estimation of wind, delivering results much different from the ones obtained through AGARD method. As will be demonstrated in Section 5.7.1, this incongruity translated into different values of estimated sideslip angle with different methods. Furthermore, at the start of the FTT (Flight Test Technique) for induction of propeller effect, the value of sideslip is hardly ever close to zero after correcting for wind with AGARD method. This error is instead smaller if enforcing the wind estimation of aircraft instrumentation suite.

Therefore, an alternative method for wind estimation was developed, so that at trim, prior to imposition of maximum throttle, corrected sideslip angle is zero. This assumption is based on the ideal behavior of the aircraft, **as if flying perfectly symmetrically when trimmed**. Of course the inherent asymmetry of the aircraft, unwanted pilot commands or other sources of discrepancy from symmetric flight model would be a detriment for this assumption, but for the sake of this analysis it is well posed. Similarly, the other legit assumption is that the wind estimated at the start of the technique is unchanged for the whole duration of the test point.

More in detail, this method still aims to determine two unknowns V_{W_N} and V_{W_E} . This time the conditions imposed are:

$$\begin{cases} \mathbf{V}_{GS} = \mathbf{V} + \mathbf{V}_W \\ \hat{\beta} = \hat{\beta}(V_{W_N}, V_{W_E}) = 0 \end{cases}, \quad (5.14)$$

in which $\hat{\beta}$ is derived from Eq. (5.9), thus function of V_{W_N} and V_{W_E} .

First equation translates into the condition:

$$V_{TAS}^2 = (V_N - V_{W_N})^2 + (V_E - V_{W_E})^2 - V_D^2. \quad (5.15)$$

As a summary of sideslip and wind estimation, synthetic flowchart depicted in Figure 5.2 shows the alternative methods evaluated (in bold the path eventually followed). Blue dashed arrows are data links from instrumentation.

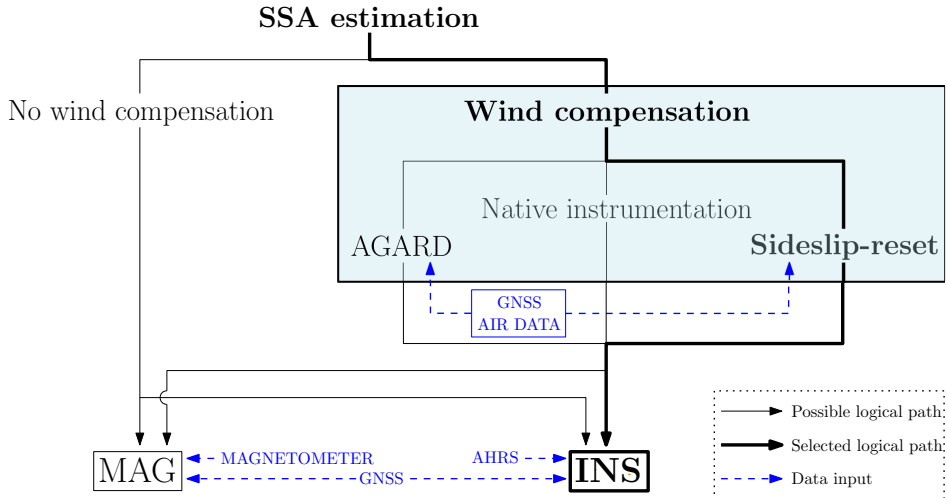


Fig. 5.2: Flowchart for the estimation of SSA

5.4 Beta-testing

The premise upon the current work is that single-engine aircraft experience an asymmetric flight condition induced by the rotation of the propeller, more evident when increasing power.

This effect should be quantitatively investigated, but unfortunately it seems there is no direct reference in literature (apart from qualitative observations, reported in Section 3.1). As a consequence, it was necessary to carry out a flight test activity aiming at investigating this phenomenon. This was done at first by means of a computer flight simulator, but main contribution was offered by a flight test mission on a real aircraft.

The purpose of "Beta-testing", as the whole activity can be recalled, was to determine SSA (at a later stage also bank angle, Φ , and time derivative of the azimuth angle, $\dot{\psi}$) resulting from propeller spinning at full power setting at different flying speeds. This kind of testing is not present in any regulatory framework (CS or FAR), neither in literature. As a consequence, a proper flight test technique (FTT) needed to be invented. Actually, two alternatives were deployed:

- **constant speed** FTT: power is raised to max continuous value, only acting on the elevator control to perform a climb with constant IAS. This technique has the advantage of avoiding possible engine and airframe over-speeds; main risk is related to engine and oil temperatures in case of too long prolonged max continuous power condition.
- **constant altitude** FTT: power is raised to max continuous value, with attitude changed to perform a wings level acceleration with constant altitude. This technique is more hazardous, since it could lead to engine and airframe over-speeds.

Both constant airspeed and constant altitude methods can be carried out with controls (ailerons and rudder) free or fixed. Trials consist of the following steps:

1. trim the aircraft at selected IAS and altitude;
2. keep rudder and aileron deflection to zero in stick-fixed or free in stick-free configuration while executing the maneuver;
3. set throttle to full power, trying to keep constant IAS (altitude increasing) or constant altitude (IAS increasing);
4. after a few seconds regain attitude, trim speed and previous heading

5.5 Computer flight simulator

The contribution of the flight simulator to the present work has been fundamental to have a first insight of the phenomenon investigated. Software *X-Plane* 11 [32] has been preferred to other alternatives. Its main advantages are precise and detailed simulation of flight physics and the possibility for the user to extract data logs of the mission, ready for manipulation.

Several tasks were completed with simulation software. First of all, it served as a way to familiarize with the problem of sideslip generation on a single-engine propeller-driven aircraft. This was done flying the truthful realization of Cessna *172 Skyhawk* aircraft, the one with greatest commonality with scale model among built-in exemplars. Familiarization

was followed by a rigorous FT activity, precursor of the test carried out on the real aircraft. Furthermore, the simulator was used to validate the methods described in Section 5.2 for sideslip angle estimation. Both of the techniques described in Section 5.4 were employed. It was also observed that the active aileron correction leads to magnitude reduction in the parameters of interest. Therefore it was decided to minimize this correction to preserve the arise of the sought phenomenon.

5.5.1 Validation of methods for sideslip angle estimation

In order to validate the procedures described in sections 5.2.1 (INS method) and 5.2.2 (MAG method) for sideslip angle estimation, it was eventually chosen to compare the results of these methods to the value of sideslip angle delivered as an output of simulation software. The validation was obtained flying a mission in complete absence of wind, choosing as test aircraft the virtual realization of Cessna 172.

X-Plane exports logs of flight data. In particular, it stores all necessary quantities for estimation of SSA (with sampling time ≈ 0.1 s):

- GNSS velocity components in an unusual coordinate system: East-Up-South. Moreover, the reference point of the frame is the NW corner of the map of the scenario of the flight.
- latitude, longitude, altitude;
- pitch, bank, azimuth angles;
- compass heading, automatically derived converting magnetic heading measured by a magnetometer.

Manipulation of GNSS velocity was necessary to refer the vector to local NED reference system. This was done with intermediate transformation into ECEF (Earth-centered-Earth-fixed) coordinate reference system, through *Matlab*'s function `enu2ecefv`. This operation required knowledge of latitude and longitude of reference point of the map, which could be easily obtained as the differences between the values of latitude and longitude at a considered time instant and the simultaneous position on the reference system, converted into an angular offset. Then, from ECEF frame *Matlab*'s function `ecef2nedv` returned components of velocity vector in local NED reference system. This whole manipulation served to remove the error (negligible but still present) related to the difference in orientation of the local tangent plane throughout the map, with respect to the one centered in the reference point.

Having obtained V_N, V_E, V_D at each specific time instant, implementation of both methods using INS and GNSS or magnetometer and GNSS was straightforward. Figure 5.3 shows how the methods deliver similar results if performing a trial with constant speed in absence of wind, with higher accuracy of INS method (if compared with the value of sideslip reported by the simulator itself). As a consequence, INS method has been selected as first choice for sideslip determination.

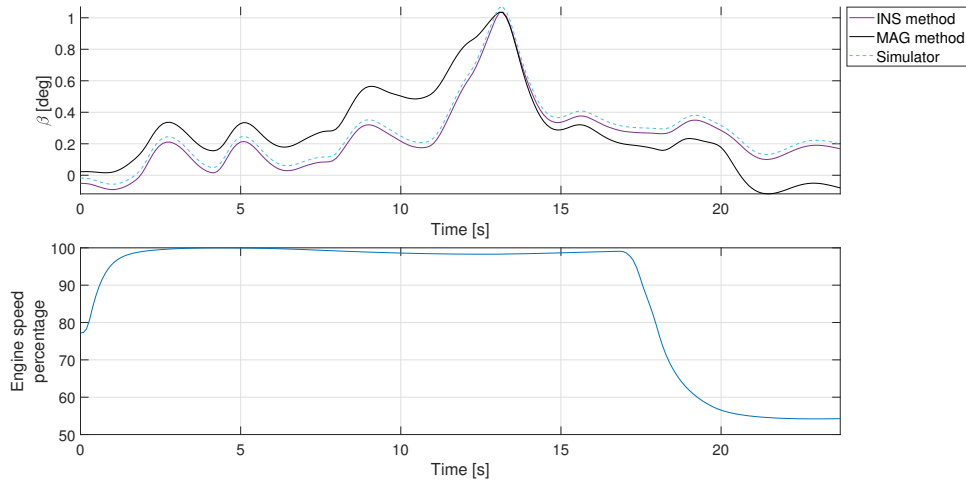


Fig. 5.3: Comparison of INS and MAG methods

A further interrogative was the ability for wind correction methods to successfully estimate sideslip angle in case of constant wind. Actually, it was previously necessary to verify that the knowledge of true wind could lead to truthful results. This is demonstrated in Figure 5.4, referred to a trial with a constant speed of 65 knots, in which constant wind of intensity 5 knots blowing from East was enforced. By setting these known parameters in the algorithm, it is evident how this solution delivers astonishingly good results, which would not be possible if neglecting wind with baseline algorithm (violet curve in Figure 5.4).

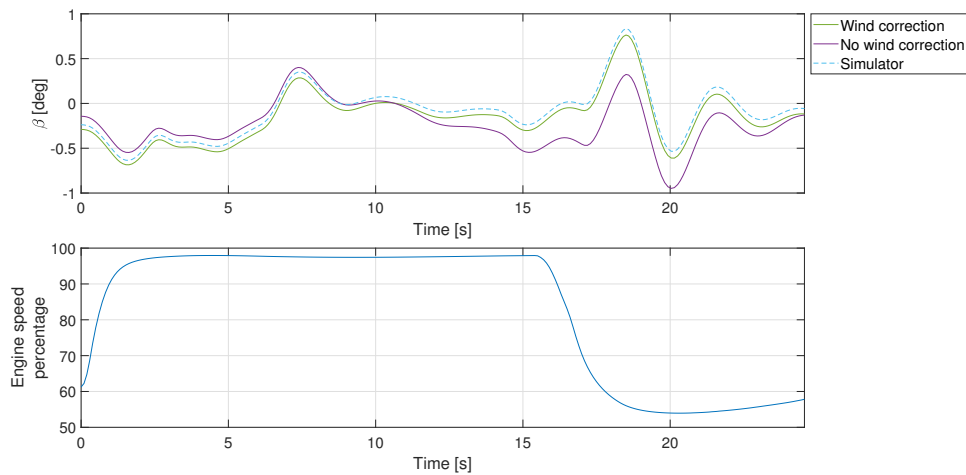


Fig. 5.4: Wind correction verification

At a later stage, it was necessary to verify the methods for wind estimations could provide accurate results on the same trial. Table 5.2 assesses this is possible with both AGARD and Sideslip-reset methods.

Method	V_W [kn]	ψ_W [deg]
Simulator	5.000	90.0
AGARD	4.990	92.0
Sideslip-reset	4.995	95.5

Tab. 5.2: Results of wind reconstruction methods

In fact, both methods deliver almost perfect estimations, especially for what concerns wind intensity. This translates into a correct derivation of sideslip angle, as shown in Figure 5.5. Besides, an element of suspicion was that, among the whole set of trials carried out, maximum sideslip angle variation never exceeded the value of 2 deg. As will be reported in Section 5.7.2, real aircraft flight test mission suggests that the effect of propeller is more vigorous than what seems from simulator, maybe because of Cessna 172 being too sluggish.

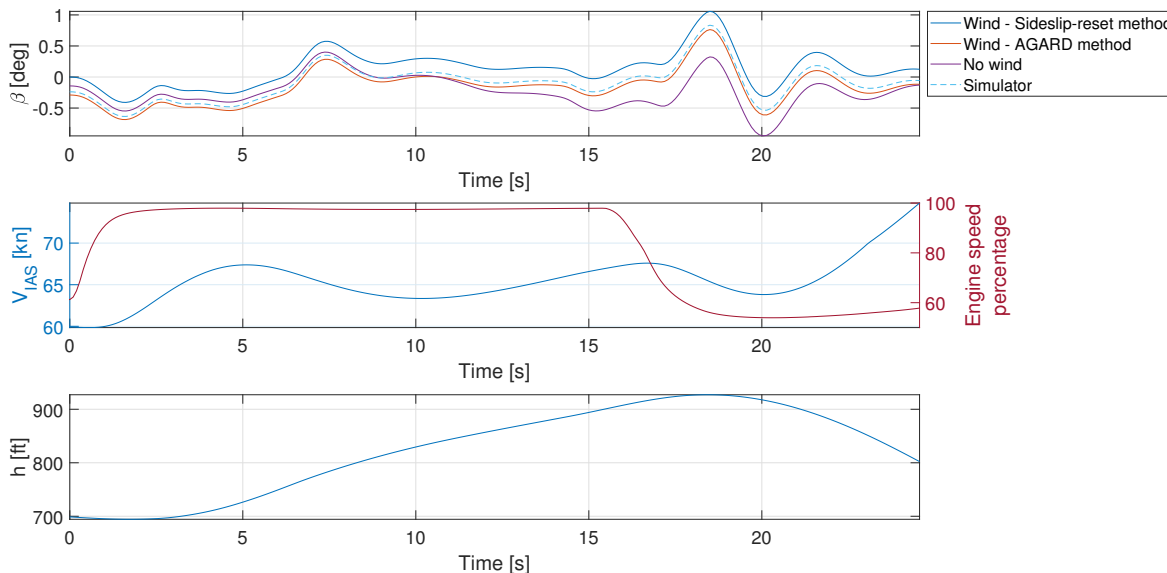


Fig. 5.5: Time history of simulator trial with constant wind

Through *X-Plane 11* it is only possible to set a constant wind throughout the simulated flight and on the whole scenario. It is not possible then to experiment wind conditions variable in space and time (apart from instantaneous gusts, not compatible with the sought conditions). Therefore it was left to real flight test experience the validation of the methods for wind estimation in case of changing conditions. This is discussed in Section 5.7.1.

5.6 Preliminary flight test activity

After the execution of simulated flight test activity, a mission was flown on a real aircraft. The in-flight test aimed to determine typical SSA for a GA aircraft, and to compare its value with the one obtained with the computer flight simulator. Here reported is the summary of most important information regarding flight test planning. Extended disclosure can be retrieved in Appendix E.

5.6.1 Test aircraft

Aircraft to be tested is Cruiser Aircraft *PS-28*, registered F-HZCE (Figure 5.7). It is a CS-VLA certified single-engine, full metal, low-wing, two-seat propeller driven aircraft for General Aviation training and private employment. In this specific version, engine adopted is a Rotax *912 ULS S2* [33], rated for 100 hp at 5800 RPM for a maximum of 5 minutes and 95 hp continuous power at 5500 RPM. It has a non-retractable landing gear and a large wing dihedral, namely 5.6 deg. This could have an influence in the test, enhancing a greater yaw-roll coupling.

Table 5.3 shows main parameters, while Figure 5.6 reports aircraft 3-view layout.

Wing span	Length	Wing area	MTOM	Empty mass
8.60 m	6.62 m	12.3 m ²	600 kg	399 kg

Tab. 5.3: *PS-28* main parameters (from POH)

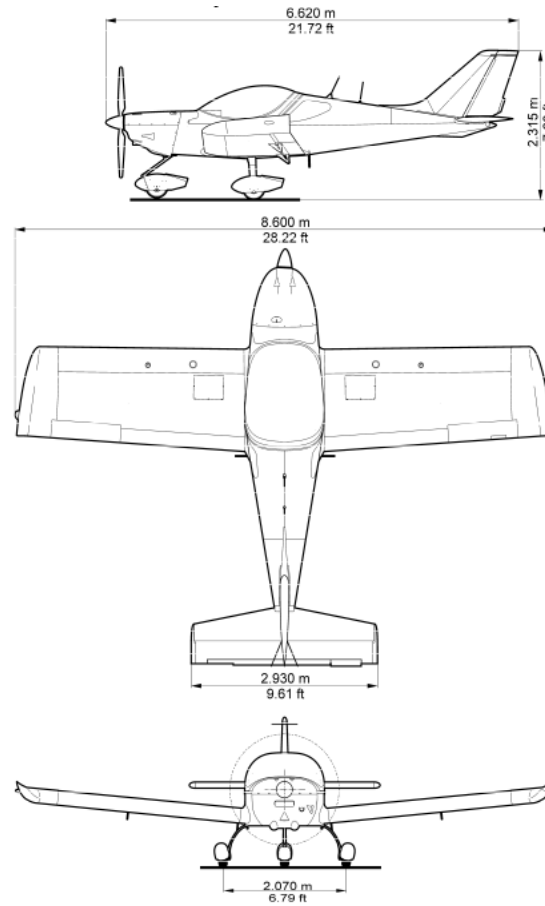


Fig. 5.6: *PS-28* 3-view representation [34]



Fig. 5.7: *PS-28* test aircraft

5.6.2 Test instrumentation

Experimental data are gathered via two sources: aircraft native instrumentation and a smartphone application. No additional instruments can be installed on-board, as every modification to the aircraft must be subjected to certification and approval process.

Aircraft native instrumentation

The aircraft is equipped with a Dynon *SkyView HDX* avionic suite [35]. It is digital and gives the opportunity to record and download flight data on any USB storage device, also after flight completion and shutdown of the suite. Table 5.4 enlists a collection of the main parameters that can be exported and are of interest for the analysis. The acquisition rate was 5 Hz, not modifiable by the pilot, being just editable from a technician. Anyway, this rate proved to be enough for the purpose.

INS	Air data	GNSS	Systems
Attitude	IAS	GPS time	Session time
Heading	CAS	GPS position	Engine RPM
Angular rates	TAS	Ground speed	Manifold pressure
Magnetic heading	OAT	Vertical speed	Barometer setting
Magnetic variation	Pressure altitude	Ground track	Wind estimation

Tab. 5.4: Dynon *SkyView HDX* exportable parameters of interest

Smartphone application

A smartphone app is employed as back-up of aircraft native instrumentation. The very same app has already been validated in 2019-2020 experimental flight test campaign in Politecnico di Milano course of "Sperimentazione in Volo", in which some students successfully employed it for testing the performance of a Cessna 172.

Modern smartphones feature a great variety of sensors, also with high precision if related to their cost. Anyway, there are a lot of issues to be accounted for:

- the third-party application installed on the smartphone could crash in every moment, without forewarning, causing the loss of all the data;
- accelerometers and gyroscope sensors (MEMS) could be influenced by aircraft engine vibrations, magnetic or electro-magnetic interference;
- the way the smartphone is strapped to the aircraft influences accelerometers and gyroscopes: if handheld, data will be completely unreliable, while fixing it to the airframe could be not easy; additionally, the strapping orientation will influence data post-processing.

Analyzing these issues, smartphone with a recording app can be employed, but with reservation. GNSS measurement (position, altitude, speed) will always be considered reliable as GNSS accuracy is greater than possible in-cabin motion.

Smartphone employed in the trial is a Samsung *Galaxy S10 SM-G973F* with *Android 10* updated on October the 1st, 2020. The software chosen for data recording is *AndroSensor* v1.9.6.3 [36]. The software records parameters at the chosen time interval and exports a *.csv* file which can later be employed for data post processing. A downside of the chosen

application is that there is no "event" button, hence the time instant of important events should be hand-written on the test card to recognize data related to a particular flight phase. Even if the acquisition rate could be faster, the chosen rate is 8 Hz, also because the smartphone app cannot match the same rate of the avionic suite.

In Table 5.5 are depicted the sensors enforced with their output parameters and limitations.

Sensor	Parameters	Range	Resolution	Delay
GNSS	Position, altitude, speed	ND	ND	ND
Accelerometers	acceleration in (x, y, z) axis	78.5 ms^{-2}	0.00239 ms^{-2}	$2000 - 180\,000 \mu\text{s}$
Gyroscope	rotation around (x, y, z) axis	17.5 rads^{-1}	$0.000061 \text{ rads}^{-1}$	$2000 - 180\,000 \mu\text{s}$

Tab. 5.5: *AndroSensors* parameter outputs

5.6.3 Test range

Flight test terminal operations were held at Albenga-Riviera international airport (ICAO: LIMG; IATA: ALL), headquarter of *Aeroclub di Savona e della Riviera Ligure*. Albenga airport is located in Liguria, 4.2 nm west of the shoreline.

Aerodrome is open to both VFR and IFR flights. LIMG tower emits hourly METAR bulletins and periodical NOTAMs, consulted before flying.

The tests were intended to be conducted above the seaside, a couple of miles out of the shoreline, in front of the city of Loano. This is a Golf-class airspace with low traffic and no restrictions. Moreover, in this area wind is expected to be constant, without major updrafts or gusts.

5.6.4 Test objectives and schedule

The planned test flight aimed to investigate the relation between power setting and airspeed with yawing moment generated by propeller spinning and consequent induced SSA, bank angle and turn rate.

Pilot in command was Davide Pasquali, with Matteo Tombolini as FTE. The planned mission schedule is presented in Table 5.6.

Activity	Duration	Fuel	Altitude
Pre-flight checks and taxi	5 min	11	GND
Take-off	2 min	11	0 – 300 ft AGL
Cruise to test range	2 min	11	300 ft AGL – 2000 ft QNH
Preliminary trials	8 min	21	2000 ft QNH
Beta testing	30 min	91	2000 ft QNH
Aerodrome approach	3 min	11	2000 – 1200 ft QNH
Landing	2 min	11	300 – 0 ft AGL
Taxi and post-flight checks	5 min	11	GND
Total	57 min	171	

Tab. 5.6: Planned flight mission sequence

5.6.5 Test execution

Test flight should have been performed waiting for a day with no wind and good meteorological conditions. Unfortunately, due to upcoming Covid-19 restrictions, the test flight had to be flown on November the 8th, starting from 14:50 local time.

As reported in NOTAM observations (available in Section E.3 of Appendix E), weather conditions were characterized by low ceiling and spot rain showers. Anyway, these factors did not affect the flight test, which lasted 53 min (63 min block time). During the entire duration of the tests, FTP monitored IAS, engine speed, temperature and diagnostics, in order to avoid hazardous situations, in particular over-speed and stall. *PS-28* avionic suite was helpful in such a demanding task, highlighting parameters out of normal-operation range on PFD, and also giving aural warning messages. Speed was prevented from exceeding V_{NO} and no unwanted stall was experimented. Anyway, the prescribed altitude of 2000 ft QNH would have been more than enough for recovery.

Preliminary part of the flight test mission served to the PIC to get used to FTTs and to identify the configuration leading to the most evident effects. The two test techniques were performed in 3 alternative configurations, to see their effect on the aircraft behavior:

- a) rudder-free + aileron-free
- b) rudder-free + aileron-fixed
- c) rudder-fixed + aileron-fixed

In Table 5.7 are reported the different test points for the preliminary trials, performed at initial 60 kn IAS and 2000 ft QNH. They were all performed raising power to max continuous value, imposing maximum throttle. Intermediate throttle settings were not tested due to limited time available. Nonetheless, propeller effects are strongly mitigated at lower power settings and can be reasonably rescaled with respect to results coming from trials carried out at max continuous power.

Test ID	FTT	Configuration	Wind
Pv1	Constant speed	Rudder & ailerons free	headwind
Pv2	Constant speed	Rudder-free & ailerons-fixed	headwind
Pv3	Constant speed	Rudder & ailerons fixed	headwind
Pv4	Constant speed	Rudder & ailerons free	tailwind
Pv5	Constant speed	Rudder-free & ailerons-fixed	tailwind
Pv6	Constant speed	Rudder & ailerons fixed	tailwind
Ph1	Constant altitude	Rudder & ailerons free	headwind
Ph2	Constant altitude	Rudder-free & ailerons-fixed	headwind
Ph3	Constant altitude	Rudder & ailerons fixed	headwind
Ph4	Constant altitude	Rudder & ailerons free	tailwind
Ph5	Constant altitude	Rudder-free & ailerons-fixed	tailwind
Ph6	Constant altitude	Rudder & ailerons fixed	tailwind

Tab. 5.7: Test points for preliminary trials

The preliminary tests showed the best configuration for control surface actuation is the rudder-fixed & aileron-fixed strategy. The perception of flight asymmetry sensed by both members of flight test crew was as its peak with this configuration. Being also the only one that could be tested in the flight simulator, it was selected for the test points of the main

part of the mission, looking for a dependence of parameters affected by propeller effect on initial airspeed. Post-processing gave further credit to this decision, since this configuration led to the most evident variations of both sideslip angle and turn rate, thus confirming the sensations of flight test crew.

After strategy selection, the main test was performed, following the schedule presented in Table 5.8.

Test ID	FTT	Wind	Trim speed
Mv1	Constant IAS	Headwind	100 kn
Mv2	Constant IAS	Tailwind	80 kn
Mv3	Constant IAS	Tailwind	60 kn
Mv4	Constant IAS	Headwind	80 kn
Mv5	Constant IAS	Headwind	60 kn
Mv6	Constant IAS	Headwind	45 kn
Mv7	Constant IAS	Tailwind	45 kn
Mh1	Constant altitude	Headwind	45 kn
Mh2	Constant altitude	Headwind	75 kn
Mh3	Constant altitude	Tailwind	45 kn
Mh4	Constant altitude	Tailwind	75 kn

Tab. 5.8: Test points for the main trials

As expected, the 100 kn trial almost showed no evidence of the pursued behavior, thus once performed with headwind, it was not repeated with tailwind. In every other conducted trial, the PIC reported that yaw dynamics was the most affected from the phenomenon, while roll was just marginally influenced. Pitch was actively controlled in order to keep constant altitude or constant speed, but the pilot reported no strange behavior or unexpected stick force. Results are available in Section 5.7.2.

After full-throttle tests, a small idle test was performed in order to verify that the asymmetric airframe generates a yawing moment opposite to that induced by propeller. Also the effect of maximum rudder deflection was investigated, to relate maximum sideslip angle achieved with the one generated by propeller effects.

5.7 Flight test data analysis

The analysis of data collected during flight test activity on the real aircraft has been carried out by making use of methods validated with flight simulator (Section 5.5.1). The only difference was the impossibility to gather ground speed components in NED frame: both smartphone and native aircraft instrumentation delivered only overall ground speed. Components were thus approximated with the rate of change of latitude, longitude and altitude over the sampling time. This approach was validated on data from flight simulator, showing good compatibility between the values directly returned by the software and the ones reconstructed from differentiation of latitude, longitude and altitude, as confirmed graphically in Figure 5.8. Moreover, vector components V_N, V_E, V_D once combined returned the same ground speed, as shown in Figure 5.9, with maximum relative error well below an enviable 5% throughout the whole set of trials.

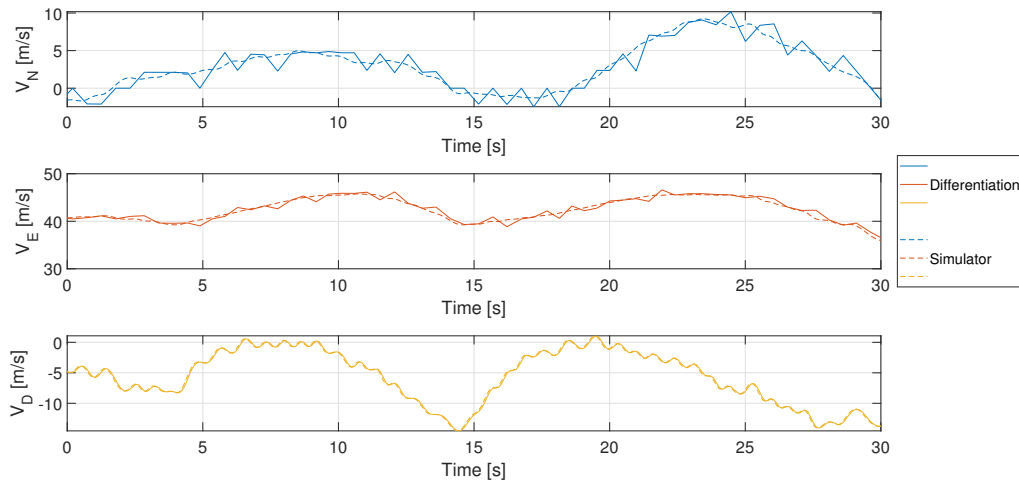


Fig. 5.8: Speed components and values derived from latitude, longitude, altitude

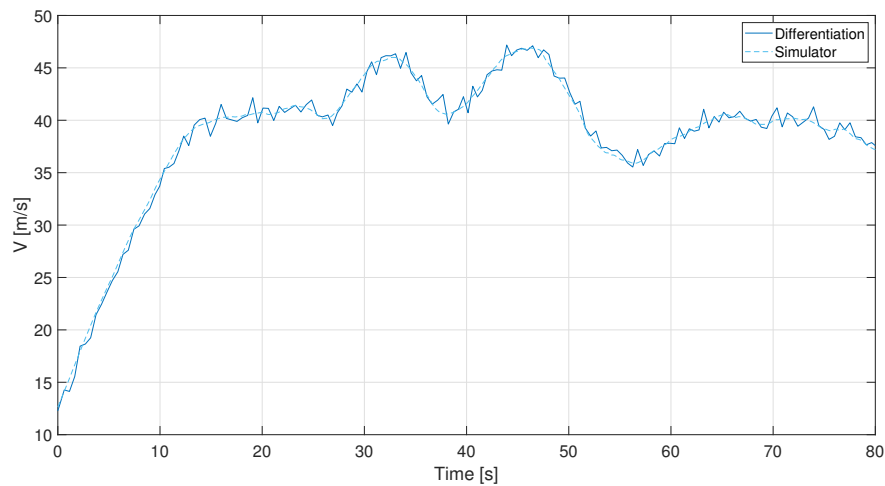


Fig. 5.9: Speed through composition of components

5.7.1 Effect of wind

As feared, the value of azimuth angle sensed by the smartphone did not prove to be reliable for the whole duration of the flight test mission, being significantly different from track angle derived from GNSS data. Fortunately, the aircraft native INS delivered likely readings for what concerned Cardan angles. Conversely, the higher sampling rate was responsible for a more noisy measurement of ground speed even after filtering. In particular, greatest error involved speed vertical component. It was then necessary to merge data from the two sources, performing time synchronization with same sampling rate of 1 Hz. This task required little effort as GPS time was returned by both.

Avionic suite of test aircraft automatically computes the true heading of the aircraft, by applying conversion to magnetic heading measured by a magnetometer, to account for declination and deviation. The suite also returns an estimation of the intensity and direction of the wind. While flying, the sensation was that the estimated direction of the wind was

changing as if chasing the track (this by the way made it impossible to perform the trials in accordance with the headwind and tailwind headings suggested by native instrumentation). This problem needed to be added to the fact wind was frequently declared variable by the suite (in fact the corresponding curve in Figure 5.10 lacks many points).

This log data were compared in Figure 5.10 with the results of wind reconstruction performed by means of AGARD and Sideslip-reset method*. Averagely, the wind blew from N-NE during the first half of the test and N-NW during the second half according to the suite.

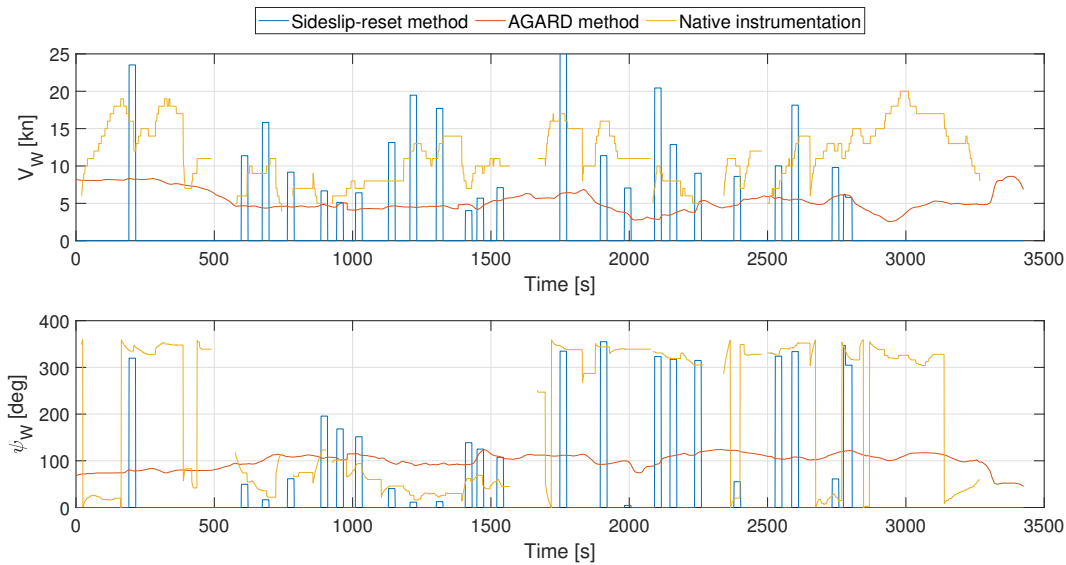


Fig. 5.10: Wind intensity and direction estimation

The estimation of wind from aircraft native instrumentation is really well followed by the estimation of wind with Sideslip-reset method. On the contrary, offline approximating calculation of AGARD method delivered almost constant values throughout the flight and in accordance with METAR and forecasts: about 5 knots from East.

AGARD method seems to be more reliable in case of constant wind conditions (as also specified in [31]), lacking instead the ability to track rapid variations of wind. Actually, a degree of freedom of the AGARD offline estimation is the number of samples accounted for at each instant before and after the one considered (variable I in Eq. (5.13)). This way it is possible to vary the sensitivity of the algorithm to local changes in the wind. Therefore, by reducing the number of samples, AGARD method tends to deliver results that are more similar to those extracted from aircraft log and Sideslip-reset method. Results in Figure 5.10 were obtained considering 200 samples. As an experiment, Figure 5.11 shows how decreasing the number of samples to 50 the results of wind estimation of AGARD and Sideslip-reset methods look alike.

Nevertheless, by increasing the sensitivity of AGARD method to local variations it was still not possible to reach the level of correspondence to the estimation performed by aircraft native instrumentation as done by Sideslip-reset method. Therefore it was preferred to keep 200 samples per instant for AGARD method, to see the effect of a long term estimation of wind on sideslip and compare it to the more sensitive Sideslip-reset method.

*Sideslip-reset method is only used to estimate wind during test points

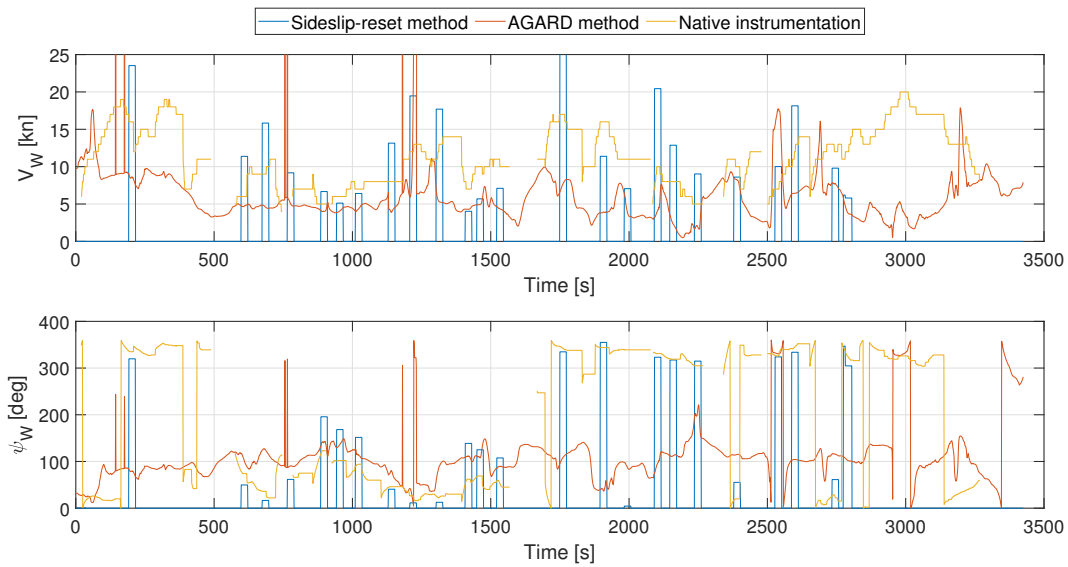


Fig. 5.11: Wind intensity and direction estimation with different time resolution

For what concerns sideslip angle estimation, the two methods (INS and MAG) returned extremely similar results. Conversely, the presence of wind influenced the trial as feared, not in terms of sideslip angle variation, but in terms of offset from zero value at the beginning of the test points. The time history of sideslip along the trials hardly ever starts from zero value as expected if compensating the effect of wind. The decision to perform the tests in both headwind and tailwind conditions proved to be clever in this sense, since it was possible to notice this inconsistency and identify a pattern related to the direction of the wind. This latter is really evident in the time history of heading and track angles reported in Figure 5.12: track angles below 180 deg are typically higher than the synchronous heading angles, whereas the opposite is valid for routes in the third and fourth quarter. Since SSA is the difference between track and heading, it is possible to understand the impact of the wind on its estimation.

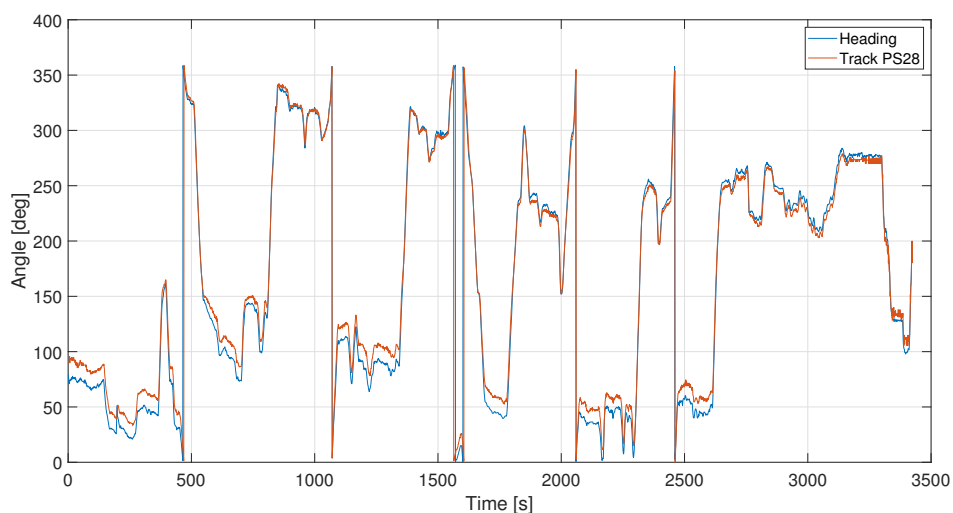


Fig. 5.12: Systematic discrepancy between heading and track angles

As anticipated in Section 5.3.2, correction of wind has been at first performed only enforcing AGARD method. The necessity to develop the alternative Sideslip-reset method derived from

having noticed that the initial offset from zero value of sideslip is averagely lower if enforcing the characteristics of the wind as estimated by the aircraft native instrumentation. In this case the offset of all the trials is almost always nearly 5 deg, whereas the offset enforcing AGARD method fluctuates randomly in the range ± 15 deg. Estimation of Sideslip-reset method solves this inconsistency, at it imposes $\beta = 0$ at engine speed ramp.

An appreciable trial with constant airspeed 80 knots (Mv2) is reported in Figure 5.13. It is possible to appreciate what has been previously stated concerning the offset of sideslip angle at the imposition of maximum throttle due to wind with the embraced methods, that is why flight test results in Section 5.7.2 are obtained enforcing Sideslip-reset method.

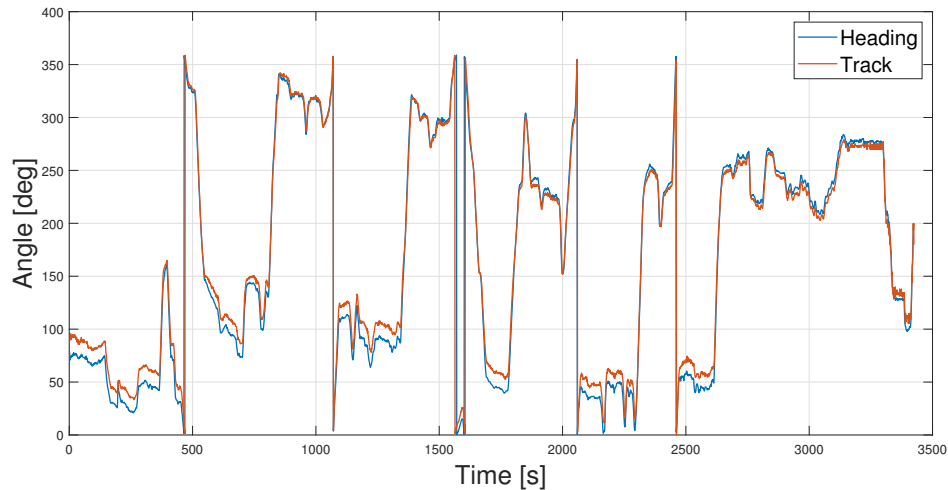


Fig. 5.13: Sideslip offset (test point Ms2)

5.7.2 Propeller effect analysis

Leaving aside the offset, the aircraft experienced a variation of sideslip angle in the range $0 \div 5$ deg after impulsive maximum throttle setting. Therefore, the extent of the phenomenon appears to be more evident than what emerged from the analysis of data from flight simulator. Of course this discrepancy is also due to the difference in performance and flying qualities of the two aircraft. In fact, test aircraft *Cruiser PS-28* adopted in the test is less sluggish than *Cessna 172*, so it is likely that this is a major reason for slipstream effect to be more severe.

After the first positive peak, sideslip tends back to zero and becomes slightly negative when in idle. The amplitude of both positive and negative peaks strongly depend on the airspeed at the imposition of maximum throttle: the lower the initial velocity, the higher the consequent variation in sideslip angle.

The dynamics of the aircraft is affected by slipstream effect not only for what concerns sideslip angle, but also in terms of turn rate. This is of major importance as its effect is directly sensed by the pilot and contributes to describe the asymmetric flight condition induced by the rotation of the propeller. By the way, turn rate $\dot{\psi}$ directly returned by the suite is better shaped than the value computed from finite differences of azimuth angle over time, which has thus been discarded.

Sideslip angle gives a quantitative description of the phenomenon forsaken, regardless of aircraft geometry, maneuverability and flying condition. On the contrary, the magnitude of $\dot{\psi}$ is intrinsically affected by these characteristics. Therefore, to share the same reference

between test aircraft and scale model, dimensionless turn rate is here defined:

$$\hat{\psi} = \frac{\dot{\psi} b}{2V} \quad , \quad (5.16)$$

where b is wingspan and V is true airspeed.

This nondimensionalization is inspired by the way in which contribution from yaw rate to yawing moment coefficient is usually scaled [37]:

$$C_N = C_{N_\beta} \beta + C_{N_r} \frac{rb}{2V} + C_{N_{\delta_a}} \delta_a + C_{N_{\delta_r}} \delta_r \quad . \quad (5.17)$$

In fact, time derivative of azimuth angle and yaw rate are closely related in straight flight, as specified in Eq. (5.18),

$$\dot{\psi} = \underbrace{\frac{\sin \Phi}{\cos \theta}}_{\approx 0} q + \underbrace{\frac{\cos \Phi}{\cos \theta}}_{\approx 1} r \quad . \quad (5.18)$$

This approach for normalization of $\dot{\psi}$ should thus return a quantity offering a direct comparison between data gathered from the real aircraft and those acquired testing the scale model. For what concerns its trend throughout the trials, it should be almost identical with that of $\dot{\psi}$ with constant speed FTT (in fact, $\hat{\psi} \stackrel{V=\text{const.}}{\propto} \dot{\psi}$). A slight difference could arise, by contrast, in constant altitude trials, due to dependence from airspeed.

Time histories of parameters affected by the propeller effect and verification of alternative tolerances of constant speed test Mv2 are depicted in Figure 5.14 as an example. Identically, Figure 5.15 shows an example of constant altitude technique, namely Mh1 test point. A further parameter analyzed was bank angle variation. The behavior is similar to that of turn rate: a negative value (i.e. left wing down for roll, nose turning left for yaw) increasing with time in case of constant speed FTT, whereas an initial peak is rapidly damped in a trial with constant altitude.

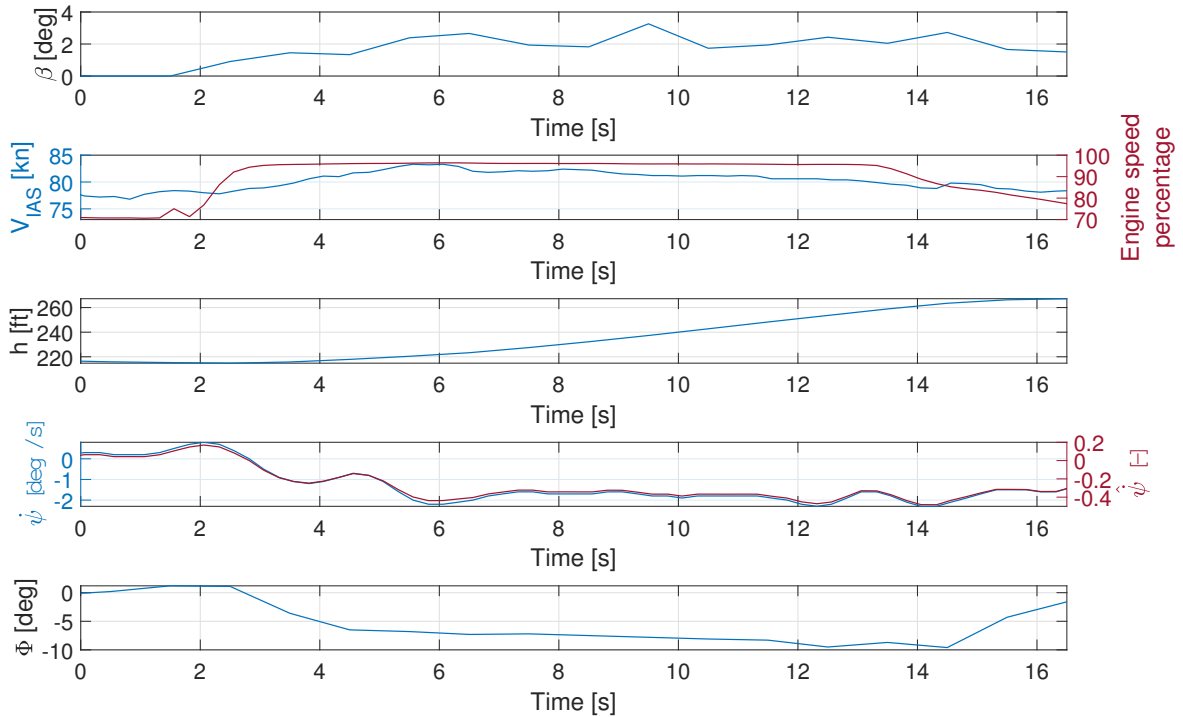


Fig. 5.14: Main test constant speed trial Mv2

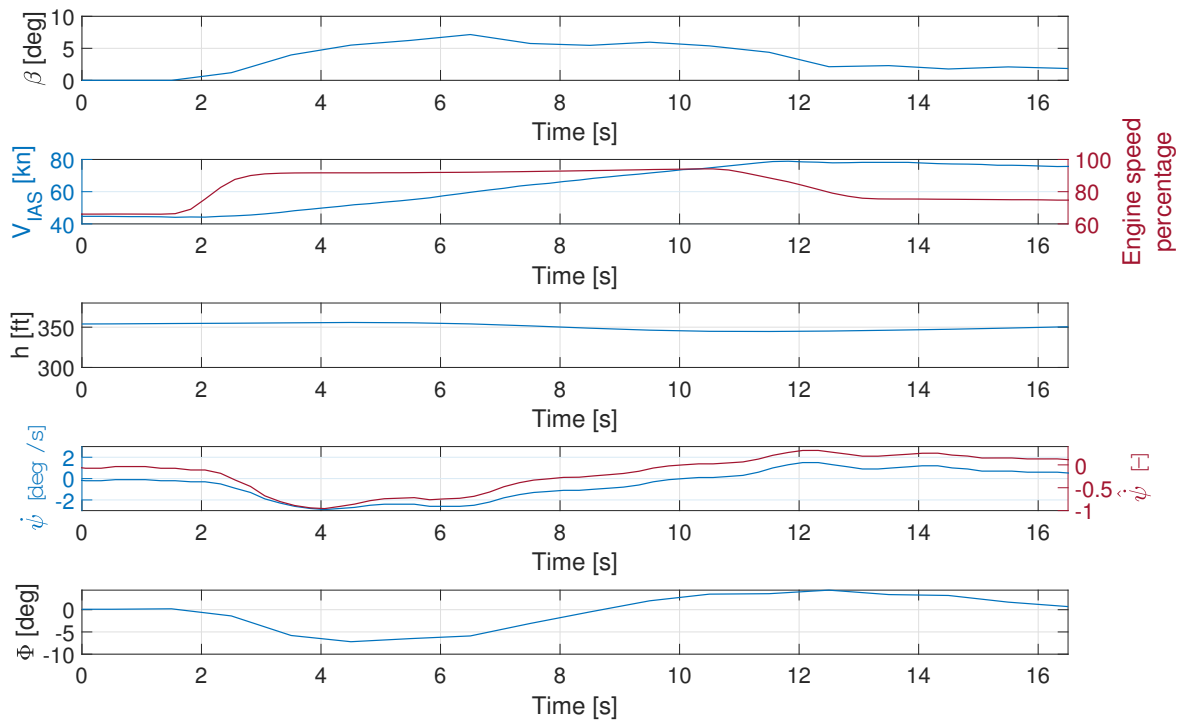


Fig. 5.15: Main test constant altitude trial Mh1

From the comparison of FTTs it is evident how engine speed experiments a different variation across the maneuver. In constant speed trials, engine speed is almost constant, whereas in constant altitude FTT it slightly increases, as a result of increase in airspeed. Probably for the same reason, from the comparison between trials it emerges that constant speed technique is responsible for a greater change in both turn rate and bank, whereas no defined difference was discovered for what concerns sideslip. Once again, initial velocity has a major impact on the amplitude of variations of turn rate and bank. This trend is well noticeable from Table 5.9, reporting trim speed and maximum values of quantities of interest.

Test ID	Trim speed [deg]	β [deg]	$\dot{\psi}$ [deg/s]	$\hat{\psi}$ [-]	Φ [deg]
Mv1	100	1.5	0.5	0.1	2.5
Mv2	80	3	2	0.4	10
Mv3	60	2	7	2	25
Mv4	80	1	1	0.2	4
Mv5	60	4	5	1.2	12
Mv6	45	5	5	1.5	20
Mv7	45	5	5	2.4	20
Mh1	45	7	2.5	1	5
Mh2	75	2	0.2	0.1	2
Mh3	45	5	1.5	0.5	5
Mh4	75	0	1	0.2	3

Tab. 5.9: Account of test points for propeller effect characterization

It is worth mentioning that the apparently high values of bank angle in constant speed trials are obtained with a progressive and gentle increase. Considering the fact the considered

test points have a long duration and position of controls is fixed, these values are, in truth, reasonable.

The alternative constrains of constant speed and altitude were not easy to be respected throughout the test points. In particular, pilot feedback highlighted that constant altitude FTT was the most demanding among the two. This was confirmed by data post-processing, showing greater precision in the respect of constant airspeed constraint in the related trials. This is partially because constant airspeed FTT is very similar to the usual profile of a climb, typically made with constant IAS. Moreover, airspeed indicator can be easily and precisely consulted to keep limited IAS variations. The aircraft was instead more prone to oscillations in altitude in the other FTT. Moreover, pilot workload is remarkably higher in this trial, especially when imposing maximum throttle, to prevent altitude variation, with also the risk of exceeding V_{NO} . Probably the use of an autopilot could provide better results for both techniques.

Chapter 6

Scaled demonstrator

6.1 Purpose

In order to demonstrate the feasibility of the concept in real-life application, this is implemented in a radio-controlled (RC) airplane model. This is out-of-doubt the fastest, cheapest and safest way to fulfill validation purposes.

Not every element contained in the Aeroswitch concept statement shall be demonstrated in the scaled demonstrator, but the key-ones were sought. Low priority objectives demonstration was postponed, in order to save time, cost and weight of the scale model. The demonstrated points shall cover:

- Multi-engine flight mode, in which the aircraft shall demonstrate normal flight behavior;
- Multi-engine One Engine Inoperative (OEI) simulation, employed for ME pilot training;
- Single-engine normal flight mode, in which the aircraft shall demonstrate a behavior similar to that of a conventional propeller-driven single-engine aircraft, namely generating a yawing moment when adding power;
- Single-engine One Electric Motor Inoperative (OEMI) emergency simulation, in order to assure safety is always guaranteed also for a single-engine rated pilot.

These points can be demonstrated mostly using off-the-shelf components to assemble the aircraft. The only one that cannot be purchased is the control unit for the six motors, identified as *EPMS* in the patent application. This has to be designed and built with a dedicated hardware and software. In this particular realization (described in Chapter 7) its name is *M3U* (which stands for Multi-Motor Management Unit). Requirement specifications of the whole system architecture are instead reported in Appendix A.

6.2 Design and component selection

All the purchased components employed to build the scale model are illustrated in this section. The selection process of the RC model took into consideration different factors:

- Similarity with real GA aircraft - non-traditional or unusual configurations are discarded;
- Simple wood construction - composite construction is more expensive and more difficult to repair or modify, while foam-based structures are less robust;
- Roomy space inside the fuselage, in order to easily host the electronic devices;

- Spare parts;
- Control surface authority, in order to allow full aircraft controllability also in upset attitude or in case of unwanted departures.

As the result of a grueling web research followed by a comprehensive evaluation process, the aircraft model selected is the Legacy Aviation *Turbo BushMaster 84*”, (*TBM* for short), or friendly nicknamed *SwitchMaster*. It is a high-wing wood-constructed aircraft. In Table 6.1 are presented its main characteristics.

Wing span	Length	Wing surface	Standard TOM
2.13 m	1.65 m	0.52 m ²	4 to 4.5 kg

Tab. 6.1: *TBM* main parameters

The *TBM* comes in an almost-ready-to-fly building kit, with just few minor mountings needed, apart from desired modifications. Along with the complete aircraft, also two spare wings have been purchased for static and wind tunnel testing. A CAD model rendering of the standard aircraft is reported in Figure 6.1.

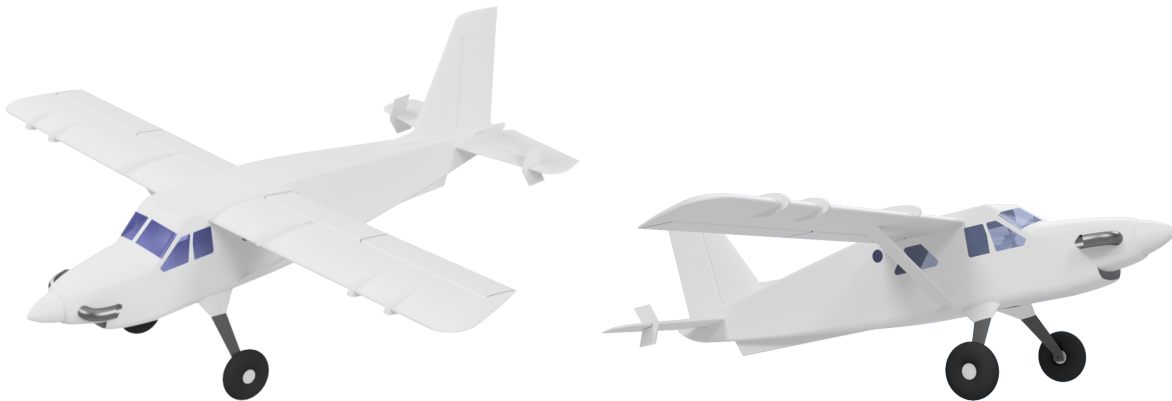


Fig. 6.1: Legacy Aviation *Turbo BushMaster* CAD representation

In Table 6.2 are presented the purchased components concurring to aircraft assembly.

Item	Brand and model	Number
Radio transmitter	Fr-Sky <i>Taranis X9D PLUS</i>	1
Radio receiver	Fr-Sky <i>Taranis RX8R-Pro</i>	1
UBEC	Fullpower UBEC <i>Pro 6A</i>	1
Flight controller	Holybro <i>Pixhawk 4</i> (with GNSS sensor)	1
Pitot-static probe	Holybro <i>Digital airspeed sensor</i>	1
Batteries	Gen Ace <i>Soaring Li-po 4S 4000 mAh</i>	6
Electric motors	Dualsky <i>XM2838EA-14 V3</i>	6
Propellers	Graupner <i>Elektro prop 10x5</i> ”	6
ESC	Zubax <i>Myxa A2</i>	6
Servos	Hitec <i>HS-225BB</i>	6
Telemetry	HolyBro <i>Transceiver Radio Telemetry Set V3</i>	1

Tab. 6.2: Buying list

The power plant chosen is the result of a market research with greatest priority on weight, reliability, excess of power and endurance, to be compatible with the purpose of the operations. In particular, electric motors are selected consulting in first iteration the *e-Calc* database [38], then websites of the vendors or producers. *Dualsky* released a complete data-sheet for the selected motor [39], an extract of which is reported in Figure 6.2.

XM2838EA-14 (860KV)

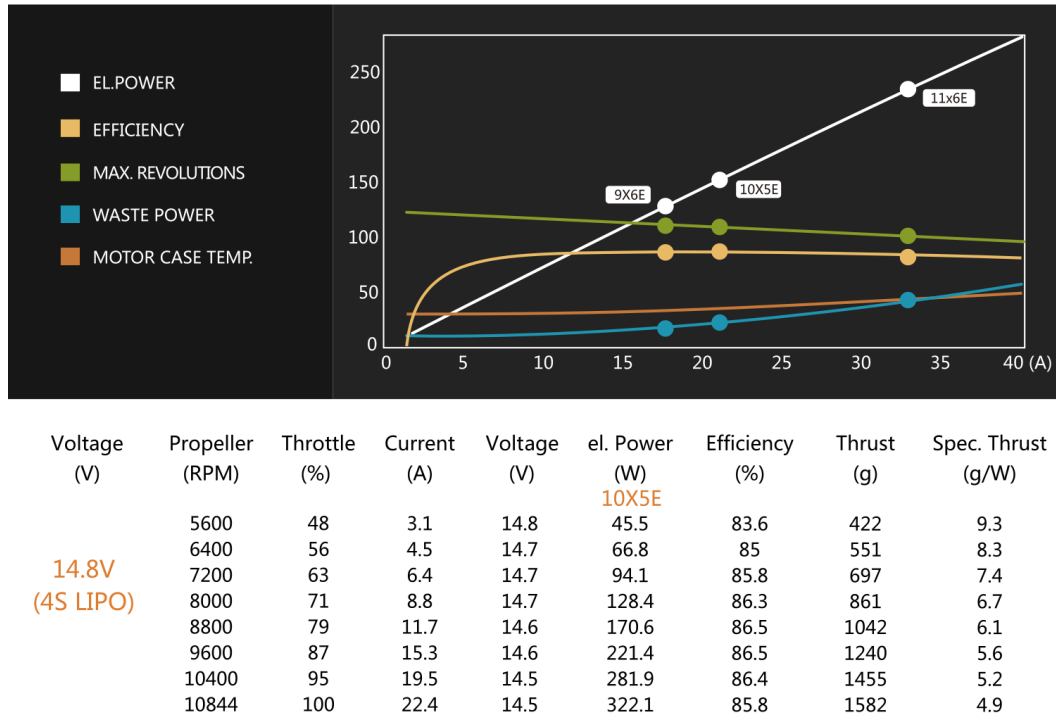


Fig. 6.2: Selected motor datasheet [39]

Following the data-sheet, propellers and battery sizing comes straightforward: respectively a 4S LiPo pack and a 10x5 in propeller, capable of providing 15.5 N of static thrust at full power, with just 22.4 A current. A 4S LiPo pack consists of a battery pack made of 4 lithium polymer cells in series configuration, for a total of 14.8 V nominal voltage. Electronic speed controllers are selected respecting values of voltage and current needed. The interface capability with CAN bus network was a second, but no less important, requirement. Zubax controllers are capable of being controlled by different kinds of data link, and to send back telemetry information, such as voltage, current, RPM, temperature and diagnostic information. This is exploited during testing for electric motor characterization, linking the ESC with a computer. Then again, all the ESCs installed in *TBM* will be controlled with a daisy-chain link exploiting the CAN interface.

Battery packs are sized to guarantee maximum current needed to enhance proper performance of the electric motors and flight time. Coupling two battery packs in parallel, total capacity is 8000 mA h and maximum current available is 240 A. In this configuration peak power is maximized, while flight time is estimated to be around 10 min with normal throttle usage.

Other items such as radio transmitter and flight controller were chosen to ensure customization and the use as flight test instrumentation, even with onboard telemetry.

6.3 Modifications

The aircraft chosen must be extensively modified to be transformed from single-engine configuration to the one with six motors. Main aspects taken into consideration are overall weight and wing structural resistance. In addition, aerodynamics of wings should not be denatured too much adding extra drag items and separation points. According to these observations, additive manufacturing could be the best choice for the construction and installation of motor supports.

6.3.1 Motor support design and testing

In this framework, the approach to design the motor support started with the building of a detailed and complete wing model with the *Inventor* CAD software. A 3-view drawing of a wing is reported in Figure 6.3, while a rendering image of the CAD model is reported in Figure 6.4. The wing is viewed in this latter from the bottom, with the film cover only on the upper surface.

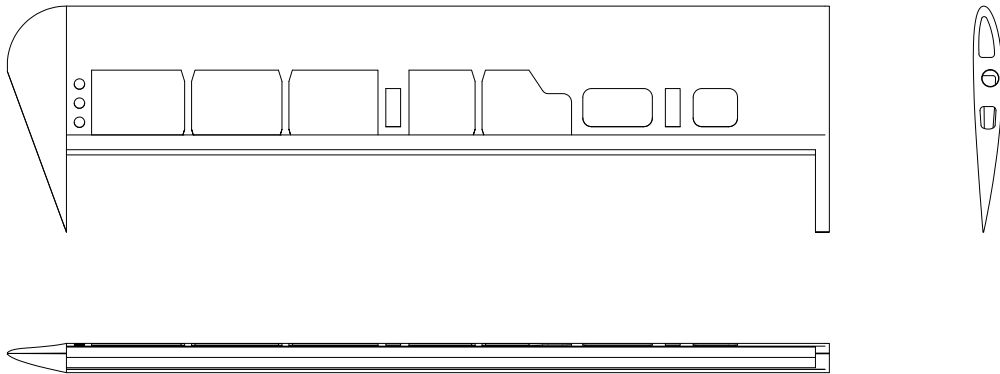


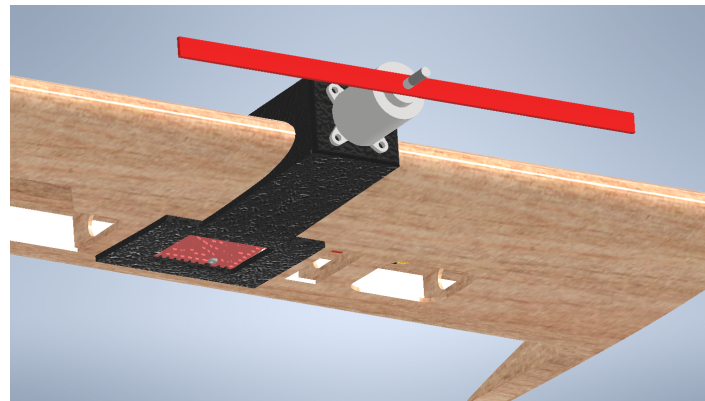
Fig. 6.3: Wing 3-view drawing



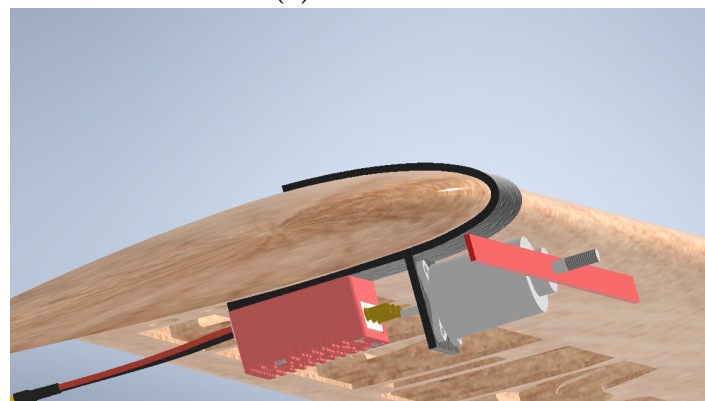
Fig. 6.4: Wing CAD model

Indeed, the first choice involves the positioning of the motors whether inside or outside the wing box. Placing them inside the wing structure would require to cut away part of the wooden structure. Even considering a different reinforcement, this solution has been discarded to preserve wing integrity.

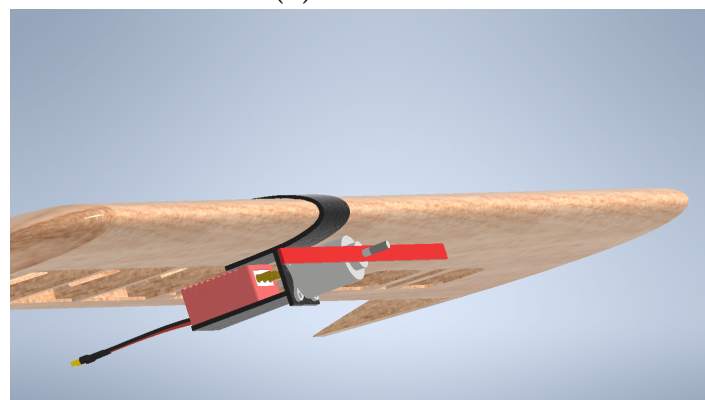
At a later stage, three alternative designs were evaluated. The first design offers the possibility to place the motor shaft aligned with the wing chord, therefore in front of the leading edge. The other two are very similar one each other, with motors placed below the wing but mounted on different kinds of supports. Design took into consideration aerodynamics, mass, stresses, load transfer to the wing and gluing surface. The three solutions are depicted in Figure 6.5, in a preliminary CAD arrangement which also includes supports of ESCs.



(a) Solution A



(b) Solution B



(c) Solution C

Fig. 6.5: Preliminary evaluation of different kind of motors support

- A) Two independent supports for the motors and the ESCs are considered. The ESCs are placed inside the wing structure, cutting the wing plastic covering and providing a flat panel to restore wing surface. The motors are placed in front of the leading edge, with propellers thus outdistanced. ESCs cables are conveyed in the wing structure, and the motors aligned with the wing represent a restrained drag addiction. Conversely, main drawbacks are ESCs cooling and the cantilever location of the motors, worsening structural loads.
- B) A unique and simple support for EMs and ESCs, thinner and, then, lighter. The cables from the ESCs to the motors can be shortened, and the controllers are placed in the airflow, with benefits on cooling. Moreover, DEP could be enhanced by placing the motors under the wing [40]. On the other hand, the drag increase could be greater and the wing covering should be anyway cut for the passage of cables.
- C) Similar to solution B, but with an extension of the support to better enclose the ESCs to increase overall stiffness.

The final choice fell to solution A, with the electric motor placed right in front of the leading edge. The conclusive and refined motor support is reported in Figure 6.6.

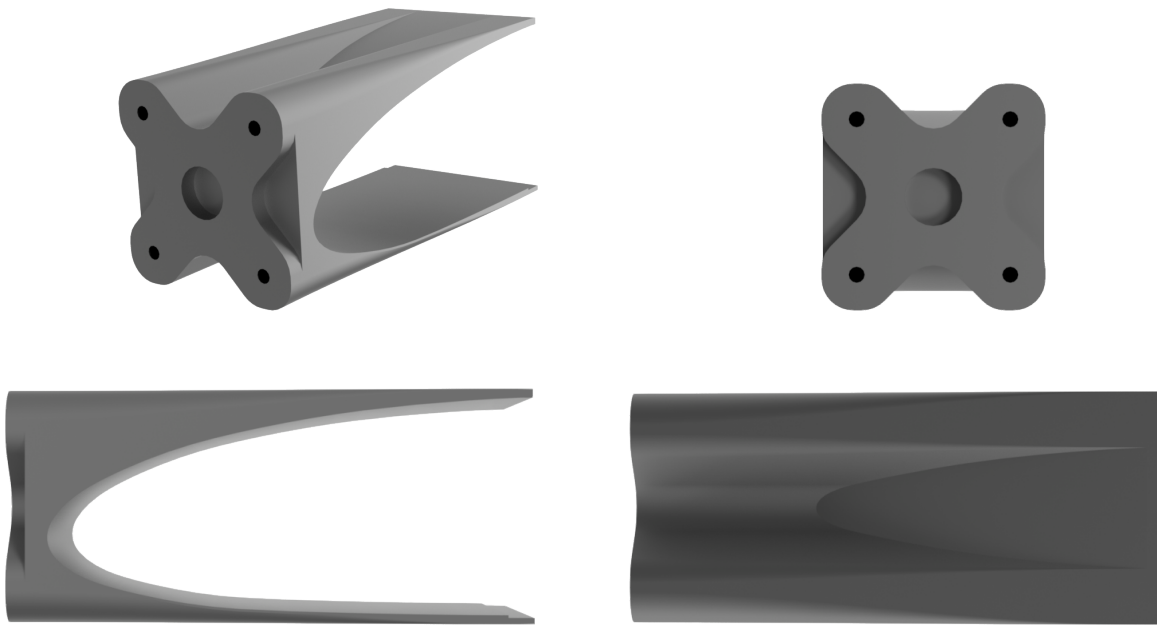


Fig. 6.6: Motor support CAD model

The motor supports are printed employing the Fortus 450 *cm* 3D printer with ASA material. ASA is a thermoplastic compound, cheap, light and with optimal strength properties [41].

A sample support was printed, to test the design in terms of strength, geometry compliance and tolerances. The ultimate versions installed only differed for minor changes. The final motor support has a mass of 25 g each, while the ESC panels are just 3 g. In Figure 6.7 are shown the first printed motor support along with the ESC support panels.

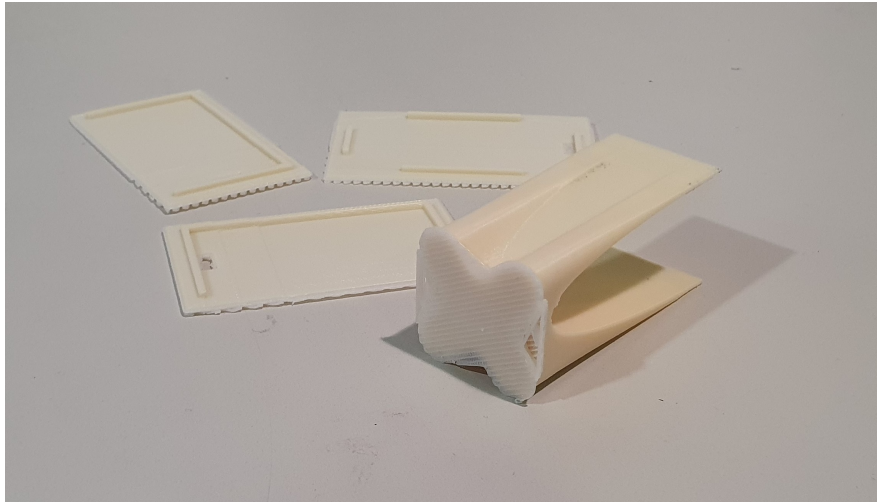


Fig. 6.7: Freshly printed motor and ESC panels

The motor support was glued with a two-part epoxy glue, applying compression clamps onto the spare wing, after removing a thin slice of covering film. It was installed in the position of the tip-motor.

After one day of consolidation, a static trial was carried out. The main purpose of the test was to check the strength of the support, glue interface and grip of self-tapping screws. Besides, wing structure was tested to check if it could carry the additional loads coming from motors installation. The wing structure itself is light but well-designed, as the *TBM* is conceived for high-g aerobatics. The "test bed" spare wing is devoid of the bottom cover and has one broken rib, therefore structural resistance of flying wing is actually greater.

Two tests were performed, to evaluate resistance to tensile and bending loads. In both tests a dummy shaft was fixed on the support with four M3x10 self-tapping screws. Calibrated weights were then hung on the shaft in two different configurations. At the same time, the wing was mounted on its own wing tube to simulate the real aircraft assembly and let it deform. When tensile load is applied, the wing is simultaneously subject to a bending moment on aircraft z-axis. Similarly, when the motor support is subject to bending, the wing is loaded both with a bending moment on x-axis and torsion. In Table 6.3 are reported the maximum loading achieved in the trial and their equivalent loads.

Trial	Load	Equivalent load condition on the support	Equivalent load condition at wing root
Tensile	3.5 kg	2.5 max motor thrust	1.25 max bending moment
Bending	3 kg	30 g pull-up	10 g pull-up

Tab. 6.3: Motor support and wing static load trial

The tests verified the wing is capable of sustaining the loads, and the support are well designed for the purpose. The same is applicable for the epoxy glue and self-tapping screws. The motor support did not highlight any deformation, stress or any kind of issue, while the wing have heavily deformed as expected, returning to normal shape as soon as the load was removed. Some pictures of the test are reported in Figure 6.8.

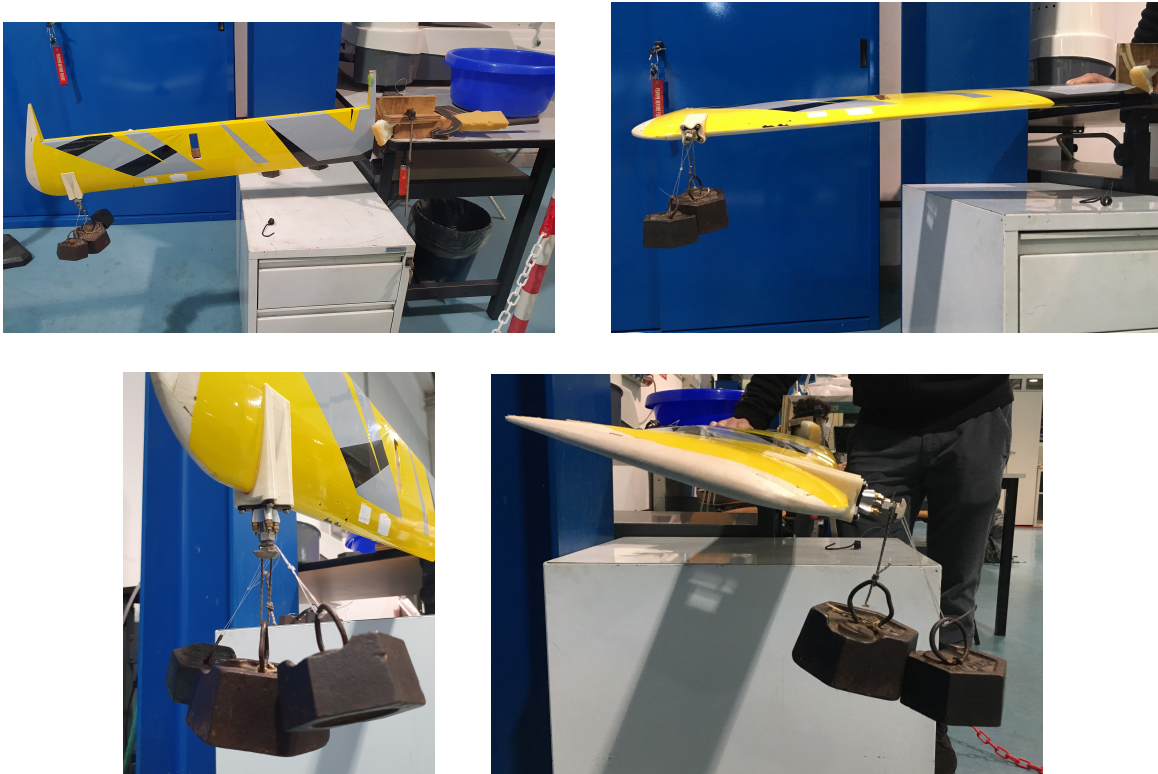


Fig. 6.8: Motor support static load test

The ESCs are placed behind the motors, inside the wing structure. Along with motor supports, also panels for embedding ESCs in the wings are 3D-printed, and they are depicted in Figure 6.7. These panels are designed to both offer support for the ESC mount, and to minimize aerodynamic contamination. They are installed on the wing exploiting self-adhesive covering material.

ESC cooling was a major source of apprehension prior to design phase. The ESCs can nominally sustain 850 W with their heat sink, or just 400 W without it. A picture of one ESC with and without heat sink is reported in Figure 6.9. The heat sink adds 29 g per controller, hence its removal was enticing. In order to assess if this solution could be applied, some test-bench trials have been carried out (see Section 8.1).

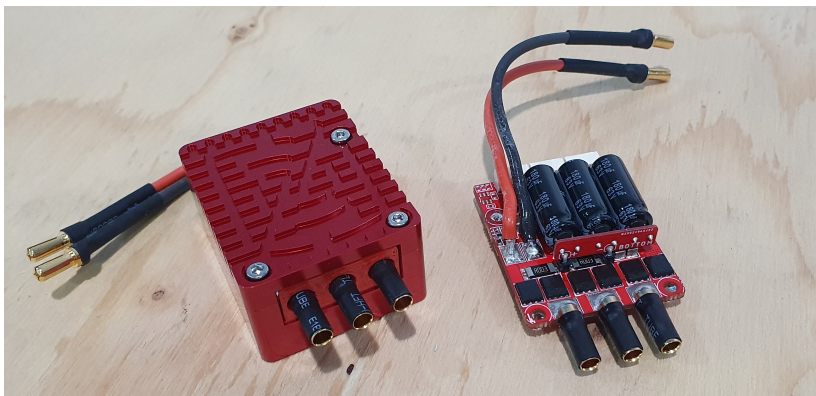


Fig. 6.9: Zubax *Myxa A2* electronic speed controller with and without heat sink

Final output of this process is reported in Figure 6.10. In the top image is represented the

wing with its three supports glued in place, while in the bottom one the same wing is shown in its final appearance with electric motors, ESCs, panels, servos and wiring installed.

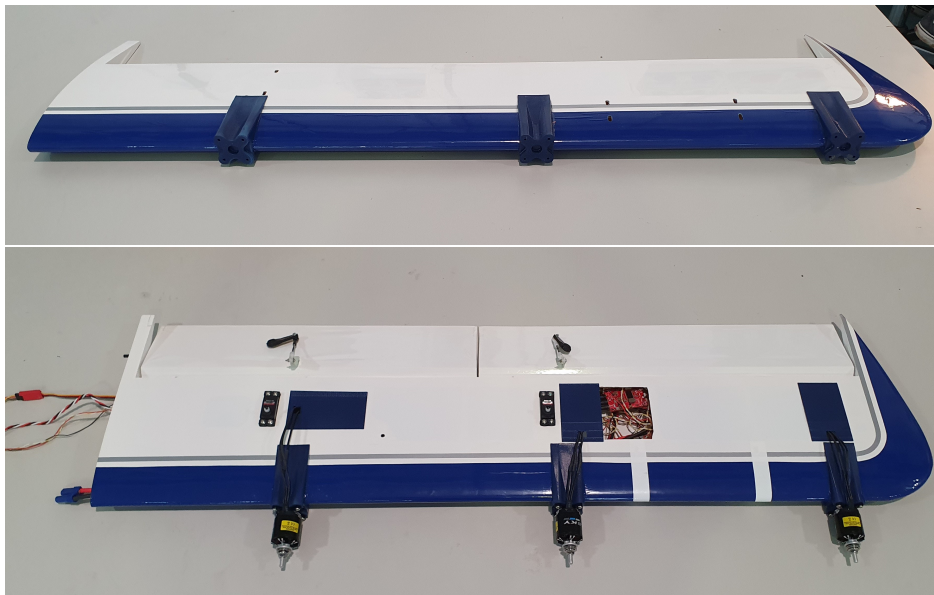


Fig. 6.10: Wing with motor supports and with the complete propulsion set

6.4 Model construction

Most of aircraft building procedures were straightforward, with just small differences from the standard. In particular, control and tail installation, landing gear assembly and servo linkages were integrally carried out according to instruction manual.

Main differences concerned installation of the motors on the wing, already discussed, electronic and wiring components and aircraft nose, originally intended to host one electric motor. A 3D printed dummy spinner has been employed to close the hole intended for the standard electric motor placed in the nose. Besides, it eased installation of the Pitot probe in front of the aircraft. Cross-sectional views of the dummy spinner and Pitot probe CAD model assembly are represented in Figure 6.11.

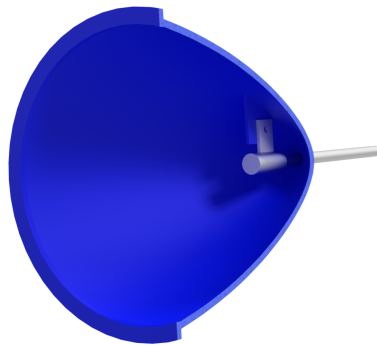


Fig. 6.11: Sectioned CAD rendering of dummy spinner and Pitot probe assembly

Some images of the aircraft build-up are reported in Figure 6.12.



Fig. 6.12: Different phases of aircraft build-up

The electronic components will be discussed in Section 6.5. It is anticipated that for what concerns wiring, the main target was to minimize voltage losses, and difference in the power supply actually sourced to each of the electric motors. Therefore, the two embarked battery packs are connected in parallel and then the wiring supplies power to all six electric motors (with cables of similar length) and electronic equipment.

Prior to the start of aircraft assembly process, every component has been weighted. Overall mass resulted to be 4.948 kg, with structural items totaling 2.39 kg. The control system contributes with 0.37 kg, whereas propulsive elements amount to 1.64 kg, plus wiring.

At build-up completion, weight and balance were checked. Center of gravity was placed approximately where suggested by *TBM* manufacturer, at 83.6 mm from the leading edge, corresponding to the 32% of the MAC. Due to the increased aircraft mass, wing loading resulted 93.3 N/m^2 , higher than typical values for the category: 80 N/m^2 for high performance RC models, while gliders exhibit from 20 to 40 N/m^2 . This characteristic could deteriorate power-off handling qualities.

6.5 Systems architecture

The whole system architecture must be designed to demonstrate the concept. A simple scheme is sketched in Figure 6.13 (notation specified is consistent in the whole dissertation).

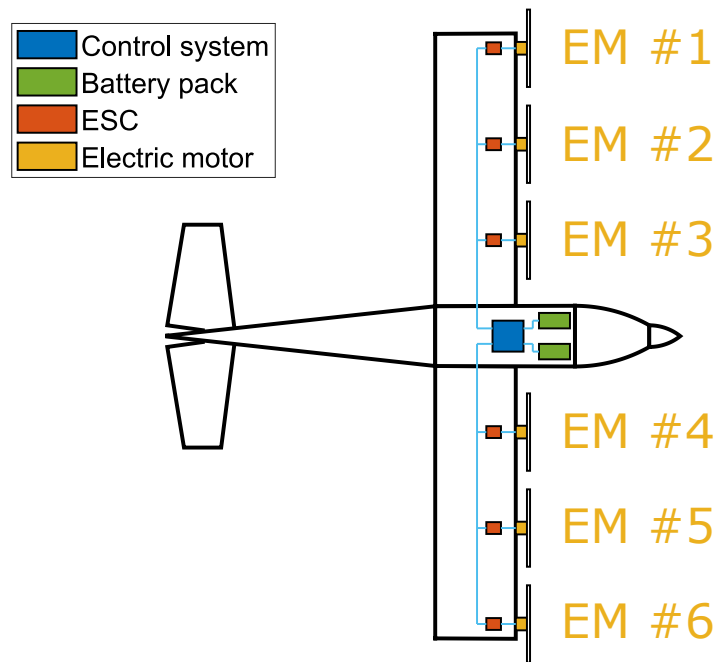


Fig. 6.13: Propulsive architecture notation

Controlling the ESCs via CAN bus connection gives considerable design freedom, simplifies the connection schemes and gives telemetry and data acquisition capability. In particular, the CAN protocol on which ESCs and flight control unit rely is UAVCAN [42].

Holybro *Pixhawk 4* control system [43] and its peripherals allow to automatically fly a specific mission or task. It is an integrated FTI unit thanks to the embedded sensors: accelerometers, gyroscopes, magnetometer, GNSS sensor and Pitot-static port. The suite is capable of manual flight control, assisted flight control or automatic flight control. Automatic flight control follows a pre-loaded path made of waypoints or areas to fly over. Assisted modes

can alternatively stabilize the aircraft, keep a straight trajectory or maintain an altitude or an airspeed (see Section 6.6.1).

Although extremely versatile, *PX4* could not provide the functionality of the conceived *EPMS* unit, which was thus designed for the purpose. Given that the scale model is only a demonstrator, the *EPMS* unit has been developed in a simpler fashion, with the pilot directly selecting the working mode and injecting the failures. In order to determine the scope of this unit, renamed *M3U* (Multi-Motor Management Unit) in this application, a requirement specification document was emitted and addressed to its only developer Professor Alberto Rolando. This document is entirely reported in Appendix A, whereas a detailed outline of the unit is described in Chapter 7.

The final output architecture of the whole control system is reported in Figure 6.14, in which data and power lines are graphically distinguished.

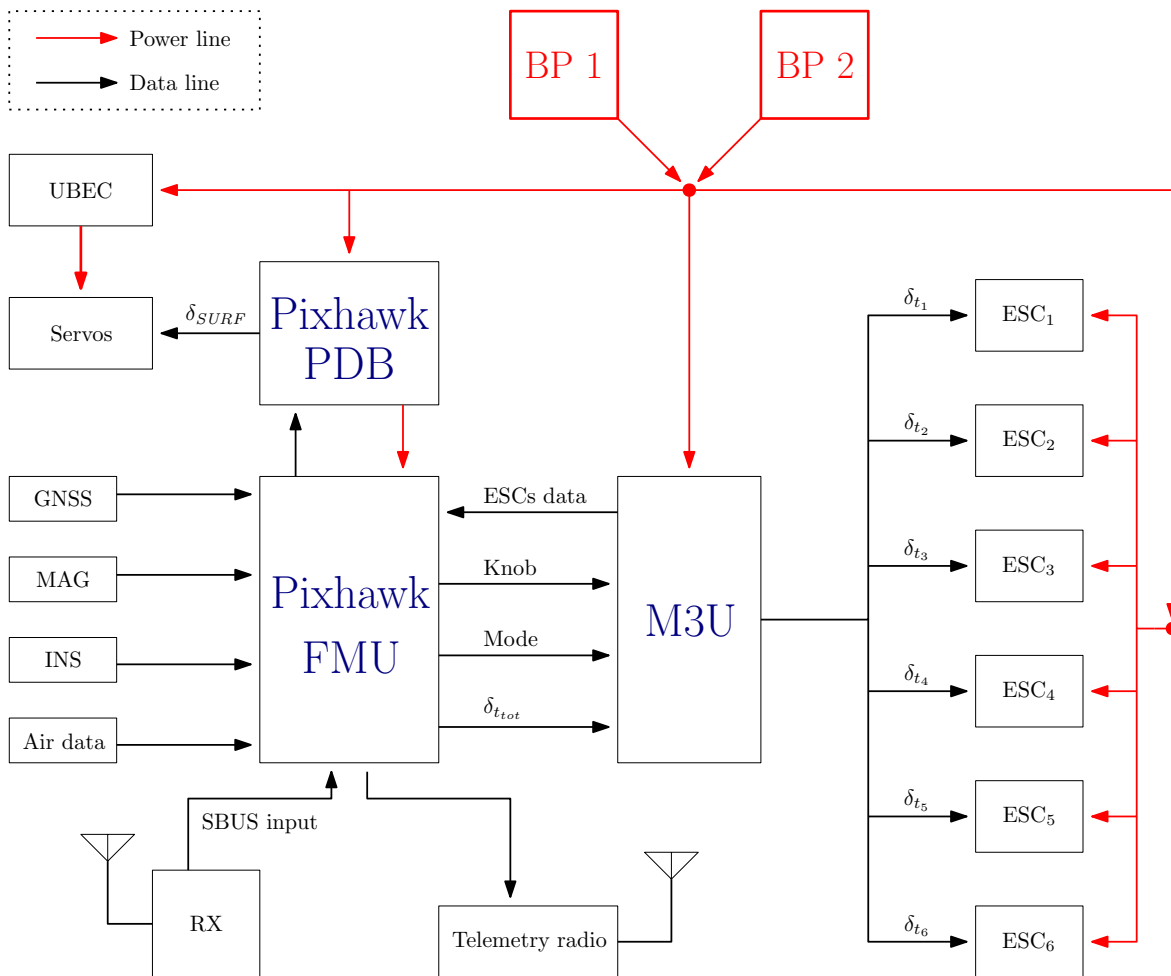


Fig. 6.14: Aircraft electrical system architecture

6.5.1 Onboard power distribution

The onboard electrical system is complex and every component has its own need and power consumption. When designing the power distribution line, major attention should be always paid to safety and reliability. A second but equally important aspect is minimization of embarked mass. Summing these requirements, the choice of a singular power line with every

component in parallel configuration comes straightforward. Providing two redundant power lines would have been too complex and heavy, also counting the already large number of embarked cables. Moreover, space, weight, electro-magnetic compatibility and complexity would have suffered from a more complex line.

Another considered solution was to provide power for electric motors and systems with two separated electrical lines. This would have implied to add a battery pack for the systems in addition to the two BPs for EMs, not adding a justifiable safety level increment. In fact, a failure of the battery for the systems would result into an aircraft loss as well, even if motors could still generate thrust.

Ultimately, each power line presents a singular point of failure, thus acceptable, as the probability of total power loss is low: the junction node between the branches is realized bolting together cable lugs of the electrical wires, and even securing it with tape. Cable lugs are not only crimped to the wires, but also soldered to them. Moreover, a singular or complete propulsive unit electrical branch failure would not influence the branch directed to flight systems. At this point, biggest failure probability is related to the single element malfunction.

Embarked battery packs have a nominal voltage of 14.8 V, but real in-flight values spans from 13.0 V to 16.6 V. They are sized in number, voltage and capacity to fit the needs of the propulsion system, namely peak power and endurance. Other onboard systems have different needs, but anyway the total energy is way less than what is required by the propulsive system. These can be summoned as:

1. **FMU** (Flight Management Unit) - the control suite is made of *Pixhawk 4* boards with external sensors and radio and telemetry receivers. Every component needs 5 V or 3.3 V stabilized, but these are provided by the *Pixhawk 4* power distribution board (PDB) which steps-down voltage from the battery packs. The total measured system consumption peak is around 0.2 A h.
2. **Servos** for control surfaces, requiring an input voltage between 5 V and 6 V, conveyed by the UBEC. Every unit draws a peak of 0.3 A h under stall load.
3. **M3U**, whose board input voltage ranges from 5 V to 30 V. It is self-regulated, thus the board is directly linked to the batteries. Power consumption is less than 45 mW.

Total overall power consumption of the electronic systems is negligible if compared to that reserved to the propulsive units.

6.5.2 Electronic speed controllers

Zubax *Myxa* electronic speed controllers offer good power capability, possibility of customization, data collection and interfacing opportunities (CAN bus interface in particular).

There are three motor control modes available:

- **Voltage** control mode: the controller modulates the specified quadrature axis voltage, ignoring the quadrature axis current, while maintaining the direct axis current close to zero. This mode imitates the behavior of a typical ESC for brushless motors.
- **Current** (torque) control mode: the controller modulates the specified quadrature axis current, while maintaining the direct axis current close to zero. Since the torque of an electric motor is linearly dependent on the magnitude of the torque-generating current, this mode allows the controller to achieve a constant torque irrespective of the angular velocity of the rotor (until the voltage modulator is saturated).

- **Velocity** control mode: the controller runs an angular velocity control loop (which is based on a simple PID controller) on top of the current control loop described earlier. The controller maintains the requested velocity by regulating the torque, realizing a close-loop control feedback on RPM setpoint.

Results of current and velocity control modes are graphically presented in Section 8.1.2.

The ESCs can execute a self-test of the motor in order to tune parameters such as flux linkage and internal resistance. Preliminary coupling between an ESC and its motor is always suggested for better functioning of propulsive units. Moreover, CAN bus dual parallel interface allows to connect the various ESCs with a daisy-chain network, also transmitting working data from every unit. Measured data from every ESCs are: voltage, current, power, torque, motor speed, temperature, status, PWM frequency, errors and warnings. A list of modified parameters are reported in Appendix D.

A CAD representation of one ESC at board level is presented in Figure 6.15.

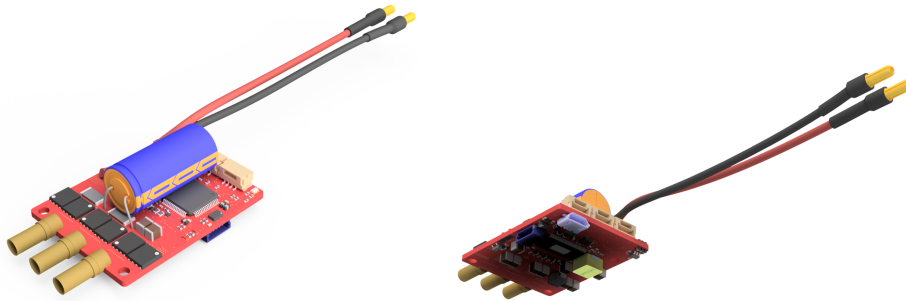


Fig. 6.15: Top and bottom rendered view of Zubax *Myxa* ESC

6.6 Flight Management Unit configuration

Holybro *Pixhawk 4* is a very versatile Flight Management Unit (FMU) and autopilot. Mainly, the board is exploited as FTI (recording data and allowing real-time telemetry, useful support of flight test activity), as power and data link distribution to actuators and *M3U* and also as an autopilot. Among the other features, the *Pixhawk 4* have standard PWM outputs and S-BUS input/output for servos and receiver interface, I²C ports, UART, CAN bus and MAVLink [44] interfaces, redundant power supply inputs and telemetry ports. Furthermore, it is able to identify failures and automatically land the aircraft in case the RC inputs are lost.

Computer interface with the *Pixhawk 4* flight control unit is *QGroundControl* ground station [45], which allows parameter tuning, firmware flashing and live telemetry. Prior to installment of the various components on the aircraft, a test rig was set-up. The rig was made of a wood panel on which various components have been progressively installed, to simplify debugging. The initial setup was with only the FMU and its PDB installed, powered by USB cable for initial configuring. Then, batteries, radio receiver, servos, GNSS receiver and Pitot probe were progressively installed, configured and tested.

In parallel, on another rig, the propulsive unit was installed. The rig served for the basic configuration of every component prior to installation on the aircraft, but, most of all, served to quicken the learning curve of functioning of various components.

The *Pixhawk 4* has an open-access firmware, that can be changed or customized freely. For the *SwitchMaster* application, baseline firmware chosen is the *PX4* in fixed-wing configuration [46]. With every component placed on the aircraft, the firmware was modified to best fit the target logic, in particular assigning every PWM output to the right control surface and

function (aileron, flaps, mode switch, etc.). *Pixhawk 4* configuration also included calibration of sensors: magnetometer, Pitot probe and other sensors have to be calibrated in order to obtain reliable data for the flight controller. This operation requires also knowledge of the relative position and orientation of the board with respect to other sensors, as the FMU embeds a Kalman-filter enhancing sensor fusion in order to determine the right attitude and rates, exploited not only for data logging but also for flight conduction.

Pitot sensor calibration consists only of determination of the probe working range and resolution. At a later stage, a proper calibration sought the relation between measured airspeed (MAS) and calibrated airspeed. This was carried out in *De Ponte* wind tunnel at Politecnico di Milano, with an extract of the test shown in Figure 6.16. The results of the calibration are reported in Figure 6.17. Low speed points, also being out of interest, have been discarded, as the error between MAS and CAS was too high. The first accepted point is at 4.3 m/s MAS, exhibiting an error of 15%, which remains almost constant at every considered speed.



Fig. 6.16: Wind tunnel Pitot calibration

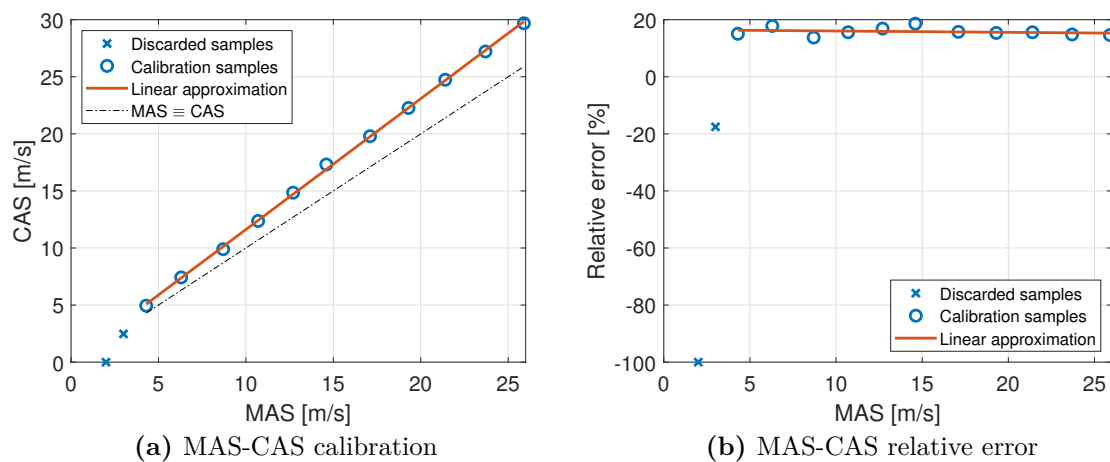


Fig. 6.17: Results of wind tunnel Pitot probe calibration

Third configuration step implies parameter tuning on the ground. The FMU allows to set an endless list of parameters, from internal PIDs tuning for automatic missions to battery voltage calibration. Many of them are referred to safety and control, thus must be set and tested, eventually iterating their values. A list of modified parameters can be retrieved in Appendix B.

At this point, parameters related to actuators were tuned. Central and limit positions, rotation direction, and radio channel assignment can be chosen to best fit every needs. In particular, limit deflections of control surfaces and corresponding inputs on the channels are reported in Table 6.4.

Control surface	Deflection [deg]		Input [-]			
Flap	-35	0.406	0	-1	38	0.831
Aileron	-47.8	1	0	0.008	38	-1
Elevator	-34.5	1	0	0.112	45.7	-0.891
Rudder	-27	1	0	0	22	-1

Tab. 6.4: Limit control surface deflection and corresponding RC input

In Figure 6.18 are reported the arrangement of various elements inside the fuselage. Electronic component placement started from *Pixhawk 4* board positioning, which should be as close as possible to the aircraft center of gravity. Then, power elements should be located as far as possible from logical elements and data cables to avoid electro-magnetic incompatibilities. As it is clear from the picture, power cables and the *Pixhawk 4* PDB are located in front of the aircraft (where also the battery packs are located, not shown in the picture), while radio receiver and *M3U* board are in the rear part. CAN bus cables are unshielded twisted pairs, as well as servos extension cables. This should avoid unwanted electro-magnetic interferences. Other components not appearing in the picture are telemetry transmitter, batteries and Pitot probe.

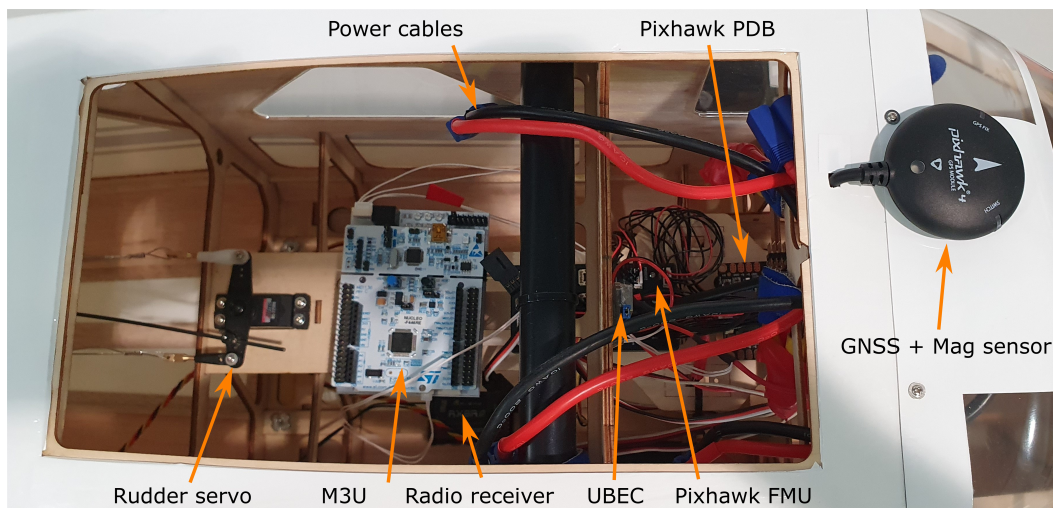


Fig. 6.18: *SwitchMaster* internal arrangement

The fourth step of tuning was made after the first flight, namely iterating and adjusting singular parameters to best fit every requirement, in particular for what concerns assisted modes. Final configured parameters are reported in Appendix B.

Among the various options and parameters, particular importance are the fail-safe related choices: auto-land mode automatically activates when battery level falls above a certain level or RC signal is lost. If the battery state of charge drops below the 20%, telemetry sends a warning message. Then, if it drops below the 15%, auto-land mode is activated. The very same happens if RC signal is lost for at least 1 s. Auto-land mode takes full aircraft control (primary and secondary flight controls) and, after a short loiter, automatically lands the airplane in the place where it previously took-off, hopefully avoiding a crash.

6.6.1 FMU flight modes

Pixhawk 4 FMU allows to control the aircraft in manual, assisted or automatic way. **Manual** control mode allows full pilot authority, with no intervention of the unit. It is selected as the normal flight mode, for take-off, landing, normal flight operations and many test point conduction.

Automatic flight mode gives to the autopilot full aircraft authority. A specific mission can be designed on *QGroundControl* and loaded onboard via telemetry link before take-off. Then, the pilot can activate the mission and the aircraft takes-off, accomplish the mission and land (or just execute the residual part of the mission if activated when already flying) without any pilot intervention, and potentially also beyond line of sight. Nevertheless, the automatic mode was never exploited in the flown missions, even because it demands an extensive tuning of PID gains to obtain good results.

Assisted flight modes split the authority between the FMU and the pilot. The FMU takes aircraft control following the activated assisted mode, with the pilot able to take action, for example imposing a turn: the FMU interprets an aileron input as a turn imposition, not as the deflection of the aileron, and acts to change the heading. Moreover, in assisted mode the command deadband greatly increases and attitude angles cannot exceed prescribed values, acting as an envelope protection system. There are several assisted flight modes, with the exploited ones here reported:

1. **Altitude control** - the climb/descent rate is controlled via the pitch/elevator stick. Once centered, the autopilot tries to maintain the current altitude, even with yaw/roll, and at any airspeed. The throttle input controls airspeed and the aircraft can drift with the wind.
2. **Position control** - with RC stick centered, FMU tries to keep heading constant, crabbing against the wind if needed, to maintain ground track in the current direction. The throttle determines airspeed (at 50% throttle the aircraft will hold its current altitude with a preset cruise speed). Pitch control stick is used to impose an ascending or descending path.
3. **Stabilized** - pilot's pitch and roll inputs are passed as angle commands to the autopilot, while the yaw input and throttle are sent directly via the output mixer to the rudder (manual control). If the RC roll and pitch sticks are centered, the autopilot regulates the roll and pitch angles to zero, hence stabilizing (leveling-out) the attitude against any wind disturbances. However, in this mode the position of the aircraft is not controlled by the autopilot, hence vehicle heading and altitude are not maintained. The vehicle climbs/descends based on pitch input and performs a coordinated turn if the roll/pitch sticks are non-zero. To achieve zero sideslip, it imposes the sideward acceleration to be null. Any manual yaw input is added to the one exploited to perform turn coordination via rudder. It is the most exploited mode for the test point execution, especially for the aerodynamic characterization. Among the others, one parameter is dedicated to assign a pitch offset to tune ability to maintain level flight.

6.7 Radio configuration

FrSky *Taranis X9D PLUS* radio transmitter [47] allows great customization. It can transmit up to 24 digital channels on 2.4 GHz frequency to a digitally binded receiver. In Figure 6.19 is reported a detailed depiction of the radio switches and controls. The same are enlisted in Table 6.5. Refer to Chapter 7 for settings related to *M3U* unit and its working modes.

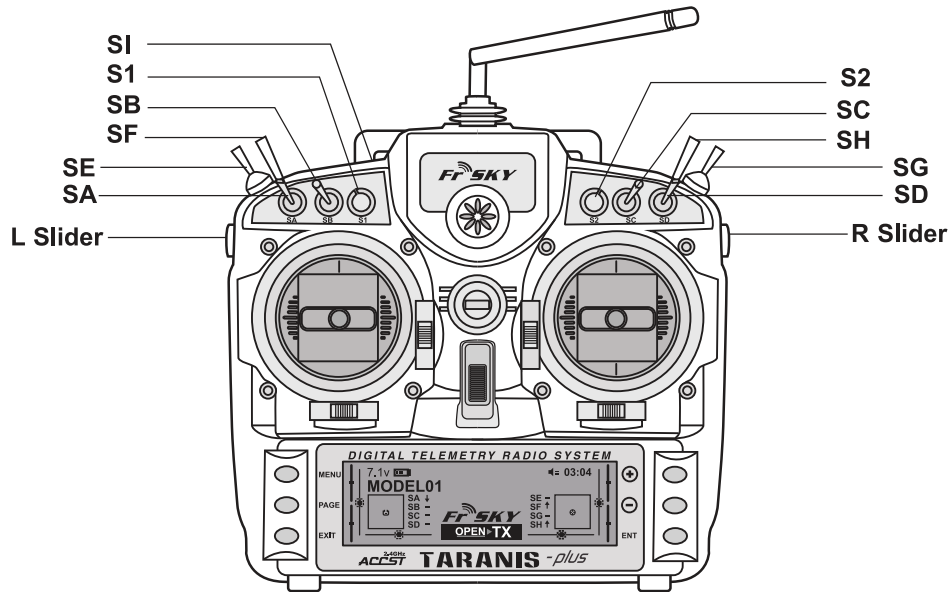


Fig. 6.19: *Taranis X9D PLUS* radio switches arrangement [47]

Switch	Type	Function	Settings
L Slider	Proportional	Asymmetry knob	-
R Slider	Proportional	Flap	-
S1	Proportional	FMU THR damping	[0 – 2]
S2	Proportional	FMU THR integrative gain	[0 – 0.4]
SA	3-Positions	Throttle mapping	OFF-ON-ON
SA	3-Positions	Flap-Elevator trim mix	OFF-OFF-ON
SB	3-Positions	Rates	High-Mid-Low
SC	3-Positions	Assisted flight modes	Manual-Altitude-Position
SD	3-Positions	Assisted flight modes	Manual-Stabilized-Stabilized
SE	3-Positions	ESC setpoint kind	RPM-RPM-RAW
SF	2-Positions	Mode switch	OFF-ON
SG	3-Positions	Propulsive control	OFF-ON-Turn coordinator
SH	2-Positions momentary	Event	-
SI	Button	Arming-Disarming	-

Tab. 6.5: *Taranis X9D PLUS* radio switches function assignment

A switch can operate on a radio channel associated with a physical output (the whole list reported in Table 6.6), with a *Pixhawk 4* or *M3U* setting or parameter or even with internal radio transmitter logical function. An example of the autopilot real-time tuning parameters are the **S1** and **S2** knobs, that aim to tune throttle damping and integrative PID gains. For what concerns transmitter logical functions, we can identify:

- flap-elevator trim mix: activates or de-activates a mix that changes the zero-setpoint of the elevator when flaps are deflected;

- rates: in the high range, full control surfaces excursion is allowed, while in the other settings this are bounded and the central command zone follows a smoother path;
- propulsive control switch: radio channel mixing imposition. This was exploited to investigate the feasibility of propulsive control, by controlling thrust asymmetry with the asymmetry knob. When in the OFF position, the asymmetry knob is disabled; when in ON position, it controls the yawing moment generated by electric motors, considering zero output when the knob is in central position (differently from what happens in *SE-norm M3U* working mode). Lastly, in the *turn coordinator* mode the switch ON associates the knob channel to the aileron channel in order to suppress adverse yawing without imposing any rudder input (details available in Section 7.3.7);
- throttle mapping: changes the way throttle channel is transmitted. When OFF, throttle stick and thrust output relationship reflects the wind tunnel test output, as reported in Section 8.1.2; when ON, the relationship between stick position and transmitted output is as represented in Figure 6.20 along with estimated thrust output. Exploiting this mapping, pilot feeling and handling should improve, helping the pilot in most challenging phases such as landing and approach.

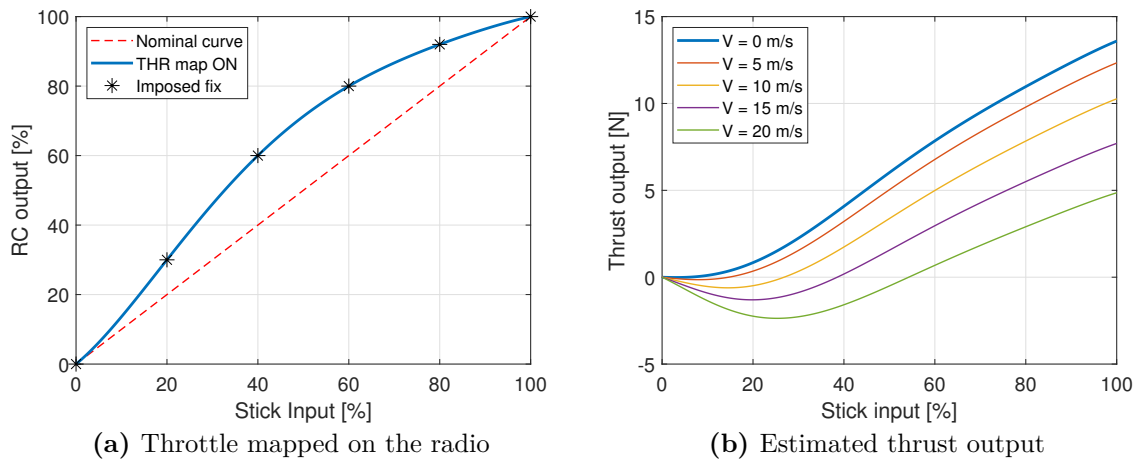


Fig. 6.20: Radio control map and its effect

Channel	Function
CH 1	Ailerons
CH 2	Elevator
CH 3	Throttle
CH 4	Rudder
CH 6	Flap
CH 7	Mode switch & ESC working mode
CH 8	Asymmetry knob
CH 9	Event
CH 11	FMU Flight mode
CH 12	FMU tuning parameter 1
CH 13	FMU tuning parameter 2
CH 16	Arming

Tab. 6.6: *Taranis X9D PLUS* radio channel assignment

Chapter 7

Multi-Motor Management Unit

The control unit employed for propulsion management is similar to what was addressed as *EPMS* in the patent application. In this application it is materialized in a simpler fashion and has been christened Multi-Motor Management Unit (*M3U*).

7.1 System description

The *M3U* board is made of two coupled components: one commercial *STM32* board and one properly designed board. The final assembly in Figure 7.1a is made of a dual level printed circuit. The bottom level is the custom one, on which electronic connectors, LEDs, jumpers and other components are soldered. This latter is reported in Figure 7.1b. The top level is the commercial one, which comprehends USB connection, CPU and the debugging part. In particular, it is the *STM32 NUCLEO-F446RE* [48]. Every employed software tool is free.

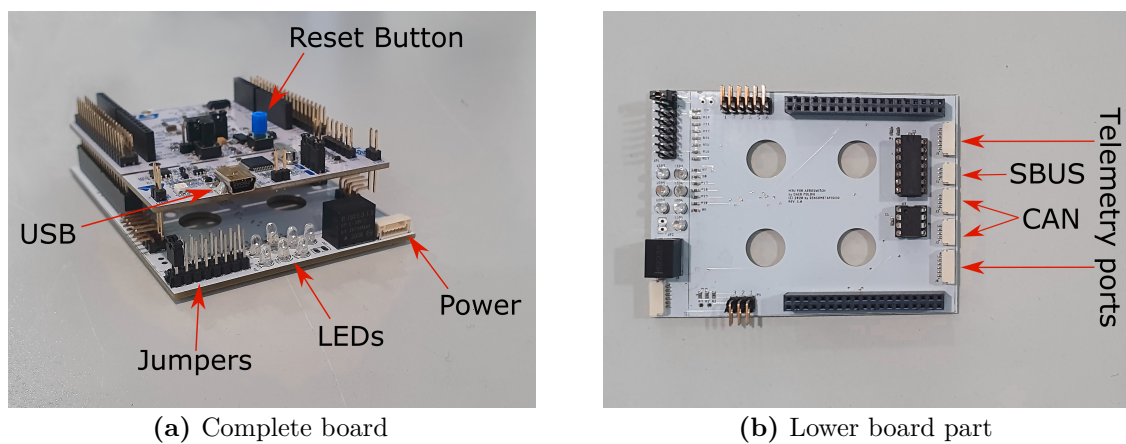


Fig. 7.1: *M3U* board and connections

A collection of the board features is here reported:

- Hardware
 - *ARM Cortex M4* core (32 bit) CPU running at 180 MHz
 - Hardware Floating-point unit
 - 128 KB SRAM + 512 KB FLASH
 - On-board peripherals (e.g. 6x asynchronous serial, 17x timer, 2x CAN, watchdog timer)

- UART for S-BUS from *PixHawk 4*
- 2x UART for telemetry in and out
- Dual port CAN for UAVCAN communication with ESCs
- 6x PWM outputs for servos control
- Software
 - Hard Real Time Operating System based (Context Switch < 800 ns)
 - Full static architecture
 - 6 tasks running at different priorities
 - ESC loop running at 50 Hz
 - 100 ms watchdog
- Performance (for firmware v1.5)
 - Power consumption: < 45 mW
 - Used Flash: 15%
 - Used RAM: 27%
 - Used CPU: 19%
 - Watchdog: never been triggered

The different peripherals and interconnections are also sketched in Figure 7.2.

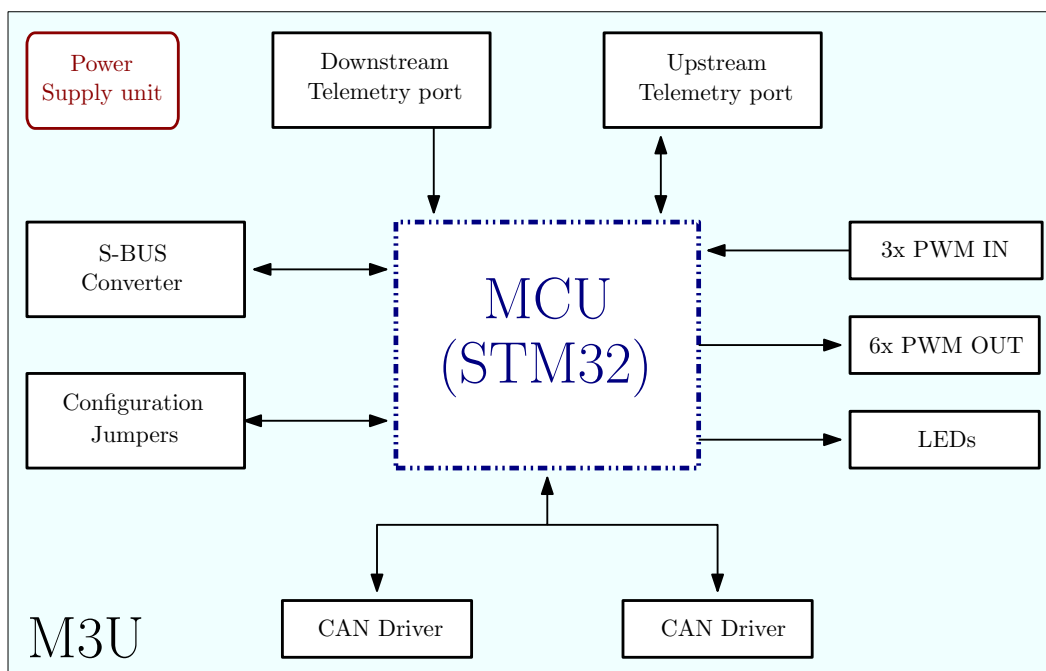


Fig. 7.2: Architecture of the *M3U* board

Every programmable device comprehends different components like CPU, program and data memories and input/output devices. Everything is mapped as a memory address, on which the CPU reads and writes. In a micro-controller (MCU), components are combined in what is called embedded electronics.

The MCU of *M3U* hosts the core *ARM Cortex M4* (which acts like a CPU), the flash memory, the RAM and multiple input/output devices. UART (Universal Asynchronous Receiver Transmitter) peripherals work on serial lines, are currently exploited for S-BUS reading, and will also be employed for future developments. Moreover, CAN devices, timers and a watchdog timer are incorporated in the MCU. The watchdog timer works with a pre-loaded counter, decremented at every clock. It must be brought to its default initial value before reaching zero, otherwise it resets the software. In the *M3U* it is set to 100 μ s.

A real-time operative system is embedded, built on a pre-compiled software. This allows to create several tasks running independently. Given that six tasks are coded, the operative system can assign the CPU usage to only one at a time. The choice is based on priority and task status. Tasks can be ready-to-run or pending, and among the ready-to-run tasks the one with highest priority has the access to the CPU. CAN reception task is the highest priority task in the *M3U*. The CPU can also work in "interrupted" mode: at hardware level a condition makes the processor save its state and interrupt the current execution when instructed by external inputs. This is called "context switch", and is at the foundation of the real-time operative systems. For instance, when an interrupt comes from CAN input communicating an incoming telegram, the interrupt routing collects the telegram, stores it in the memory, sends it to the corresponding task and releases the interrupt, because interrupts can be set at very close time intervals.

The *M3U* tasks are, in order of priority:

1. CAN reception
2. S-BUS reception
3. CAN transmitting
4. ESC task
5. LED task
6. Idle task

Message reception has the highest priority because data delivered by peripherals could be overwritten if not instantaneously collected. The S-BUS from *Pixhawk 4* sends messages at 100 000 Baud, corresponding to 10 000 symbols per second at 10 bit per symbol. The CPU speed is 180 MHz, therefore one symbol takes 5.5 ns to be transmitted. When a telegram arrives, UART receives it and the corresponding task queues it before progressively processing each one. The UAVCAN protocol foresees that once in a second every device transmits its status, and it conveys the command to the ESCs every 100 μ s after collecting the setpoints from the ESC task.

ESC task is fast enough to calculate the setpoints and save them after having gathered throttle, knob and mode setting from the S-BUS. After the integrity check is verified, it writes down the setpoints.

The idle task is executed when no task is ready-to-run. It puts the CPU into sleep mode, turning off the clock and enhancing energy saving. Hardware timers serve to plan CPU awakening, with the same purpose of energy spare.

The concurrent management of tasks is not trivial: some tasks could be reading while others are writing on the same memory locations. Thanks to the "Inter-Process Communication" (IPC) it is possible to protect some operations in order to prevent data split when coming from the same source at different timestamps. This whole system is detrimental for the realization of a simple software, but is paramount in case of more complex realizations. This way, real-time systems ensure determinism and have great safety against bugs.

7.2 On-board integration

In Figure 7.3 is reported the logic behind the command chain on which the *M3U* is based. Pilot inputs coming from RC receiver and the *Pixhawk 4* control module is processed inside the *M3U* in function of the selected working mode.

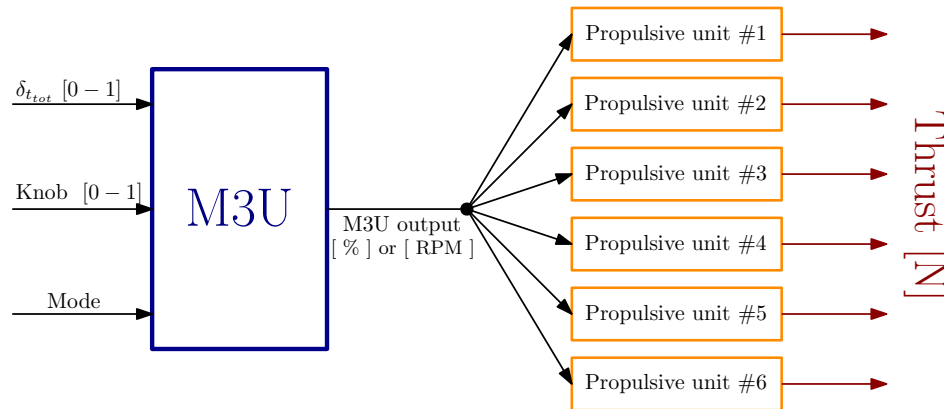


Fig. 7.3: Block scheme of the *M3U* command chain

Resulting setpoints are sent via CAN bus to the six propulsive units (assembly of ESC, EM and propeller), which generate thrust. As cleared from Figure 7.3, the whole system works in open control loop configuration, without any feedback. The only available control loop in the thrust chain is made by ESCs and relative motors, that can be controlled with setpoint on RPM in the related control mode. This is the result of the choice of keeping the system as much simple as possible, in this specific case to shorten development time.

CAN bus allows to distribute data to the entire system, giving a read-back of every propulsive unit parameters which are used for telemetry. Onboard CAN bus network configuration is reported in Figure 7.4. *Pixhawk 4* FMU is connected to the network in order to record data coming from the singular ESC and the *M3U* status. The *Pixhawk 4* board is internally terminated, while on the other side of the chain a $120\ \Omega$ resistor terminates the network.

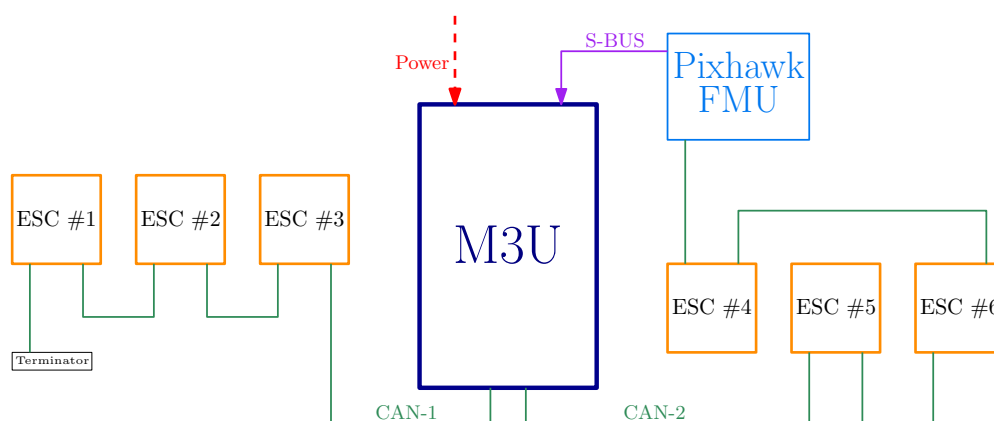


Fig. 7.4: Onboard CAN bus network configuration

M3U and propulsive units assembly can be seen as multiplicative blocks with their transfer functions: the *M3U* takes one input and produces six outputs multiplying the input for a coefficient based on the input itself and the selected control law, while the propulsive units take the *M3U* output and convert it to physical thrust. Inside the propulsive units, ESCs

can be set to manage the receiving information as alternatively a setpoint on RPM, motor electrical current or voltage, as already described in Section 6.5.2.

Exploiting $M3U$ coefficient mapping, it is also possible to change the relationship between pilot setpoint and thrust output. For instance, it could be possible to revert the second order shape to a linear one. This possibility is actually not exploited, as the same was more easily done via radio transmitter software (acting on every motor setpoint at the same time).

The $M3U$ have three different data inputs from the S-BUS port, a set of physical jumpers, LEDs and different electrical interconnections (CAN bus, PWM). A USB port is dedicated to firmware uploading and debugging. Data inputs come from the RC line, and are throttle, mode and asymmetry percentage. Throttle setpoint is imposed from the stick by the pilot. It is in percentage, with a total of 2048 intermediate reading (this resolution is defined by radio and receiver technology). The mode switch has only two adjustments, corresponding to ON and OFF status. OFF status always corresponds to the nominal and safest condition, with all six motors running evenly. When the switch is on the ON position, the control law selected on ground via physical jumpers on $M3U$ board is activated. Led lights on the board are a good and fast way to check proper functioning. The asymmetry percentage channel also has a proportional excursion range, and will be later described.

7.3 Working modes

7.3.1 Outline

Four working modes were conceived, corresponding to the concept to be demonstrated. They are here reported in order of priority:

- multi-engine normal mode (*ME-norm*);
- single-engine normal mode (*SE-norm*);
- single-engine One Electric Motor Inoperative mode (*SE-OEMI*);
- multi-engine One Engine Inoperative mode (*ME-OEI*).

Including a fail-safe mode and the later-introduced propulsive control mode, total working combinations are 14, each coupled with a jumper configuration, as displayed in Table 7.2.

UAVCAN protocol allows to send different telegrams to the ESCs. Communication also involves the in-flight selection of the control law that the electronic speed controllers must follow. As explained in Section 6.5.2, ESCs can be controlled with three alternative settings. Default one is that imposing calculated RPM setpoint via feedback control loop. Therefore, when following this control law, the telegram contains the index related to "RPM control mode", followed by the imposed setpoint, ranging from 0 to 11 000 RPM. Another exploited possibility is the so-called "RAW control mode", in which the ESCs control the motors in open-loop, simply imposing a potential difference proportional to the message contained in the telegram, which ranges from 0 to 1.

These two control modes can be activated with a radio signal, without any lag on motors response. No further radio channel assignment is needed, as the mode switch itself is exploited, providing four different PWM ranges (each with its relative thresholds) on the $M3U$ and in the radio mixer. The four settings correspond to "Mode OFF - RPM setpoint", "Mode ON - RPM setpoint", "Mode OFF - RAW setpoint" and "Mode ON - RAW setpoint". The four configurations were selected through a combination of two different radio switches, one dedicated to the choice of setpoint logic while the other related to operating mode, to lower the pilot workload.

A representation of the *M3U* working modes is reported in Figure 7.5.

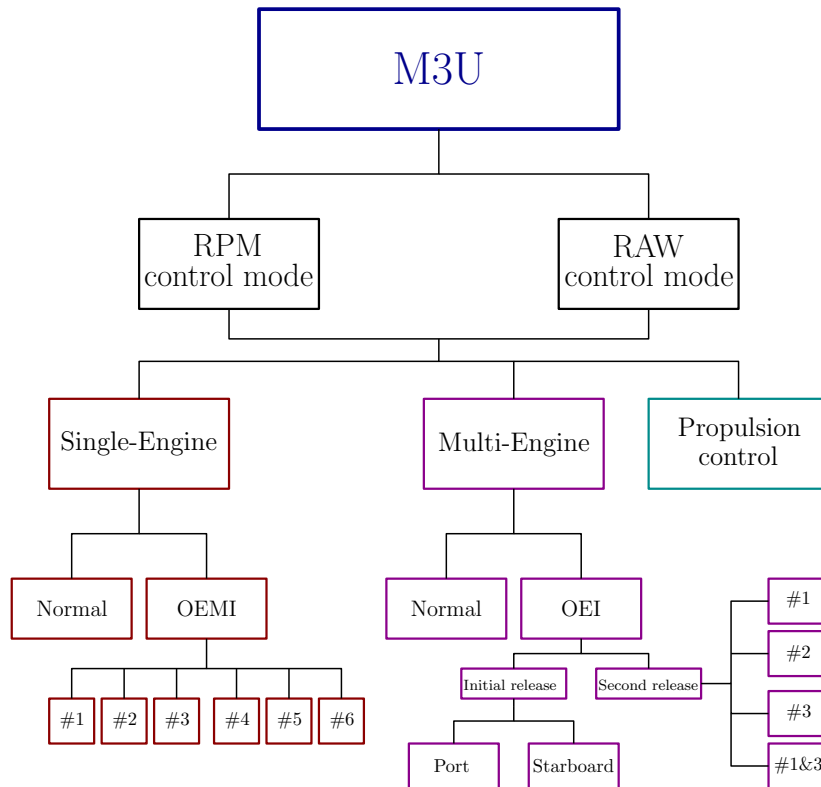


Fig. 7.5: *M3U* working modes tree

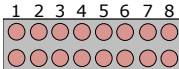
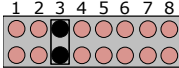
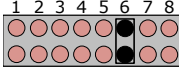
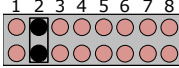
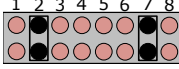
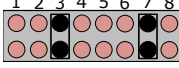
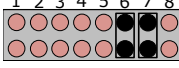
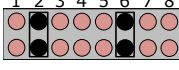
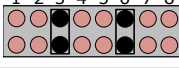
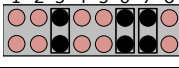
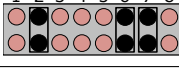
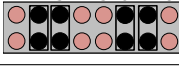
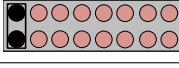
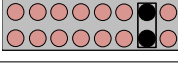
The several *M3U* firmware editions developed and flashed on the board are enlisted in Table 7.1. Every working mode corresponds to a specific combination of physical jumpers on the board, as reported in Table 7.2. The board has 8 jumpers, but not every slot is freely assignable without software intervention.

Version	Date stamp	Details
v1.0	10-02-2021	First bench test release
v1.1	15-02-2021	Initial operational capability
v1.2	23-02-2021	Full capability - RAW setpoint added
v1.3	03-03-2021	<i>ME-OEI</i> first version
v1.4	05-03-2021	Propulsion control capability added
v1.5	12-03-2021	<i>ME-OEI</i> second version

Tab. 7.1: *M3U* firmware release history

The first release served to verify functioning of every system and perform preliminary and long-run tests. Moreover, it was exploited to calibrate the commands.

The second version was the first tested in flight although not including the ultimate set of operating modes. Later releases achieved full operational capability, with working modes and relative logic analyzed and modeled in the following sections.

Jumper	Working mode	LED flashes
	<i>ME-norm</i>	1
	<i>ME-OEI Port</i>	2
	<i>ME-OEI Starboard</i>	3
	<i>SE-norm</i>	4
	<i>SE-OEMI-M1</i>	5
	<i>SE-OEMI-M2</i>	6
	<i>SE-OEMI-M3</i>	7
	<i>SE-OEMI-M4</i>	8
	<i>SE-OEMI-M5</i>	9
	<i>ME-OEI-M3</i>	10
	<i>ME-OEI-M2</i>	11
	Propulsive control	12
	<i>ME-OEI-M1</i>	13
	<i>ME-OEI-M1+M3</i>	14

Tab. 7.2: *M3U* jumpers configuration

7.3.2 Safety modes

"Safety first" is a mandatory statement in the aviation field. As a consequence, two safety working modes are embedded inside the *M3U* firmware: *Fail-safe* and *Downgraded* modes. *Fail-safe* mode, as suggested by its name, automatically activates when a failure occurs. If the *M3U* receives no input through the S-BUS or the system crashes, *Fail-safe* mode puts every motor setpoint always to zero.

The *Downgraded* working mode, instead, is automatically activated when the *M3U* cannot execute a command or is unable to trace the operating mode from the combination of physical

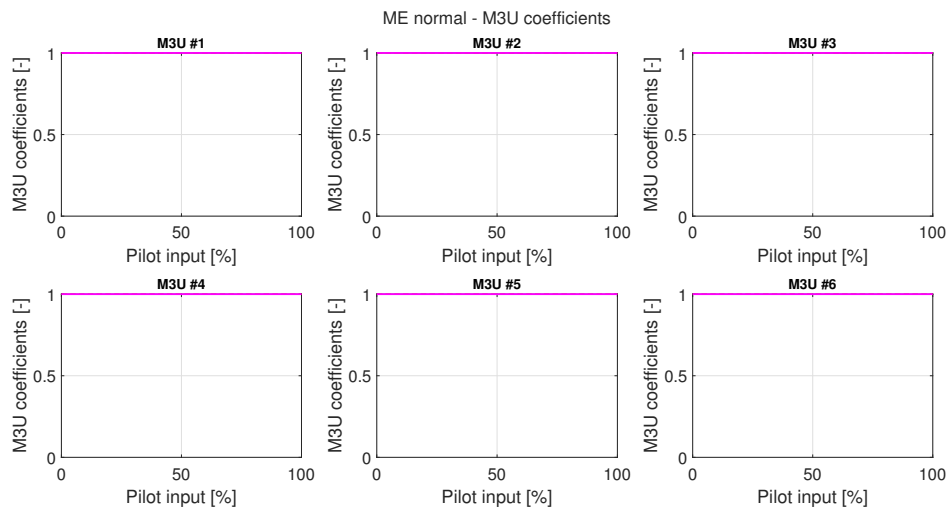
jumpers at system start-up or in flight. It also starts working if the *M3U* computational load is too high. The *Downgraded* working mode is numerically identical to the *ME-norm* mode, in which every motor setpoint is identical.

7.3.3 Multi-Engine normal

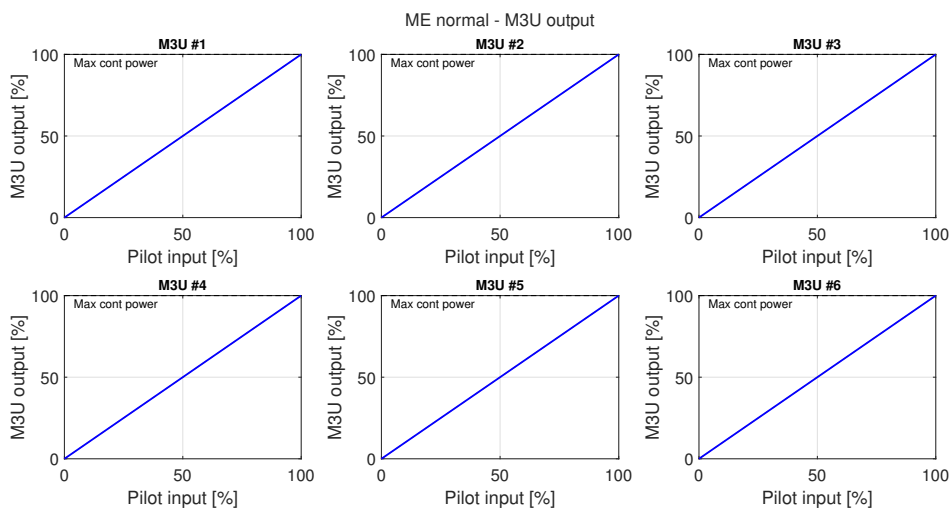
ME-norm is the standard and most simple working mode. It is the control law exploited when the mode switch is in OFF position, hence in normal flight conditions, and also when internal consistency checks fail. The purpose of this working mode is normal and non-simulated emergency flight control with full power available and no asymmetry. In this mode, all electric motors work in the same fashion, in an even and uniform way.

Multi-engine normal mode corresponds to the working mode of a multi-engine aircraft. Therefore, the relationship between pilot input and *M3U* output is straightforward, being the multiplicative factor equal to 1 for every motors and setpoint, namely:

$$\delta_{t_{1,2,3,4,5,6}} = 1 \cdot \delta_{t_{tot}} \quad . \quad (7.1)$$



(a) *M3U* internal coefficients



(b) *M3U* input-output relationship

Fig. 7.6: *M3U* control law for the multi-engine normal working mode

These coefficients are shown in Figure 7.6, along with the relation between $M3U$ input and output. In the second graphs, a dashed line marks the region of maximum continuous power for the electric motors. This corresponds to 100% of real motor maximum power, as "de-rating" is only exploited in the single-engine modes.

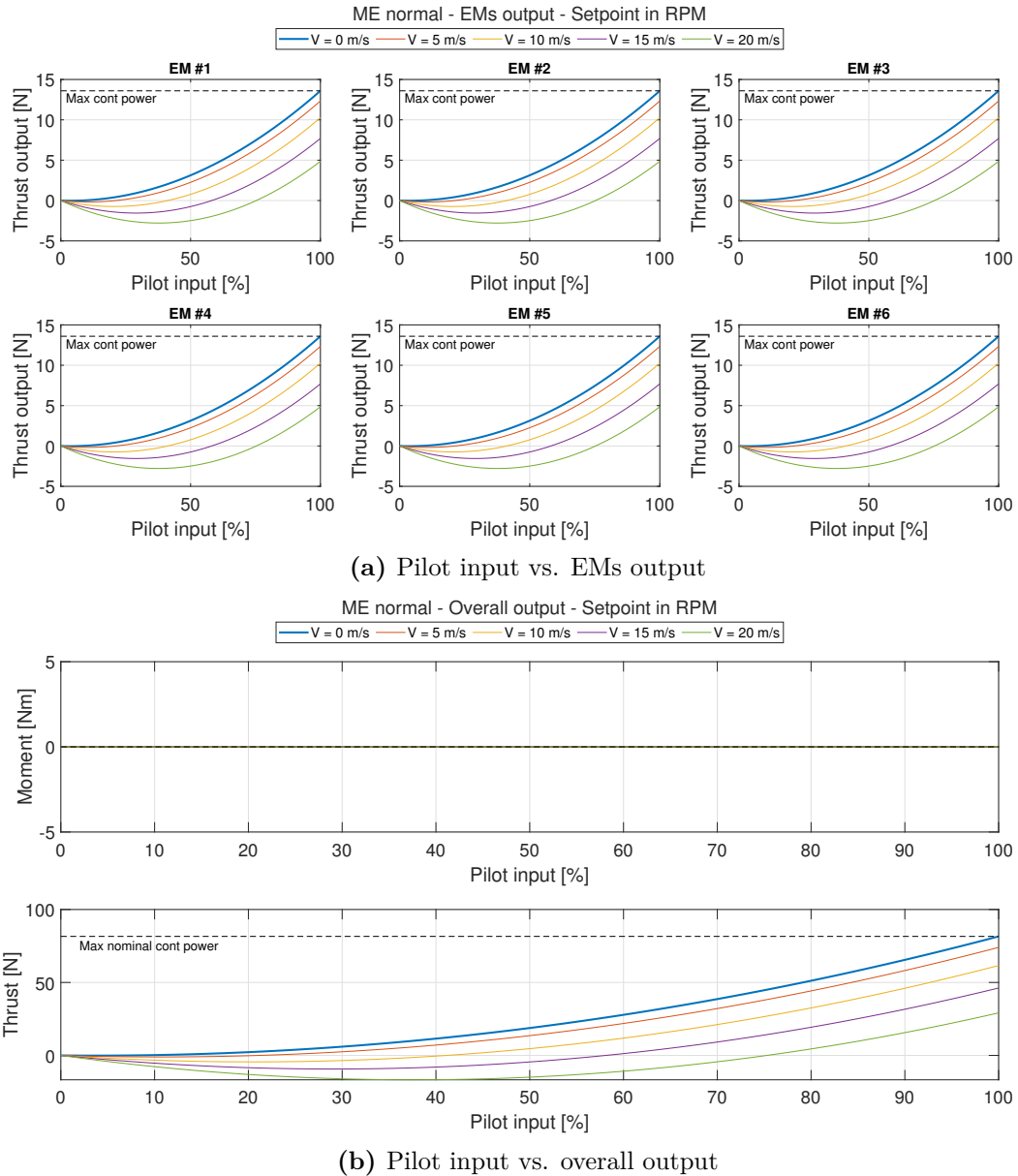


Fig. 7.7: Output simulation for the multi-engine normal working mode (RPM control)

A simulation of the output coming from every EMs and the resulting total output are depicted in Figure 7.7 setting the ESCs in RPM control mode. The output curves are built with an interpolation developed on data gathered through wind tunnel testing (see Section 8.1.2) and moment calculation took into consideration the placement of motors with respect to the aircraft longitudinal axis. The same is represented in Figure 7.8 for the electric current control mode. The hypothesis behind this and the following simulations is that every propulsive unit has the same characteristics (i.e. shares the same output).

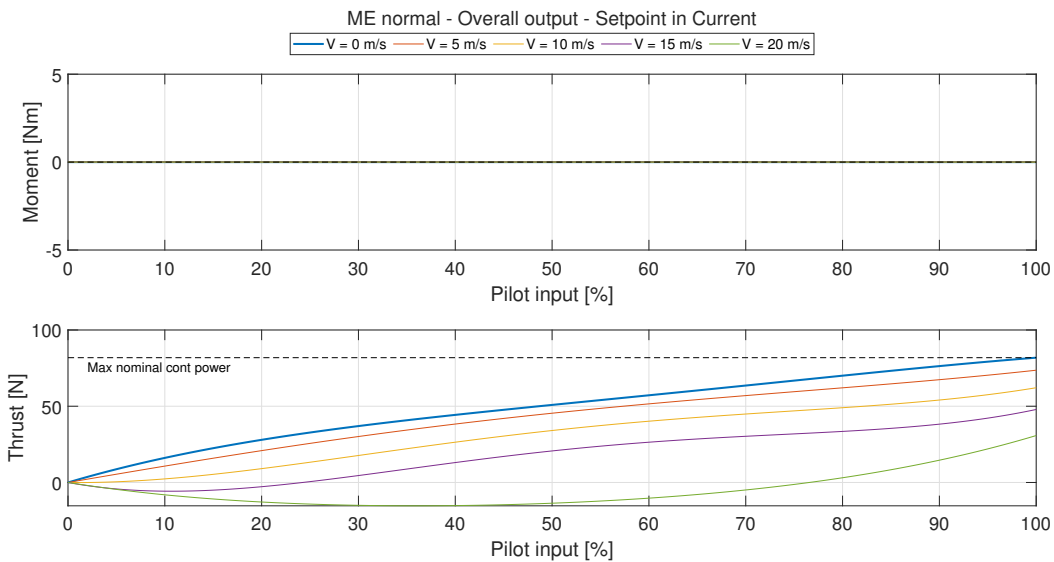
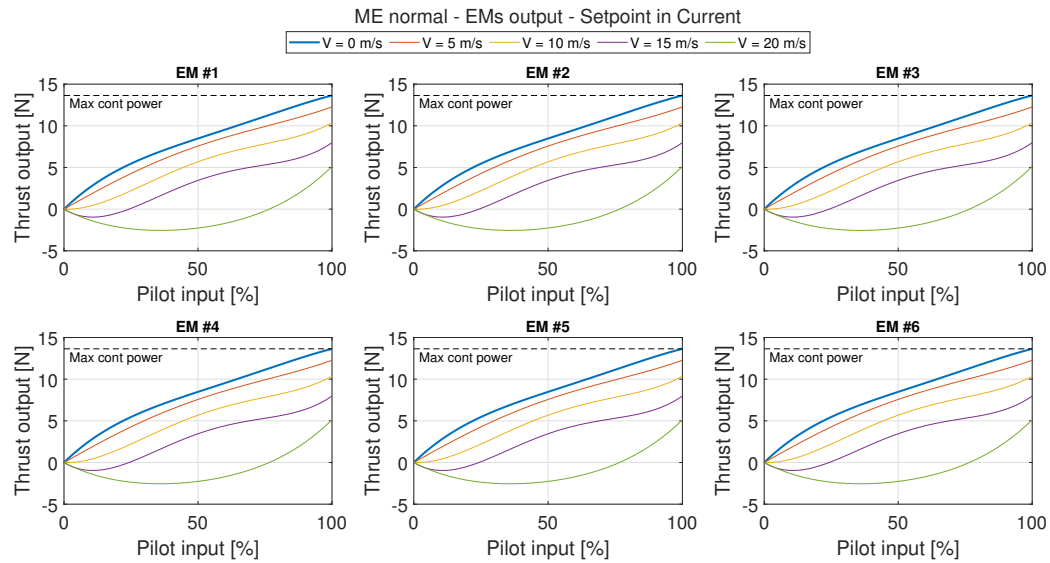


Fig. 7.8: Output simulation for the multi-engine normal working mode (current control)

7.3.4 Single-Engine normal

SE-norm is the simulation of single-engine characteristics, subject of the patent application. In this working mode, outer motors work differently from the four inner ones, to produce a yawing moment similar to the one of a real General Aviation single-engine propeller-driven aircraft. The purpose of the simulation is not to pursue a specific quantitative objective, just considered as a reference, but to emulate a general behavior. Just like every airplane has its own stalling speed, but everyone must be safely flyable, the same is pursued with this in-flight simulation, looking at the bigger picture.

Real aircraft behavior has been investigated both with computer simulator flight testing and with real aircraft flight testing in Chapter 5. It can be summoned as a generation of sideslip angle, turn rate and bank angle after a power increase starting from trimmed flight.

The higher the airspeed, the smaller are these effects.

From a theoretical point of view, the behavior of a single-engine could be achieved applying a different setpoint to the most external motors. The strategy implemented in the *M3U* is the same as that conceived in *EPMS*, designed for *Trybrid*: the four central motors work in a straight and even way, corresponding to the pilot setpoint. Motor #1 and #6 obey to a lower and higher setpoint, respectively. This reflects into a thrust unbalance, which leads to a yawing moment, with the same effect of propeller slipstream on a single-engine aircraft. The definition of percentage of asymmetry needed is one of the objectives of *TBM* flight testing.

Keeping the same asymmetry unbalance percentage at every throttle setting leads to an increment of generated yawing moment as throttle increases, as experienced on a real aircraft. Keeping the same setting also for every airspeed results in a lower yawing moment when airspeed increases. This latter, summed to the counter-acting lateral force contribution from the airframe, that increases when airspeed increases, should exactly match the real aircraft behavior of having a lower SSA at higher airspeeds.

In Figure 7.9 is reported a simulation demonstrating what has been stated. This simulation refers to the *Trybrid*, but no qualitative difference is expected from the *SwitchMaster* as the two aircraft are very similar from every point of view. The modeling is made upon Borri's simplified formulation to equilibrium [49], accounting for stability and control derivatives, center of gravity position, aerodynamic parameters and propeller thrust related to airspeed. Looking at the curves, it is clear how SSA and consequential deflection of control surfaces to restore trim decrease when the airspeed increases.

Another feature exploited by single-engine simulation (both for normal and emergency conditions) is the motor de-rating. Full scale electric motors allow a high percentage of overrating if well cooled. In some state-of-the-art motors this can reach up to 150% of nominal motor power [11]. This behavior is welcomed both for normal and emergency simulated single-engine aircraft, allowing more freedom in the control framework. However, this feature is not readily available for small RC electric motors, and is simulated the other way round by imposing a de-rating. In this way, full throttle position in nominal conditions corresponds to the 66.67% of true maximum setpoint. In other words, real full power setting is the 150% of the de-rated value. As already stated, this is applied in both *SE-norm* and *SE-OEMI* modes, for consistency, and should not represent a risk given the massive amount of specific excess power.

Activating the mode switch, after having set the right jumper on the ground, the single-engine simulation starts. In this control law another driver comes into play: the asymmetry knob. Through a knob on the radio transmitter, the pilot can impose the desired percentage of thrust asymmetry. When the radio knob is in its zero position, thrust asymmetry is 0%, hence all six electric motors work evenly, with a maximum continuous setpoint equal to the 66.67% of the maximum available. When the knob is turned to 100%, coefficients of motor one and six change linearly with pilot input, sharing their lowest point (throttle position to 0%). Motor #6 highest point (throttle position to 100%) corresponds to the maximum motor setpoint, while motor #1 situation is mirrored.

For every other intermediate knob position, the system calculates the curve slope. After

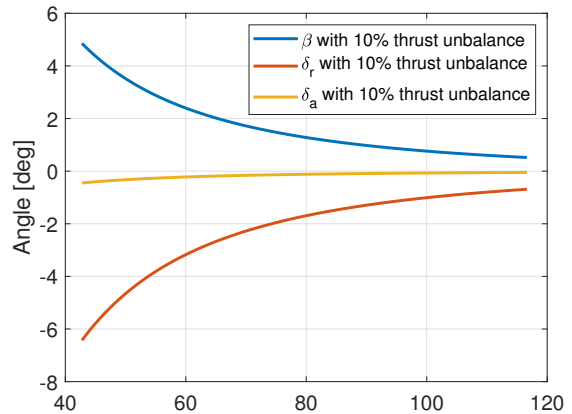


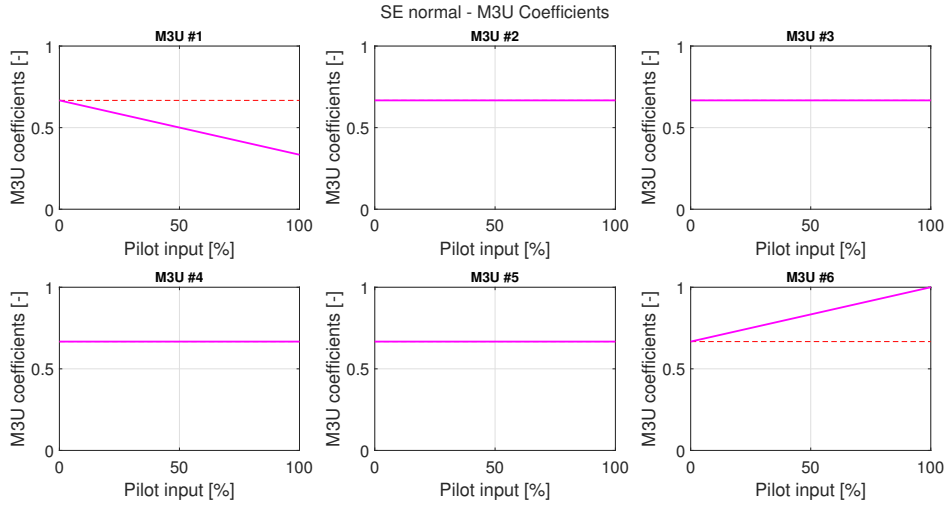
Fig. 7.9: SE simulation on the *Trybrid*

the flight simulator flight testing, the continuous power percentage was raised to 80% in order to have a greater excess of power. These coefficients are shown in Figure 7.10, along with the relation between $M3U$ input and output when the knob is set to 100%. Equations included into the $M3U$ software for the SE -norm mode are:

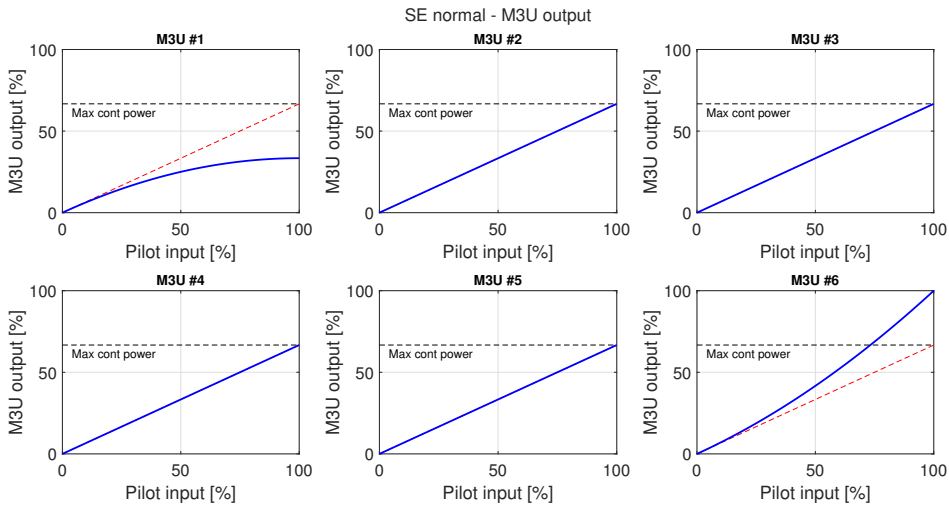
$$\Delta \mathcal{P}^{[\%]} = \delta_{knob} \cdot (\mathcal{P}_{\max}^{[\%]} - \mathcal{P}_{\max \text{ cont}}^{[\%]}) \quad (7.2)$$

$$\begin{cases} \delta_{t_1} &= (\mathcal{P}_{\max \text{ cont}}^{[\%]} - (\Delta \mathcal{P}^{[\%]} \cdot \delta_{t_{tot}})) \cdot \delta_{t_{tot}} \\ \delta_{t_{2,3,4,5}} &= \mathcal{P}_{\max \text{ cont}}^{[\%]} \cdot \delta_{t_{tot}} \\ \delta_{t_6} &= (\mathcal{P}_{\max \text{ cont}}^{[\%]} + (\Delta \mathcal{P}^{[\%]} \cdot \delta_{t_{tot}})) \cdot \delta_{t_{tot}} \end{cases}, \quad (7.3)$$

where $\delta_{t_{tot}}$ stands for pilot input setpoint, whereas δ_{t_i} is the output of $M3U$ to the i -th propulsive unit. $\mathcal{P}_{\max}^{[\%]}$ is max power percentage (default value is 100%), whereas $\mathcal{P}_{\max \text{ cont}}^{[\%]}$ is referred to max continuous power. As already stated, ultimate value of this latter is 80%. $\Delta \mathcal{P}^{[\%]}$ enforces desired output setpoint variation on motors #1 and #6, and thus thrust asymmetry.

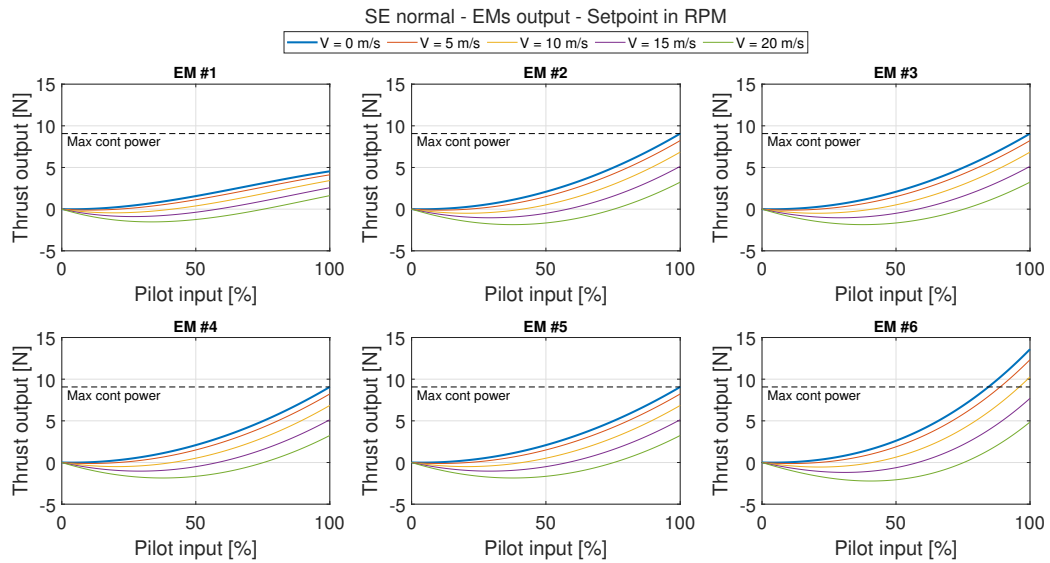


(a) $M3U$ internal coefficients

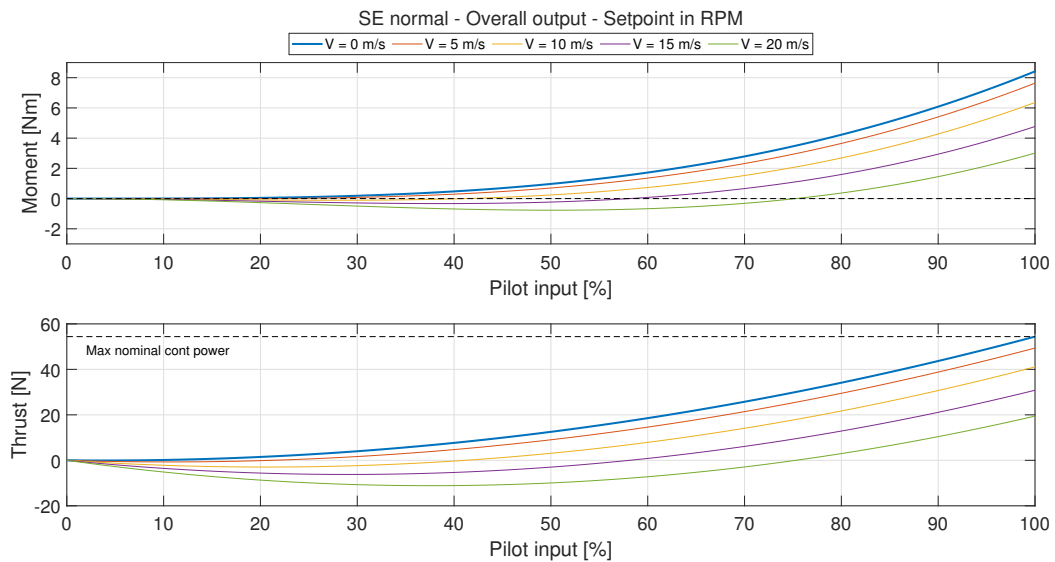


(b) $M3U$ input-output relationship

Fig. 7.10: $M3U$ control law for the single-engine normal working mode (knob at 100%)



(a) Pilot input vs. EMs output

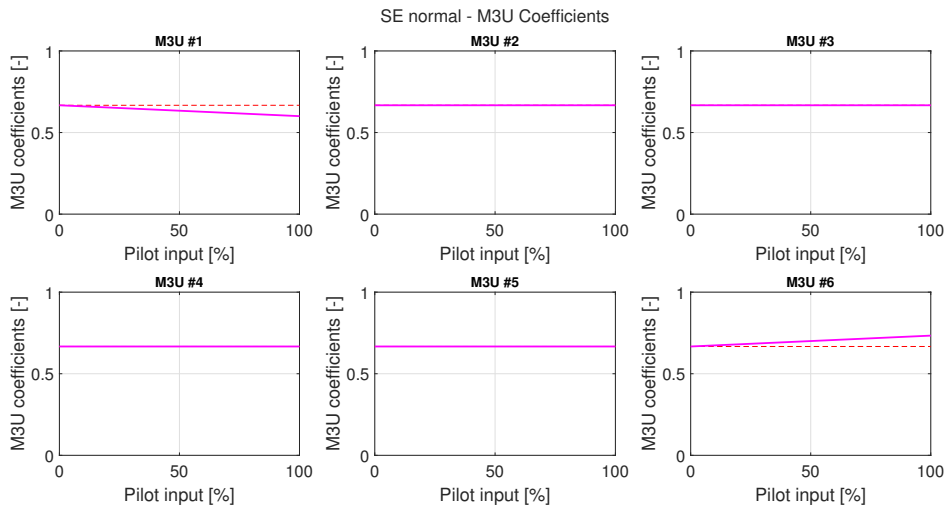


(b) Pilot input vs. overall output

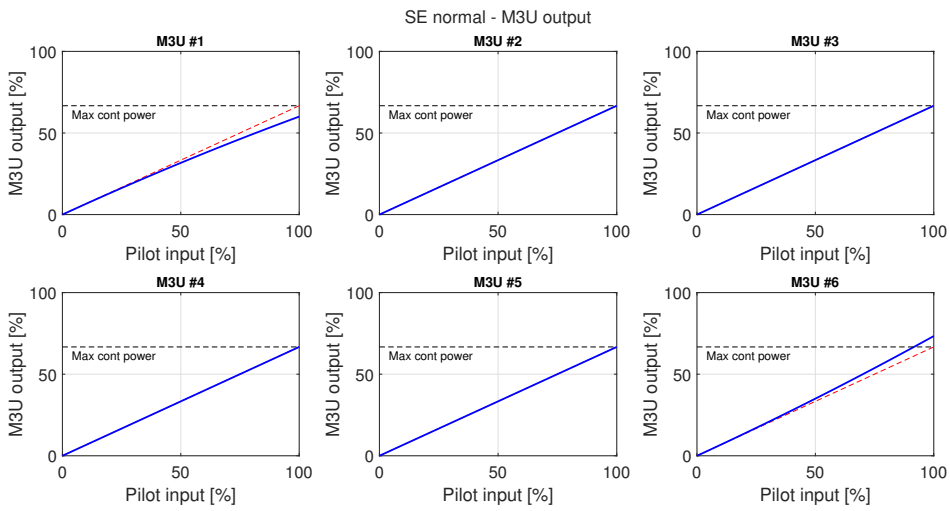
Fig. 7.11: Output simulation for the single-engine normal working mode (knob at 100%)

A more realistic asymmetry value is expected to be around the 20%, for which $M3U$ coefficients and outputs are reported in Figure 7.12.

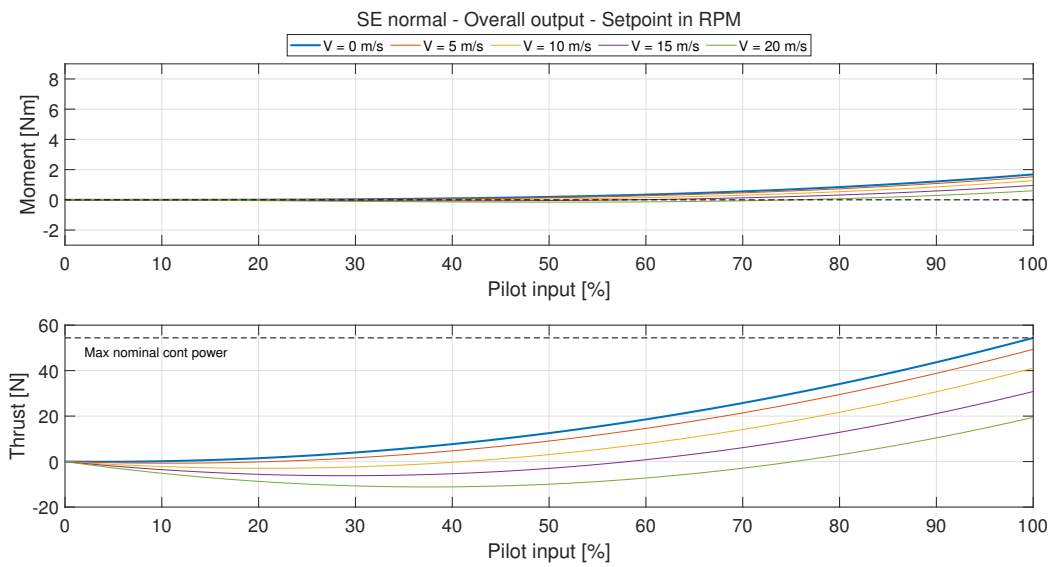
The same thrust asymmetry could be achieved at maximum throttle setting, simply imposing constant coefficients (as happens for inner motors). This simpler control law has no dependence on pilot input, but is less accurate. On the contrary, the $M3U$ input-output relationship of second order type for the outboard motors positively reflects on the overall output: generated yawing moment at 50% throttle is 1/10 of the maximum one, and with the 20% knob setting it is negligible. This better reflects the real GA airplane behavior, in which the asymmetry is more noticeable at high throttle settings. This control law also managed to enforce asymmetry at all throttle settings, rather than at setpoints higher than a prescribed value. Reduction of induced yawing moment with increasing airspeed is confirmed by the following graphs, again in accordance with the behavior of a real single-engine aircraft. Another positive aspect is the overall thrust being independent from the knob setting.



(a) *M3U* internal coefficients



(b) *M3U* input-output relationship



(c) Simulation output

Fig. 7.12: *M3U* single-engine normal mode (knob at 20%)

7.3.5 Single-Engine One Electric Motor Inoperative

When a multi-engine aircraft suffers from the failure of an engine, it enters into a really tough asymmetric flight condition. Only well trained pilots can handle this hazardous situation, therefore the greatest part of hours flown for the multi-engine rating are conducted to manage this scenario. This is why a single-engine rated pilot is not able to manage such emergency situation. No regulatory board will ever make a multi-engine aircraft flyable by a single-engine rated pilot. Therefore the whole system must demonstrate that, once put in single-engine mode, the airplane is always controllable by a SE rated pilot or student pilot, even in emergency case.

An electric motor is less subject to failures than an internal combustion engine, but the chance of entering into a one-electric-motor-inoperative condition is non-negligible, especially if accounting for bird-strikes, propeller damages or other unfortunate events. Therefore, *M3U SE-OEMI* mode aims to demonstrate full aircraft controllability after a motor failure, even when a single-engine pilot is in command. As a consequence, flight testing of this working mode takes directly into account aircraft handling qualities: pilot-in-the-loop behavior is essential, as long as pilot feeling and handling capability. From a quantitative point of view, trimmed flight should be achieved with deflection of control surfaces not far from normal situation and without a major flight asymmetry.

Five different configurations of *M3U* jumpers corresponding to as many *SE-OEMI* conditions were conceived. In particular, the fact they are only five instead of six is because simulated failures of motors #1 and #6 share the same working mode. For what concerns the failure of one of the two inner or central motors, they were all tested although the aircraft being symmetric, thus with no difference expected between shutting down motors on starboard or port side.

Once the mode switch is flipped to ON, the selected motor is turned off, while the others are managed in a way to ensure flight controllability. In details, total available thrust should be maximized while the generated yawing moment must be as close as possible to zero or at most to the SE reference value. Optimal situation could be reached adopting foldable propellers, which reduce drag produced by the dead motor. The time was the most critical constraint in the procurement of propellers having the pursued specifications, with both senses of rotation. It was thus necessary to give up on foldable propellers.

The best way to achieve the desired behavior is to embed a controller (PID or LQR) inside the *M3U* which actively regulates every motor to follow a desired SSA setpoint. SSA should have been reconstructed starting from data received from the *Pixhawk 4* telemetry output. This was not a feasible solution for the particular application, mainly due to the limited development time available. Acquiring data in real time from the flight control unit, automatically calculate SSA and implement the right control law and gains was not feasible. A second strategy was to follow the very same strategy as for the other modes, but introducing also an airspeed dependence. Also this was too much time-consuming, so discarded.

The eventually adopted procedure is still analytic, but of easier software and hardware implementation. Starting from results of propulsive unit wind tunnel testing, an approximated curve relating motor speed with thrust generated is built only upon the range of flight speed of interest, reported in Figure 7.13. This is later exploited to calculate motor thrust at a mean flight speed. When shutting down a motor, the most external operative motor on the opposite side of the dead one is exploited to achieve the right yawing moment, while the remaining four motors spin in normal fashion. For example in case of simulated failure of one of the most external motors, there is no more proper solution than shutting down the corresponding one on the opposite side and operate the remaining four, up to maximum non-continuous power. In the other cases, the required setpoint of most external motor is calculated enforcing

the approximated curve and real motor placement with respect to the longitudinal axis, to impose equilibrium. As a result, yawing moment with one electric motor inoperative will be identically null only for one flight speed, but will be of a sufficiently small magnitude for every flight speed of interest. The purpose is that the effects are always less pronounced than the ones generated in *SE-norm* mode.

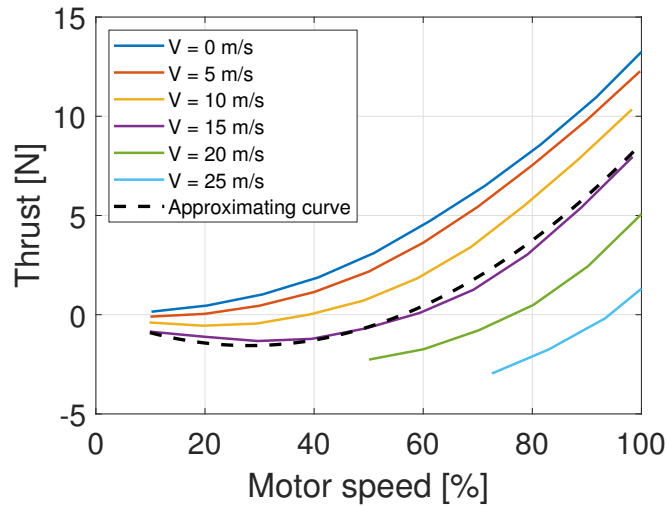


Fig. 7.13: Curve approximating the results of propulsive unit wind tunnel testing

The only problem is that the obtained approximating curve suffers from a bad behavior at low RPM, due to the braking action of motors when flying at high speed. Namely, when imposing 0% input setpoint, the original curve would have implied an output of 60%. Consequently, in order to avoid this unwanted behavior, the curve has been modified to bring the throttle to zero in correspondence of the lowest input values. Then, the modified curve has been approximated again with a fifth-order polynomial to determine the right coefficient to feed the *M3U* control law. This last curve is reported in Figure 7.14 when the dead motor is the number 2, along with the modified one.

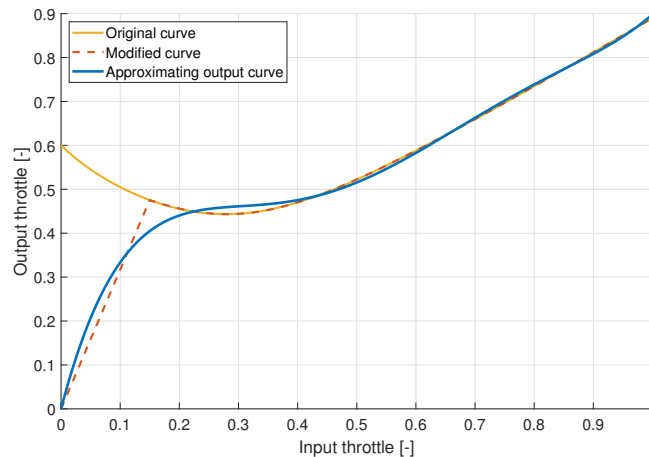


Fig. 7.14: Motor #6 control law for *SE-OEMI-M2* mode

At process completion, conditions enforced into the *M3U* software for the *SE-OEMI-M1* mode

(and for EM #6 in symmetric way) are:

$$\begin{cases} \delta_{t_1} = 0 \cdot \delta_{t_{tot}} \\ \delta_{t_2} = 1 \cdot \delta_{t_{tot}} \\ \delta_{t_3} = 1 \cdot \delta_{t_{tot}} \\ \delta_{t_4} = 1 \cdot \delta_{t_{tot}} \\ \delta_{t_5} = 1 \cdot \delta_{t_{tot}} \\ \delta_{t_6} = 0 \cdot \delta_{t_{tot}} \end{cases} . \quad (7.4)$$

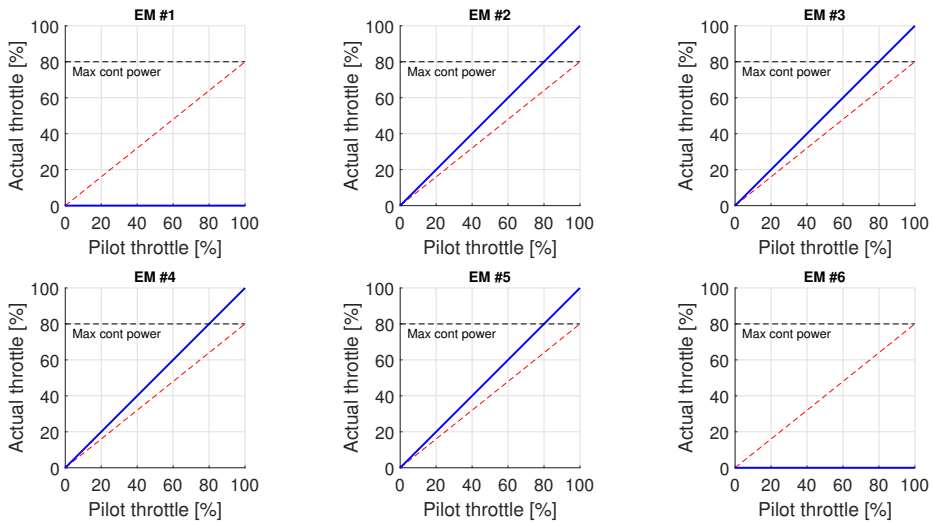
The conditions imposed in *SE-OEMI-M2* mode (and with indexes reversed in case of M5) are:

$$\begin{cases} \delta_{t_1} = 1 \cdot \delta_{t_{tot}} \\ \delta_{t_2} = 0 \cdot \delta_{t_{tot}} \\ \delta_{t_3} = 1 \cdot \delta_{t_{tot}} \\ \delta_{t_4} = 1 \cdot \delta_{t_{tot}} \\ \delta_{t_5} = 1 \cdot \delta_{t_{tot}} \\ \delta_{t_6} = \begin{bmatrix} 10.0268 & -31.9470 & 38.4642 & -21.2242 & 5.4392 \end{bmatrix} \begin{bmatrix} \delta_{t_{tot}}^5 \\ \delta_{t_{tot}}^4 \\ \delta_{t_{tot}}^3 \\ \delta_{t_{tot}}^2 \\ \delta_{t_{tot}} \end{bmatrix} \end{cases} . \quad (7.5)$$

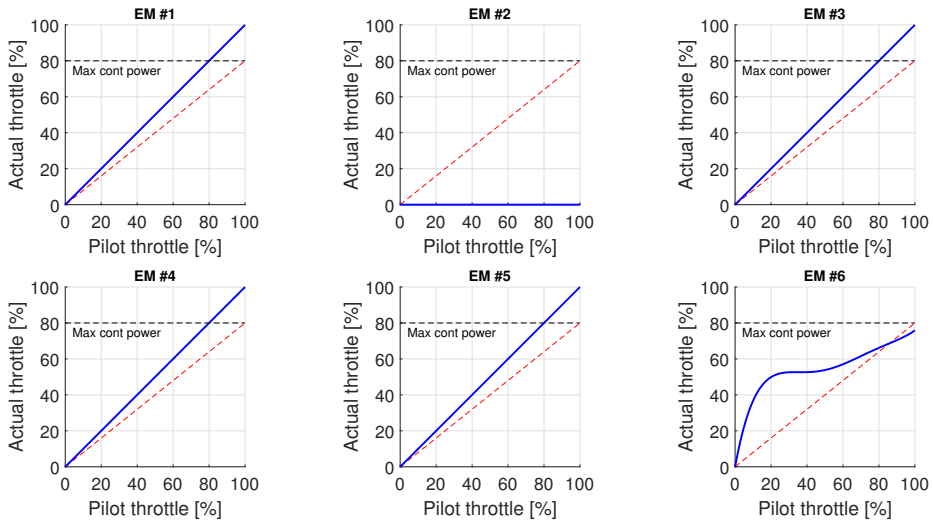
Lastly, *SE-OEMI-M3* mode (and mirror case *SE-OEMI-M4*) prescribes:

$$\begin{cases} \delta_{t_1} = 1 \cdot \delta_{t_{tot}} \\ \delta_{t_2} = 1 \cdot \delta_{t_{tot}} \\ \delta_{t_3} = 0 \cdot \delta_{t_{tot}} \\ \delta_{t_4} = 1 \cdot \delta_{t_{tot}} \\ \delta_{t_5} = 1 \cdot \delta_{t_{tot}} \\ \delta_{t_6} = \begin{bmatrix} 12.5783 & -38.2395 & 43.2658 & -21.8284 & 5.1224 \end{bmatrix} \begin{bmatrix} \delta_{t_{tot}}^5 \\ \delta_{t_{tot}}^4 \\ \delta_{t_{tot}}^3 \\ \delta_{t_{tot}}^2 \\ \delta_{t_{tot}} \end{bmatrix} \end{cases} . \quad (7.6)$$

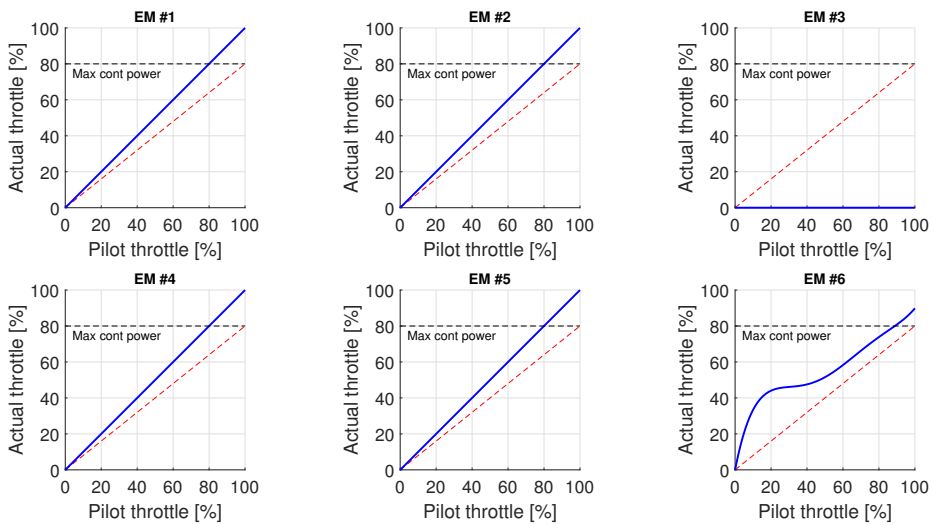
The resulting output motor setpoints for cases *SE-OEMI-M2* and *SE-OEMI-M3* are depicted in Figure 7.15, in which it is clear how maximum continuous power is set at 80% instead of 66.67%. Total outputs are instead reported in Figure 7.16. Total yawing moment is non-zero for the three reported airspeeds, but its magnitude is still restrained and expected to be within the *SE-norm* predicted behavior, even if failure of motor #2 is the most challenging scenario. In fact, these estimations suggest that total generated yawing moment is lower when most inboard motor fails, if compared to *SE-OEMI-M2* case. Future developments will manage to better tune the coefficients to improve the behavior at low power settings, so that the sign of yawing moment does not change throughout the envelope.



(a) SE-OEMI-M1

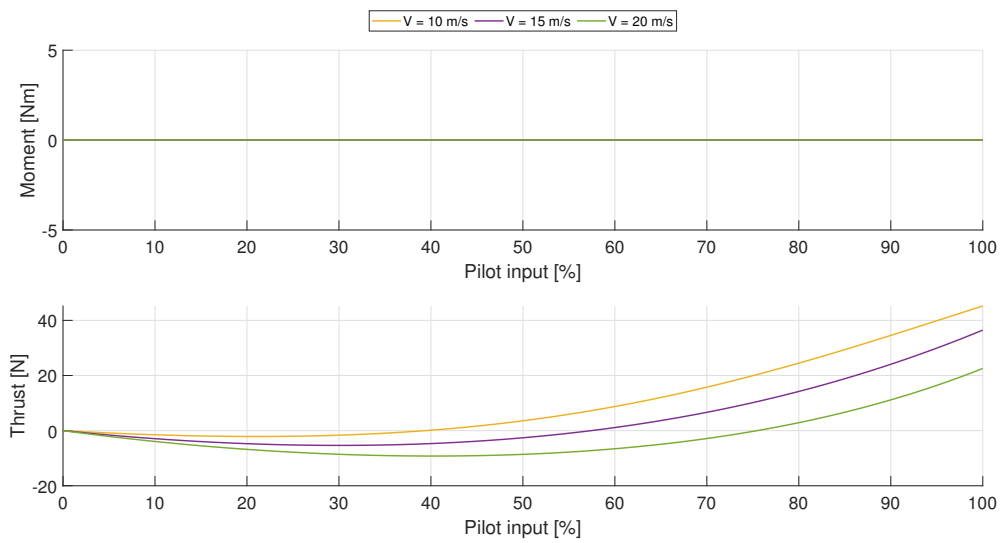


(b) SE-OEMI-M2

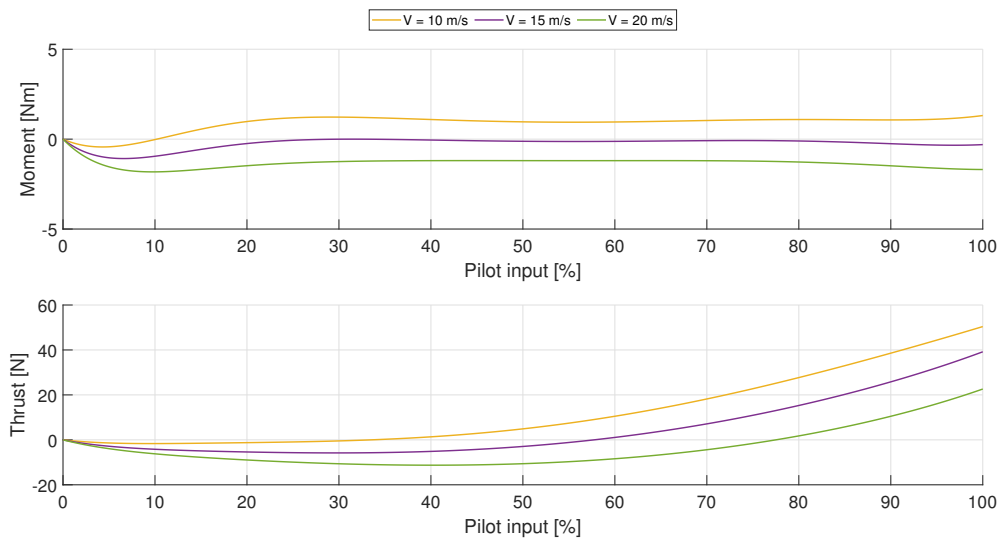


(c) SE-OEMI-M3

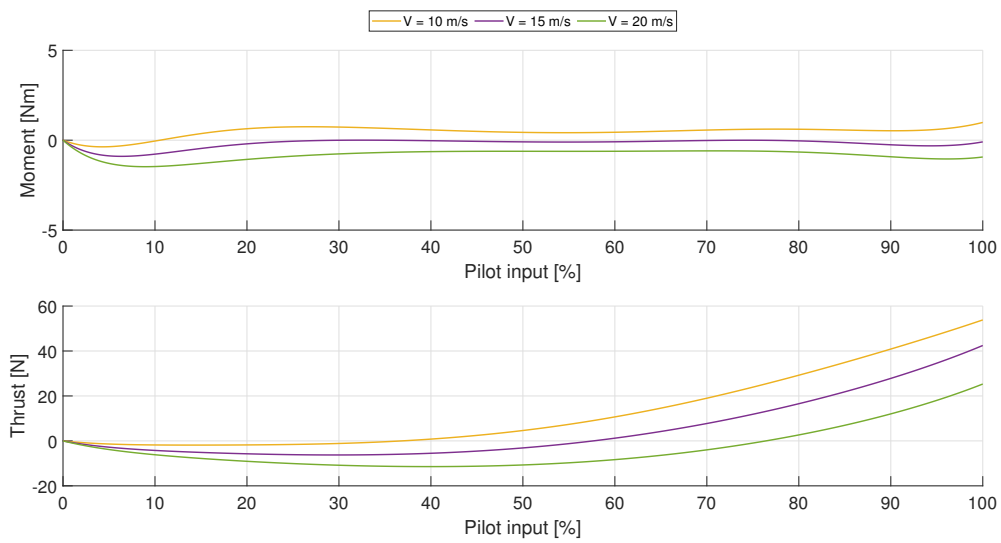
Fig. 7.15: Motors setpoint curves for OEMI modes



(a) *SE-OEMI-M1*



(b) *SE-OEMI-M2*



(c) *SE-OEMI-M3*

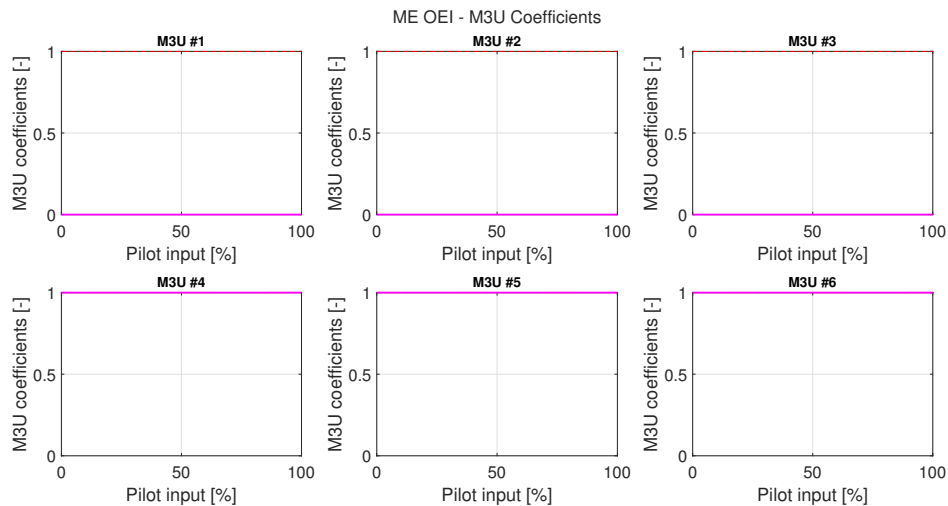
Fig. 7.16: Pilot input vs. overall output for OEMI modes

7.3.6 Multi-Engine One Engine Inoperative

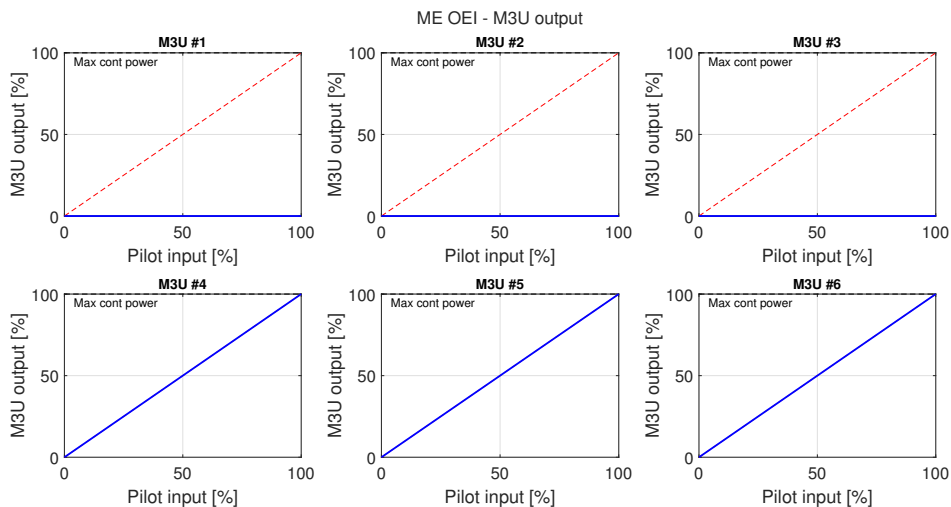
ME-OEI allows to fly a simulated One Engine Inoperative condition of a real twin-engine aircraft. This maneuver is often simulated in real pilot training by putting one engine to idle and feathering its propeller. It is a really important procedure, as the pilot has to learn how to manage a hard emergency situation. Besides the thrust asymmetry and its consequences, training pilot has to take into account several other factors, such as minimum controllability speed and maximum power applicable: as airspeed reduces, rudder becomes less effective and flight asymmetry intensifies, leading to a loss of control. Conversely, applying too much power to the operating engine generates a too big yawing moment, possibly escalating in a spin.

CS-23 and FAR-23 certifications requires that the pilot can control the aircraft with full rudder input, maximum 5 deg of bank angle, flying in straight line and climbing, besides the definition of a minimum control speed [29]. This requirement inspired OEI simulation.

When the *M3U* jumper is set in *ME-OEI* mode, and the mode switch is ON, control law changes from *ME-norm*, putting to idle all the three motors on one side. Given that the airframe is symmetric and EMs are counter-rotating, there is no "critical side" exhibiting worse controllability, but port and starboard case are anyway implemented.



(a) *M3U* internal coefficients



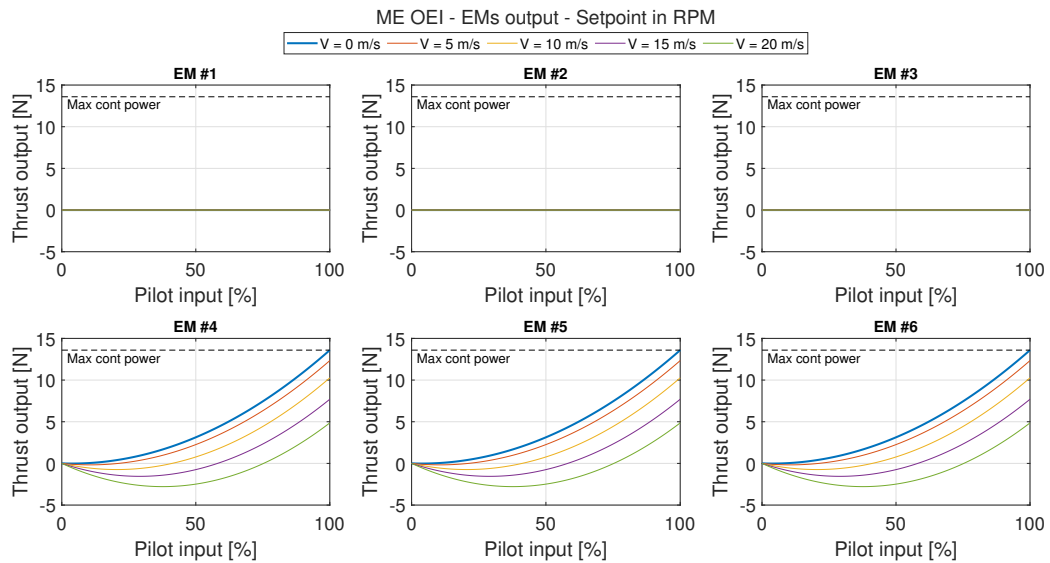
(b) *M3U* input-output relationship

Fig. 7.17: *M3U* control law for the multi-engine OEI working mode

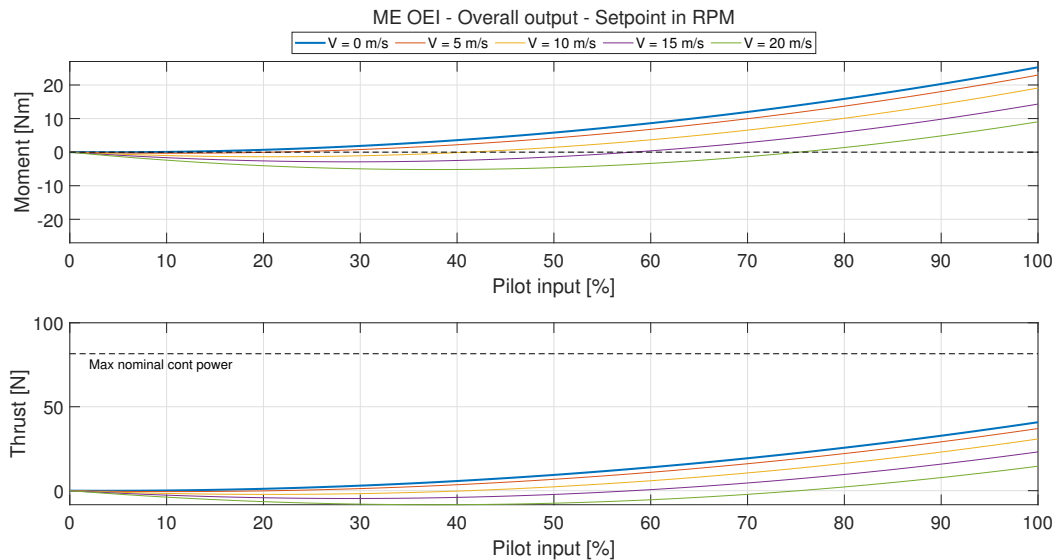
$M3U$ coefficients on one side remain the same, while on the other they are set to zero at all throttle percentages. Equations exploited in $M3U$ software are (starboard case):

$$\begin{cases} \delta_{t_{1,2,3}} &= 1 \cdot \delta_{t_{tot}} \\ \delta_{t_{4,5,6}} &= 0 \cdot \delta_{t_{tot}} \end{cases} \quad (7.7)$$

The values of these coefficients are graphically reported in Figure 7.17, along with the relation between $M3U$ input and output. Together with the maximum continuous power lines, the red dashed lines represent the nominal working condition. The simulation of the output of every EMs and the total output are depicted in Figure 7.18 with the RPM control mode.



(a) Pilot input vs. EMs output



(b) Pilot input vs. overall output

Fig. 7.18: Output simulation for the multi-engine OEI working mode (RPM control)

Modification

What has been previously described refers to the originally-thought control law for the *ME-OEI* mode. The choice of shutting-down three motors on the same side is intended to maximize similarity with a real twin-engine in OEI condition, with no thrust on one side. Anyway, the *TBM* is not designed to be a real, certified, multi-engine aircraft, thus controllability enhanced by control surfaces is not enough to withstand this demanding condition, as later illustrated in Section 9.7. Moreover, three motors inoperative on the same side enormously exaggerate the yawing moment produced by thrust asymmetry. Also certification for bigger aircraft categories (FAR-25 and CS-25) only requires aircraft controllability when the most critical engine fails, not for all engines on one side. The disparity of induced yawing moment with respect to the case of a General Aviation multi-engine aircraft, is confirmed by Figure 7.19.

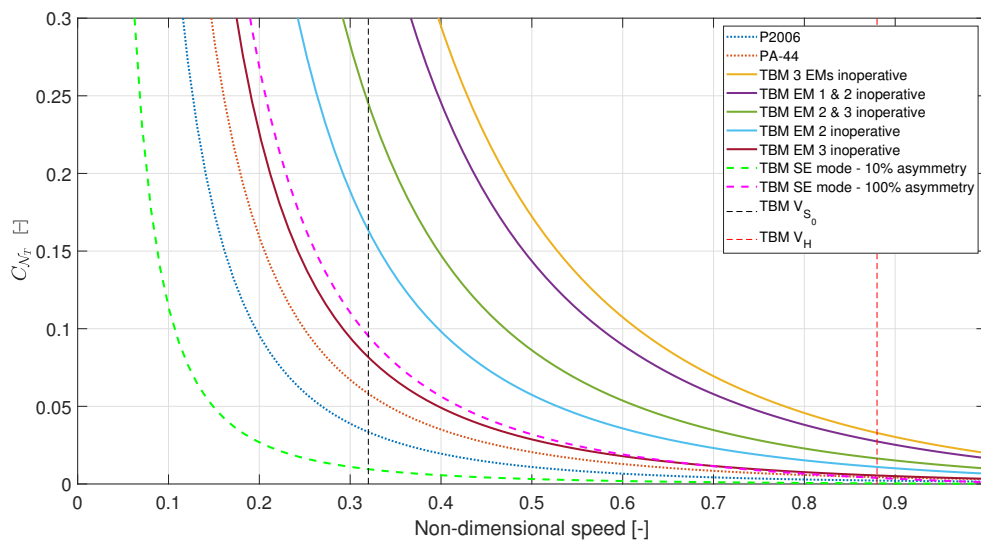


Fig. 7.19: Yawing moment coefficient comparison between the TBM and two GA ME airplanes

To compare different aircraft classes, non-dimensional yawing moment coefficient generated by the thrust, namely C_{N_T} , is exploited. It enables to compare airplanes with different span, mass and general dimensions. The coefficient is plotted against a non-dimensional speed (dividing the speed for the maximum speed achievable by the considered aircraft) to further improve comparability. Determination of C_{N_T} also includes drag generated by the dead motors in the *SwitchMaster* (also this from wind tunnel testing, Section 8.1.2). The considered General Aviation multi-engine airplanes are Tecnam *P2006T* and Piper *PA-44 Seminole*. The two aircraft are equipped with Rotax *912 S3* rated at 100 hp and Lycoming *IO-360* rated at 200 hp. Thrust generated at different speeds by the two engines can be retrieved in [50]. These are well-diffused certified multi-engine aircraft, hence the yawing moment generated in OEI condition is an indicative reference for the category.

The right *ME-OEI* simulation should therefore generate a yawing moment close to the one of the presented GA aircraft: this seems to be the situation for which motor #3 is inoperative, which anyway generates less yawing moment than in *SE-norm* condition when the asymmetry

knob is set to 100%. This corresponds to imposing the following conditions:

$$\begin{cases} \delta_{t_{1,2,4,5,6}} &= 1 \cdot \delta_{t_{tot}} \\ \delta_{t_3} &= 0 \cdot \delta_{t_{tot}} \end{cases} . \quad (7.8)$$

The presented situation can also be visualized in the simulation reported in Figure 7.20.

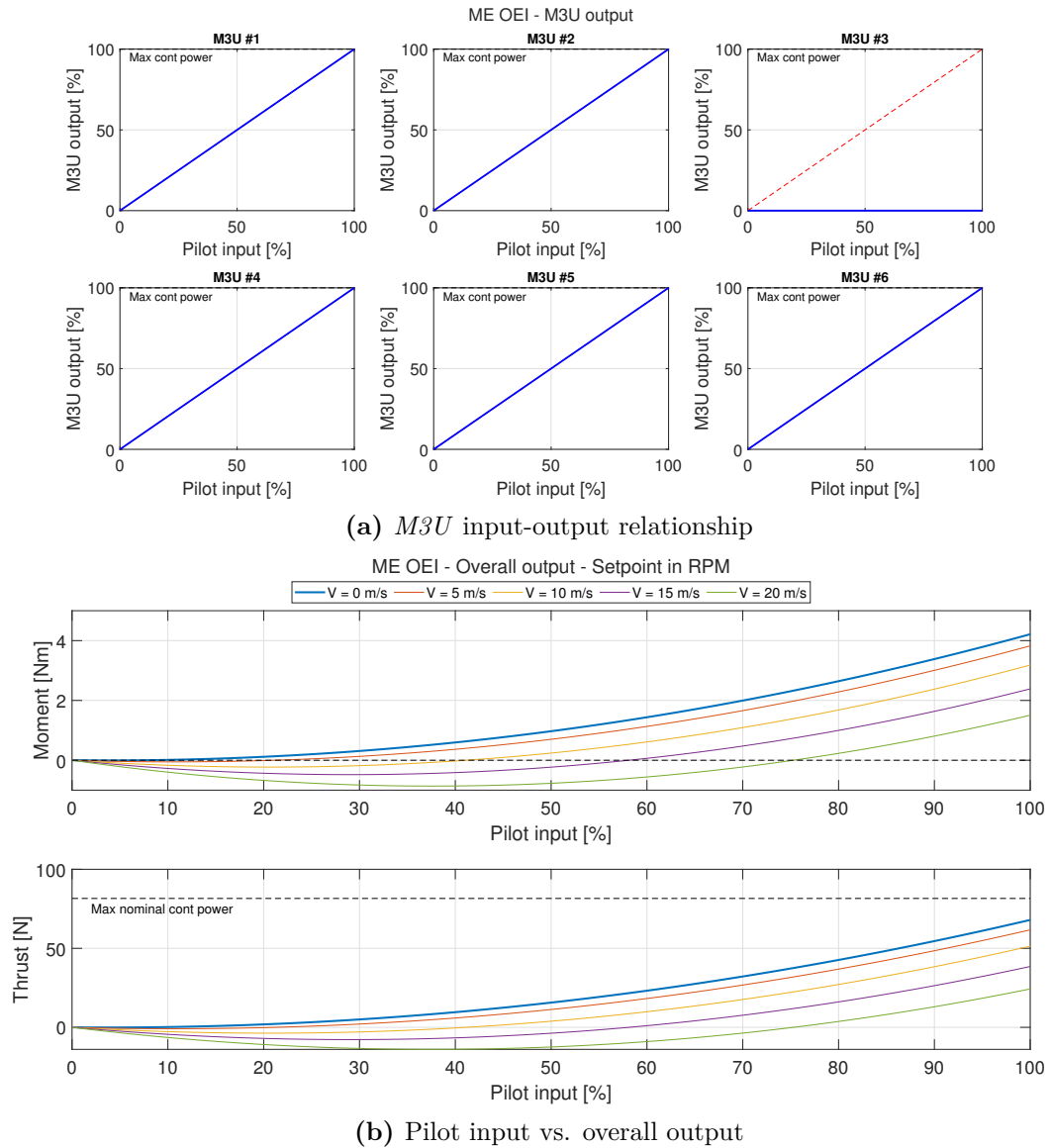


Fig. 7.20: Output simulation for the reviewed multi-engine OEI mode (motor #3 failure)

The pilot should be able to control the aircraft with manual input, even if the *SwitchMaster* is not designed as a ME GA aircraft, and therefore could not meet certification standards. Additionally, also motor #2 inoperative condition (which is tougher) is provided and tested.

At a later stage, two new and more unbalancing working modes have been integrated in the last version of the *M3U* firmware. The first one consists of imposing motor #1 inoperative, which is philosophically the closest to "most critical engine" requirement in certification. The second aims to further increase thrust asymmetry, shutting-down both motor #1 and #3 at the same time.

7.3.7 Propulsive yawing control mode

Given that the *M3U* board allows great versatility and customization, propulsive yawing control is implemented even if not envisaged in the patent application. The final purpose of the propulsive yawing control is to perform a gentle turn without employing the control surfaces. This should allow to reduce drag, and could lead to the complete removal of the rudder surface through a novel aircraft design embedding the technology. In order to remove the vertical tail surface, not only yaw control must be guaranteed, but also static and dynamic stability need to be assured.

In the following implementation, yawing control has been implemented in a highly simplified and basic version, with the only purpose of demonstrating its feasibility. Lorenzo Alberti further investigates it in his master's thesis [3]. Currently described simple realization started from the *SE-norm* implementation, slightly modifying it in order to let the asymmetry knob to apply thrust asymmetry in both directions. When the slider on the radio transmitter is centered, all the motors work in the same fashion. When it is moved to one side or to the other, motors generate asymmetry to the left or right side. In this simple realization, the pilot should turn only acting on the asymmetry knob, without intervention on rudder and ailerons.

Control laws enforced in *M3U* software to realize the yawing control mode are:

$$\begin{cases} \Delta \mathcal{P}_{up}^{[\%]} = (\delta_{knob} - 0.5) \cdot (\mathcal{P}_{max}^{[\%]} - \mathcal{P}_{max\ cont}^{[\%]}) \\ \Delta \mathcal{P}_{down}^{[\%]} = -(\delta_{knob} - 0.5) \cdot (\mathcal{P}_{max}^{[\%]} - \mathcal{P}_{max\ cont}^{[\%]}) \end{cases} \quad (7.9)$$

$$\begin{cases} \delta_{t_1} &= (\mathcal{P}_{max\ cont}^{[\%]} + (2 \cdot \Delta \mathcal{P}_{up}^{[\%]} \cdot \delta_{t_{tot}})) \cdot \delta_{t_{tot}} \\ \delta_{t_{2,3,4,5}} &= \mathcal{P}_{max\ cont}^{[\%]} \cdot \delta_{t_{tot}} \\ \delta_{t_6} &= (\mathcal{P}_{max\ cont}^{[\%]} + (2 \cdot \Delta \mathcal{P}_{down}^{[\%]} \cdot \delta_{t_{tot}})) \cdot \delta_{t_{tot}} \end{cases} \quad (7.10)$$

$\Delta \mathcal{P}_{up}^{[\%]}$ and $\Delta \mathcal{P}_{down}^{[\%]}$ enforce output setpoint variation on motors #1 and #6, thus induce the forsaken thrust asymmetry.

In Figure 7.21 are reported the motor setpoints related to thrust input when the asymmetry knob is at its limit positions on one side or on the other. In Figure 7.22 the very same is represented in terms of total thrust and induced yawing moment output.

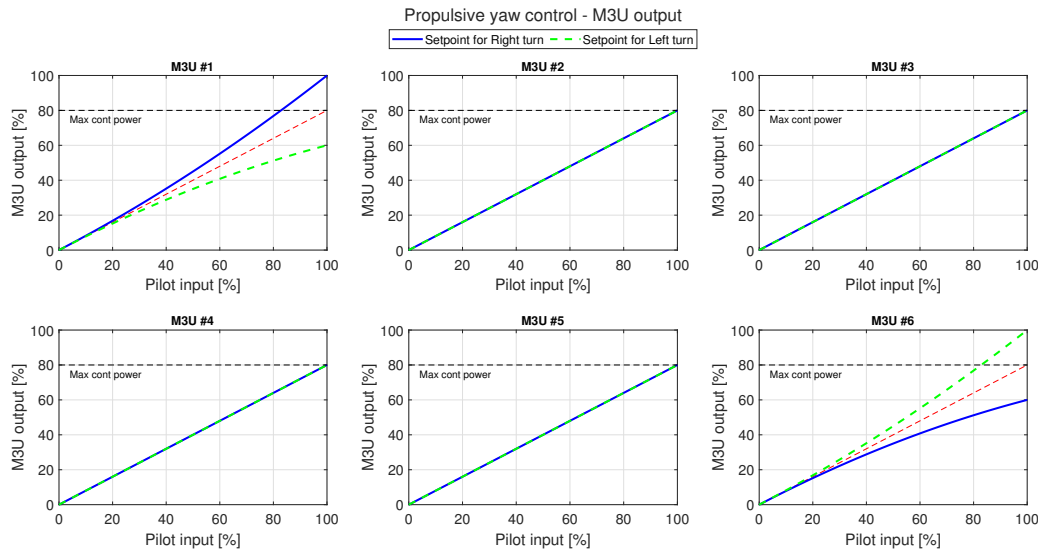


Fig. 7.21: *M3U* input-output relationship for propulsive yawing control

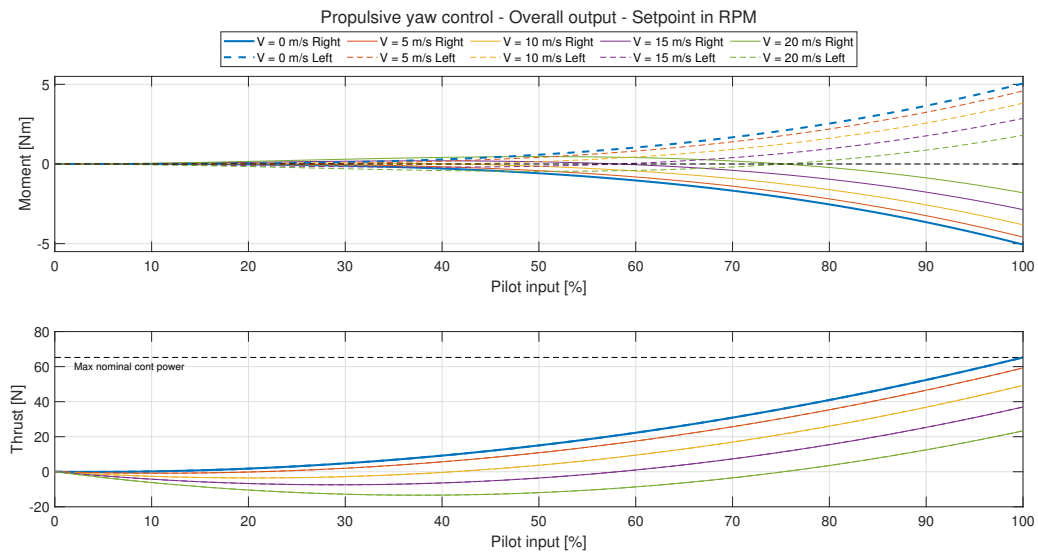


Fig. 7.22: Pilot input vs. overall output for propulsive yawing control

Turn coordination with thrust asymmetry

A radio transmitter mixer allows to couple the asymmetry knob channel to the ailerons channel: this enforces an automatic turn coordinator when the mix is ON. When the pilot acts on the ailerons, the setpoints of the motors change following the turning direction, avoiding the need of rudder intervention to counteract adverse yawing moment. The right percentage of mixing intervention is to be found through trial-and-error in the flight test campaign.

Chapter 8

Preliminary testing

Preliminary testing before the flight campaign is mandatory and essential, from different points of view. First of all, safety: even if dealing with a scale airplane, safety must be guaranteed at all times, to avoid any damage on the aircraft or people and items in the surroundings of the flying field. Secondly, test conduction allows to understand how systems and the airframe work and behave.

The preliminary tests carried out on the whole system are described in the following sections. An incremental approach has been followed, from bench test of the control system to the wind tunnel testing of a perfect replica of the wing mounted on the *SwitchMaster*.

8.1 Bench and ground testing

In parallel with aircraft construction, ground and bench tests have been carried out, starting from trials on the rig and finishing with a demonstrative taxi test. These have multiple purposes, and the stages completed were:

1. test bench of the propulsive unit: ESCs and motors proper working, parameter setting via USB connection, power consumption, produced heat and possible issues with different state of charge of the batteries;
2. wind tunnel propulsive unit test: thrust, consumption, behavior at different wind speeds and incidence and estimation of endurance;
3. wind tunnel test of the wing with and without propulsive units;
4. hardware and electromagnetic compatibility ground tests;
5. failure and fail-safe tests;
6. system response on the ground in different working modes;
7. taxi tests: on-ground controllability and radio range check.

8.1.1 Propulsive unit bench testing

The first conducted test is the propulsive unit bench test. One electric motor coupled with its propeller and ESC is fitted on a wooden support, locked to the ground in a safe environment. The ESC is connected to a battery pack and to a computer via USB link. Zubax provides a software called *Kucher* to program and control the ESC in real time, reading output parameters. Preliminary assignment of ESC parameters is made to correctly match the

characteristics of the motor (e.g. the number of poles and maximum allowable current). Then, a self-test automatically detects parameters such as internal resistance and winding flux, to optimize the system.

After this procedure has been completed, the motor can be actuated safely. Trials were made starting from an idling regime and slowly increasing the RPM setpoint up to the maximum value, at which *Kucher* notifies the saturation of electrical RPM input. After the first run, the trial has been replicated many times, also in the opposite sense of rotation, to ensure every item is working correctly and without overheating. The maximum rotational speed achieved is 10 850 RPM, with a peak current of 17 A when the battery pack is fully charged.

Furthermore, some long-run full power tests have been executed. The motor has been kept at full power for 4 min, with the ESC once equipped with its heat sink and once without it. At trial conclusion, the maximum ESC temperature was 47 °C, while EM and battery temperature were in the normal working range. After 4 min of full power run, the battery pack absorbed 1040 mA h of energy in recharge.

Another full-power test tried to replicate the condition of the ESC installed in the wing. Removing the heat sink, the ESC was covered with a plastic skunk, then closed in a small cardboard box and put out of the flow of the propeller. The test consisted of applying full power for 6.5 min, while monitoring temperature evolution. Maximum allowable working temperature reported on the ESC data-sheet is 85 °C. At the end of the trial, maximum value was 74 °C. This test was crucial to decide to embark the ESCs without its heat sink. In Figure 8.1 is reported a screenshot from *Kucher* software at the trial completion.

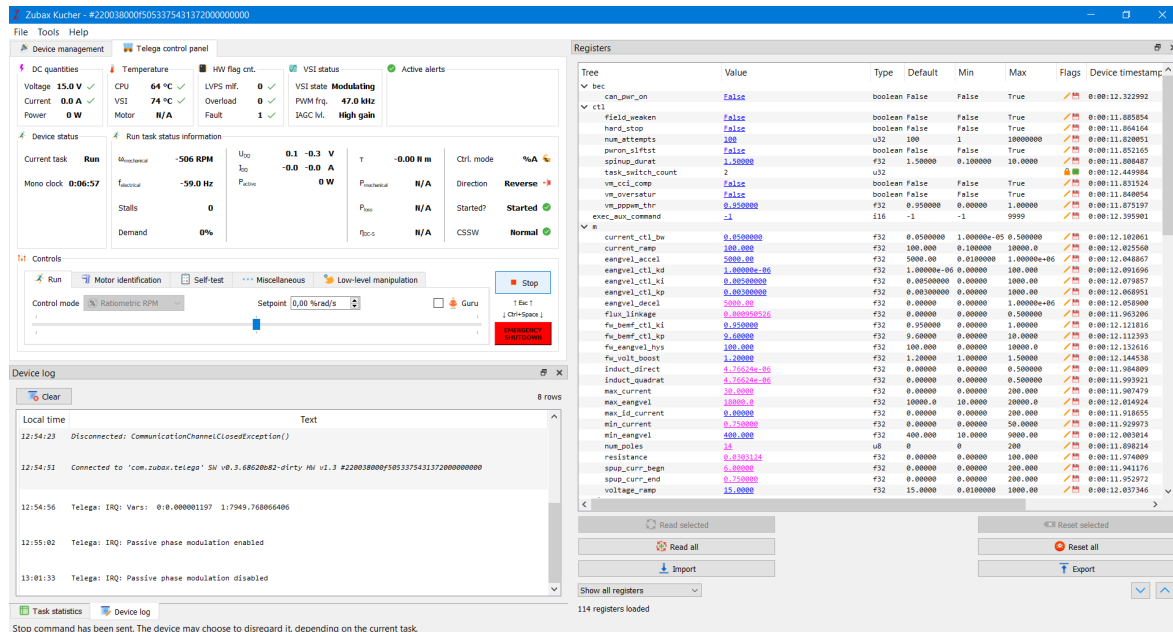


Fig. 8.1: *Kucher* visualization of most though ESC temperature test, at trial end

8.1.2 Propulsive unit wind tunnel testing

A propulsive unit (EM + ESC + propeller) wind tunnel test campaign was carried out. This had the purpose of characterizing the propulsive system at different wind speed and to investigate how the SSA (or AOA) influences the performances.

The wind tunnel test section has a dimension of 1 x 1.5 m, enough for the test, as propeller disk diameter is 25 cm. The propulsive unit is made of Graupner *E-prop* 10x5 in propeller, the electric motor, the ESC and two battery packs in parallel, in order to assure good endurance. The ESC is controlled via USB linkage to an external computer. The use of battery packs, instead of a power supply unit, have the drawback of the dependence from the state of charge of the batteries (SoC), an example of which is reported in Figure 8.2.

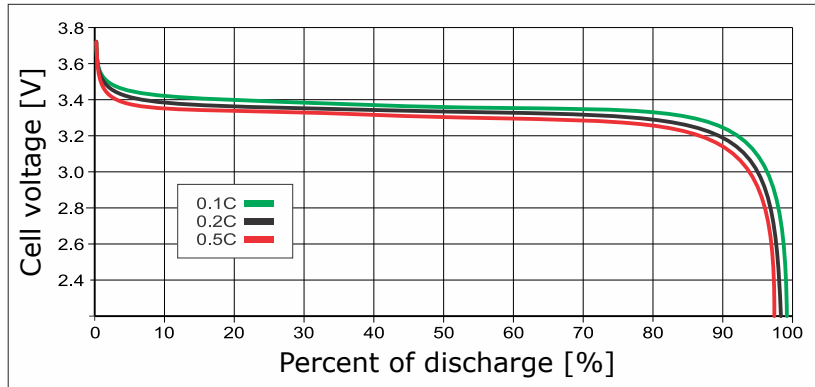


Fig. 8.2: Typical lithium battery discharge characteristic [51]

Available power of Lithium battery packs is constant immediately after the initial discharge. Most of the tests have been conducted in this flat part of the curve. Actually, at trial completion, battery packs consumption never exceeded half of their capacity, so no lower states of charge were experienced during the test. The test setup is depicted in Figure 8.3.

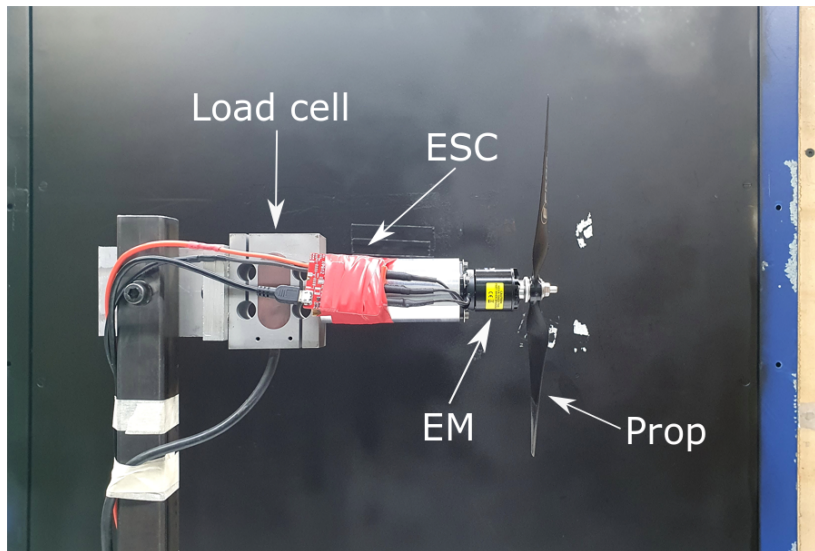
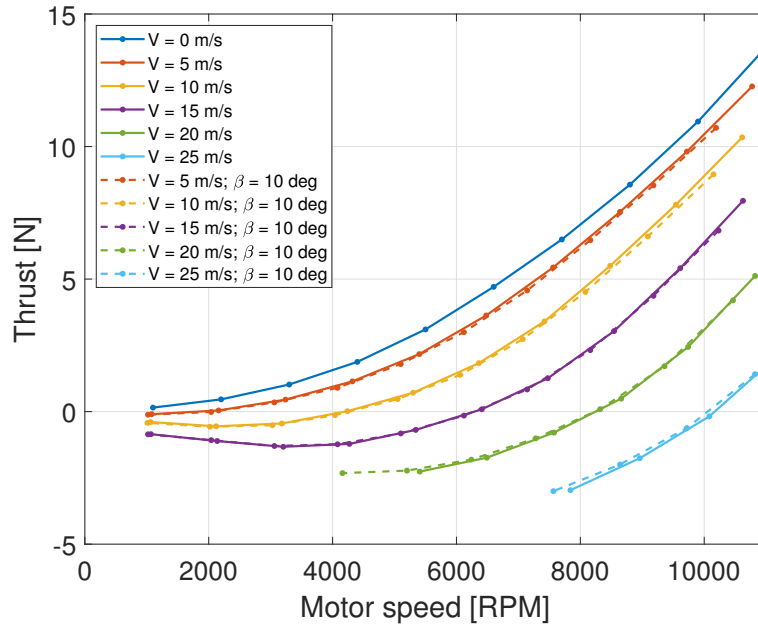


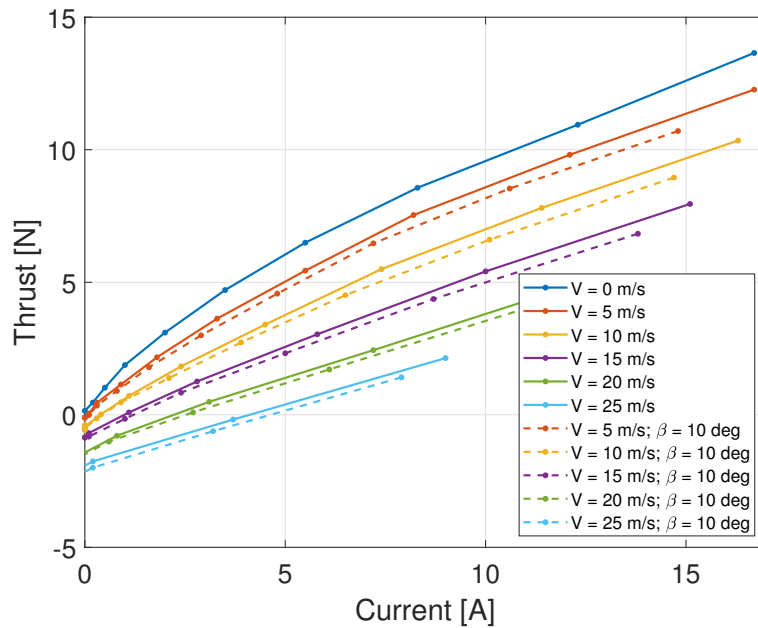
Fig. 8.3: Wind tunnel testing propulsive system setup

The first test output is the static thrust: this is slightly lower than what reported on the producer datasheet, as it resulted to be 13.65 N. Among the possible reasons, most probable are the propeller installed, being different from the one considered by the manufacturer, the self-induced airflow in the closed circuit wind tunnel (approximately 2 m/s) and the different working conditions. However, total static thrust with 6 motors should be 81.90 N, therefore no lack of power is expected on the real airframe. Moreover, on a positive note is the drawn electric current, which never went above 17 A.

The zero-thrust speed resulted to be 29 m/s, therefore motor trials have been performed up to 25 m/s. In order to understand the relation between thrust and SSA, also tests with the motor assembly tilted with respect to the relative wind direction have been carried out. In Figure 8.4 are reported the main outputs of wind tunnel testing. The two graphs represent the same test, but with a different control method. The above one exploits a setpoint on motor speed in terms of radiometric RPM. For the second one, the setpoint is made on electric current (therefore on torque).



(a) RPM control method



(b) Electric current control method

Fig. 8.4: Main output of propulsive system wind tunnel testing

The analysis of wind tunnel data led to different considerations:

- **SSA influence:** the influence of SSA up to 10 deg is negligible with both control methods. This seems to be non-consistent with the current-setpoint graph, in which the dotted lines are below the solid ones. This is only due to the different state of charge of the battery packs at the moment of the trial (the same is noticeable also with the RPM setpoint, in which the maximum thrust value does not reach the same as 0 deg SSA). For a SSA of 20 deg the behavior changes, leading to the thrust reduction depicted in Figure 8.5. According to what was experienced during *PS-28* flight test, such high angle should not be of interest for the demonstrator.

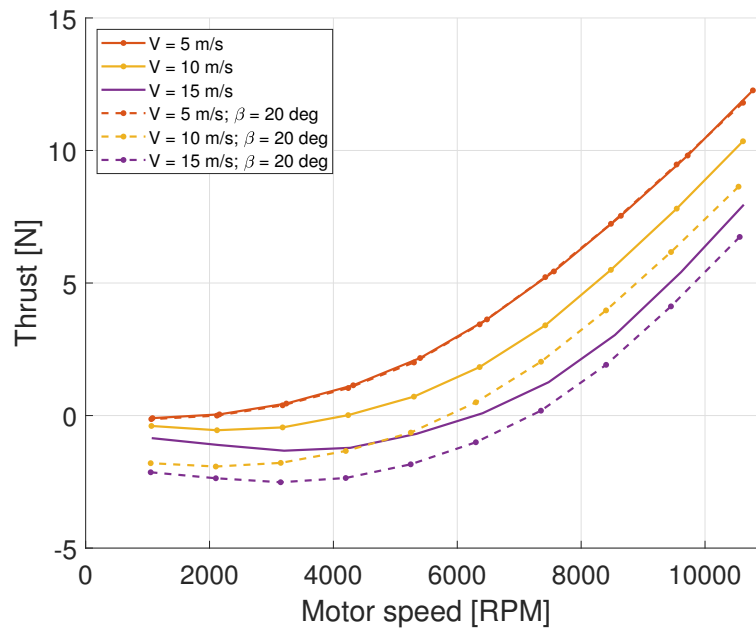


Fig. 8.5: Thrust results with a SSA of 20 deg

- **Input-output relation:** the relation from the pilot setpoint to the approximated thrust output is quadratic if controlled in RPM, while it is of the fourth order if in electric current control method (but nearly-linear). With RPM control method, each pilot setpoint biunivocally corresponds to a singular rotational speed. On the contrary, with current setpoint, command saturation makes it impossible to reach maximum current value at some flight speeds. For instance, with a flight speed of 20 m/s, maximum thrust is achieved at 70% of pilot setpoint. This could represent an issue for the flight conduction.
- **Regenerative braking:** the ESC allows the motor to be employed as a generator, absorbing energy from wind and converting it into electrical energy. With current control method this is impossible, as the allowable motor range is $[0 - 100\%]$. With RPM control method, high wind speeds and low setpoints lead to electric current flowing back to the batteries. In wind tunnel testing this latter has been experimented up to -1.3 A, with a maximum recharge power of 21 W. No issues arose from the propulsive system in this scenario, and battery packs should be able to cope with a charging current (which corresponds to around -8 A from the total six motors). Nevertheless, this behavior should be further investigated, as other onboards system could be damaged

or malfunctioning due to electro-magnetic interferences, back current or unwanted phenomena.

- **Thrust vs. speed:** thrust variation with wind speed has an almost linear scalability. This is reported in Figure 8.6: the curves could be approximated with a bundle of straight lines.

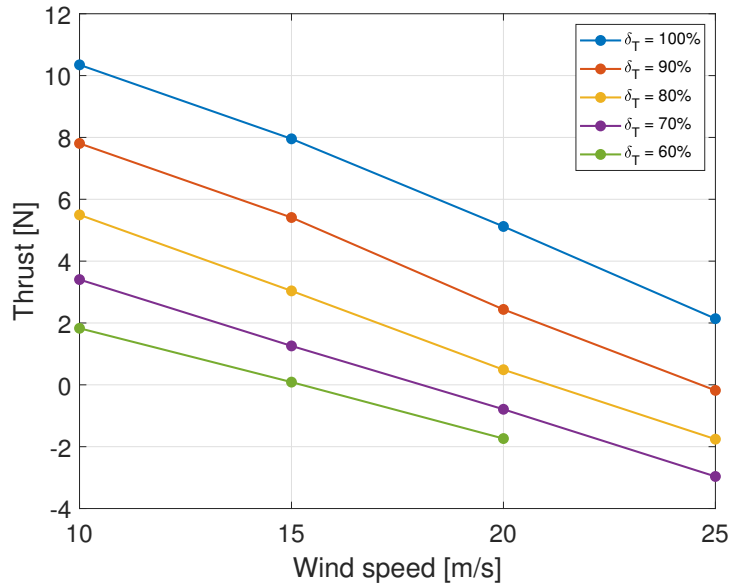


Fig. 8.6: Thrust scaling with wind speed

- **Expected endurance:** total on-board capacity of the batteries is 8000 mA h. Accounting for the 6 motors running at maximum thrust with the airplane held in place, calculated endurance is less than 4 min. However, this latter is an unlikely scenario. Then, considering the consumption measured in the wind tunnel at 15 m/s with a mixed throttle usage, estimated endurance rises to 10 min, also applying a safety margin of 20% to account for wiring dissipation.

8.1.3 Wing wind tunnel testing

Wing wind tunnel testing consists of two activities: testing of the original wing and testing of the wing with propulsive units installed. Test conduction and analysis of results are entrusted to the master's thesis of Andrea Santeramo, and here only major results are reported. *Politecnico di Milano De Ponte* closed circuit wind tunnel has been exploited for the execution of both tests. Test chamber dimensions are 3 m x 1.5 m x 1 m. One important thing to be noticed is that the wind tunnel wing is not just a scale copy of the flying one, but the very same from aerodynamic, structural and propulsive points of view. Therefore, Reynolds and Mach numbers similarity is always guaranteed.

The two different setups are represented in Figure 8.7. From the pictures, the dummy half fuselage placed on the wind tunnel floor can be noticed.

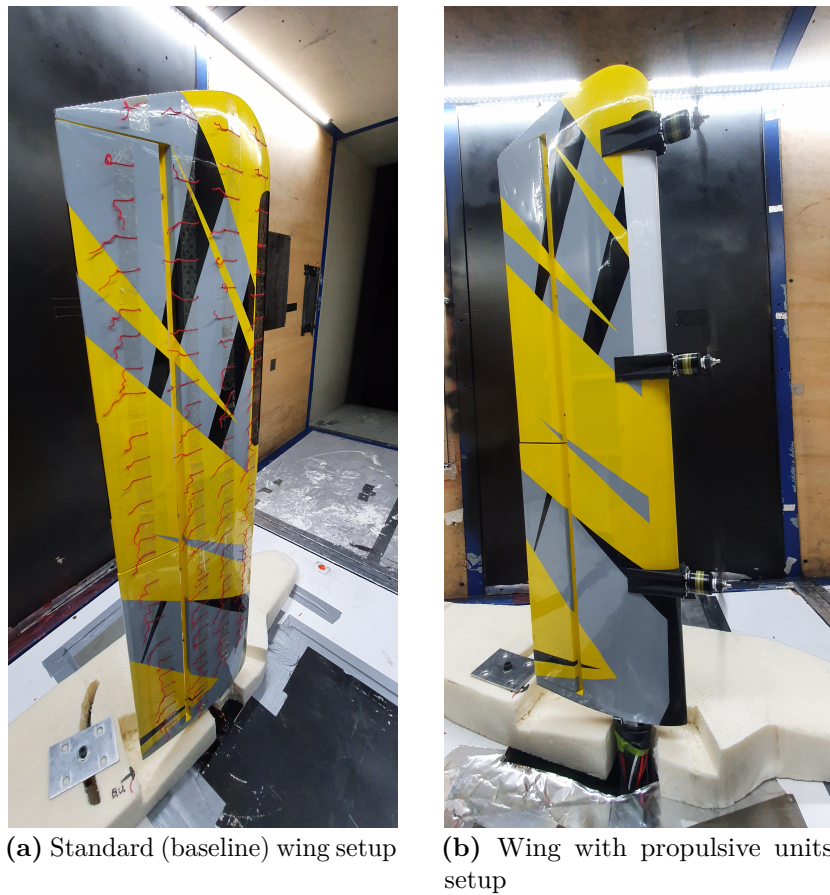


Fig. 8.7: Wind tunnel testing of the aircraft wing

Original wing lift and drag polar curves are reported in figures 8.8 and 8.9. These tests have been replicated at different wind speeds, from 10 m/s to 25 m/s, but the results are overlapped due to negligible Reynolds number differences. Also tests with +10 deg and -10 deg SSA have been carried out, but resulted in negligible variation from the 0 deg SSA baseline configuration, apart from a slight increase in the drag coefficient.

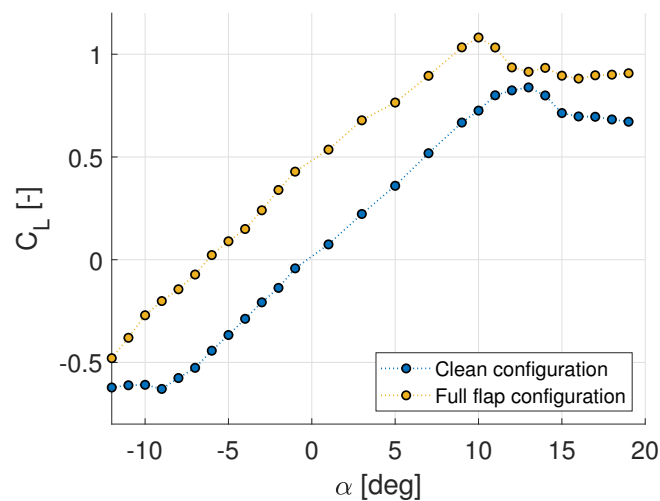


Fig. 8.8: Standard wing ($C_L - \alpha$) curve

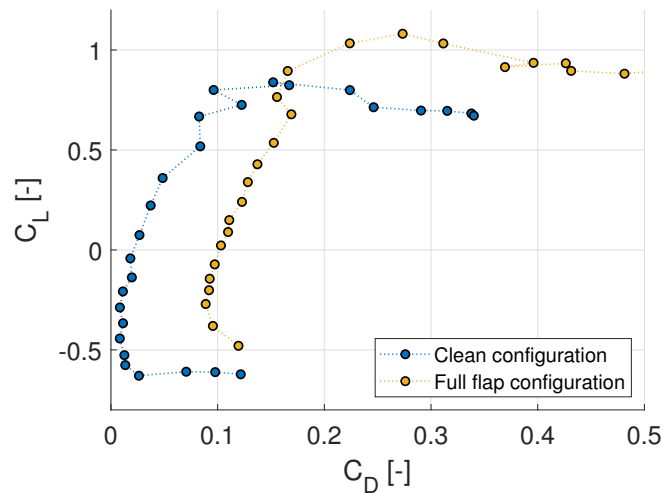


Fig. 8.9: Standard wing drag polar curve

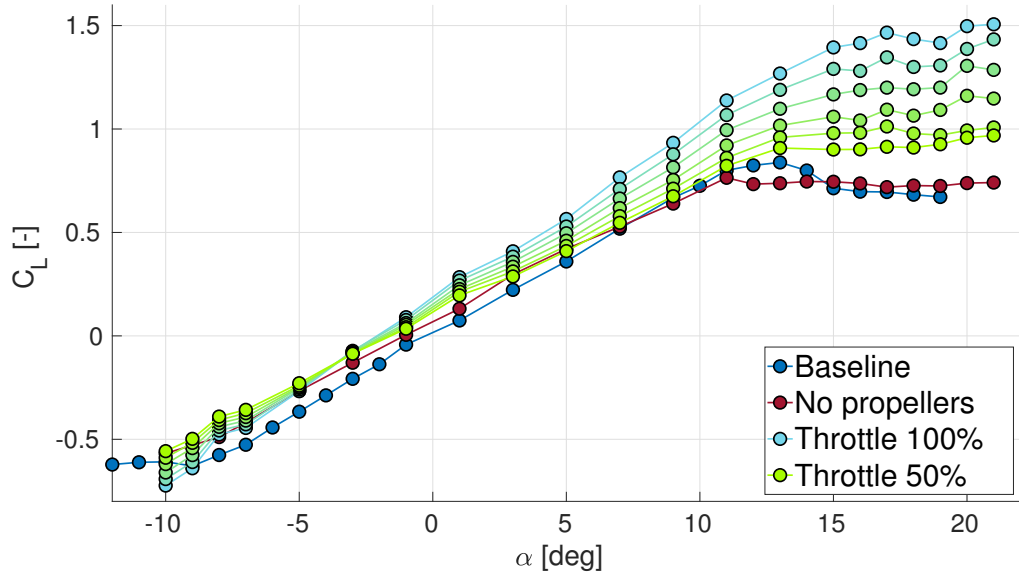
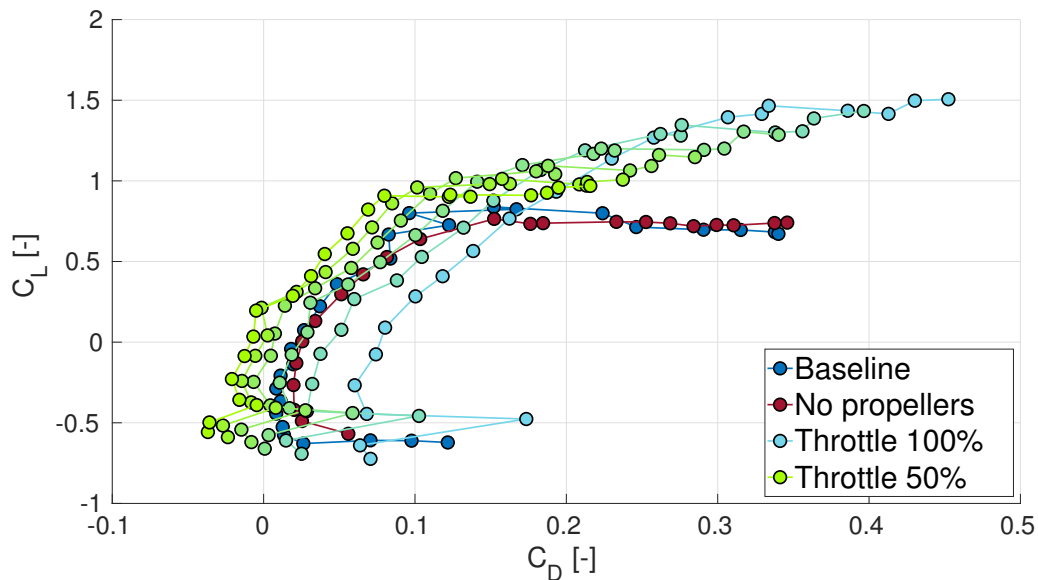
After completion of this first test cluster, the wing has been modified in the very same way as the flying one. The only differences are on ESCs data cables and power supply. Installed data cables include USB for direct computer control (exploiting the *Kucher* software) instead of the CAN network, while power supply is entrusted to a high power AC-DC converter. This latter allowed to speed up (no need of interrupting trials to recharge the battery packs) and increase overall safety of the test campaign. The same level of performance of the flying wing is ensured by imposing a precise RPM setpoint.

Trials surveyed many different combinations of AOA, SSA, setpoints (even non-uniform), flap settings and wind speed. Onset of instability or unknown phenomena was averted, to ensure flight safety of the *SwitchMaster*. In particular, tested working logic of the motors are:

1. EM #1, #2, #3 working evenly at different setpoints;
2. EM #2, #3 working evenly at different setpoints, EM #1 out;
3. EM #1, #3 working evenly at different setpoints, EM #2 out;
4. EM #1, #2, working evenly at different setpoints, EM #3 out;
5. EM #2, #3 working evenly at different setpoints, EM #1 working at higher and lower setpoints;
6. EM #1 working at different setpoints, EM #2, #3 out;
7. EM #2 working at different setpoints, EM #1, #3 out;
8. EM #3 working at different setpoints, EM #1, #2 out;
9. EM #1, #2, #3 working evenly at different setpoints but with outboard-up direction of rotation (with right-hand turning propellers);

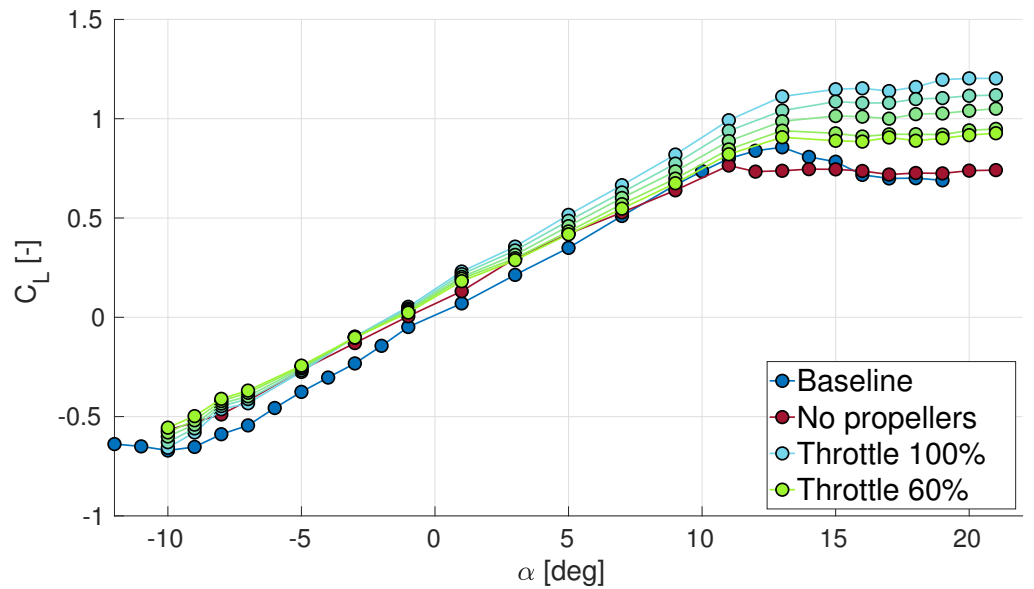
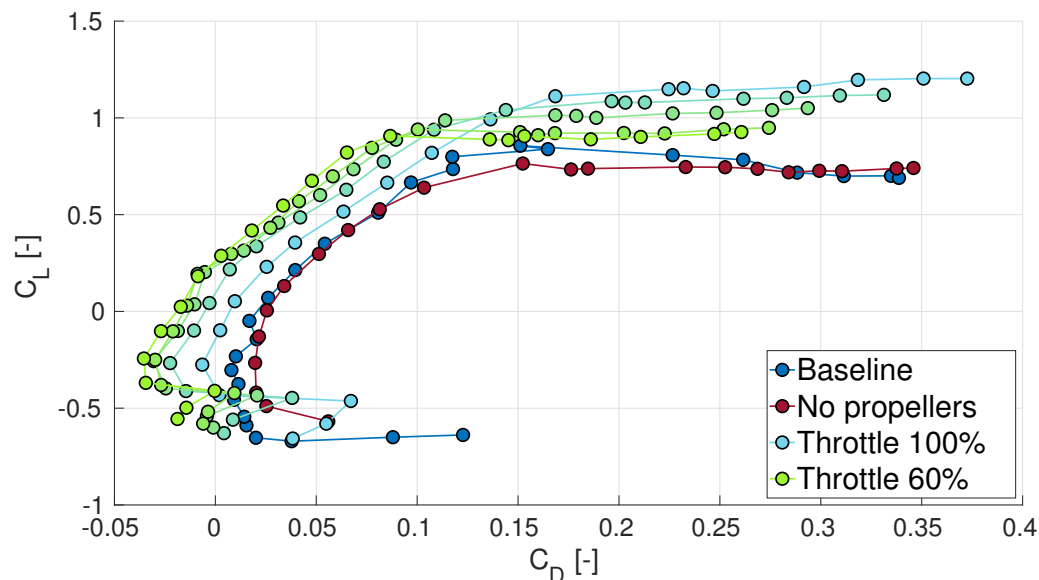
For every illustrated combinations, tests with different wind speed, SSA, AOA, throttle setting and flap deflection have been carried out. First of all, the wing was tested with propulsive units installed, but without propellers, in order to estimate the influence of added components on aerodynamic properties. The first trial enforced the three electric motors running evenly. Given that EMs impose a velocity jump in the airflow, aerodynamic coefficients now strongly

depend on the incoming wind speed. The results of the tests are depicted in figures 8.10 and 8.11 for two different asymptotic wind speeds. The presented results confirm that lift coefficient increases as V_∞ decreases, thanks to the increase in local dynamic pressure induced by rotation of propellers. Drag polar curves exhibits high drag coefficient at low speed. This is the direct consequence of the accelerated and extremely turbulent airflow due to wing blowing, that implies a higher induced drag. As the airspeed increases, the propellers generate a lower thrust, thus the increase in local dynamic pressure is lower, too. Then, the effect of blowing is less effective and induced drag decreases.

(a) Blown wing ($C_L - \alpha$) curve

(b) Blown wing drag polar curve

Fig. 8.10: Blown wing wind tunnel testing results, $V_\infty = 15$ m/s

(a) Blown wing ($C_L - \alpha$) curve

(b) Blown wing drag polar curve

Fig. 8.11: Blown wing wind tunnel testing results, $V_\infty = 20$ m/s

One issue arisen during the campaign is the accuracy of the balance: this is of the same order of magnitude of the force measured in the direction of the airflow, related to drag. Therefore, in all tests there is a systematic absolute error of ± 2 N. As a consequence, considering the relative error, the smaller is the measured forces, the greater is the effect of the systematic error on the measurement itself. An example of the phenomena is at low throttle setpoints, where the force measured by the balance and the thrust generated by the motors differ by less than 1.5 N. To take account of this, Figure 8.12 reports the polar curves with uncertainty bars. It is possible to notice how, considering the uncertainty, drag coefficient values are physically acceptable. Clearly, the measurement instrumentation was not optimal for accurately measuring the drag coefficient.

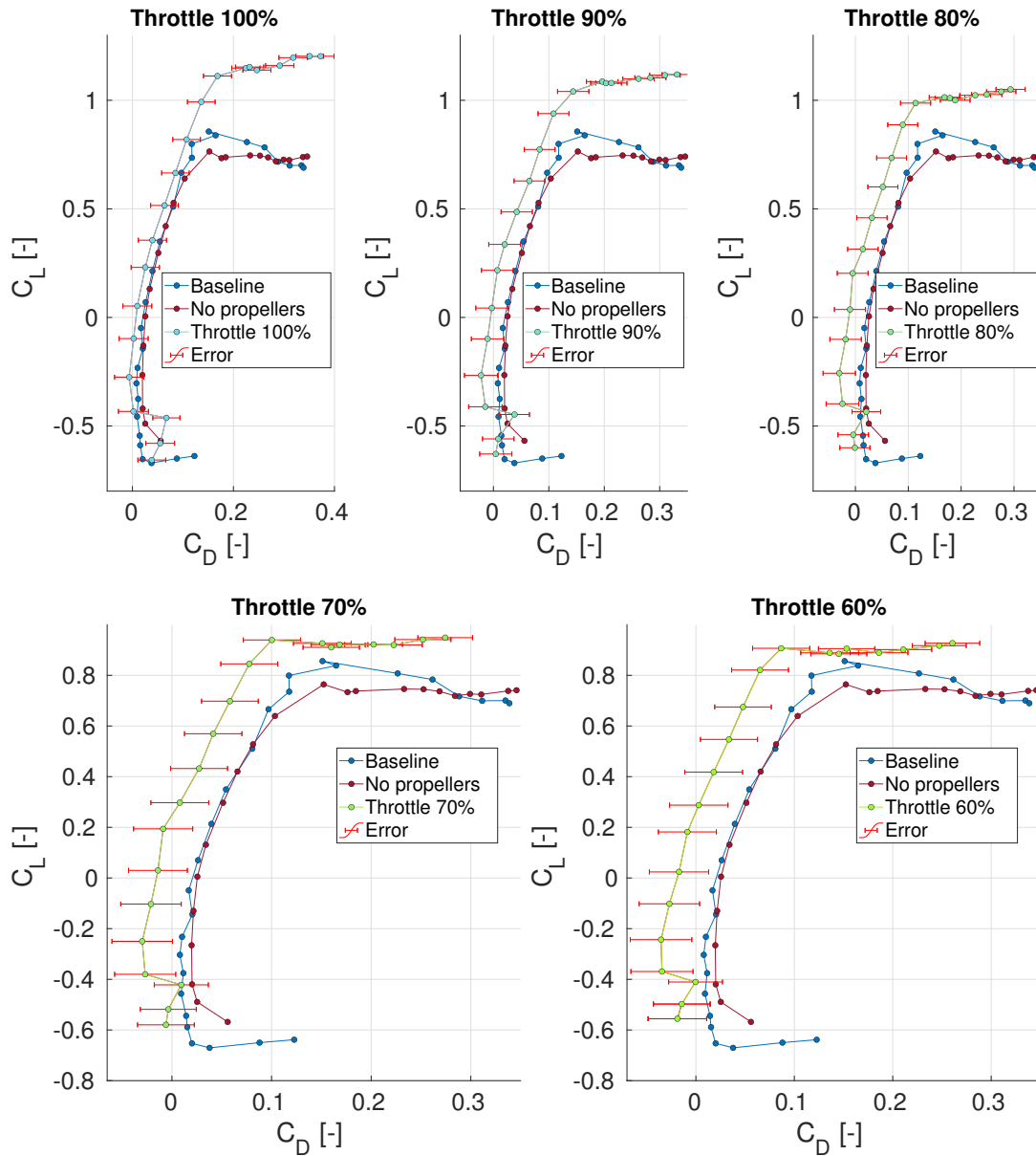
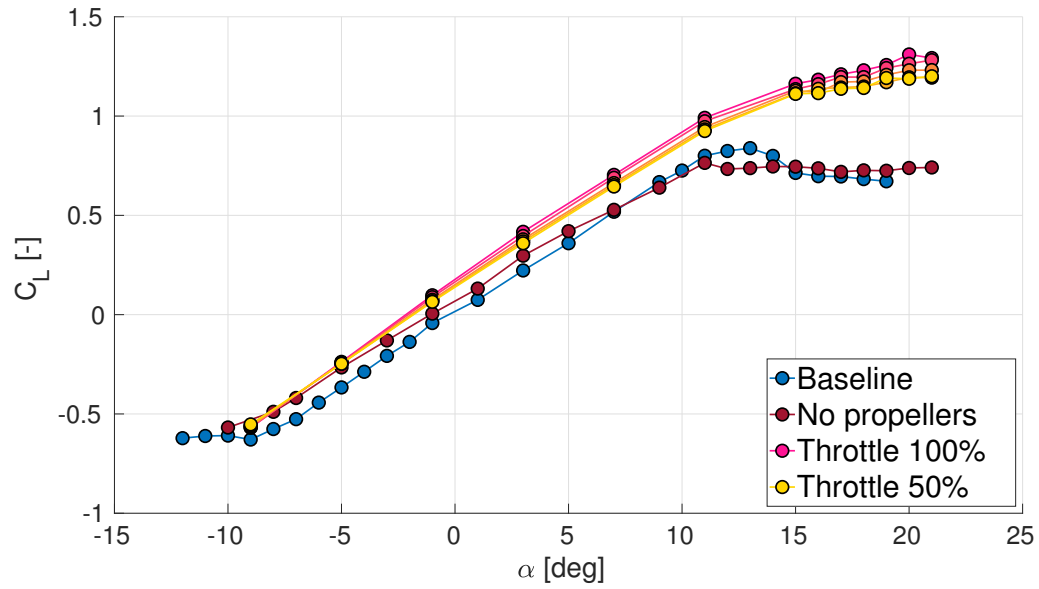
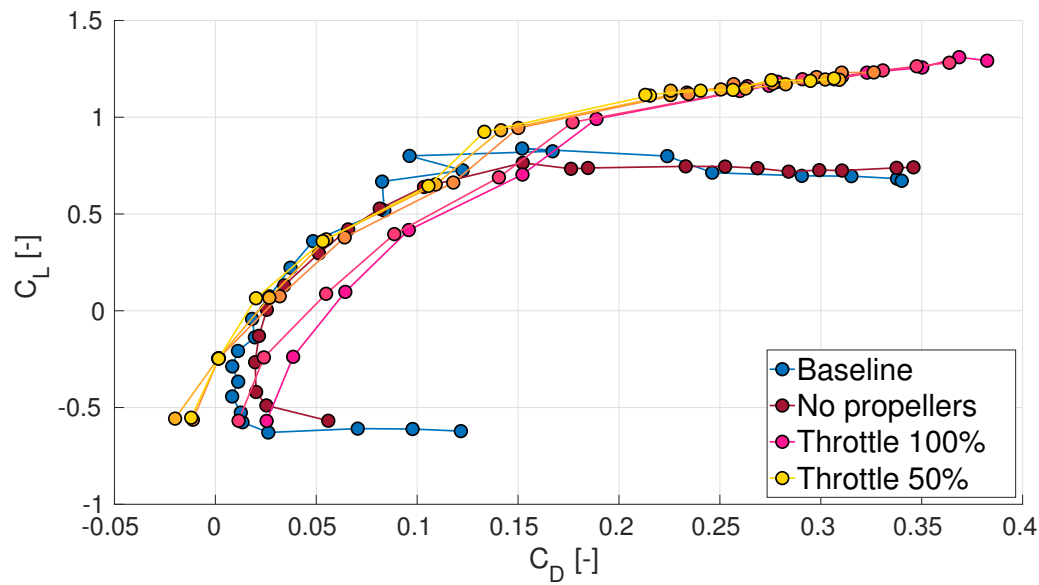


Fig. 8.12: Blown wing wind tunnel polar plot with uncertainty bars at different motors setpoints, $V_\infty = 20$ m/s

Other two tests of interest enforce the wing in single-engine configuration and in multi-engine OEMI. These are represented in Figure 8.13 and 8.14, respectively.

(a) Blown wing ($C_L - \alpha$) curve

(b) Blown wing drag polar curve

Fig. 8.13: Blown wing wind tunnel testing results in single-engine configuration, $V_\infty = 15$ m/s

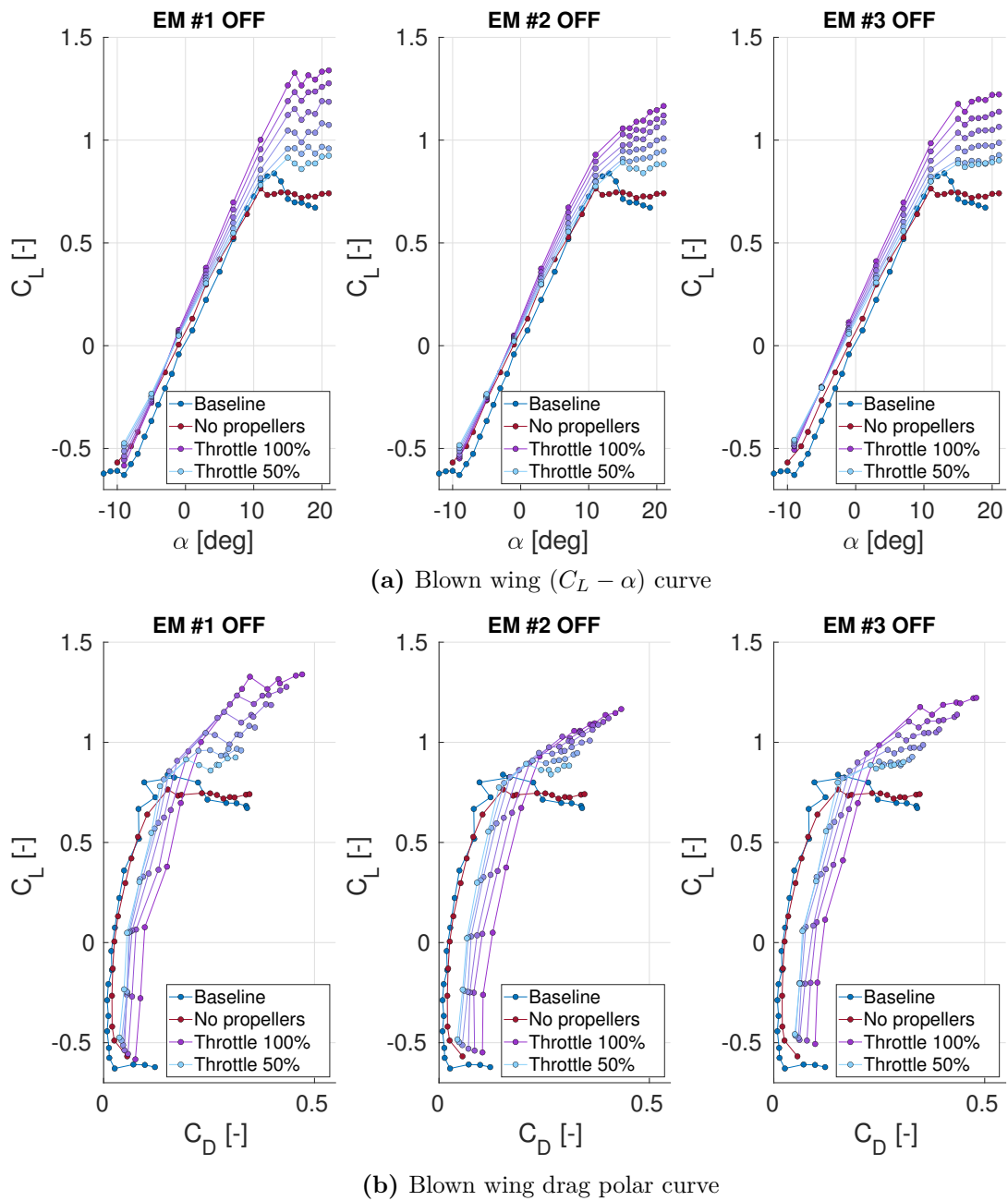


Fig. 8.14: Blown wing wind tunnel testing results in multi-engine OEMI configuration, $V_\infty = 15$ m/s

The reported results underline consistency with predictions, and were obtained without the onset of instability or other unexpected phenomena. The entire activity was indeed a success, establishing safety is always guaranteed no matter what propulsive configuration is enforced, laying the foundation for flight test campaign.

The entire dissertation on the wind tunnel test campaign is well exposed and analyzed in the master's thesis of Andrea Santeramo [4].

8.1.4 Ground, hardware and fail mode testing

Once *SwitchMaster* building procedure was completed, many ground tests have been carried out prior to maiden flight. These activities were mainly oriented on debugging and verification of every system, not having the purpose of collecting data. Concerns were basically on safety. Many tests were also carried out with electric motors armed, eventually not installing the propeller to reduce the related risks. Completed tests are:

- Control surface excursion and zero-position check.
- Failure of connectors: with all systems running, several electrical connectors have been intentionally disconnected. For instance, disconnecting the S-BUS from the *M3U* makes the board entering in *Fail-safe* mode, in which power is cut, with the control regained instantaneously when the signal is restored. Disconnection of one of the two battery packs have no effect, apart from reduced endurance. Disconnection of sensors or CAN input from the FMU prevent from entering in automatic flight modes, but manual control is not affected.
- Removing one or more *M3U* bridges from its place have no effect, as the board reads the corresponding working mode only at start-up.
- Electromagnetic compatibility check: power cables subjected to high electric current are placed close to wires transmitting data, to see the effects of electrical interference. In this test, max throttle was imposed to the EMs with propellers installed, in order to have the maximum electric current flowing in the cables. Simultaneously, control surfaces could be correctly actuated, without verification of any unwanted phenomena. The picture in Figure 8.15 highlights the density of data cables and power cables in the wing, from which arose the need of such a test.

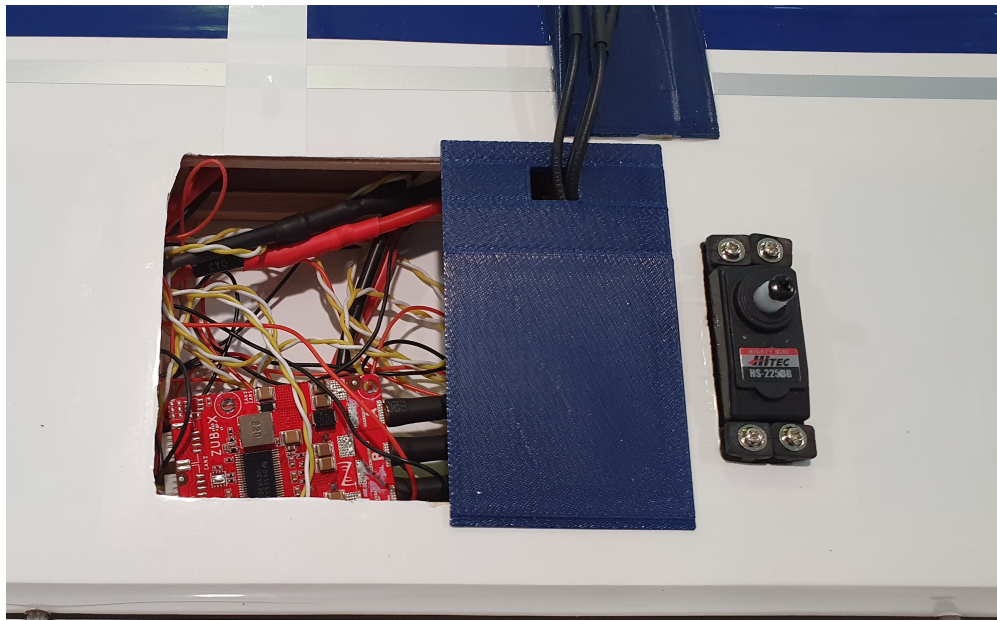


Fig. 8.15: A view on one ESC installation

- Radio range check: progressive increase of distance between radio transmitter and receiver, always in line of sight. Two people alternatively control the radio or monitor

the aircraft, coordinating radio inputs and related surface deflections through telephone contact. No interference, glitches or issues arose during the test.

- Turning OFF the radio transmitter while the systems are armed is instantaneous recognized by FMU.
- For every different *M3U* working mode, consistency between output setpoints and actual speed of motors is checked: input setpoints, retrieved connecting *M3U* to a computer via USB connection, are compared to the output obtained connecting the ESCs to the computer and reading the RPM value in the *Kucher* software.
- Long-run test: every system (including the *M3U* and propulsive units) has been kept turned on for 1 h and then tried again. This should verify if cumulative computational errors arise, compromising working capability of the systems.
- Motors have been kept continuously at full throttle for 5 min without any issue, neither exceeding suggested maximum temperatures.
- Taxi testing: low speed taxiing test have been executed with just two propellers working, in order to verify ground controllability.

Every ground test has been completed with full success, allowing the aircraft to be considered ready to fly.

8.2 Computer flight simulator testing

Lorenzo Alberti, aeronautical engineering thesis candidate, developed a full-working *SwitchMaster* model in the commercial computer flight simulator *X-Plane 11*. This served as a benchmark before flying the real aircraft to investigate different aspects related to propulsion. An image extracted from the simulator is depicted in Figure 8.16.



Fig. 8.16: The SwitchMaster in *X-Plane 11*

Flying the *SwitchMaster* in the simulator was really useful both to understand the airplane dynamics and controllability, and to identify issues before completing *M3U* firmware coding and real flight testing. In particular, two main problems were first experienced: motor saturation in current-setpoint mode and maximum continuous power setting.

When the ESCs are commanded with the current-setpoint control law, thrust curve is saturated at high speed as reported in Section 8.1.2. Initially, this specific behavior was only assumed to affect the thrust curve and pilot feeling, but indeed have a strong effect on the SE modes. Setpoint at which saturation is experienced changes with the airspeed. Thrust asymmetry in *SE-norm* mode implies that motor #6 could be saturated even if the others are not. When this happens, yawing moment generation cannot be controlled. Actually, this problem could be solved inducing the desired yawing moment thanks to the lower throttle imposition to motor #1. Nevertheless, total available thrust reduces as well with this working logic. Furthermore, saturation problem also appears in *SE-OEMI* modes, for which the solution is no more straightforward.

The second issue noticed concerns the available power in *SE-norm* mode when RPM control law is set. Due to the fact thrust curve can be approximated with a parabola, the de-rating of the EMs to 66.67% of their maximum value resulted in a too low thrust output, not sufficient to trim the aircraft. This does not happen with the current-setpoint, as its almost linear curve gives back higher thrust value, with the same de-rating percentage. The solution eventually applied consisted of limiting de-rating in the RPM control mode, so that maximum setpoint is 80%: this improves trim capability and leaves broad margins to generate the correct yawing moment.

In conclusion, test flights in the computer flight simulator environment may not fully represent real behavior, but were extremely useful to identify issues and mitigate the risks.

8.3 Familiarization flights

The conclusion of building procedure and preliminary tests paved the way to the *SwitchMaster's* maiden flight. It occurred Wednesday the 17th February 2021 in Ceriano Laghetto model aircraft flying field, 10 km North-West of Milan. The location has a grass runway and it is far from any building, house or vertical construction. The only hazard is represented by the close Cogliate ultra-light airfield, whose radio frequency is always monitored.

After the pre-flight checks, the aircraft was ready to fly. The planned mission was simple: after take-off and initial climb, the pilot tried to trim the aircraft acting on the radio transmitter. After some circuits above the field, power-off, stalls and low speed regimes were tested at high altitude in order to get practice before landing. A rule always applied in the whole campaign was that FTE and FTP communicated one each other, in order to share and note down every consideration and feedback.

First impression applying full throttle was that specific excess of power in take-off is really high. The aircraft gained speed in a smooth and fast way, shortly raising its tail above the ground, allowing the pilot to rotate. Initial climb began with a high flight path angle. Immediately after being airborne, the pilot realized how difficult was to keep the proper attitude, as the aircraft handling was not satisfying. Particularly, a high tendency to dynamic divergence appeared when applying the elevator command, with strong oscillations on the pitch axis. Flight conduction was really difficult, and got even worse at low speeds. The airplane resulted unable to glide with throttle brought back to idle, descending with a fast and steep path, even if spontaneously entering in a nose-up attitude. After some failed low-speed approaches, landing was challenging, but luckily without any consequence.

In Figure 8.17 are reported some pictures taken the day of the first flight.



Fig. 8.17: Photographs from the *SwitchMaster* maiden flight

On the first day of testing, 6 flights were completed, all dedicated to aircraft tuning and pilot familiarization. Also FMU assisted flight modes have been tried.

Tuning

In the first flight debriefing phase, it was clear that many problems needed to be solved. Pilot judged the aircraft really difficult to fly, assigning a Level 8 in the Cooper-Harper piloting rating scale [52]. Main identified issues were:

- **Center of gravity location:** it resulted too rearward for the aircraft configuration. This was the greatest issue and the main problem for aircraft stability. The center of gravity location has been moved forward relocating batteries in the subsequent flights, reaching a final position of 64 mm from the leading edge of the wing. This corresponds to the 24.6% of mean aerodynamic chord (previously it was at 32% of MAC). This solved stability problems and in-flight oscillating behavior.

- **High wing loading** is an unsolvable problem, mainly responsible for bad handling qualities at low speed.
- **Propeller hub** is placed above the vertical position of the center of gravity. This translates into the generation of a pitching moment, depending on the imposed throttle setpoint. Trimming the aircraft for low-throttle regimes will result in a nose-down moment when adding power, and the opposite. This tendency could be mitigated setting up a mixing between throttle and elevator channels on the radio transmitter. Anyway, this aspect was set at pilot's will as not highly problematic.
- **Landing flare** maneuver is complicated also due to high wing position with respect to the ground: being the wings 46 cm above of the contact point of the landing gear with the ground, flare is executed out of ground effect (as MAC is 26 cm); this adds some difficulty to an already complicated landing maneuver.
- **Ground roll** is challenging: high vertical location of the center of gravity and high masses on the wings (also in tips) favors bouncing in landing or skidding on the ground. These issues are not solvable, and the only viable option is to perform a really smooth landing maneuver, which is greatly complicated by the wind, especially if with crosswinds and gusts.
- **Motor behavior at low stick percentage** is erratic: when the throttle is brought back to a low percentage, the ESCs tries to reach the RPM value prescribed by the *M3U* setpoint. This results in windmilling and makes the propellers act like speedbrakes. This is greatly exaggerated by the stick-thrust mapping relationship, resulting in great part of the stick excursion for which the propellers behave like speedbrakes. Moreover, the propeller spinning in front of the wings at setpoint which is dissimilar to the freewheeling one greatly disturbs the airflow behind it, producing turbulence and possibly disrupting the airflow. Three methods have been applied to mitigate these phenomena: in first instance, the pilot changed his piloting technique, performing a low speed but high-power approach in full-flap configuration, bringing the throttle to idle only at touch-down. Secondly, the radio mapping illustrated into Section 6.7 and the RAW ESC control mode discussed in Section 7.3.1 have been implemented. Radio mapping greatly helped the pilot in the landing maneuver, while RAW ESC mode contribution is negligible. Different setups could also be examined in future applications. Another way of mitigating this phenomenon could be changing the propellers adopting a higher blade pitch configuration. For example, a 10x8 in propeller could offer greater thrust at low setpoint regime (or, at least, smaller braking action).

Some of the illustrated modifications managed to improve the handling qualities, allowing a good flight conduction and execution of test points. Landing behavior remains complicated, but the pilot understood how to better manage it, conducting a high RPM approach with full flap deflection.

Tuning of some parameters of the FMU was required too. In particular, in altitude and position modes, throttle management needed to be tuned acting on damping and integrative gains, because its response was wrongly oscillating. For what concerns the stabilized mode, the standard pitch setpoint needed to be tuned, as the aircraft climbed with stabilized mode activated.

General behavior

Several subsequent flights investigated the *SwitchMaster* performance and behavior. Available thrust at low speed results overabundant, being vertical climb almost possible. The aircraft

exhibits a good basic aerobatic ability, and flight conduction at normal and high flight speed is smooth.

Stall behavior in idle regime is ambiguous: if the elevator is fully deflected, it resembles a controllability stall, whereas in normal flight a roll-break could appear. When adding a full elevator command, the airplane enters a nose-up descending path with the wings slightly oscillating on the roll axis. This is probably due to the horizontal tail stalling, given the high command deflection. Conversely, when speed is reduced with constant altitude in a more "traditional" approach to reach stall, a roll-break could arise. In both circumstances stalling speed is around 9 m/s.

Behavior with flap deployed is more stable relatively to roll axis than in clean configuration. Stall speed is between 7 m/s and 8 m/s. The aircraft must be trimmed again when deflecting the flaps, with a pitched-down elevator control as expected from flight mechanics theory.

High power-high AOA flying condition is guaranteed by the airflow energization enhanced by the EMs. The speed added to the airflow on the wings by the spinning propellers helps to fly at a really low speed with high pitched-up attitude. Moreover, in such highly pitched-up attitudes a significant thrust component contributes to equalize the weight vector. This way, speed can decrease up to really low values, in the order of 6 m/s, but continuous control surface and throttle intervention is required to keep constant altitude.

Landing technique differs from those of a real General Aviation airplane or a conventional radio controlled aircraft due to the wing blowing. A steep approach is not easy to perform as it is typically done on RC aircraft. The most suitable technique enforces a small descending path angle. Although comparable in magnitude to the typical values of a real aircraft (-5 deg), this should be compared actually to the approach of a RC model, well more abrupt. Moreover, flaps are fully deployed and throttle is not released till touch-down to avoid the unpredictable behavior experienced at low power regimes. The landing flare is performed only when really close to the ground, and throttle brought to idle only at touch-down instant. This behavior is confirmed by time history of landing of one of the flights of the campaign, reported in Figure 8.18*.

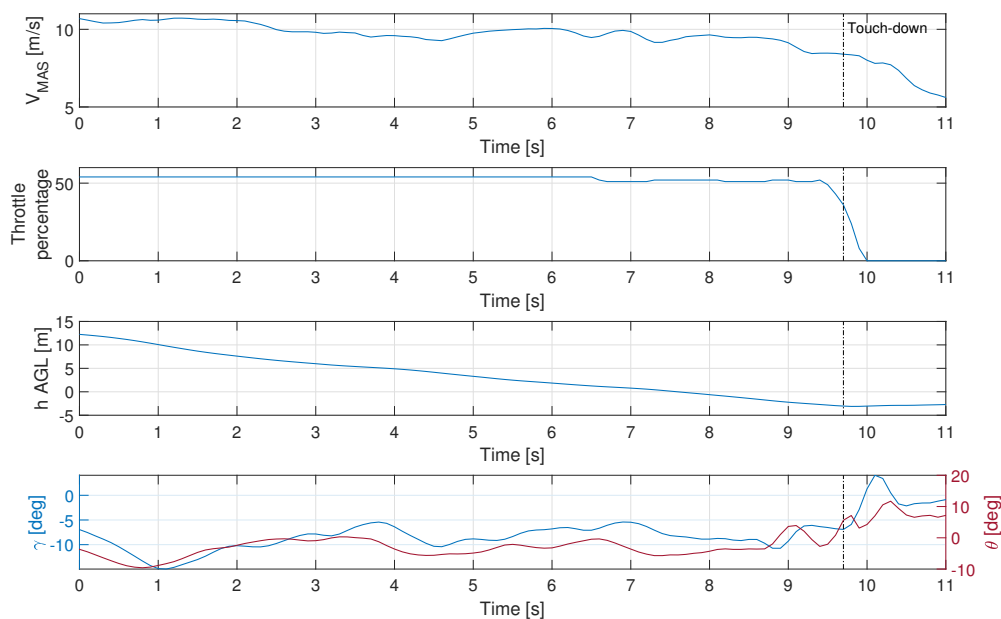


Fig. 8.18: Illustrative time history of landing technique

*Time instant of touch-down was cross-checked notifying a peak in normal load factor

Chapter 9

Flight testing

The present chapter describes planning, execution and data analysis of the flight test campaign. Safety was the main driver of the whole activity, thus carried out with preliminary validation of flight test techniques, followed by progressive expansion of the envelope. Topics were tested in order of priority and hazard profile.

9.1 Test campaign planning

The main topics of flight test campaign can be condensed as follows:

1. **Familiarization flights:** comprehending the maiden flight and the subsequent ones for pilot familiarization and systems tuning, as described in Section 8.3. These first flights also served to become familiar to the FTT and *ME-norm* mode demonstration.
2. **Patent validation flights**, subdivided in:
 - (a) *SE-norm* mode demonstration: first objective is the identification of a proper range for asymmetry percentage knob, so that behavior experienced is similar to that of a real GA SE airplane. At each flight completion, pilot's perceptions are combined with results of data analysis, in order to confirm the right asymmetry percentage to employ. At a later stage, most suitable percentages will be employed in another set of flights in which the same FTT illustrated in Section 5.4 is repeated to validate the results.
 - (b) *SE-OEMI* demonstration: every electric motor inoperative condition is tested in order to demonstrate a behavior similar to the *SE-norm* mode also in emergency condition. Even if the aircraft is symmetric with respect to longitudinal plane, tests are repeated for inoperative motors on both starboard and port sides.
 - (c) *ME-OEI* mode demonstration: the purpose is to demonstrate the pilot can still control the aircraft in this arduous situation, properly acting on control surfaces. Aim of this working mode is to compare the aircraft to a twin-engine in OEI training activity. Particular care should be taken in this hazardous activity.
3. **Aircraft characterization:** investigation of performance, mainly related to aerodynamics (to support thesis of Andrea Santeramo [4]) and flight dynamics (to increase the fidelity of the simulator developed by Lorenzo Alberti [3]). In particular, aircraft drag polar is retrieved exploiting different FTTs, given the uncertain effectiveness of these techniques on a RC airplane. Planned techniques are "Level-Acceleration-Decelerations" (LAD), "Trim shots", "Rollercoaster" and "Sawtooth glides" [53]. On the other hand,

dynamic characteristics are investigated with particular focus on inertial characteristics, maximum rates and response to excitation of dynamic modes.

4. **Propulsive control** demonstration: use of thrust asymmetry set with asymmetry knob to enhance directional control. First objective is to complete flat turns without the need to act on the rudder. Second task is automatic turn coordination, mixing asymmetry knob channel with the one controlling ailerons. These features are only tested to evaluate their feasibility and effectiveness.

Flight test campaign planning schedule is reported in Table 9.1*.

Mission	Date	Flight	Topic
1	17/02/2021	1-6	Familiarization
2	22/02/2021	1-3 4-5	Familiarization SE normal (1,2)
3	24/02/2021	1 2 3 4 5	ME normal (1) SE normal (3) SE-OEMI-M1 (1) SE-OEMI-M2 SE-OEMI-M3
4	26/02/2021	1 2 3	SE-OEMI-M4 SE-OEMI-M5 (1) OEI M1, M2, M3 inop.
5	02/03/2021	1 2 3 4 5 6 7	Assisted FMU modes LAD clean Trim shots clean ME normal (2), SE KNOB 100% LAD flap, trim shots flap Glides Rollercoaster
6	09/03/2021	1 2 3 4 5 6	OEI M3 inop., modes (1) OEI M2 inop., body rates Flat turn, turn coordination (1) SE normal (4) SE-OEMI-M5 (2), modes (2) SE-OEMI-M1 (2)
7	23/03/2021	1 2 3	OEI M1 inop. OEI M1, M3 inop. Turn coordination (2)

Tab. 9.1: Test campaign summary

*Numbers enclosed in brackets represent repetitions

9.2 Data acquisition and FTI

The flight test activity had the objective of characterize working modes from both qualitative and quantitative points of view. This latter was accomplished by means of a tailor-made flight test instrumentation, consisting of the integration between *Pixhawk 4* FMU and related sensors. A first set of sensors is embedded in the suite, namely accelerometers, gyroscopes and barometer. Then, magnetometer, GNSS sensor and Pitot-static probe are paired to the flight control module. Moreover, the FMU takes inputs from the *M3U* via UAVCAN link, from which it receives diagnostic messages and data coming from the ESCs. Sensors working parameter, sensitivity and tolerances are reported in Appendix C.

Data could also be live streamed through a telemetry link. This was extremely useful during the trials, mainly looking-up timestamps, altitude, measured airspeed, heading and pitch. These valuable references were used to fill flight test cards and to guide the pilot.

Pixhawk 4 saves flight data as log files on a SD card, in the .ulog format. Several third party services are suggested in *PX4* documentation, but their main feature is to graph the data on mission basis. On the contrary, post-processing required data manipulation, meaning an alternative approach was necessary. Eventually, .ulog files were imported in *Matlab* environment and converted into a *struct*, so that data handling was not an issue. Actually, each stored variable has a specific frequency of acquisition, uncannily slightly changing over time, with also non-synchronous start of recording. These characteristics, along with the extremely convoluted procedure to be developed for *Matlab* struct generation, led to initial exploitation of the .csv file generated by telemetry, in place of .ulog file. This had in fact the advantage of saving at a specific synchronous time instant the values of acquired variables. Main drawbacks were the acquisition rate of only 1 Hz, and the fact of storing just a limited set of variables.

Previously mentioned deficiencies of telemetry log, forced to persist on .ulog file. In particular, a compromise solution was applied, namely a first-order hold (FOH), reconstructing each variable as a piecewise linear approximation of the sampled signal. This was possible exploiting built-in *Matlab*'s function `resample`, that allows to resample nonuniform data to a new rate. This rate was fixed at 10 Hz, twice the value that proved to suit for real aircraft FT data. Most signals undergo a downsampling, as outlined in Table 9.2, avoiding aliasing through a polyphase antialiasing filter still exploited by `resample` function.

Field	Parameter(s)	Original rate
<code>actuator_controls_0</code>	Throttle, δ_a , δ_e , δ_r , δ_f	200 Hz
<code>actuator_controls_3</code>	Knob, Mode	20 Hz
<code>airspeed</code>	MAS, OAT	100 Hz
<code>esc_status</code>	RPM setpoint, current, voltage, temperature of ESCs	4 Hz
<code>input_rc</code>	Event	80 Hz
<code>commander_state</code>	Semi-automatic modes	4 Hz
<code>vehicle_acceleration</code>	Accelerations	20 Hz
<code>vehicle_air_data</code>	Static pressure	20 Hz
<code>vehicle_angular_velocity</code>	Body angular rates	300 Hz
<code>vehicle_attitude</code>	Attitude and heading	20 Hz
<code>vehicle_global_position</code>	Altitude, latitude, longitude	50 Hz
<code>vehicle_gps_position</code>	Speed in NED frame	50 Hz

Tab. 9.2: Log data fields and sampling rate

The only problem occurring when resampling a signal is when considering the value of an angle ranging from 0 deg to 360 deg. Azimuth angle is the only one affected from this issue (pitch and roll are always vary within a restricted range): a small change in heading when headed north is responsible for a step variation of 360 deg in azimuth angle. Apart from the fictitious intermediate samples between 0 deg and 360 deg, easily correctable, main problem is derivation of $\dot{\psi}$. In fact, when crossing the direction of the North, time derivative of azimuth angle would experience a false spike. To solve this singularity, if the difference between the values of ψ at two subsequent time instants is greater in absolute value than 180 deg, a ± 360 deg correction is applied. In equation form:

$$\Delta\psi := \psi_{i+1} - \psi_i = \begin{cases} \Delta\psi - 360 \text{ deg} & \Delta\psi > 180 \text{ deg} \\ \Delta\psi + 360 \text{ deg} & \Delta\psi < -180 \text{ deg} \end{cases} . \quad (9.1)$$

Log data delivers spatial orientation through unit quaternion notation, then converted into equivalent values of bank, pitch and azimuth angles.

As a side note, the activation of assisted flight modes is confirmed by variable `main_state` in the field `commander_state`. In particular, this variable assumes value 1 in altitude control mode, 2 in position control mode and 8 in stabilized flight mode. The pilot can also notify with a switch on the radio the occurrence of events. This action finds direct correspondence in the variable `input_rc` of the log data.

9.3 General considerations

9.3.1 Concept validation

Main FTTs deployed to test the scale model were the same as those tested on the real aircraft: constant speed or altitude trials imposing maximum throttle (described in Section 5.4). Configuration was stick-fixed, to replicate the behavior tested on the real aircraft. By the way, stick-free configuration could not be considered due to the way in which servos are actuated. It was verified in post-processing that the pilot would only act on the longitudinal control, leaving ailerons and rudder locked, under penalty of cancellation of the trial.

The conduction of the test on the scale model overturned the verdict of real aircraft flight test activity, in which the execution of constant altitude FTT resulted more problematic. On the contrary, greater difficulty was experienced to respect tolerances during constant speed FTT. This issue was even more problematic due to the complete absence of reference for the pilot for what concerns the value of speed throughout the trial. Communication with FTE consulting live telemetry was paramount in this sense, but the success of the test mainly depended on the sensibility of the pilot. With the experience came a better knowledge of the behavior of the aircraft, leading to sufficiently precise handling.

The other lesson learned during scale model flight test campaign dealt with the effect of non-smooth air on the trials. A small featherweight aircraft as the one tested is extremely susceptible to wind gusts. As a consequence, many test points were compromised by impulsive variations in wind intensity and thus their results could not be accounted for. To cope with this issue, the duration of the test points was progressively reduced to 6 seconds on average (approximately one third of the duration of a test point on *PS-28*), to limit the likelihood of perturbations in the middle of the trials. Besides, as soon as the pilot felt any disturbance, he instantly reduced the throttle setting and trimmed the aircraft, thus preserving the healthy portion of the trial. This explains why time histories of examined quantities during a few test points exhibit impulsive variations close to the finish of the trial, prior to throttle release.

Other possible reasons for premature ending of a test point were due to airspace limitations, the violation of forsaken tolerances or the wrong use of controls.

Generally speaking, the behavior of the scale model is representative of that of a real aircraft. This assertion is supported by both the feedback from FTP and the analysis of flight test data. The differences in configuration, geometry and flight test conditions have an impact on the aircraft slipstream effect, as anticipated when comparing results from real FT activity performed on *PS-28* with those obtained from preliminary analysis of the behavior of Cessna *172 Skyhawk* reconstruction implemented in *X-Plane 11* simulator. The airframe of *PS-28* and *SwitchMaster* mainly differ for their wing position (low wing in *PS-28*, high wing in *SwitchMaster*). Another source of discrepancy is represented from the value of wing dihedral, up to 5 deg on *PS-28* against the 1 deg of *SwitchMaster*. Therefore, on the paper, less interaction between roll and sideslip was expected on the *SwitchMaster*, namely a lower value of bank angle induced by yawing moment. Nevertheless, the overall combination of other effects, such as mass distribution, returned similar results.

Another strategy to validate the patented concept could have enforced in-flight determination of the rudder deflection required to contrast induced yawing moment. Assisted flight modes could have been exploited, for example position control mode, in which the FMU tries to keep a constant track angle and altitude, suppressing external disturbances. The asymmetry reproduced to in-flight simulate single-engine propeller effects could be seen as an external disturbance, as well. Post-processing would have returned the rudder deflection. Nevertheless, this strategy has not been enforced due to the lack of direct reference to what happens on a real single-engine aircraft: flight test activity on *PS-28* could not return any information about rudder control imposition, to be compared with *SwitchMaster*.

9.3.2 Aircraft characterization

Along with patent validation flights, other topics were covered in the campaign. In particular, main objectives were:

- aircraft aerodynamics characterization, to evaluate the in-flight effects of DEP, contributing to the thesis work of Andrea Santeramo [4];
- aircraft flight dynamics characterization, to increase fidelity of the simulator developed by Lorenzo Alberti [3].

For what concerns the aircraft aerodynamics characterization, main target is determination of the C_L - α and drag polar curves. Methods enforced followed what already presented in FT literature [53, 54, 55], highlighting high uncertainty of these techniques. Then, other performed tests concerned aircraft dynamic response to excitation on both longitudinal and lateral-directional controls and maximum rates of pitch, roll and yaw. FTT for aerodynamic characterization are here briefly reported:

- **Level-Acceleration-Decelerations (LAD)** - throttle is set to perform an acceleration or deceleration while the aircraft flies straight and level. Lift and drag coefficients can be determined in the idle section of the maneuver. A modification to this technique was forced from the available flying field geometric boundaries and the absence of the need for the accelerated part of the FTT: the maneuver starts from trim at maximum airspeed, then throttle is put to idle and altitude maintained up to minimum control speed. Difficulties came from keeping constant altitude, even in assisted flight modes.
- **Trim shots** - the aircraft is trimmed at a specific combination of elevator deflection and throttle input, to match a desired airspeed. Force and power equilibrium equations

can be enforced to retrieve lift and drag coefficients. Drag is computed through the estimation of available power. Main uncertainties come from mechanical motor efficiency and propulsive efficiency of propellers.

- **Sawtooth glides:** power is set to idle and the aircraft follows a descending path at a prescribed airspeed. Also in this case it is difficult to keep constant speed and rate of descent.
- **Rollercoaster:** the pilot imposes a pull-up followed by a push-over starting from trim. Even if smoothly applied, this technique implies a dynamic maneuver. Its execution is extremely difficult, as low aircraft inertia complicates the following of a smooth path.

The four illustrated methods are different alternatives to investigate the same parameters, and could appear redundant. Anyway, at least in an initial phase, the four were all exploited in order to determine the most effective ones.

For what concerns aircraft flight dynamics, main goal was determination of maximum body rates. In particular:

- Maximum roll rate was obtained through tonneau maneuvers, executed at different flying speed. They were performed imposing full aileron deflection, in order to maximize rotation speed.
- Maximum pitch rate is more difficult to determine, as it involves a high normal load factor and can possibly produce power-on stall. Pull-up, push-overs, Schneider turns and loops are exploited in order to obtain the maximum pitch rate. A Schneider turn is a minimum radius turn with 90 deg bank angle. As a matter of fact, roll-break occurred in both Schneider turns and loops when the elevator has been brought to full deflection. Therefore, maximum pitch rate is the one corresponding to instants before the roll-break in these maneuvers.
- Maximum yaw rate was determined through full rudder deflection in a flat turn, both on left and right sides.

In addition, a low-priority task was characterization of dynamic modes. Dutch Roll and Short Period excitation requires a doublet input on rudder and elevator, respectively. Phugoid mode instead requires a smooth speed variation from trim. **Unfortunately, none of the dynamic modes could be successfully excited.**

9.4 Multi-Engine normal conditions

The objective of the test was to verify the aircraft could proceed in straight flight in multi-engine normal mode, thus with a complete symmetric propulsion, without any sideslip. Such a result, theoretically taken for granted prior to the test, was anyway verified to have a confirmation. Moreover, being the first configuration in which beta-testing was carried out on *SwitchMaster*, it served for the pilot to familiarize with the scale model and assure that prescribed FTTs were compatible with the case.

FTP did not notified any undesired trend both in straight and turning flight, thus not portending any asymmetry. Constant speed and constant altitude FTT exhibited the same average result, namely the scale model moving forward with an acceptable sideslip angle (in the range ± 2 deg) due to perturbations, as experienced by heading and bank angles. This behavior is a common thread throughout the range of trim speed, and thus confirms the aircraft flies symmetrically when also thrust distribution is symmetric. This statement is

supported by time histories of quantities of interest reported below. In particular, figures 9.1 and 9.2 refer to trials at constant speed, with two different MAS at trim, whereas figures 9.3 and 9.4 are as many examples of constant altitude trials.

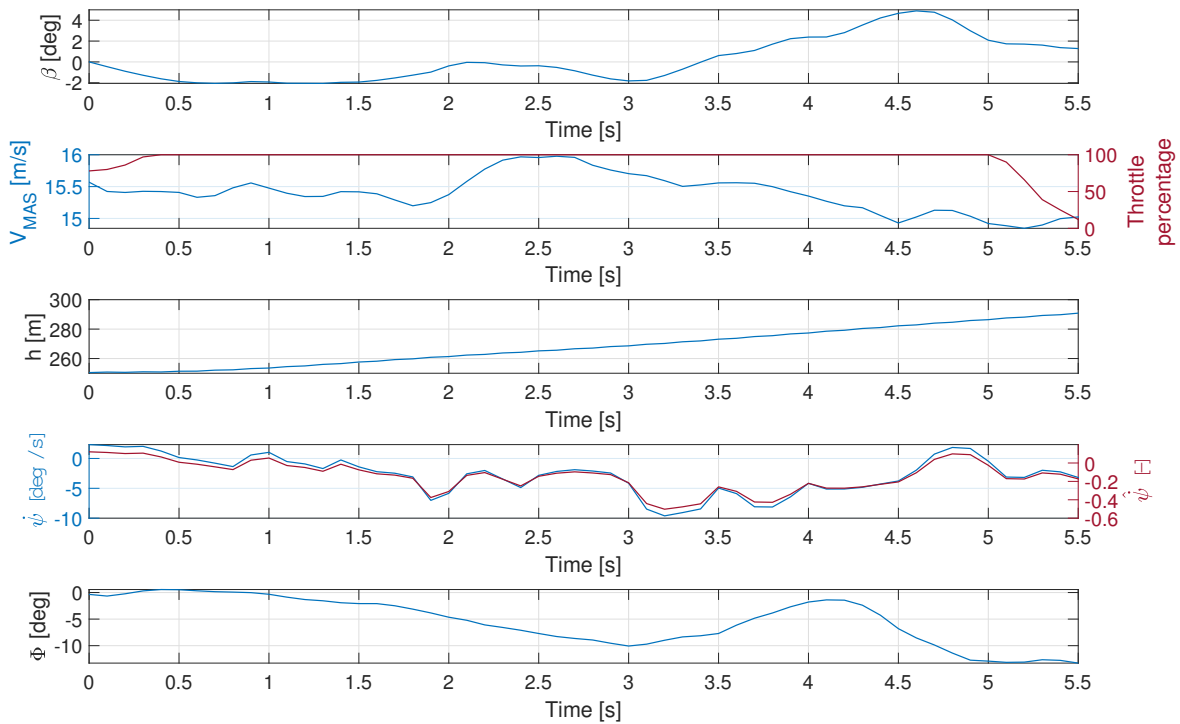


Fig. 9.1: Multi-engine normal, constant speed trial MAS = 12.5 m/s

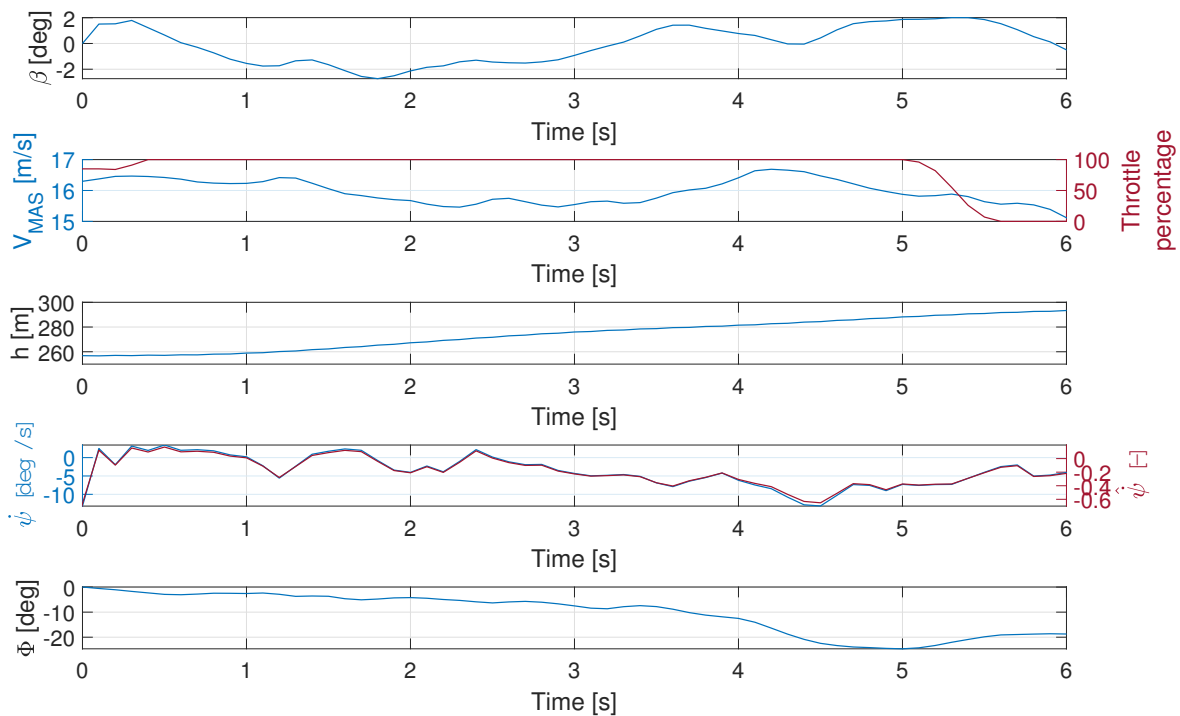


Fig. 9.2: Multi-engine normal, constant speed trial MAS = 16 m/s

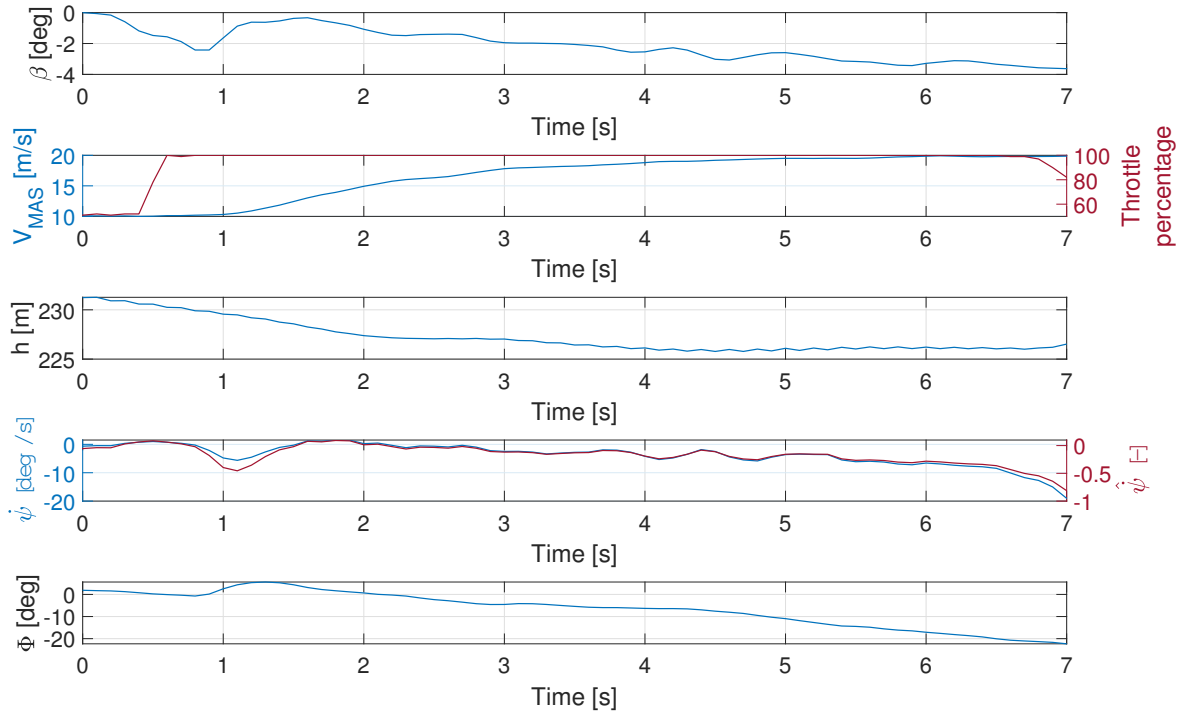


Fig. 9.3: Multi-engine normal, constant altitude trial MAS = 10 m/s

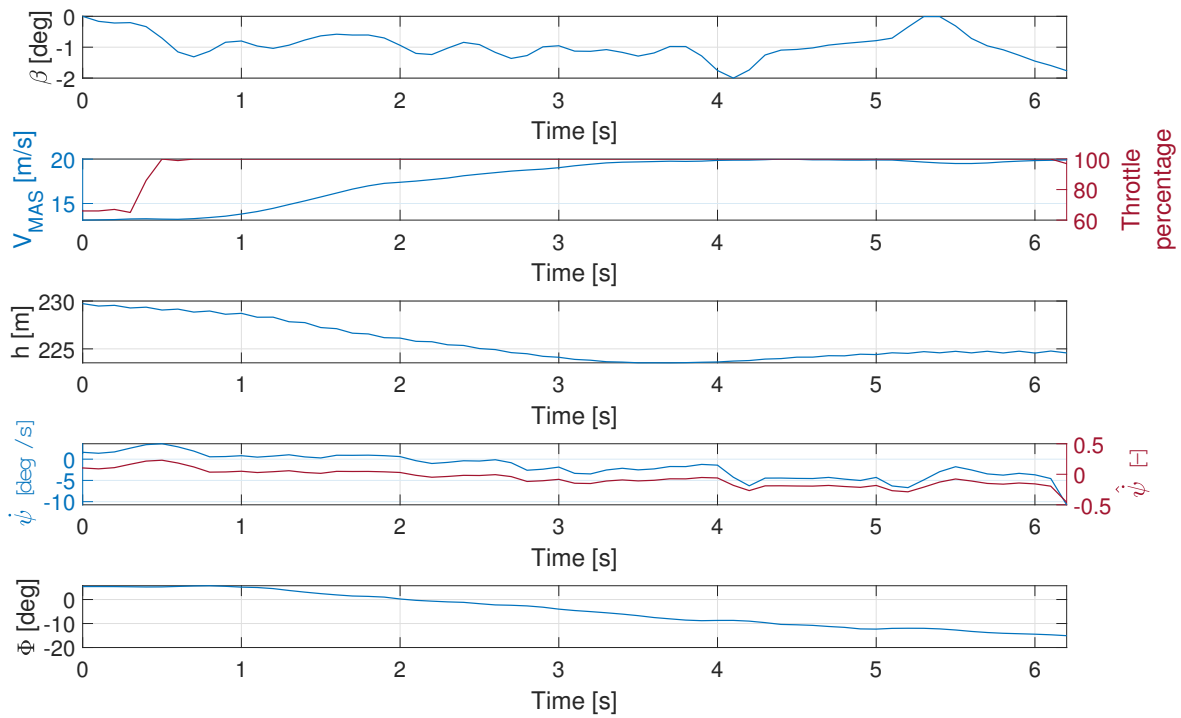


Fig. 9.4: Multi-engine normal, constant altitude trial MAS = 12.5 m/s

9.5 Single-Engine normal condition

The core of the entire work behind this master thesis, and more in general Aeroswitch project, lies precisely in single-engine simulation with a multi-engine aircraft. This premise explicates the importance of flight test data analysis of single-engine simulation reported in this section.

At this stage of flight test campaign came into play the tuning of the knob adjusting imposition of thrust asymmetry to most outboard electric motors. Familiarization flights contributed to limit acceptable setting of the knob within approximately the 40% of possible excursion, to which the regulation on the radio was remapped. In fact, adjustment at higher values would introduce a too severe condition, exceeding the desired pilot workload and compromising the handling.

In this framework, most part of successful test points were performed with the knob set at values between 10% and 25%. The actual value imposed could only be discovered in post-processing, due to the way in which the knob was adjusted on the radio, by pilot's feel. Only middle position could offer a reference. In retrospect, a discrete switch could have provided a more precise tuning, reducing flight test variables.

The set of trials performed covered different values of trim speed and knob setting. Leveraging the whole set of test points of the campaign, it is possible to identify a common pattern of results depending on the conditions, outlined in tables 9.3 and 9.4. As a side note, values reported are only referred to the reasonable section of each test point, not considering divergence induced by the undesired boundary conditions, wind gusts chief among them. Time histories of one test point per trim speed are available in figures 9.5, 9.6, 9.7, related to constant speed FTT, and figures 9.8, 9.9, 9.10, related to constant altitude FTT.

Input		Output				
MAS	Knob	β [deg]	$\dot{\psi}$ [deg/s]	$\hat{\psi}$ [-]	Φ [deg]	Ref.
10 m/s	14%	3.5	20	1	25	Fig. 9.5
	17%	3.5	20	2	20	
	21%	6	15	1.2	20	
	23%	8	15	1.2	20	
12 m/s	11%	4	20	1	20	Fig. 9.6
	23%	6	15	1.5	20	
14 m/s	21%	7	20	1.5	25	Fig. 9.7
	23%	2.5	20	0.8	20	

Tab. 9.3: Effect of knob and trim speed on flight symmetry in constant speed FTT

Input		Output				
MAS	Knob	β [deg]	$\dot{\psi}$ [deg/s]	$\hat{\psi}$ [-]	Φ [deg]	Ref.
10 m/s	19%	6.5	8	0.5	14	Fig. 9.8
	23%	5	14	1	6	
12 m/s	9%	2.5	6	0.4	1	Fig. 9.9
	14%	2	10	0.6	10	
	23%	2	7	0.5	10	
14 m/s	32%	3	15	1	15	
	14%	2.2	8	0.5	12	Fig. 9.10
	23%	1.5	7	0.4	6	

Tab. 9.4: Effect of knob and trim speed on flight symmetry in constant altitude FTT

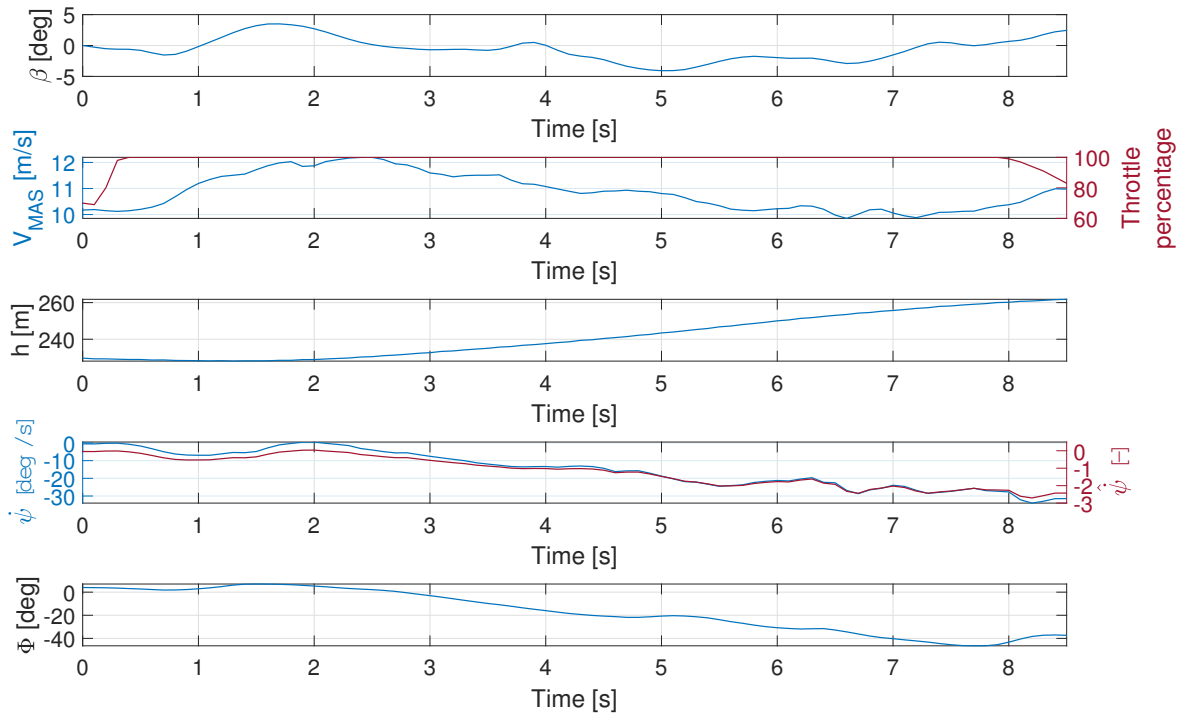


Fig. 9.5: Single-engine normal, constant speed trial (MAS = 10 m/s, knob = 14%)

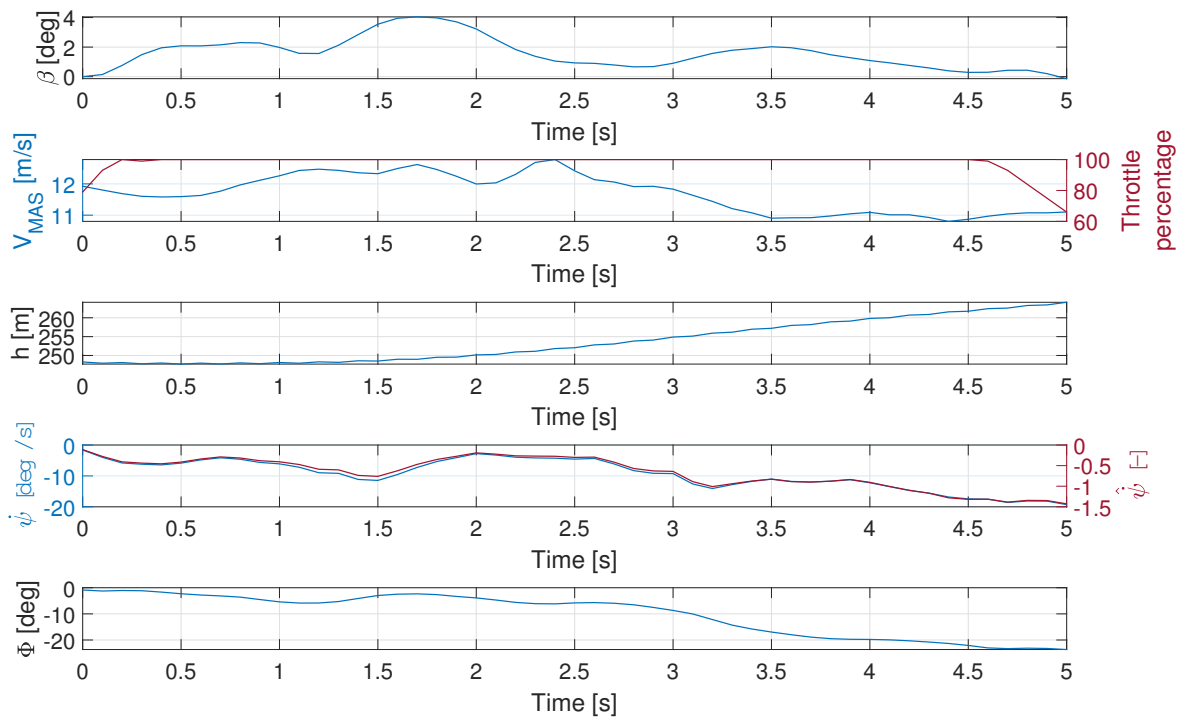


Fig. 9.6: Single-engine normal, constant speed trial (MAS = 12 m/s, knob = 11%)

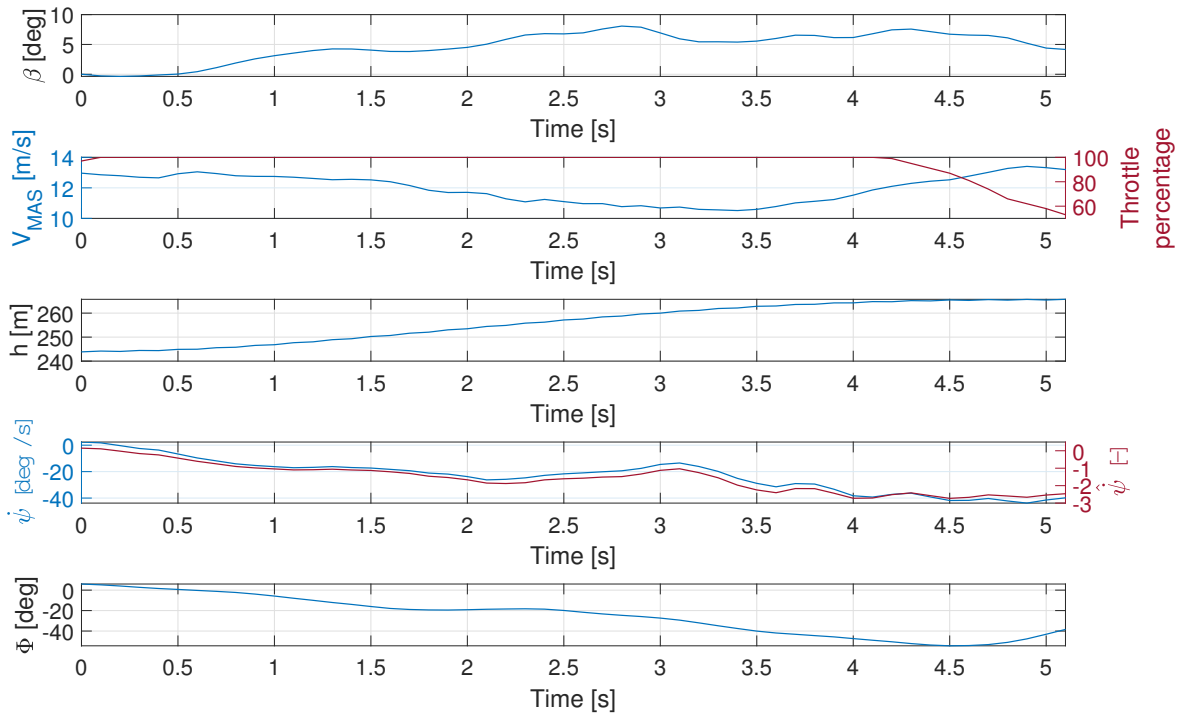


Fig. 9.7: Single-engine normal, constant speed trial (MAS = 14 m/s, knob = 21%)

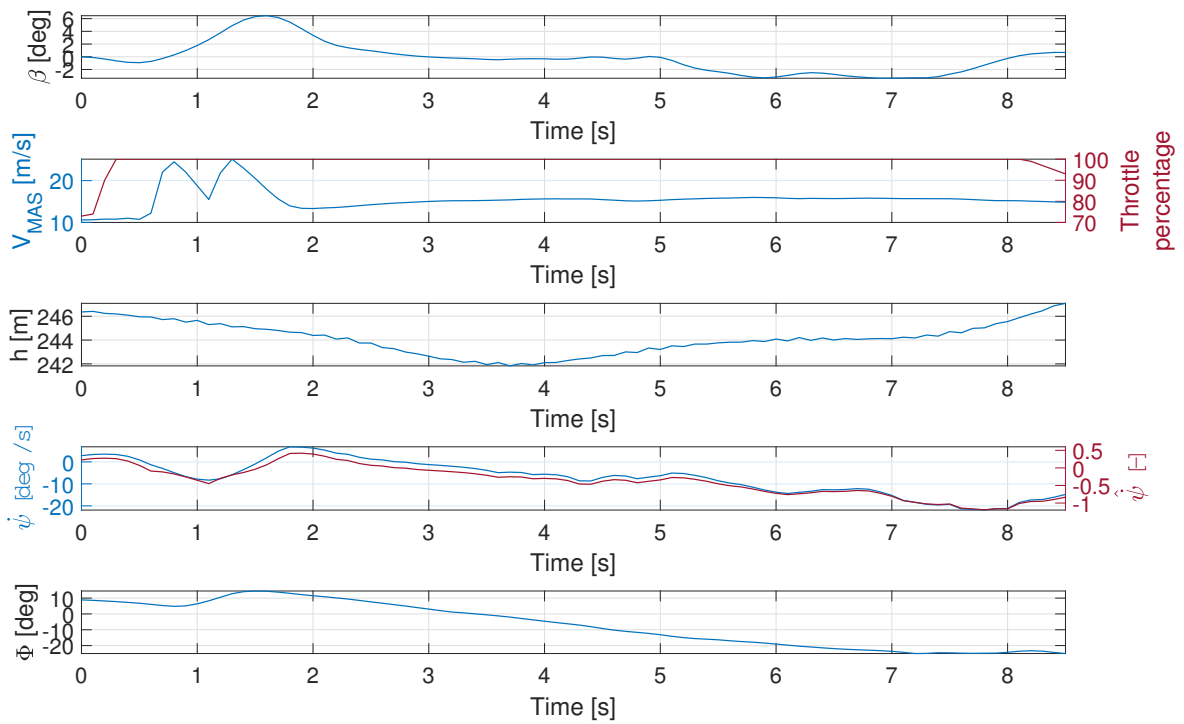


Fig. 9.8: Single-engine normal, constant altitude trial (MAS = 10 m/s, knob = 19%)

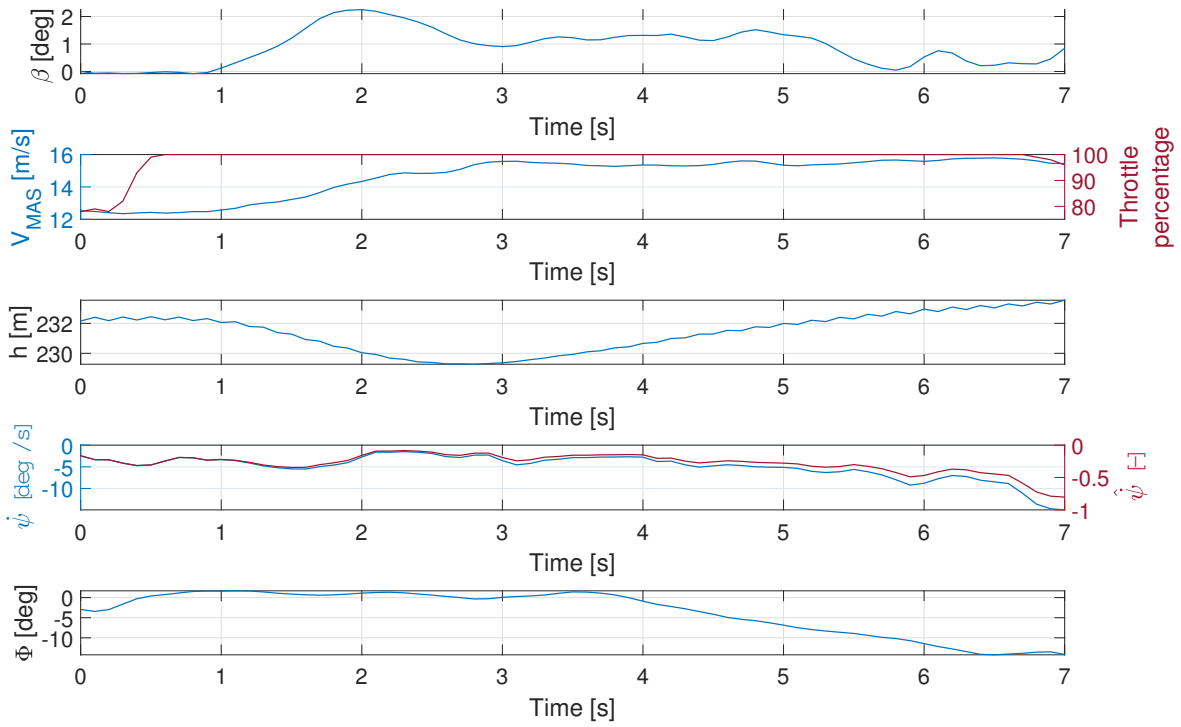


Fig. 9.9: Single-engine normal, constant altitude trial (MAS = 12 m/s, knob = 9%)

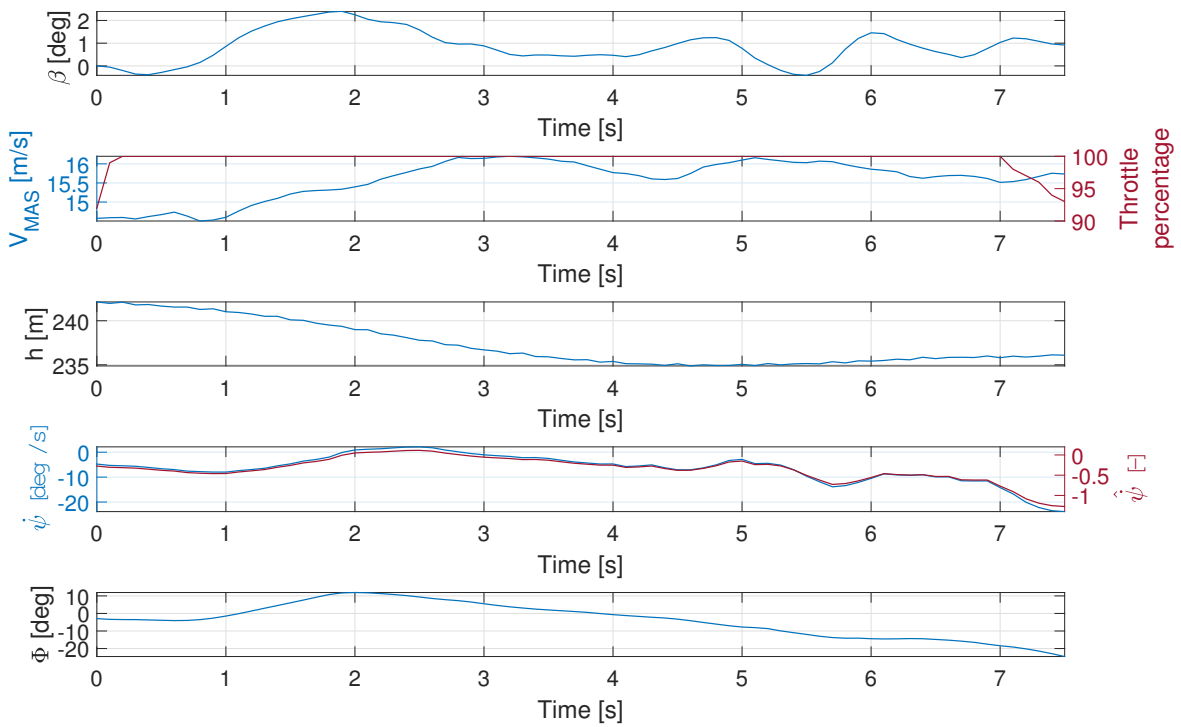


Fig. 9.10: Single-engine normal, constant altitude trial (MAS = 14 m/s, knob = 14%)

Obtained results confirmed predictions of what had been experienced in the FT activity on the real aircraft, namely:

1. higher trim speed reduces the effect of thrust asymmetry;
2. higher thrust asymmetry induced with knob setting leads to a greater imbalance in all quantities of interest (β , $\dot{\psi}$, Φ);
3. constant speed FTT is responsible for a more severe perturbation of straight flight;
4. bank angle and time derivative of azimuth angle exhibit a negative peak in constant altitude FTT, then damped, whereas they monotonically decrease in constant speed FTT.

These statements are backed up by time histories of most meaningful test points, previously reported. Pilot's feedback in straight and maneuvering flight and the account of the results in tables 9.3 and 9.4 both suggest that the most suitable value of knob setting is extremely low, to preserve handling qualities. Thrust asymmetry with knob at 10% induced a sideslip angle variation in the range $2 \div 5$ deg, in line with what had been experienced on real aircraft FT activity. Pilot workload is not increased with respect to multi-engine flight mode, apart from forsaken rudder imposition. In a gentle turn at high throttle setting some difference is felt when left turning, if not compensating with the rudder. Then again, a sloppy pilot could safely fly the aircraft as well, with no unexpected behavior arising also in upset flight.

As anticipated, no absolute comparison with *PS-28* can be made in terms of absolute turn rate, since dynamics of the scale model is faster. The value of $\dot{\psi}$ experienced in the test was 15 deg/s on average in constant speed FTT, twice what was measured in constant altitude counterpart. Typical values of *PS-28* were thus half of those of *TBM*. Conversely, non-dimensional turn rate $\hat{\psi}$ is pleasantly comparable among the two aircraft, typically in the range $0.5 \div 2$. Similarly, maximum bank angle was 20 deg on average in constant speed FTT, against the 10 deg of constant altitude FTT, thus only slightly higher than corresponding results of *PS-28* testing.

Asymmetry condition was only tested at a prescribed altitude, to mitigate the risks associated with the activity. It would have been interesting to investigate the same condition during take-off ground run, but this would have entailed a too hazardous test. In fact, this flight phase is extremely critical on a RC aircraft. Moreover, this demonstrator is only intended for validation of the concept, meaning the risk of a crash was not justifiable.

9.6 One Electric Motor Inoperative conditions

Main objective of this analysis is to verify that the differential thrust imposition to residual electric motors is capable of maintaining a sufficient level of flight symmetry for the whole range of speeds. This would guarantee that a single-engine pilot could withstand the eventuality of a failure of one electric motor. The original goal was that the aircraft would never sideslip, exhibiting a perfect cancellation of yawing moment through the contribution of each motor. The impossibility to implement closed loop sideslip compensation, or airspeed feedback to update *M3U* throttle-thrust coefficients, led to relax this constraint. Moreover, perfect symmetry is something actually not necessary. Even a single-engine rated pilot should be capable of dealing with a restrained flight asymmetry, compensating with the rudder (as in response to propeller slipstream effect). In conclusion, the forsaken behavior should not exceed the value of β , $\dot{\psi}$ and Φ typical of single-engine simulation. In case residual yawing moment is inducing a sideslip, it would be desirable that the pilot would need to push right pedal to

maintain straight flight, as in single-engine simulation (see Section 3.1). This behavior was not specifically prescribed in the design of *M3U* throttle-thrust coefficients, but its implementation would be straightforward in future developments.

Electric motors actuation is perfectly symmetrical when facing OEMI condition due to failure of an electric motor on one wing or the other. Nevertheless, for sake of completeness, both starboard and port electric motor failures were tested, also to see if the behavior was opposite between symmetrical cases. Only the case of shut-down of EM #6 was spared, being in perfect analogy with the simulated failure of mirror EM #1. To avoid redundant repetitions, only results of cases of failures injected on port electric motors are reported in the following displays.

The tests were performed in the same fashion as single-engine simulation, namely with constant speed or altitude trials, imposing maximum throttle. A build-up approach was always followed to assure that the level of residual asymmetry would not represent a threat for the safety of the scale model. The differential actuation of residual electric motors makes the test not particularly hazardous while keeping rudder and aileron controls locked in middle position. Testing the level of thrust asymmetry induced by a more severe condition as that of OEI simulation was not instead compatible with these FTTs, thus requiring a more conservative approach as will be discussed in Section 9.7.

"Sideslip-reset method" implemented for sideslip angle estimation, compensating the effect of the wind, lies on the hypothesis that the aircraft is flying symmetrically prior to imposition of maximum throttle. This assumption is quite consistent with the conditions at the start of trials for beta-testing with one electric motor inoperative. In fact, yawing moment induced by residual thrust asymmetry is almost identically null at limited power settings, according to the simulations carried out for identification of coefficients to be fed to *M3U*. This is also confirmed by pilot feedback, not requiring any rudder input at all to keep flight symmetry as long as the aircraft flies at low speeds with these propulsive emergency configurations.

9.6.1 Motor #1 inoperative

The first OEMI mode tested was that simulating shut down of EM #1. The corrective action induced by *M3U* consists of turning off the mirror electric motor on the opposite side. Therefore same flight condition is experienced when imposing failure of EM #6.

This condition was the first tested also because on paper perfect flight symmetry should be achieved, for the way in which control acts, as previously described. Nevertheless, a possible interrogative regarded the residual excess of power still enhanced by only four electric motors working. Preliminary flight phases made sure this requirement was satisfied. Then, constant speed and constant altitude FTT were carried out to investigate quantitatively if the aircraft could fly on a straight line. As expected, this objective was easily accomplished, no matter of trim speed or flight test technique exploited. Indeed, the aircraft behaved even more symmetrically than in multi-engine normal mode. This could be the direct consequence of fewer manufacturing discrepancies coming into play.

Two meaningful examples, related to test points performed at the same trim speed with opposite techniques, are reported in figures 9.11 and 9.12.

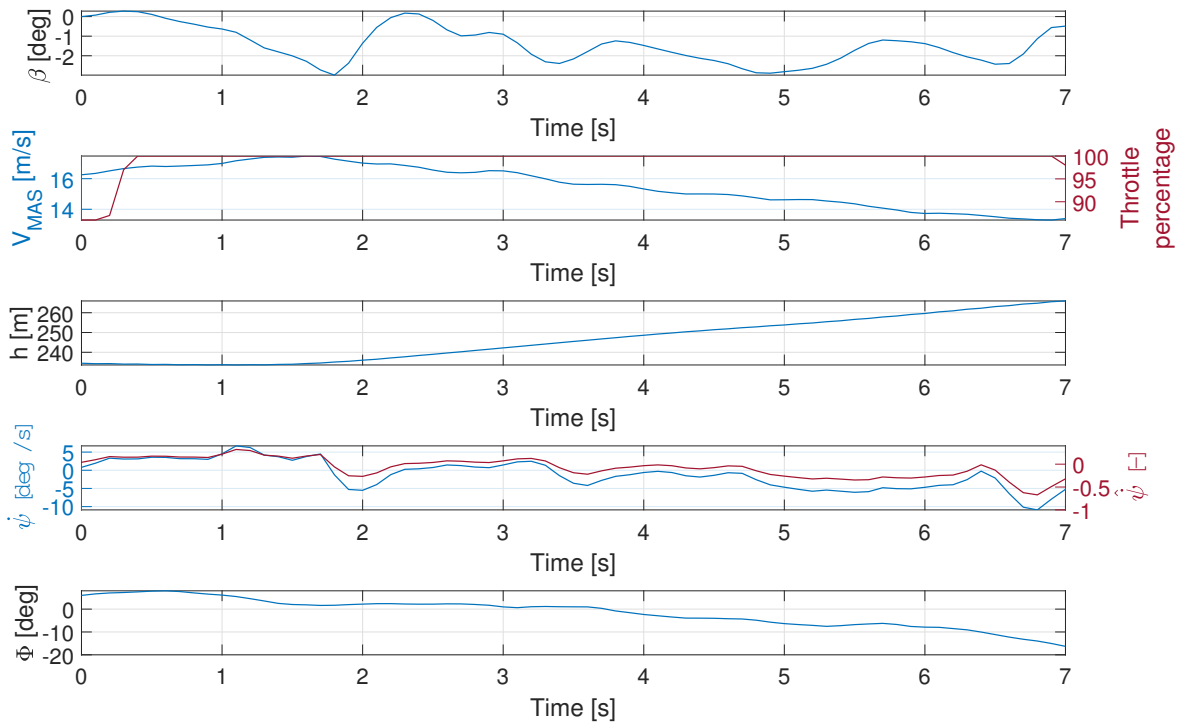


Fig. 9.11: M1/M6 inoperative, constant speed trial

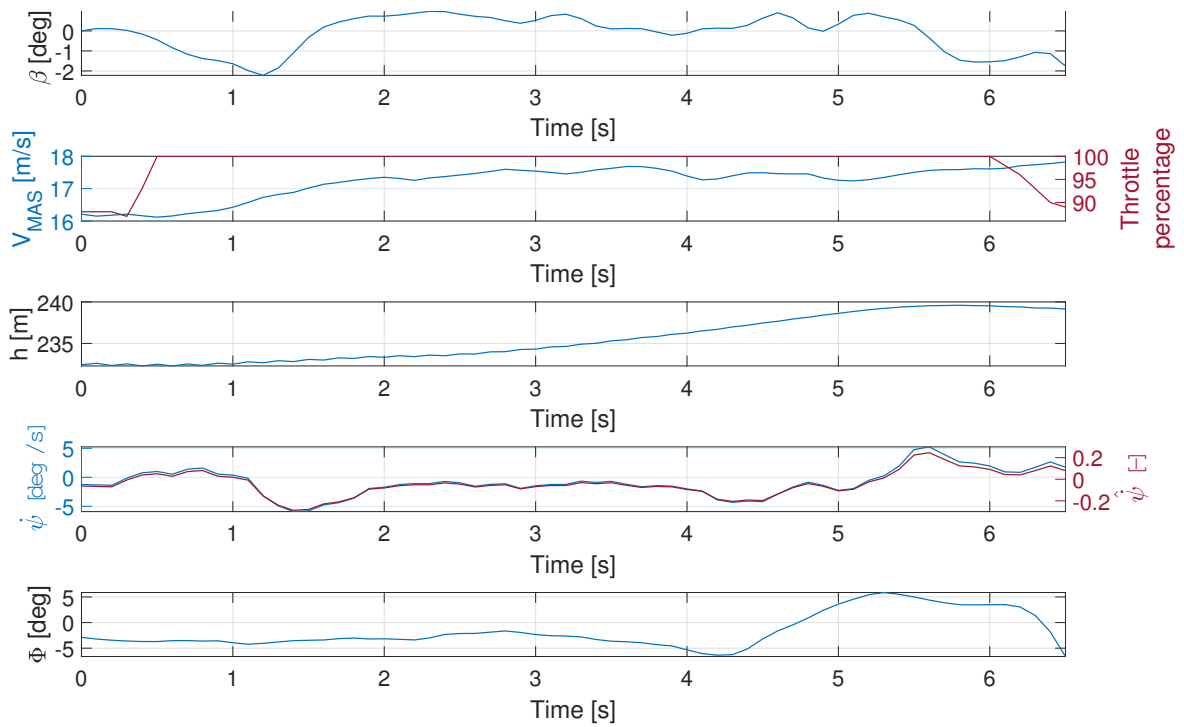


Fig. 9.12: M1/M6 inoperative, constant altitude trial

9.6.2 Motor #2 inoperative

Among the possible scenarios of OEMI conditions, the failure of EM #2 (or mirror EM #5) is on the paper the most detrimental to flight symmetry. This is evident when looking at the estimated yawing moment induced by residual thrust asymmetry, shown in Figure 7.16b. The condition is in fact less optimal than the corresponding case of *SE-OEMI-M3* (Figure 7.16c). Nevertheless, at true airspeed close to 15 m/s the behavior should be acceptable.

Guided by this hope, flight testing activity aimed to verify theoretical predictions. Once again, general feedback from the pilot was complemented by quantitative observations in constant speed and altitude FTT. In particular, flight handling seems slightly downgraded with respect to normal operations and *SE-OEMI-M1*, but the difference is very subtle. The scale model is still precisely controllable, even if thrust asymmetry is not always guaranteed, and the effects do change with speed. In fact, maximum asymmetry is experienced when imposing high thrust at low speed. The effects do not exceed what could be experienced in normal operation as a consequence of wind gusts. General behavior is thus satisfactory, with good likeness of single-engine normal mode in both straight and turning flight. More in detail, test points at high airspeed typically experienced a positive sideslip angle, whereas lower trim speed are related to negative SSA. This is consistent with the sign of predicted residual yawing moment available in Figure 7.16c. This behavior is also confirmed in turning flight at high regimes: the aircraft tends to skid when left turning, against the slip induced by right turning.

As for the numbers, maximum sideslip angle was always approximately 5 deg. This value is encouraging since comparable to that induced by SE normal simulation. As previously anticipated, the golden standard would have been always inducing a positive sideslip, which instead is disproved by the trials. Perturbations of bank angle and turn rate are restrained too, thus the working mode has pleasantly proven to provide a successful management of OEMI condition. This conclusion is supported by meaningful test points: Figure 9.13 is indicative of a trial at constant speed with high MAS, whereas Figure 9.14 is the dual case of constant altitude FTT at high MAS.

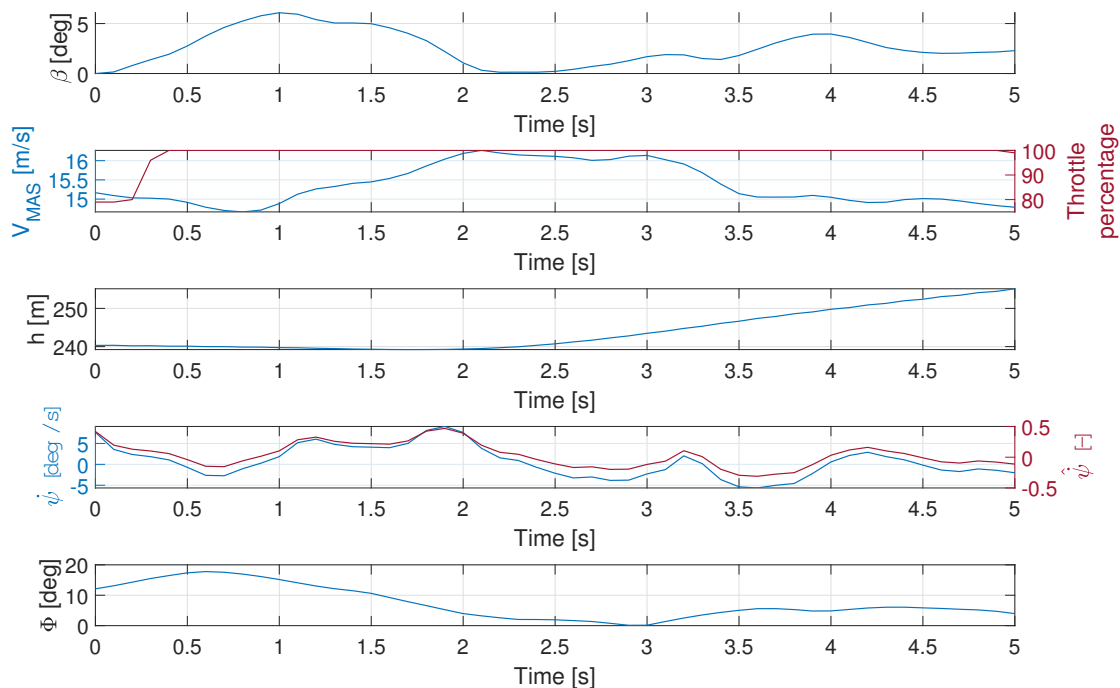


Fig. 9.13: M2 inoperative, constant speed trial

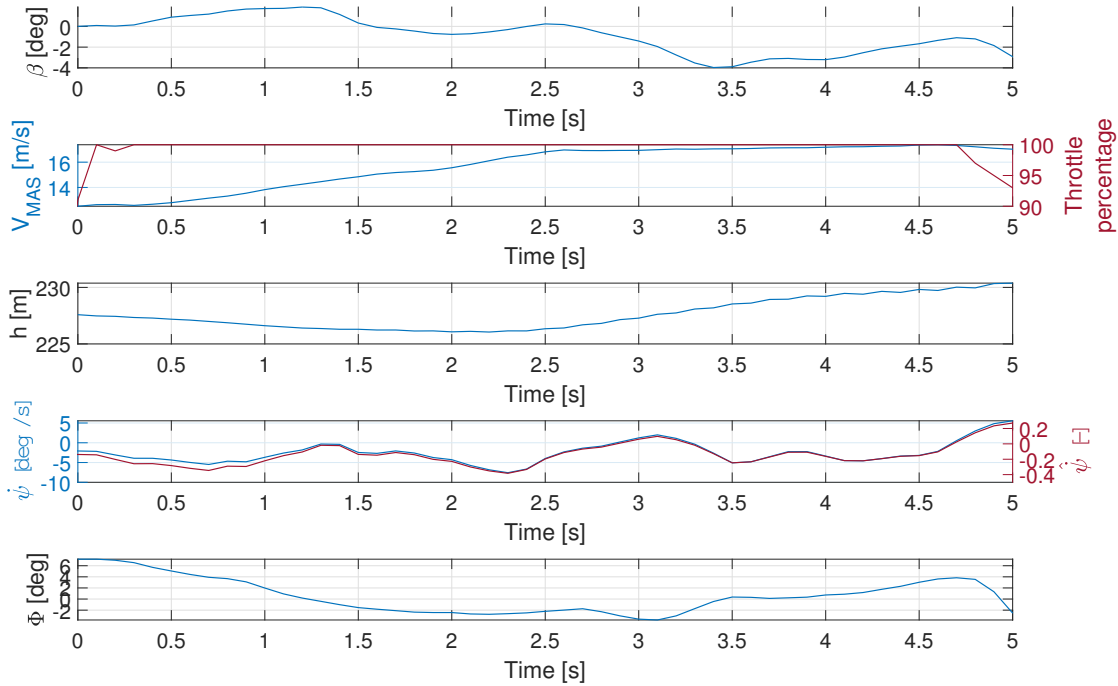


Fig. 9.14: M2 inoperative, constant altitude trial

9.6.3 Motor #3 inoperative

The condition of EM #3 (or mirror EM #4) inoperative represents the third possible scenario of OEMI simulation. In terms of effectiveness of thrust distribution among residual motors to recover flight symmetry, it should exhibit a better behavior than what is experienced in *SE-OEMI-M2*. In fact, as already stated, residual yawing moment is slightly lower, throughout the speed envelope. This translates into the expectation of a less pronounced sideslip from flight testing activity. This was the case, indeed: maximum β was always lower than 2 deg.

The tendency of induced β to be negative at low airspeed, as opposed to positive values at high trim speed is once again experienced, in analogy with predictions. As a side note, the confirmation of this trend gives credit to the prediction of overall yawing moment, based on the measurement of thrust of a single motor at different wind tunnel speeds. An account of OEMI testing is thus outlined in Table 9.5, whereas the cases of constant speed trial with high trim MAS and constant altitude starting from a low trim speed are respectively reported in figures 9.15 and 9.16.

EM inoperative	β [deg]
EM #1 & EM #6	0
EM #2	$\left\{ \begin{array}{l} < 5 \quad \text{MAS} > 12 \text{ m/s} \\ > -5 \quad \text{MAS} < 12 \text{ m/s} \end{array} \right.$
EM #3	$\left\{ \begin{array}{l} < 2 \quad \text{MAS} > 12 \text{ m/s} \\ > -2 \quad \text{MAS} < 12 \text{ m/s} \end{array} \right.$

Tab. 9.5: Account of sideslip variation in OEMI testing

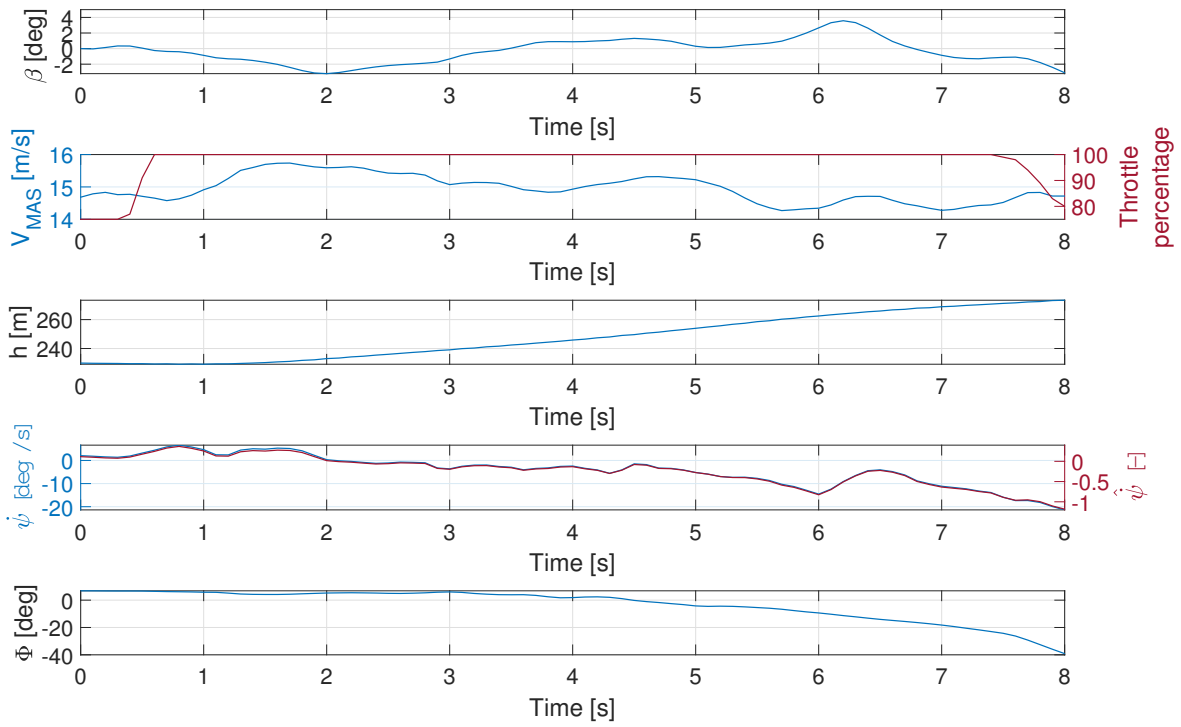


Fig. 9.15: M3 inoperative, constant speed trial

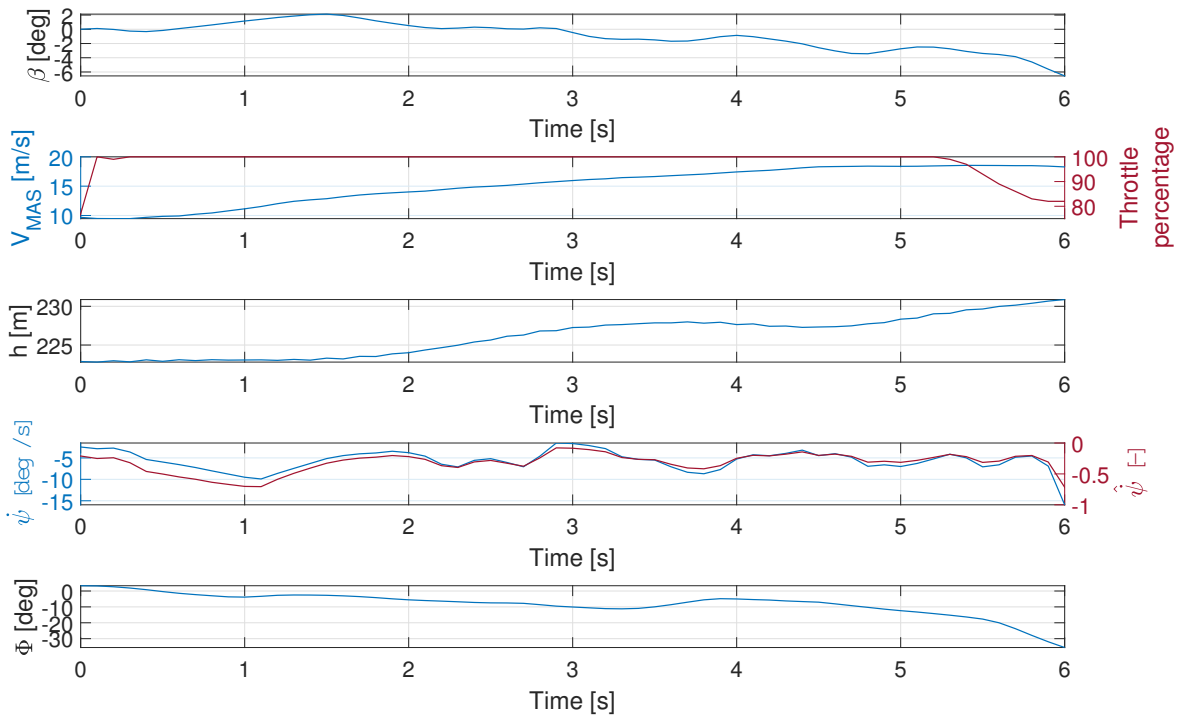


Fig. 9.16: M3 inoperative, constant altitude trial

9.7 One Engine Inoperative conditions

One engine inoperative simulation is an hazardous activity. The purpose is to replicate the behavior of a twin-engine, inducing a severe thrust asymmetry, with the pilot still capable of controlling the aircraft acting on control surfaces. Therefore, constant speed or altitude trials imposing maximum throttle, deployed in single-engine or OEMI simulations, are not compatible with this condition. In fact, rudder and ailerons are fixed in these FTTs. Then again, thrust asymmetry induced by electric motors could be tested with these techniques, but the trials would be too hazardous still due to complete non-actuation of control surfaces.

Indeed, OEI simulation was carried out in a very simple fashion: the pilot would try to flight in a straight line as much as possible through proper imposition of controls, with sufficient excess of power to climb. Post-processing quantifies the entity of these corrective actions, to verify if they are consistent with desired behavior, and assure that requirements from regulations are respected. This time, "Sideslip-reset method" implemented for sideslip angle estimation, compensating the effect of the wind, could not be applied due to non respect of assumptions ($\beta \neq 0$ at trim).

In the first instance only configuration with 3 motors on the same side inoperative was considered as a way to simulate OEI condition. In all fairness, it was not sufficiently studied prior to the activity and the outcome of the test, with even the aircraft entering in a spin was partially unexpected. The alternative strategy of imposing maximum possible thrust asymmetry through knob setting in *SE-norm* mode was exploited.

Taking a step back, a build-up approach was followed: several other configurations were tested, shutting down one or more electric motors, progressively increasing the magnitude of yawing moment induced by thrust asymmetry. A rough estimation of the yawing moment generated in the configurations tested is outlined in Table 9.6.

Mode	Yawing moment
EM #3 out	1x
EM #2 out	2x
EM #1 out	3x
EM #1 & EM #3 out	4x
3 EMs inoperative	6x

Tab. 9.6: Configurations for OEI simulation

This estimation is based as usual on the hypothesis that each motor is able to generate the same thrust and does not consider the effect of drag induced by electric motors in idle.

9.7.1 Three motors inoperative

The first configuration tested for OEI simulation consisted of the shut down of three electric motors on the port side (EM #1, #2, #3). As anticipated, it proved to induce a too severe asymmetric condition, even diverging into a spin. Only the taken precautions along with ability and responsiveness of the pilot saved the scale model from a catastrophic accident.

The feedback from the pilot testified the complete unpredictability of the behavior of the model, with the impossibility to fly on a straight line. Yaw-roll coupling increased severely the workload, requiring extensive use of ailerons, ultimately resulting in departure. Only at low power settings the aircraft was on the edge of controllability, whereas increasing throttle values compromised test conduction. This trend is confirmed by time histories of parameters of interest collected in figures 9.17 and 9.18.

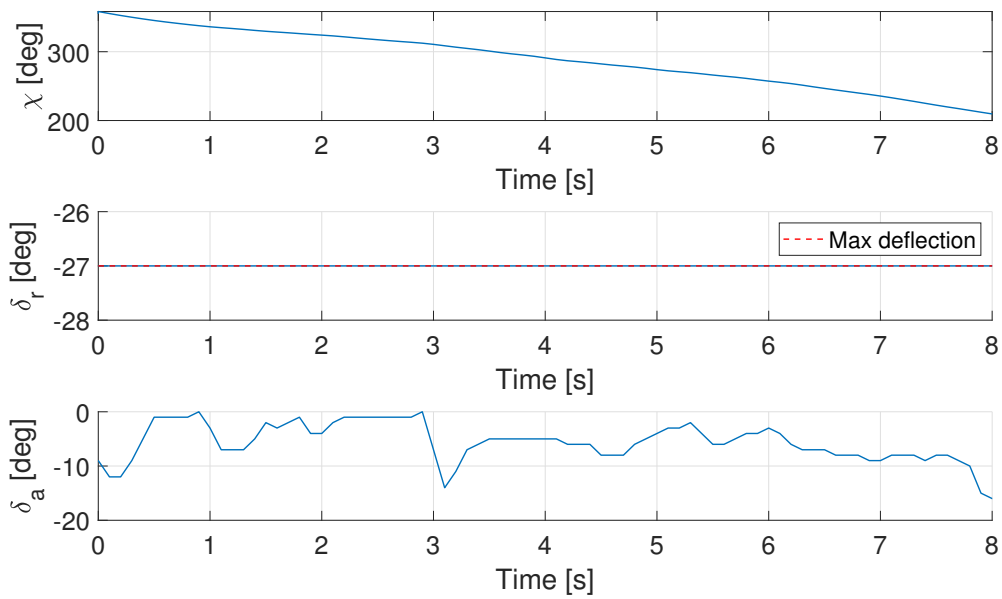


Fig. 9.17: 3 EMs inoperative - effect of controls on track angle

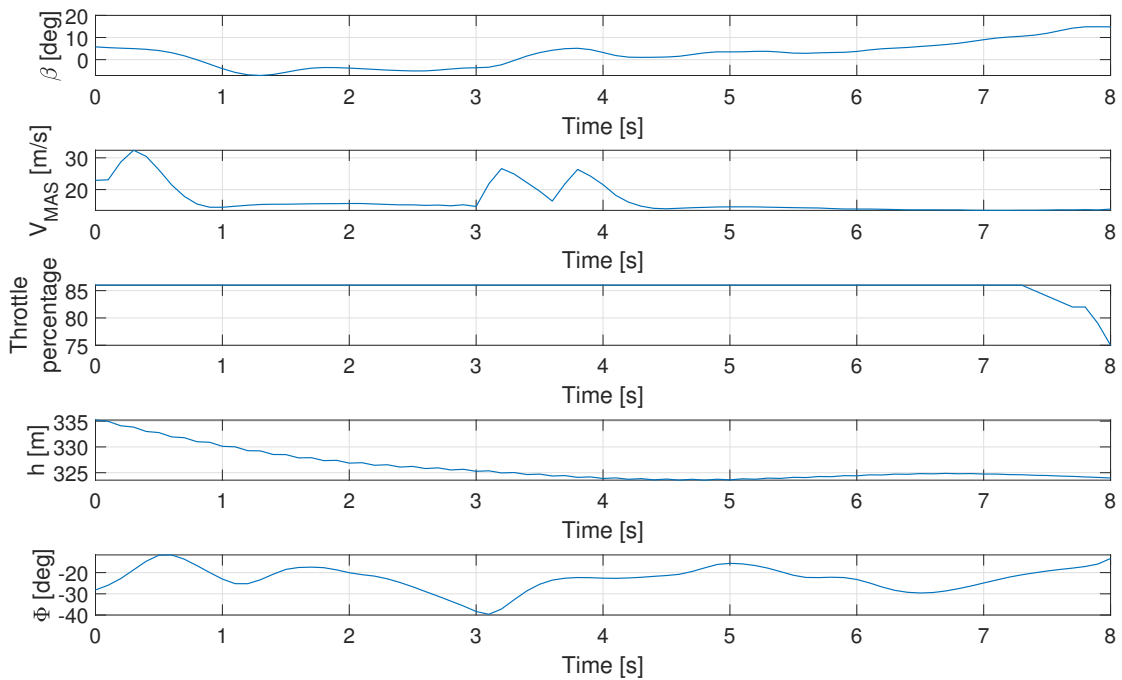


Fig. 9.18: 3 EMs inoperative - other quantities of interest

This specific trial is the proof of inability to maintain constant track angle at high throttle settings, even if applying maximum rudder deflection (negative as expected, to turn to the right) and flying with a severe sideslipped heading. The oscillation of airspeed is the demonstration of the lack of equilibrium. Moreover, a positive bank angle would be required to contrast left turning tendency, whereas this and other trials exhibit an unlikely negative bank angle, although imposing the prescribed corrective action with the ailerons (negative, to turn right). The aircraft is even descending, being unable to maintain level flight due to downgraded power. This list of deviations leaves no room for interpretation, exposing the necessity to look for alternatives for OEI simulation.

9.7.2 100% knob

Preliminary tests in single-engine mode restrained the setting of knob adjusting thrust asymmetry within approximately 40% of admissible excursion. In fact, higher values of this parameter was not compatible with single-engine simulation and affected general aircraft handling. Conversely, in the framework of OEI simulation, a more severe thrust asymmetry could well suit for the purpose. Therefore, an attempt with maximum knob setting was carried out, with results reported in figures 9.19 and 9.20.

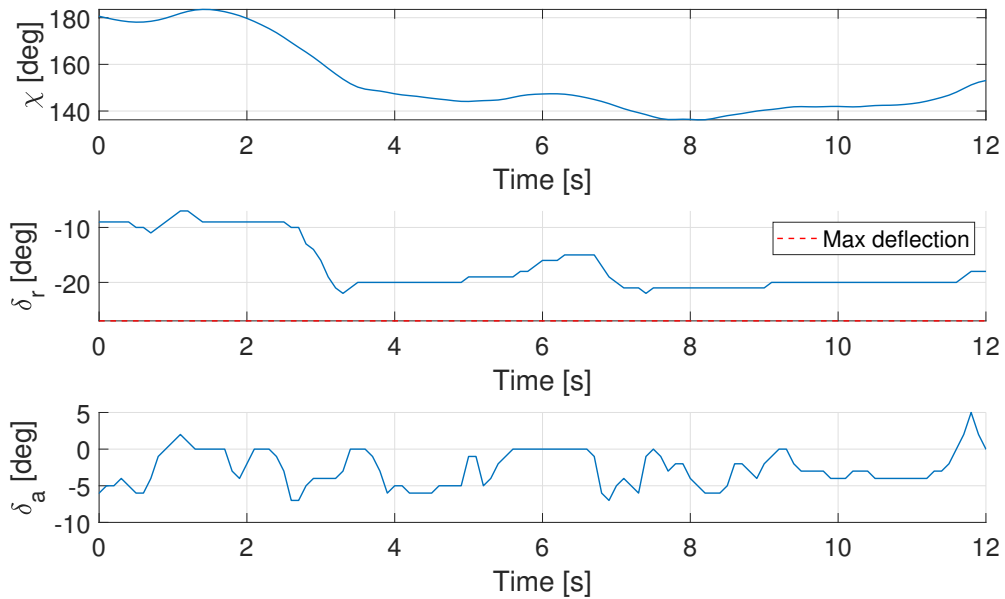


Fig. 9.19: 100% knob setting - effect of controls on track angle

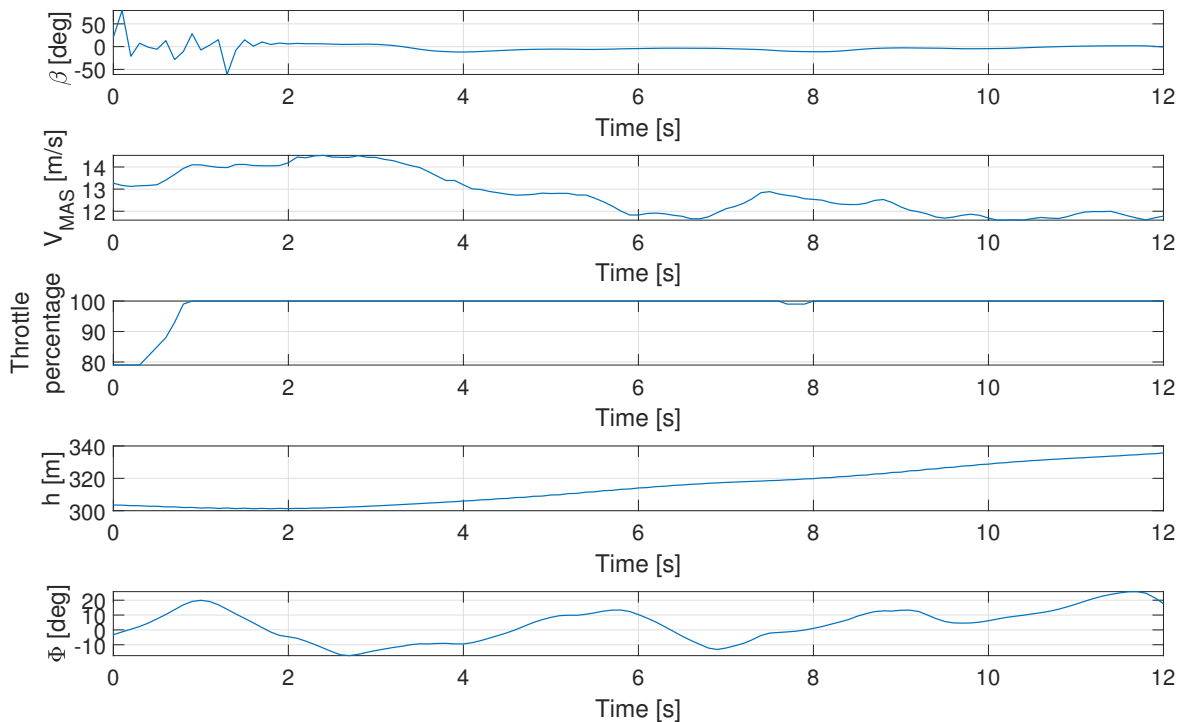


Fig. 9.20: 100% knob setting - other quantities of interest

The results exhibit a more gentle behavior with respect to simulation with 3 EMs inoperative on the same side. The aircraft could almost proceed with constant track angle (with the exception of the time instant immediately after maximum throttle imposition), with also a less intense use of rudder control. Equilibrium could be achieved, with bank angle still widely exceeding indicative limit value of 5 deg. Climb capability was instead guaranteed, as a consequence of overall power installed not too much dissimilar to that of normal operations. This is evident in the forsaken increase of altitude testified by Figure 9.20.

Main deterrent to this solution is that although obtaining similar effects to the ones affecting a twin engine with OEI, the causes are extremely different: no motor actually stops propelling in SE mode and available power is not sufficiently penalized with respect to normal mode. This solution was thus discarded, whereas simpler alternatives, such as turning off one or more motors, could easily reproduce similar conditions with also the same causality.

9.7.3 Motor #3 out

After the extremely demanding conditions experienced in first attempts for OEI simulation, more conservative solutions were tested. The most cautious one consisted of turning off EM #3, in order to minimize the yawing moment induced by thrust asymmetry (without reprogramming the control of other electric motors as done in related OEMI simulation). In fact, the most inboard motor subtends an arm that is half of the central one and one third of the most outboard. Therefore, this trial served as baseline to characterize the phenomenon.

As expected, the effect of just shutting down the most inboard motor did not succeed in imposition of a yawing moment worthy of One Engine Inoperative condition. The aircraft results able to proceed in straight flight, just requiring a minimal imposition of directional control. In particular, rudder deflection reached 10 deg, far from the available 27 deg. Besides, ailerons are almost kept centered, with bank angle never exceeding 10 deg. Pilot workload increase is minimal and any pilot, even SE rated, could contrast the thrust asymmetry.

These considerations can be well summoned by time histories of one of the trials, available in figures 9.21 and 9.22.

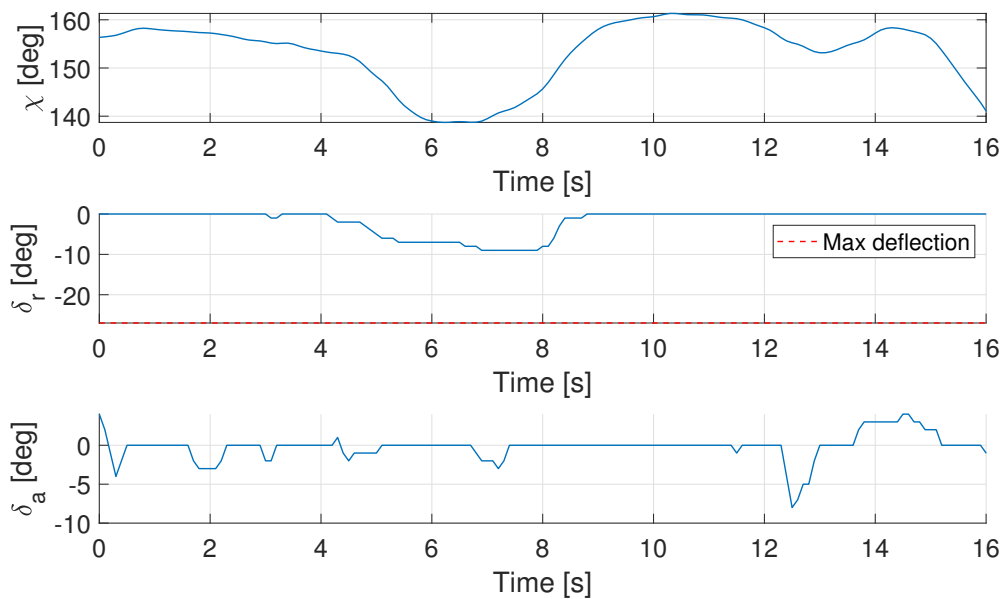


Fig. 9.21: EM3 inoperative - effect of controls on track angle

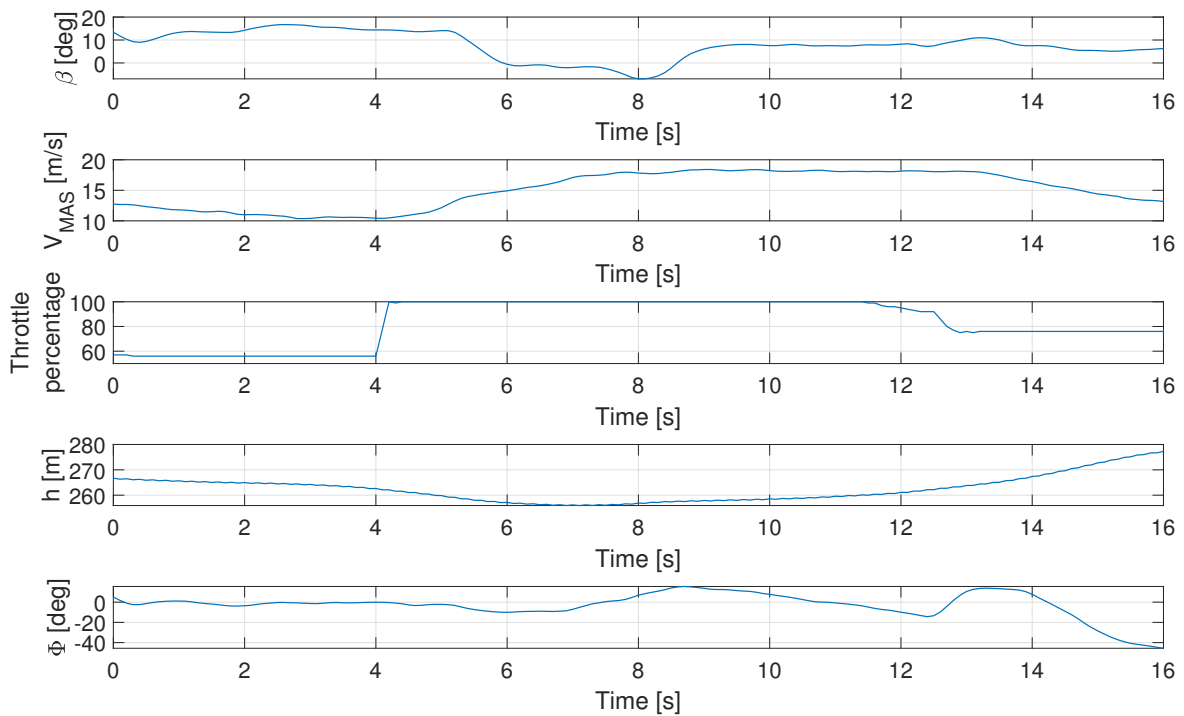


Fig. 9.22: EM3 inoperative - other quantities of interest

9.7.4 Motor #2 out

Second iteration of motors shut-down for OEI simulation implemented the case of EM #2 inoperative. This condition should imply twice the effect of turning down most inboard motor, described in Section 9.7.3. Besides, other considerations related to interactions of the airflow with the fuselage and control surfaces play a role. This presumed inconsistency is validated by FT results. In fact, the RC model exhibited once again a symmetric behavior, although having doubled induced yawing moment, on paper.

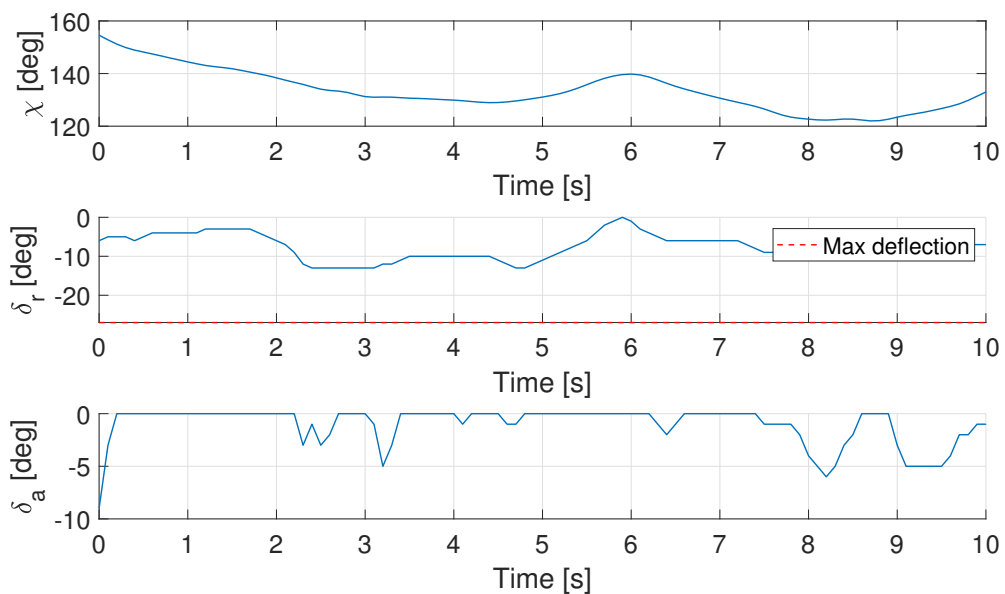


Fig. 9.23: EM #2 inoperative - effect of controls on track angle

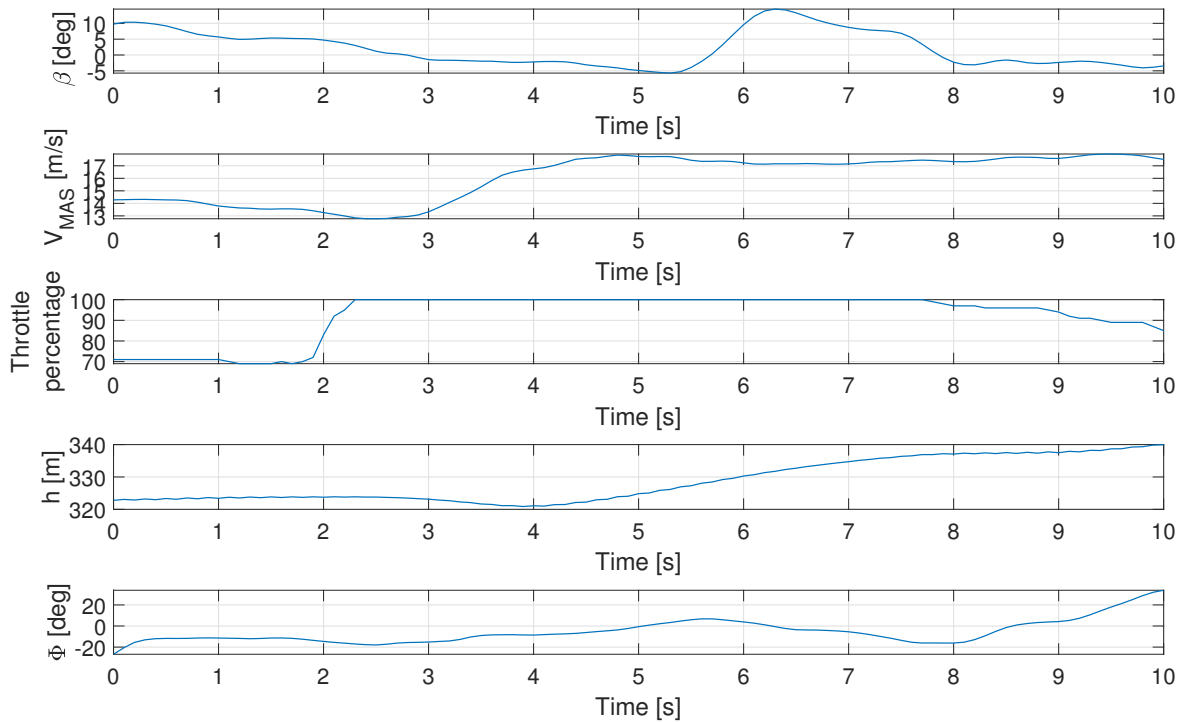


Fig. 9.24: EM #2 inoperative - other quantities of interest

On the contrary, time histories of parameters of interest, reported in figures 9.23 and 9.24, do not confirm the expected discrepancy from the snapshot of same trial with EM #3 inoperative (figures 9.21 and 9.22).

Once again, straight flight was too easily achieved, with just a limited increase in rudder deflection with respect to previous case, still far from maximum imposition. Also lateral dynamics is not remarkably affected. A more pronounced deviation is instead sensed in turning flight, thus requiring greater situational awareness of the pilot in the execution of maneuvers. Nevertheless, the workload experienced is still far from a suitable description of OEI case.

Indeed, an average condition among the ones previously mentioned seemed the best alternative, halfway between 3 EMs inoperative and the last two attempts with alternatively EM #3 or EM #2 turned-off.

9.7.5 Motor #1 out

The case of failure of most outboard electric motor (EM #1 or EM #6) is the most demanding in terms of induced yawing moment unbalance. As a consequence, higher rudder and aileron deflections were expected with respect to the cases of EM #2 or EM #3 inoperative. This was indeed confirmed by flight test trials, whose typical behavior is well represented by time histories reported in figures 9.25 and 9.26.

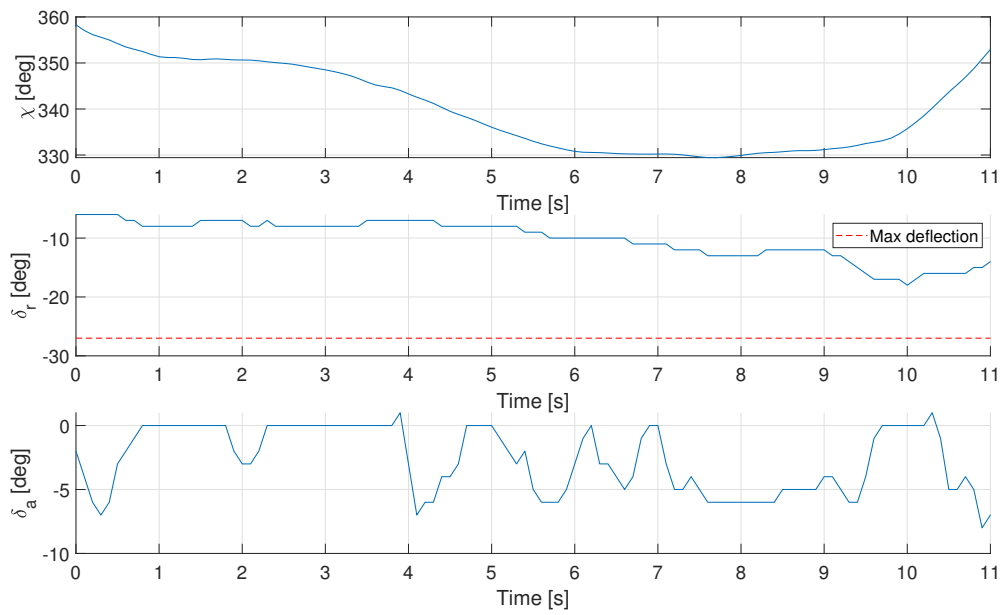


Fig. 9.25: EM #1 inoperative - effect of controls on track angle

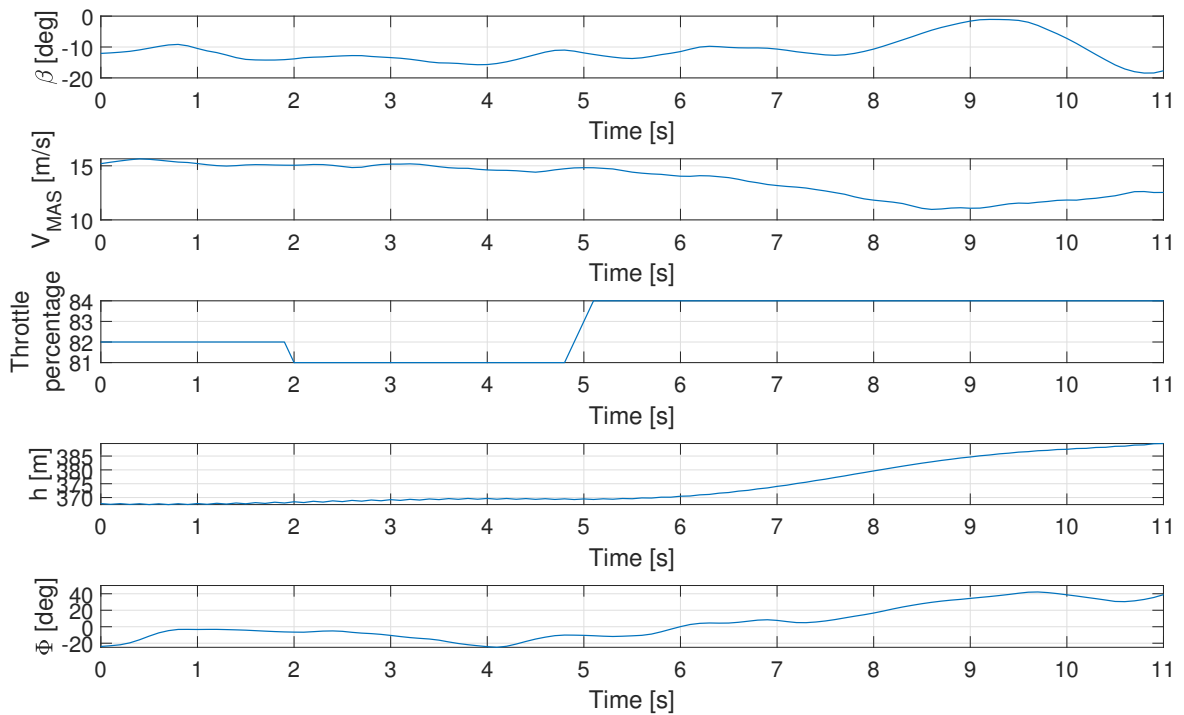


Fig. 9.26: EM #1 inoperative - other quantities of interest

Required rudder input is pronounced and close to maximum available deflection. The condition also requires a more demanding effort to actuate the ailerons, both in terms of maximum deflection applied and frequency of inputs. This also translates into a greater bank angle, anyway confined to reasonable values. Climb capability is not surprisingly assured. All in all, these premises are an excellent basis to select this configuration to simulate the behavior of a twin with one engine inoperative.

9.7.6 Motors #1 & #3 out

Despite shut down of EM #1 seemed the best compromise, a further and final attempt was made to retrieve OEI condition. The tested configuration exploited EM #1 and EM #3 simultaneous idling. Experienced condition is once again similar to the imposition of three EMs on the same side (Section 9.7.1). In fact, maximum rudder deflection was required, without succeeding in keeping constant track angle. Moreover, despite the remarkable aileron deflection, resulting roll angle is negative, to demonstrate no equilibrium could be reached. The only upside is the climbing capability ensured even with two electric motors inoperative.

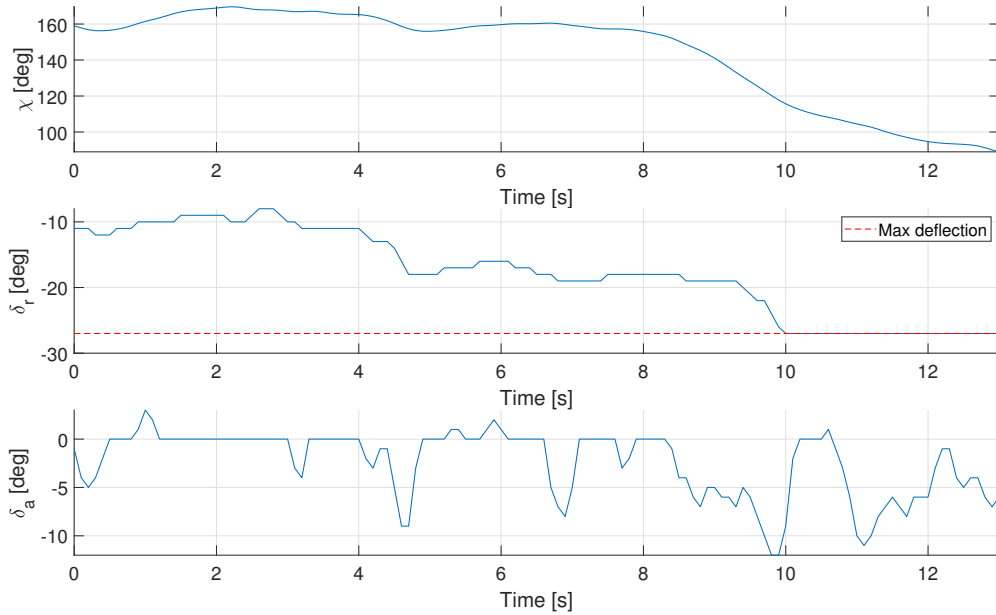


Fig. 9.27: EM #1 & EM #3 inoperative - effect of controls on track angle

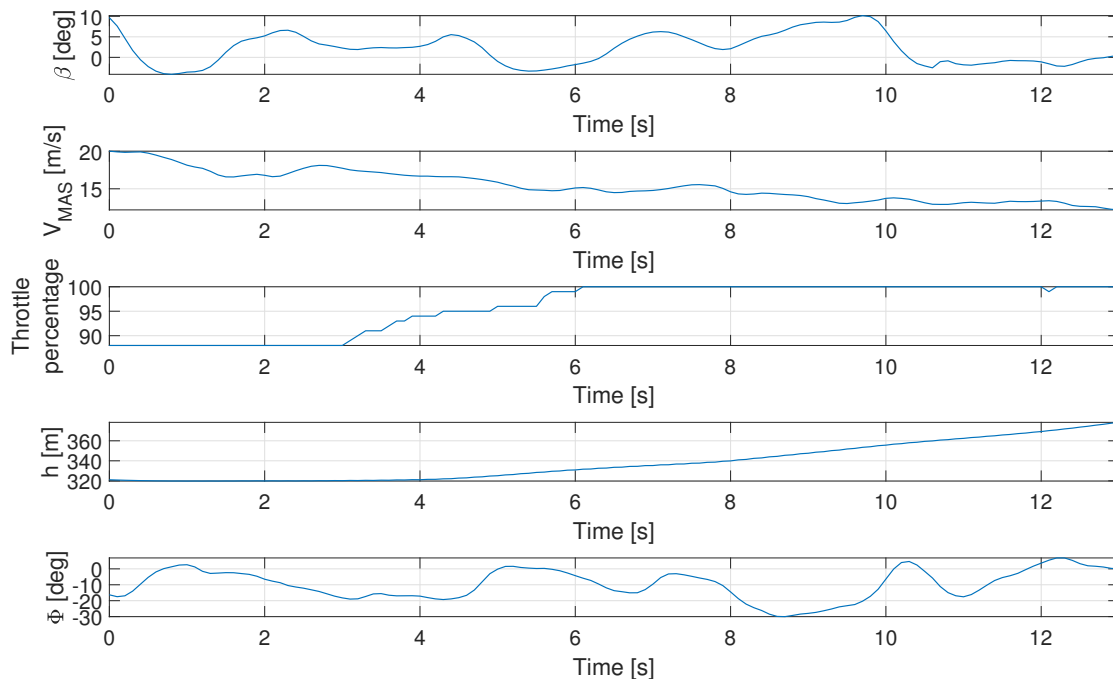


Fig. 9.28: EM #1 & EM #3 inoperative - other quantities of interest

This test backs-up the choice to **exploit EM #1 inoperative to simulate OEI condition**. This is also the condition that better embodies the prescriptions from the regulations. In fact, EASA CS-23 [29] specifies "critical engine inoperative" should be considered to assess the capability to withstand OEI condition. The case of EM #1 inoperative represents the forsaken configuration, indeed.

Main results of all experimented configurations for OEI simulation are collected in Table 9.7.

Mode	Straight flight	Rudder	Ailerons	Bank
3 EMs inoperative	No	Full (27 deg)	12 deg	No equilibrium
100% knob	Yes	20 deg	5 deg	20 deg
EM #3 out	Yes	10 deg	2 deg	10 deg
EM #2 out	Yes	12 deg	4 deg	10 deg
EM #1 out	Yes	15 deg	6 deg	20 deg
EM #1 & EM #3 out	No	Full (27 deg)	12 deg	No equilibrium

Tab. 9.7: Results of OEI simulation testing

9.8 Aerodynamics and flight dynamics characterization

Aircraft aerodynamics characterization flight tests aimed to determine lift and drag coefficients. Unfortunately, most of the executed FTT failed to return desired parameters, as forecast.

The "Rollercoaster" FTT has been executed with several attempts, but a smooth execution of the maneuver was really difficult, given the aircraft fast dynamics. Moreover, great uncertainties in speed and altitude variation in the various trial points increased the overall difficulty, preventing from the gathering of suitable data. Same considerations apply to "Sawtooth glide" FTT, where constant rate of descent could not be maintained. This, combined with the impossibility to accurately determine track airspeed during the test and the airspace limitations, led to the discard of this FTT after some trials.

The modified "LAD" initially gave promising results. Despite the difficulties in trimming the *SwitchMaster* at maximum speed, the initially determined relation between lift coefficient and angle of attack seemed to be consistent with the one coming from wind tunnel testing. Nevertheless, the drag polar returned is not acceptable, with non-homogeneously distributed points and even some negative drag coefficients. This is probably due to altitude variations (even if stabilized mode has been exploited) and propeller-wing interaction. Therefore, also the modified "Level-Acceleration-Decelerations" flight test technique has been rejected for drag polar determination.

Conversely, lift coefficient estimation seems reasonable, but results are omitted in this outline since consistent with the ones obtained with "trim shots" (once again everything is documented in Andrea Santeramo's thesis [4]), the only technique giving an acceptable estimation of drag. This method starts from trim equilibrium at a given speed, and retrieves lift and drag coefficients from forces and power equilibrium equations. The "trim shots" were executed both in manual flight mode and stabilized flight mode. Starting from the recorded flight data, power applied to electric motors is available from the values of current and voltage related to each ESC. Available power can then be estimated leveraging both propulsive and mechanical efficiency.

Data analysis is part of Andrea Santeramo's master's thesis, and here only shortly displayed. Mechanical efficiency (ratio between electric motor shaft power and electrical power required)

is reported on electric motors producer datasheet, while propulsive efficiency (ratio between available power and electric motor shaft power) is output of wind tunnel testing of the propulsive unit. This latter is computed as a function of the propeller advance ratio, namely:

$$\eta_P = J \cdot \frac{C_T}{C_P} \quad , \quad (9.2)$$

$$J = \frac{V_\infty}{n \cdot D} \quad . \quad (9.3)$$

Mechanical and propulsive efficiency are reported in Figure 9.29.

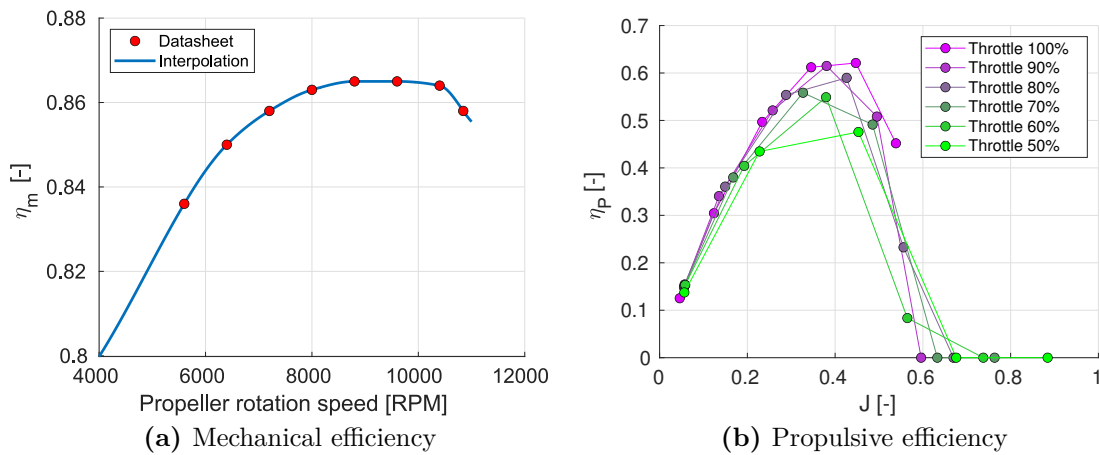


Fig. 9.29: Electric motors mechanical efficiency and propulsive efficiency

Along with the already discussed problems experienced in conduction of the different FTT, drag polar curve determination is strongly influenced by the propeller blowing, typical of the DEP architecture. In a conventional airplane, lift and drag are functions of speed and AOA. In a DEP aircraft, throttle setpoint is a third and equally important variable. This is also shown in the wind tunnel test campaign outputs, in which the lift coefficient curve is strongly influenced by motor setpoint at constant airspeed. The problem when actually flying the aircraft is that not all combinations can be tested, but just the ones enforcing equilibrium (trim). Therefore, it is not possible to draw lift and drag polar curves for every throttle and airspeed settings as was done in wind tunnel testing campaign.

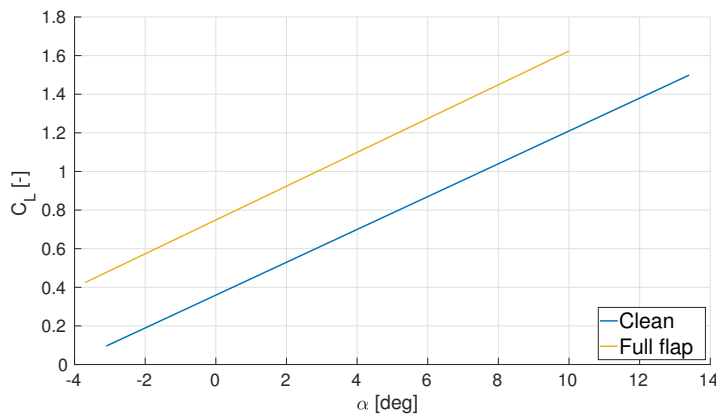


Fig. 9.30: C_L - α of trim shots test

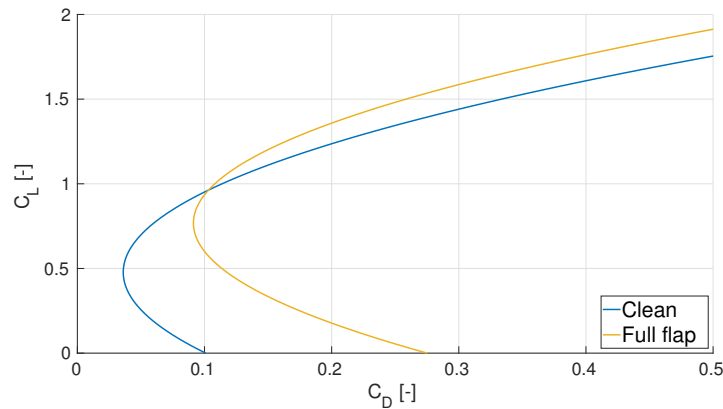


Fig. 9.31: Polar curves of trim shots test

Lift curves reported in Figure 9.30 are referred to clean and full-flap configurations. They are obtained with first order approximation, whereas drag polar curves in Figure 9.31 are of parabolic type. Only trim shots enforcing steady conditions were considered. Extra test points in full-flap configuration at high AOA delivered outstanding results. Clearly, this is an unstable condition. However, it should be noted that thanks to the thrust of the propellers and the wing blowing effect it is possible to maintain a non-stall and controllable condition at 6 m/s, which is below the power-off stall airspeed, verified to be 8 m/s. This result is the ultimate proof of the aerodynamic performance enhancement offered by DEP. The only drawback is that it is difficult to hold such an upset attitude, with the additional difficulties experienced in the flare (outlined in Section 8.3). Nevertheless, this extremely remarkable results are collected in Table 9.8, along with the other performance indicators.

Configuration	Max C_L [-]	Max α [deg]	$C_{L\alpha}$ [rad^{-1}]	C_{D0} [-]	$C_{D_{min}}$ [-]
Clean	1.9	13.2	4.87	0.101	0.036
Full-flap	3.30	16	5.02	0.275	0.091

Tab. 9.8: High AOA trim shots in full flap configuration

For what concerns aircraft flight dynamics, results of maneuvers for maximum angular rates determination are summoned in Table 9.9.

Component	Test maneuver	Value [rad/s]
Roll	Tonneau	4
	Pull-up	1
Pitch	Push-over	2
	Schneider turn	1.5
	Loop	2.5
Yaw	Flat turn	0.5

Tab. 9.9: Body angular rates determination

9.9 Yaw control

Along with operating modes concurring to the validation of patent submission, propulsive yaw control modes were tested. Although being assigned low priority, these activities managed to deliver a first rudimentary insight in the potential of propulsive yaw control.

Both strategies outlined in Section 7.3.7 were tested:

- flat turn achieved with thrust asymmetry imposed through asymmetry knob;
- automatic turn coordination in which asymmetry knob channel is mixed with aileron channel.

The purpose was to evaluate feasibility of both strategies at a preliminary stage, without having a proper target to be verified in data analysis. Encouraged by positive results of current activity, future research will presumably deepen the knowledge and characterization of propulsive yaw control.

9.9.1 Flat turn with thrust asymmetry

Yaw control was tested trying to complete a flat turn without imposition of neither aileron nor rudder. It is worth mentioning that flat turns are unconventional and so untried for the test pilot. Main novelty is related to complete suppression of lateral control, substituted with the properly mapped asymmetry knob, inducing the condition of thrust asymmetry described by Eq. (7.10). In particular, the knob in the middle position corresponds to an output of approximately 50%. Right turn instead is performed with the output at 100%, whereas left turn is on the opposite value of asymmetry knob of 0%.

Several attempts verified the aircraft can turn according to predictions, with a safe and unsurprising behavior. Omission of aileron control was initially counter-intuitive, but the fact the pilot was not accustomed to flat turns is to blame. In fact, FTP had the spontaneous tendency towards actuating ailerons to contrast the turn, to keep the wings flat, which was actually not necessary. By the way, bank is always minimal.

An example of flat turn is highlighted in Figure 9.32, showing the trajectory of the aircraft, with time histories of most relevant parameters reported in Figure 9.33.

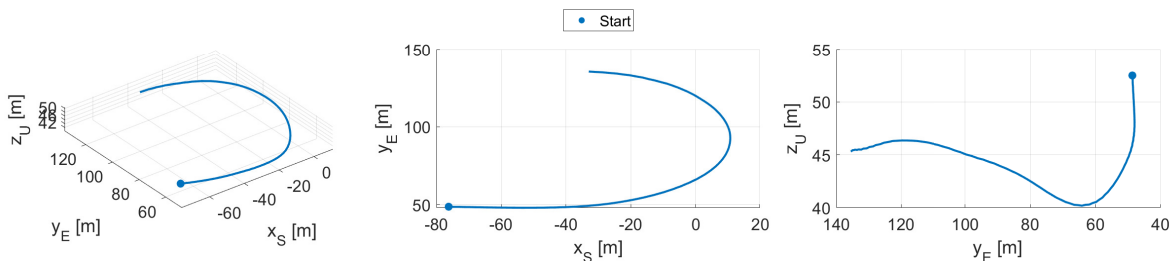


Fig. 9.32: Trajectory in flat turn

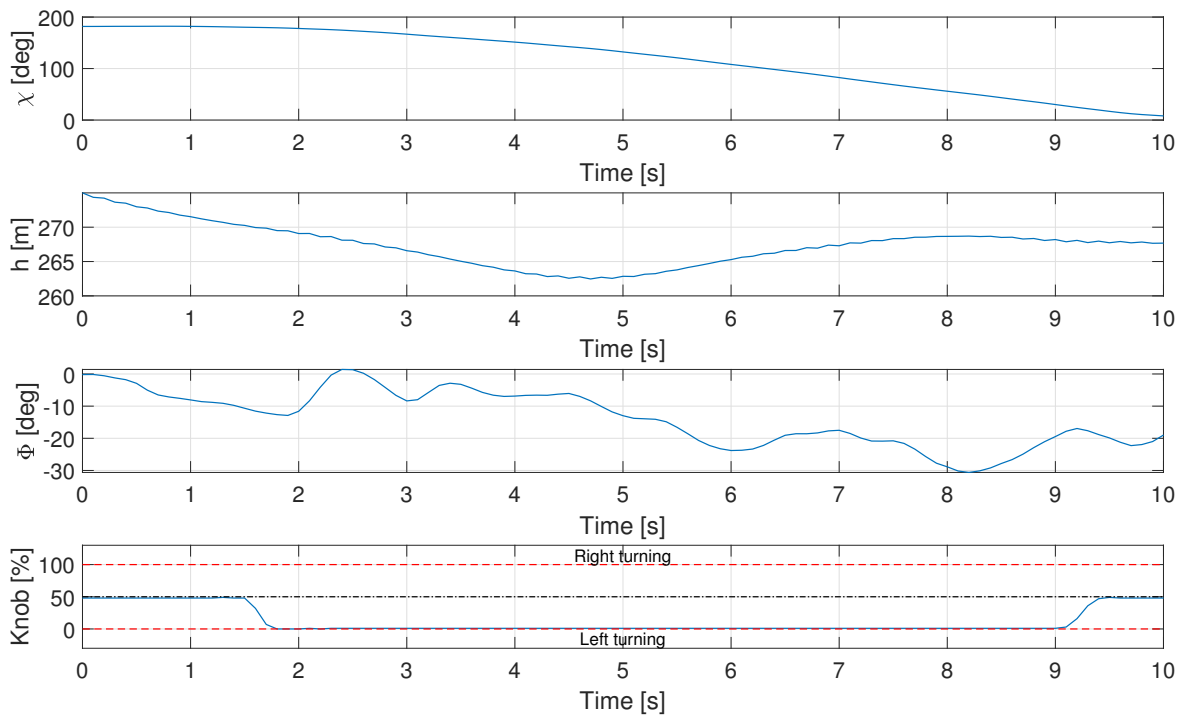


Fig. 9.33: Time histories of flat turn

Turn radius resulted the most important factor of a flat turn. The turn under consideration was willingly executed with a small turn radius, to cope with limitations of the available airspace. It has been shown that a tight turn still requires actuation of ailerons and elevator to achieve desired rate. Other attempts were made increasing turn radius (only partial turns could be made due to limitations), with the aircraft effectively completing the maneuver, while the pilot was almost a motionless spectator. This is encouraging, in the prospective of the exploitation of this solution on a commercial airliner. On this application, flat turn would be gentle of course, maximizing the benefits of this feature.

The aircraft geometry and configuration is another important factor. Preliminary feedbacks with such a conventional configuration with high wing were positive. Testing of other aircraft categories would be utmost attractive. In case flat turn would become the standard, control surfaces acting on lateral-directional dynamics could be probably downsized, with a remarkable impact on performance.

9.9.2 Turn coordination with thrust asymmetry

Encouraged by the good response of flat turn attempts, turn coordination with propulsive yaw control was tested. The objective was to correct the sideslip induced in a turn. Such effect is described in Figure 9.34 by time history of a turn in which no other input than aileron deflection is applied.

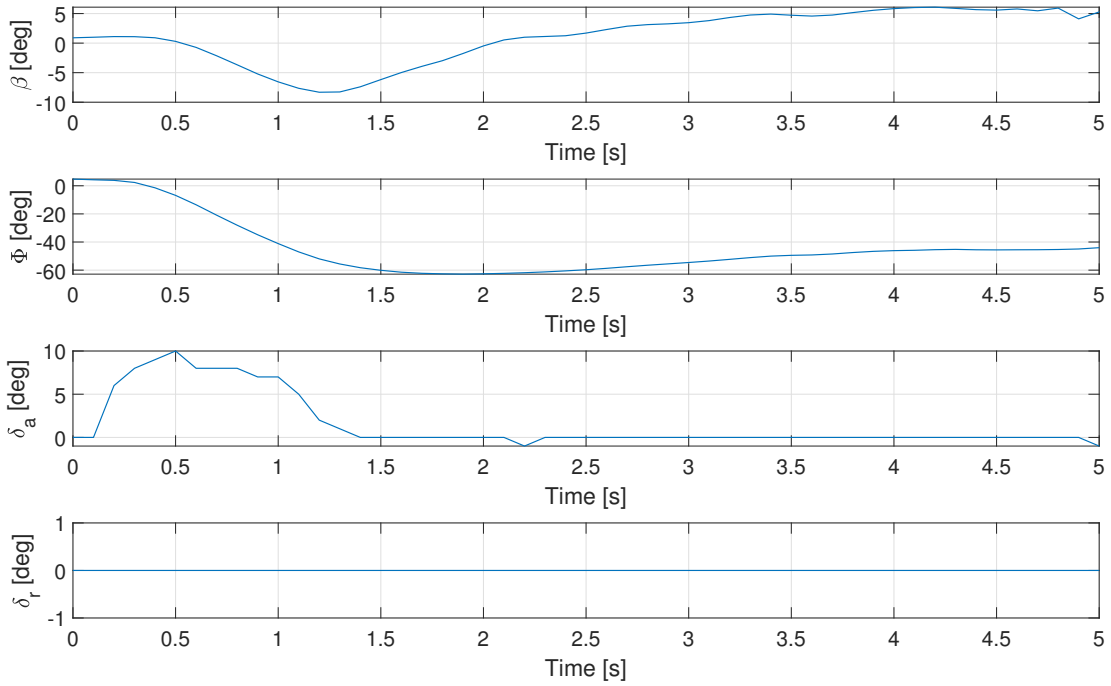


Fig. 9.34: Non-coordinated turn

Conversely, turn coordination is typically obtained enhancing a deflection of the rudder to avoid the slip, as applied in the maneuver described in Figure 9.35, showing sideslip limitation, with values well below 10 deg exceeded in Figure 9.34.

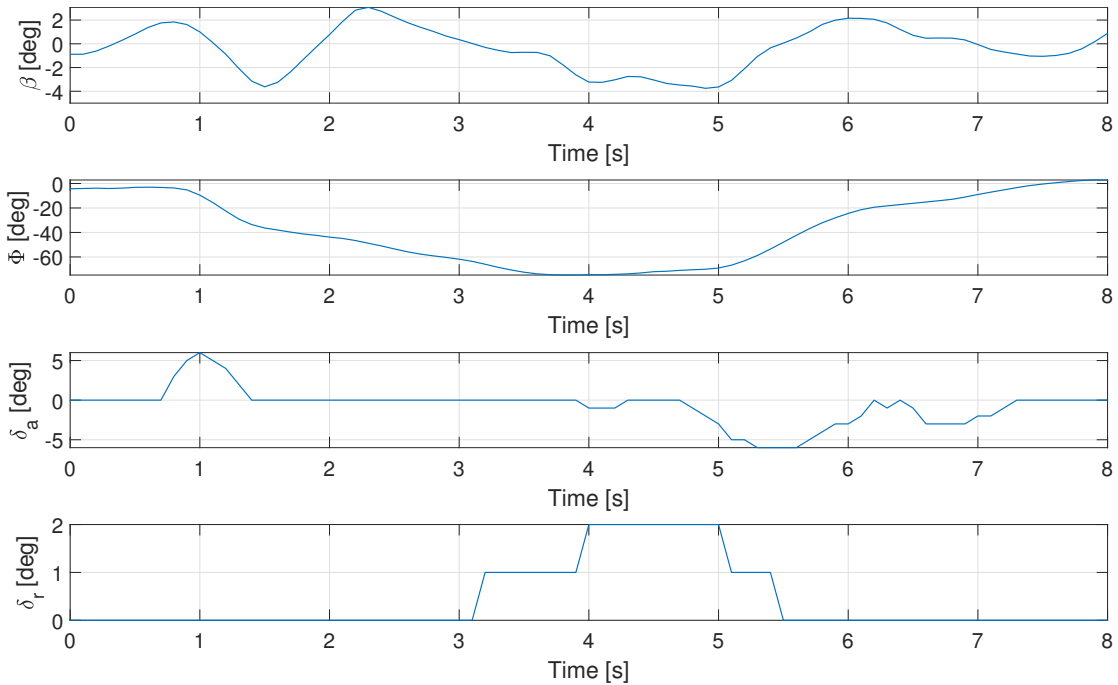


Fig. 9.35: Turn coordinated with the rudder

In this framework, rudder deflection is replaced with thrust asymmetry. Moreover, asymmetry knob is not actuated any longer, being automatically interfaced with aileron control: the setpoints of electric motors change to counteract adverse yawing moment and follow the

direction of the turn induced by ailerons. Forsaken behavior is achieved adding to asymmetry knob channel the information related to the position of the aileron control, multiplied by a gain. This gain was initially kept low to verify mixing sign was correct. Due to an unknown cause, the value of asymmetry knob not applying any action changes when activating turn coordination. The change is very restrained, passing from an output of 49% to 48%, but anyway was considered to evaluate the effect of thrust asymmetry. Figure 9.36 is referred to a trial in which the gain was at 40%, meaning for example in a right turn a positive aileron deflection of 8 degrees corresponds to a knob setting of 54%. The effectiveness of turn coordination can be evaluated from time history of estimated sideslip angle (Figure 9.37).

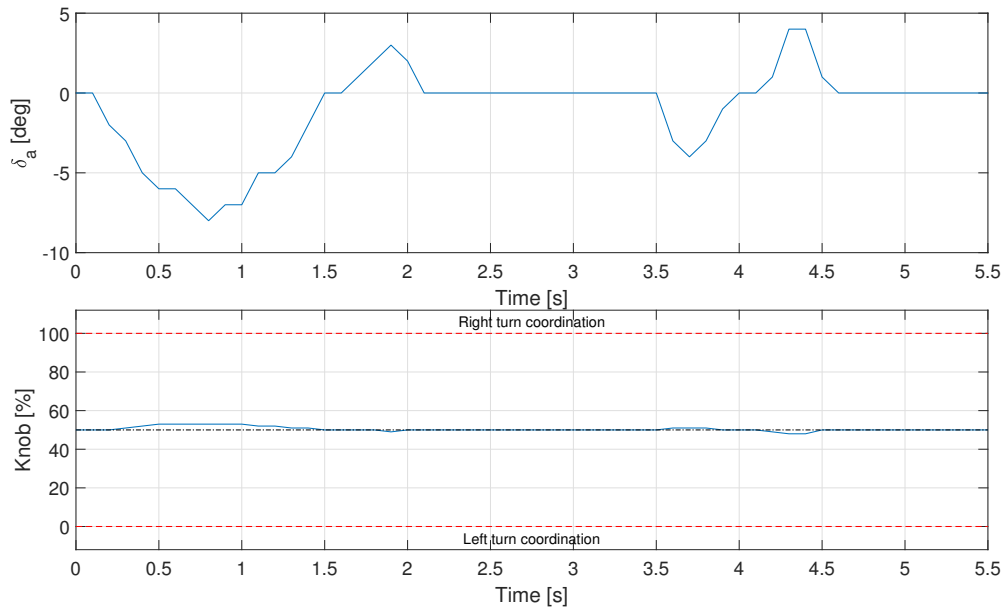


Fig. 9.36: Time histories of controls in thrust-coordinated turn with 40% gain

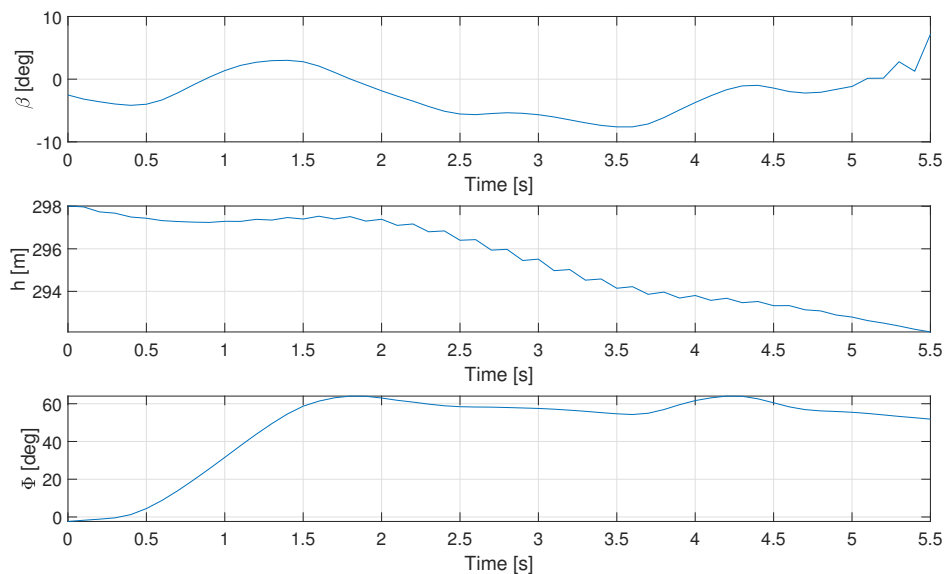


Fig. 9.37: Effect of thrust-coordinated turn on parameters of interest with 40% gain

Through trial-and-error much better behavior was achieved increasing the coupling. As an

example, figures 9.38 and 9.39 report results of a trial enforcing a gain of 80%, twice the initial value.

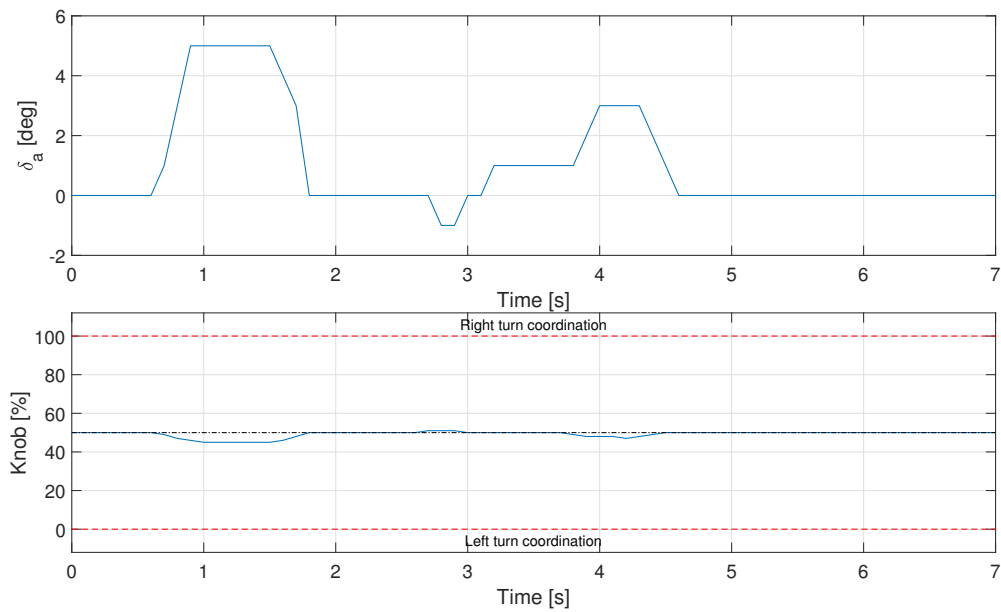


Fig. 9.38: Time histories of controls in thrust-coordinated turn with 80% gain

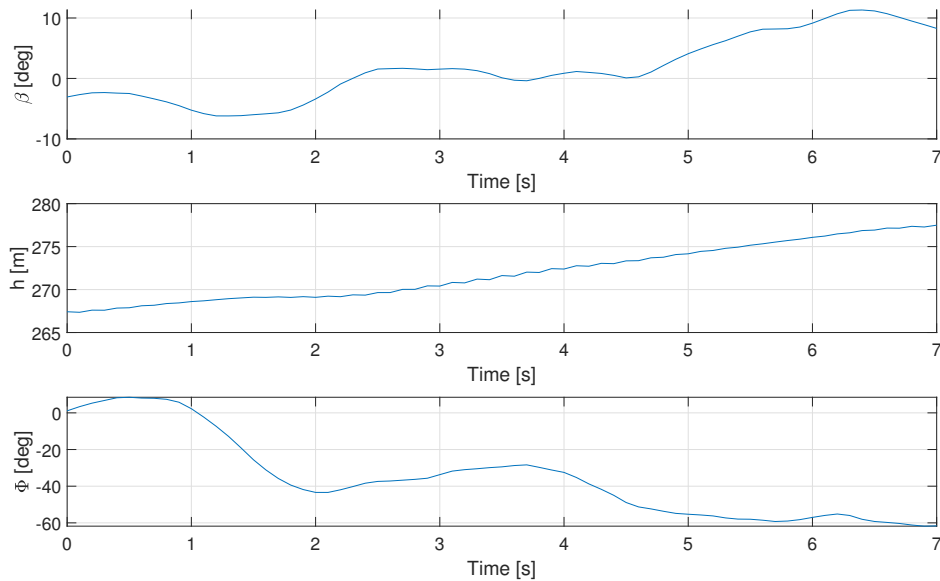


Fig. 9.39: Effect of thrust-coordinated turn on parameters of interest with 80% gain

All in all, the primary objective that inspired the implementation of these modes was accomplished. Future developments will delve into details of the very promising feature of yaw control.

9.10 Analysis of FTT differences between a GA aircraft and a RC aircraft

At the end of the campaign it is possible to identify common trends in the behavior of the RC scale model, and differences in flight conduction and FTT execution with respect to a full-scale General Aviation airplane. The pilot of *SwitchMaster* is also in possess of a Private Pilot License (PPL) for GA airplanes, and was indeed the FTP in command in the real aircraft test flight illustrated in Section 5.7.2. Even if of limited experience, and with incomparable skills with respect to those of a professional pilot or even more a flight test pilot, his critical sensibility and reported perceptions have been taken into consideration.

Several differences were perceived, even if the *SwitchMaster* airframe configuration is similar to many GA aircraft (i.e. the well-known Cessna 172). First of all, differences in wing loading, specific excess of power and inertial properties have a big impact on flight conduction. Every maneuver with the *SwitchMaster* is fast and rapid. Maximum rates are high, and rotations starts as soon as the command is applied, without any lag (at least according to what is perceived). The RC aircraft tends to remain in the last prescribed attitude, while a GA airplane naturally returns to a wing-level horizontal flight condition in a smooth way, due to static stability characteristics. Consequently, the RC airplane is highly influenced by gusts. Given that trim condition depends on airspeed, it is really difficult to find and keep a trim point, as airspeed varies in a fast way during the flight.

Another important difference concerns in-flight perceptions when piloting the scale model. In fact, body acceleration cannot be sensed by the pilot. Moreover, on-board instrumentation is not clearly and continuously consulted for the correct flight conduction and trim conditions determination. A RC pilot has no other possibility than entrust his eyes to determine speed, altitude and attitude of the airplane. This also complicates the keeping of a constant altitude or constant speed flight path. Visual altitude determination is highly influenced by the reference frame (i.e. ground slope, obstacles, etc.), but also by airplane position, flight direction and attitude. The absence of instrumentation can be partially mitigated by the telemetry stream, continuously read by the FTE, even if fast speed readings variation complicates the entire framework.

These last aspects directly reflects on every FTT, in which precise execution of both initial trim point and following maneuvers are of critical importance. Moreover, dynamic response, time needed to complete the technique itself and available airspace have great influence on FTTs, too. Even if the *SwitchMaster* is not a fast aircraft, available airspace over the airfield is entirely covered within a few seconds. Also the difficulties of clearly seeing the airplane from great distance complicates the tests. This led to the necessity of flying on a rectangular pattern to lie within the prescribed area. On a GA airplane, instead, a test can be conducted keeping steady straight flight for minutes without any deviation. This aspect led to the necessity of reducing duration of all FTTs, and even to modify the LAD technique. As illustrated in the previous sections, while *PS-28* test point lasted 30s, the same test for the *SwitchMaster* lasted around 5s.

LAD test conduction would have been difficult to be executed without the applied modification: the original maneuver starts from an intermediate trim speed, then the throttle is brought to idle till minimum airspeed is reached, then brought to the maximum to accelerate, and once again to the minimum until initial flight speed is regained. In the *SwitchMaster* testing, thanks to the fact the acceleration part was not necessary, the maneuver began reaching maximum speed before aligning on the correct path. The deceleration follows a turn necessary to reach the correct heading, at which the aircraft is trimmed at maximum speed (often exploiting the *Pixhawk* assisted mode). Throttle is brought to idle until minimum flight

speed is reached, concluding the test point. As already said, the most difficult part is to correctly trim the aircraft: altitude and speed variations are difficult to be correctly judged, while attitude variation are fast, wide and greatly sensitive to external disturbances.

Talking about dynamic maneuvers, on a GA aircraft the pilot has direct feedback from the situation thanks to its body perception, while this is obviously not available in the RC airplane. Moreover, a maneuver can be executed with stick-free or stick-fixed, whereas on the RC counterpart only stick-fixed is permitted. These aspects, combined with the high frequency of the dynamic modes, led to the impossibility of excitation of the Short Period and the almost instantaneous damping of the Dutch Roll and Phugoid.

Generally speaking, flight testing of a RC airplane seems to be more difficult than the one of a full-scale aircraft, and even returns less accurate results. Anyway, several advantages still makes it convenient, if not mandatory. First of all, systems are simpler than those of a real aircraft. Moreover, benefits on safety, affordability, implementation time and legal aspects are unquestionable. These last aspects are paramount when a novel concept must be tested or demonstrated.

Chapter 10

Conclusion

The main goal of the present thesis is to provide a complete preliminary demonstration of the AeroSwitch concept. This was achieved by developing and testing a remotely-piloted model aircraft, intended as fully-functional scaled demonstrator, obtained through a major modification of a commercial product to integrate a Distributed Electric Propulsion (DEP) system. This demonstrator was able to successfully emulate the desired behavior in all relevant flying modes. The original control unit that was designed and implemented to enforce such modes was able to successfully work throughout the full ground and flight test campaign, as well as the rest of the propulsive and airframe components that were integrated in the model aircraft. As a result, this provided a general validation of the complete AeroSwitch concept, opening the path for future developments. Particularly, the unique single-engine in-flight simulation was fully successful.

The following provides a schematic overview of the activities carried out within this work:

- A commercial radio-controlled model aircraft has been successfully modified in order to accommodate six electric motors on the leading edge of the wings, together with the related hardware.
- A customized control unit, the *M3U*, has been developed to control the motors individually according to multiple control laws, enforcing the planned in-flight simulations necessary for validating the AeroSwitch concept.
- A substantial experimental activity, including component bench tests and wind tunnel tests, has been accomplished to determine system functional characteristics and collect performance data.
- Single-engine propeller effects could be effectively isolated with the conceived flight test techniques, consisting in the imposition of maximum throttle at constant speed or altitude. Deviation from flight symmetry is highly damped at high speed, and real aircraft flight testing served to better understand the phenomenon.
- Single-engine in-flight simulation exhibits the generation of sideslip, turn rate and bank angle at high-power regimes, in perfect harmony with a real General Aviation aircraft. The scale of these phenomena can be adjusted by acting on a regulating knob. The most suitable setting seems at 10% asymmetry conditions, as inspired by the comparison with the data collected during the flight test activity carried out on a Cruiser Aircraft *PS-28*.
- Single-engine emergency condition with one electric motor inoperative (OEMI) has also been validated in all possible scenarios. This is exploited with the imposition of a specific setpoint to each of the electric motors still operating through the *M3U*. The

residual yawing moment is restrained at all throttle settings, and flight symmetry is never compromised beyond what is experienced in normal single-engine operational condition. Airspeed control implementation in the *M3U* may further refine the tuning. With the current logic, this has an effect on the sign of the residual tendency to rotate, consistently with preliminary yawing moment estimations. Hence, the wind tunnel measurement of the thrust generated by the individual propulsive unit is confirmed to provide accurate results.

- In-flight simulation of One Engine Inoperative (OEI) conditions required a significant change in perspective, but was eventually achieved. The scaled model could not properly maintain straight flight when shutting down all three motors on the same side, even with pilot intervention. This is the direct consequence of the motors placement along the entire span of the wing. Also, the estimation of yawing moment coefficient generated by thrust unbalance confirmed the results of the flight test activity. In fact, the level of flight asymmetry experienced was far more severe than the equivalent OEI condition on a typical twin-engine aircraft. Taking a step back, a build-up approach was followed to match the desired behavior, shutting down one or more electric motors. Eventually, the condition could be well reproduced with only the most outboard motor inoperative. This also embodies what is prescribed in the regulations for what concerns OEI situation, specifically when stating the "critical engine inoperative" conditions.
- The preliminary evaluation of the feasibility of propulsive yaw control delivered encouraging results. Flat turns could be completed in level flight with the imposition of thrust asymmetry only. Turn coordination was equally achieved through active propulsion control, even if the optimal tuning of this effect must be investigated further. These results may lay the foundations for a future substantial reduction of the rudder control surface for a DEP aircraft.
- DEP effects have been investigated in one of its first flying practical realizations. The accomplished flight test activity confirms the predicted increase in lift coefficient due to wing blowing. Conversely, at low throttle settings, the propeller windmilling highly disturbs the airflow on the wing, negatively affecting flight conduction. The unconventional landing procedure with high RPM approach and a reduced flare better coped with the different handling qualities in this peculiar phase. Foldable propellers or a different control logic in the motor actuation are possible solutions to this problem.

10.1 Future developments

Based on the previous discussion, it is possible to identify several research opportunities. The following considerations hint at possible future developments based on the activities carried out so far. The list is ordered according to the increasing amount of resource needs:

- Optimized propellers: foldable propellers with a higher pitch should ensure better gliding characteristics, improved low-speed handling qualities and possibly high-RPM performance increments;
- Airspeed control implementation and closed-loop feedback control on sideslip in the *M3U*: better single-engine OEMI flight characteristics, closer to normal condition;
- Number of motors working as a function of throttle input (ex. motor shut-down in cruise): this is expected to lower the drag in cruise, as well as possibly be of help in the final approach.

- Yaw control refinement.
- Refined drag measurement in wind tunnel: strain gauges may be installed and a balance with higher resolution may be adopted.
- Automatic deflection of control surfaces: this should allow single-engine emergency condition with more than one electric motor inoperative to be autonomously managed by the *M3U*.
- Different positioning of motors, to better investigate DEP effects.
- Hybrid-electric propulsion, to enhance flight endurance and range.
- First full-scale aircraft realization.

The AeroSwitch team would be eager to delve into these possible developments, encouraged by the results presented herein. Our greatest hope clearly lies in the future realization of a full-scale General Aviation aircraft embedding the AeroSwitch concept.

Bibliography

- [1] *AIAA students design competition webpage*. URL: <https://www.aiaa.org/get-involved/students-educators/Design-Competitions>.
- [2] *Switch2Product innovation challenge webpage*. URL: <https://s2p.it/>.
- [3] L. Alberti. “Project AeroSwitch: Development of the flight simulator of a Distributed Electric demonstrator”. MSc thesis. Politecnico di Milano, 2021.
- [4] A. Santeramo. “Project AeroSwitch: Aerodynamic study of a Distributed Electric Propulsion demonstrator”. MSc thesis. Politecnico di Milano, 2021.
- [5] K. Matsuki and K. Ozawa. *General concepts*. 2009.
- [6] G. Pistoia. *Electric and hybrid vehicles: Power sources, models, sustainability, infrastructure and the market*. Elsevier, 2010.
- [7] L. Alberti, D. Pasquali, A. Santeramo, and M. Tombolini. *Trybrid - a new concept for General Aviation trainer*. AIAA Graduate Team Aircraft Competition 2019-2020. Politecnico di Milano, 2020.
- [8] G. Zubi et al. “The lithium-ion battery: State of the art and future perspectives”. In: *Renewable and Sustainable Energy Reviews* 89 (2018), pp. 292–308.
- [9] M. J. Lain, J. Brandon, and E. Kendrick. “Design Strategies for High Power vs. High Energy Lithium Ion Cells”. In: *Batteries* 5.4 (2019), p. 64.
- [10] *MAHEPA consortium website*. URL: <https://mahepa.eu/>.
- [11] *Compact Dynamics website, aviation subsection*. URL: <https://www.compact-dynamics.de/en/aviation/>.
- [12] *Pipistrel E-811-268MVLC engine presentation*. URL: <https://www.pipistrel-aircraft.com/aircraft/electric-flight/e-811/>.
- [13] M. D. Patterson, J. M. Derlaga, and N. K. Borer. “High-lift propeller system configuration selection for NASA’s SCEPTOR distributed electric propulsion flight demonstrator”. In: *16th AIAA Aviation Technology, Integration, and Operations Conference*. 2016, p. 3922.
- [14] *NASA Systems Analysis and Concepts Directorate website*. URL: <https://sacd.larc.nasa.gov/x57maxwell/>.
- [15] K. A. Deere et al. “Computational analysis of a wing designed for the X-57 distributed electric propulsion aircraft”. In: *35th AIAA applied aerodynamics conference*. 2017, p. 3923.
- [16] A. Matrone. “Performance-based preliminary sizing of aircraft with distributed propulsion”. MSc thesis. Politecnico di Milano, 2019.
- [17] *Pipistrel Alpha Electro presentation*. URL: <https://www.pipistrel-aircraft.com/aircraft/electric-flight/alpha-electro/>.

- [18] *Pipistrel Velis Electro presentation*. URL: <https://www.pipistrel-aircraft.com/aircraft/electric-flight/velis-electro-easa-tc/>.
- [19] C. E. Riboldi et al. "Predicting the effect of electric and hybrid-electric aviation on acoustic pollution". In: *Noise Mapping 7.1* (2020), pp. 35–56.
- [20] *Rolls-Royce ACCEL website*. URL: <https://www.rolls-royce.com/innovation/accel.aspx>.
- [21] *European Commission H3PS in the Horizon 2020 programme website*. URL: <https://ec.europa.eu/inea/en/horizon-2020/projects/h2020-transport/aviation/h3ps>.
- [22] *H3PS Rolls-Royce website*. URL: <https://www.rolls-royce.com/media/our-stories/discover/2020/high-power-high-scalability-hybrid-powertrain-h3ps.aspx>.
- [23] *H2fly HY4 Aircraft*. URL: <https://h2fly.de/>.
- [24] S. Gudmundsson. *General aviation aircraft design: Applied Methods and Procedures*. Butterworth-Heinemann, 2013.
- [25] F. A. Administration. *Pilot's Handbook of Aeronautical Knowledge*. Flight Standards Service, 2016.
- [26] *AIAA Graduate Team Aircraft Competition 2019-2020 request for proposal*. URL: https://www.aiaa.org/docs/default-source/uploadedfiles/membership-and-communities/university-students/design-competitions/34876-2019-2020-rfp---ga-trainer-family.pdf?sfvrsn=d5fc59e0_0.
- [27] L. Trainelli, C. E. Riboldi, L. Alberti, D. Pasquali, A. Santeramo, and M. Tombolini. *Velivolo plurimotore simulante un monomotore via hardware e software (Multi-engine airplane simulating a single-engine airplane by hardware and software)*. Italian patent application (priority date May 8, 2020).
- [28] *FAA 2018 Survey*. https://www.faa.gov/data_research/aviation_data_statistics/general_aviation/CY2018/.
- [29] EASA. *Certification Specifications for Normal, Utility, Aerobatic and Commuter Category Aeroplanes*. 2015.
- [30] B. L. Stevens, F. L. Lewis, and E. N. Johnson. *Aircraft control and simulation: dynamics, controls design, and autonomous systems*. John Wiley & Sons, 2015.
- [31] B. D. Mather. "Estimation of Air Flow Angles Derived from an Inertial Navigation System". In: (2010).
- [32] A. M. Laminar Research Company. *X-Plane website*. URL: <https://www.x-plane.com/>.
- [33] *Rotax 912 operator's manual*. URL: https://www.rotax-owner.com/pdf/OM_912_Series_ED4_R0.pdf.
- [34] *PS-28 POH*. URL: https://cruiseraircraft.cz/uploads/PS-POH-1-1-13_R1-1.pdf.
- [35] *Dynon Skyview HDX user guide*. URL: https://dynonavionics.com/includes/guides/SkyView_HDX_Pilots_Users_Guide-Rev_E_v15_4.pdf.
- [36] *Androsensor website*. URL: <http://www.fivasim.com/androsensor.html>.
- [37] M. H. Sadraey. *Aircraft design: A systems engineering approach*. John Wiley & Sons, 2012.

- [38] *eCalc database*. URL: <https://www.ecalc.ch/>.
- [39] *Dualsky electric motor datasheet*. URL: <http://www.dualsky.com/motor/d1d64c63-f50e-36ff-211b-3e32cb18ac66.shtml>.
- [40] L. Veldhuis. "Review of propeller-wing aerodynamic interference". In: *24th International Congress of the Aeronautical Sciences*. Vol. 6. 1. 2004.
- [41] *ASA datasheet*. URL: https://www.stratasys.com/-/media/files/material-spec-sheets/mss_fdm_asa_0418a.pdf.
- [42] *UAVCAN - Uncomplicated Application-level Vehicular Computing And Networking*. URL: <https://uavcan.org/>.
- [43] *Holybro Pixhawk 4*. URL: <http://www.holybro.com/product/pixhawk-4/>.
- [44] *MAVLink - Lightweight messaging protocol for drones*. URL: <https://mavlink.io/en/>.
- [45] *QGroundControl ground station for MAVLink protocol*. URL: <http://qgroundcontrol.com/>.
- [46] *PX4 autopilot firmware*. URL: <https://px4.io/>.
- [47] *FrSky Taranis X9D PLUS radio transmitter manual*. URL: <https://www.frsky-rc.com/wp-content/uploads/Downloads/Manual/X9DP/X9D%20PLUS-manual.pdf>.
- [48] *STM32 board website*. URL: <https://www.st.com/en/microcontrollers-microprocessors/stm32f446.html>.
- [49] M. Borri and L. Trainelli. "Basic airplane equilibrium and stability revisited". In: *International Conference on Aeronautical Science and Air Transportation (ICASAT) Tripoli*. Vol. 23. 2007, p. 25.
- [50] L. Pascale and F. Nicolosi. "Design and aerodynamic analysis of a light twin-engine propeller aircraft". In: *26th Congress of International Council of the Aeronautical Sciences (ICAS)*. Vol. 1. 2008, pp. 3890–3904.
- [51] *Typical lithium battery discharging behaviour*. URL: https://www.victronenergy.com/media/pg/15958-Lithium_Battery_Manual-html5/en/battery-charging-and-discharging.html.
- [52] M. Standard. "Flying qualities of piloted aircraft". In: *US Dept. of Defense MIL-STD-1797A* (1990).
- [53] R. D. Kimberlin. *Flight testing of fixed-wing aircraft*. American Institute of Aeronautics and Astronautics, 2003.
- [54] D. T. Ward, T. W. Strganac, and R. Niewoehner. *Introduction to Flight Test Engineering, Kendall*. 2001.
- [55] F. N. Stoliker et al. *Introduction to flight test engineering*. Citeseer, 1995.
- [56] *PX4 full parameter reference*. URL: http://docs.px4.io/master/en/advanced_config/parameter_reference.html.
- [57] *Autopilot TDK inertial measurement unit datasheet*. URL: <https://3cfeqx1hf82y3xcou1108ihx-wpengine.netdna-ssl.com/wp-content/uploads/2021/03/DS-000143-ICM-20689-TYP-v1.1.pdf>.
- [58] *Autopilot Bosch inertial measurement unit datasheet*. URL: <https://www.mouser.com/datasheet/2/783/BST-BMI055-DS000-1509583.pdf>.

- [59] *Autopilot barometric pressure sensor datasheet*. URL: https://www.te.com/commerce/DocumentDelivery/DDEController?Action=showdoc&DocId=Data+Sheet%7FMS5611-01BA03%7FB3%7Fpdf%7FEnglish%7FENG_DS_MS5611-01BA03_B3.pdf%7FCAT-BLPS0036.
- [60] *Autopilot Pitot sensor datasheet*. URL: https://www.te.com/commerce/DocumentDelivery/DDEController?Action=showdoc&DocId=Data+Sheet%7FMS4525DO%7FB2%7Fpdf%7FEnglish%7FENG_DS_MS4525DO_B2.pdf%7FCAT-BLPS0002.
- [61] *Autopilot magnetometer unit datasheet*. URL: <http://www.isentek.com/data/IST8303%20Datasheet.pdf>.
- [62] *Autopilot GNSS sensor datasheet*. URL: https://www.u-blox.com/sites/default/files/NEO-M8-FW3_DataSheet_UBX-15031086.pdf.
- [63] *Zubax Myxa full parameter reference*. URL: <https://forum.zubax.com/t/quick-start-guide-for-myxa-v0-1/911/4>.
- [64] *ENAV website*. URL: <https://www.enav.it/sites/public/it/Home.html>.

Appendix A

System architecture requirement specifications

A.1 Scope

- 1.1 The objective of the AeroSwitch propulsive architecture is to let a multi-engine aircraft be flown also as a single-engine by a single-engine rated pilot.
- 1.2 The objective of the RC scale model is to demonstrate the feasibility of such propulsive architecture and the goodness of conducted flight in various operating modes.
- 1.3 In single-engine normal operating conditions, it shall be possible to introduce a prescribed asymmetry in thrust to generate a yawing moment, to simulate the effects of propeller rotation on a single-engine aircraft.
- 1.4 In single-engine emergency operation with one electric motor inoperative, the system should guarantee flight symmetry by properly delivering power to remaining motors.

A.2 Equipment and components

A.2.1 TX-RX radio control

- 2.1.1 The aircraft shall be controlled with a radio control TX, communicating with on-board RX.
- 2.1.2 RC shall communicate the operating mode selected and control the aircraft in case of manual flight.

A.2.2 Autopilot

- 2.2.1 The aircraft equipped with AeroSwitch propulsive architecture shall be flown under the supervision of an autopilot.
- 2.2.2 The Autopilot shall be used for either autonomous flight or assisted manual flight.
- 2.2.3 The Autopilot shall be interfaced with items necessary to determine aircraft state:
 - a) Gyroscope
 - b) Accelerometer

- c) GNSS
- d) Possibly others.

2.2.4 The Autopilot shall be interfaced with Pitot-static probe for measured airspeed determination.

A.2.3 Electric motors

2.3.1 The aircraft equipped with AeroSwitch propulsive architecture shall be propelled by 3 pairs of BLDC motors symmetrically mounted on the wings, for a total of 6 EMs. The motors shall be placed so that the yawing moment induced by the thrust generated by most outboard EM is equivalent with the sum of the moments generated by two inboard EMs.

A.2.4 Propellers

2.4.1 Fixed pitch propellers shall be keyed to shafts of EMs.

2.4.2 Propellers on opposite semi-wing shall be counter-rotating.

A.2.5 Electronic speed controllers

2.5.1 The speed of each EM shall be controlled through an ESC.

2.5.2 Each ESC shall be *UAVCAN* protocol enabled, in order to return voltage, current, RPM and temperature.

2.5.3 Each ESC shall be connected with *M3U* with a *CAN* bus.

A.2.6 *M3U*

2.6.1 *M3U* (Multi Motor Management Unit) communicates with ESCs and Autopilot. It shall elaborate the output of Autopilot (overall required power), in order to reproduce the desired flying mode (injected to Autopilot from TX) and set an appropriate level of power to feed EMs through ESCs.

2.6.2 *M3U* shall receive telemetry data from Autopilot and the output of ESCs. It shall be able to store this information for post-processing and eventually to communicate live with the ground station.

2.6.3 *M3U* shall receive a further proportional input from Autopilot to be exploited in working mode reported in §3.5.

2.6.4 *M3U* shall be powered from on board main power bus.

2.6.5 *M3U* should distribute the appropriate level of power to feed the EMs through ESCs as prescribed by pre-determined look-up tables.

2.6.6 *M3U* shall run 2 independent processes: Process A shall be in charge of EM 1, EM 4 and EM 5, whereas Process B shall be in charge of EM 2, EM 3 and EM 6. In this way, in case of failure of one of the two processes, the other could guarantee thrust symmetry.

2.6.7 One Process shall be communicating with the other in order to share their status. If a Process should crash, the other one shall be capable of recognition and should enter in a Safe mode bypassing the operating mode selected.

- 2.6.8 *M3U* shall detect parameters of ESCs that are out of their safe operating envelope (e.g. temperature) and shut down the corresponding EM, send a warning to ground station, until normal parameters are restored. A maximum of 2 EMs shall be shut down.
- 2.6.9 *M3U* shall also simulate fictitious "Maximum continuous power" and "Maximum non-continuous power" ranges for the electric motors, in order to reproduce the behavior of full-scale electric motors.
- 2.6.10 All operating modes shall be available in *M3U* unit at once, or just two of them shall be available in order to be easily controllable by pilot. If the latter is selected, Mode 1 will always be §3.1, while the other will be uploaded in the system on the ground, on pilot desire.

A.2.7 Ground station

- 2.7.1 A ground-based computer application shall communicate with *M3U* via wireless telemetry link, according to MAVLink messaging protocol.
- 2.7.2 It shall display real-time data, to serve as a "virtual cockpit" and to control the aircraft in flight.
- 2.7.3 It shall be interfaced offline with *M3U* to receive logs.

A.3 Operating modes

A.3.1 All engines operative (Normal) Multi-Engine mode

- 3.1.1 In case of Multi-Engine mode selection, the request of power prescribed by Autopilot shall be equally distributed among the EMs. No distinction between continuous and non-continuous power ranges should be done, and real maximum power of electric motors will always be available. This shall be standard flight mode.

A.3.2 (Emergency) Multi-Engine mode with three electric motors inoperative on the same side

- 3.2.1 In case of Multi-Engine emergency mode selection, the request of power prescribed by Autopilot shall be equally distributed among the EMs still working. 3 EMs on same wing shall be arrested exploiting ESCs brake function. This simulates the OEI condition of a twin engine aircraft.

A.3.3 All engines operative (Normal) Single-Engine mode

- 3.3.1 In case of Single-Engine mode selection, the request of power prescribed by Autopilot shall be differentially distributed among the EMs, according to what is reported in §3.3.2.
- 3.3.2 Power shall be distributed among the EMs, to introduce an asymmetry in thrust, depending on the values of power required by Autopilot, pre-determined by look-up tables.

A.3.4 (Emergency) Single-Engine mode with One Electric Motor Inoperative (OEMI)

- 3.4.1 In case of Single-Engine OEMI mode selection, a pre-determined EM shall be arrested exploiting ESCs brake function. The request of power prescribed by Autopilot shall be differentially distributed among the EMs still working, according to what is reported in §3.4.2 and §3.4.3.
- 3.4.2 Power shall be distributed among the EMs still working, in a manner so that overall required power is delivered, and flight symmetry is maximized (overall yawing moment generated is minimized).
- 3.4.3 The alternative shut-down of different EMs shall be exploited. A look-up table shall specify the inoperative motor and power setting for the remaining ones.

A.3.5 All engines operative (Normal) Single-Engine mode - Alternative

- 3.5.1 In case of Single-Engine mode selection, the request of power prescribed by Autopilot shall be differentially distributed among the EMs, according to what is reported in §3.5.2.
- 3.5.2 Power shall be distributed among the EMs, to introduce an asymmetry in thrust, depending on the values of power required by Autopilot and the additional proportional input. This modality should be capable of directly calculate every ESC setpoint directly basing on the two given inputs.

A.3.6 Safe mode

- 3.6.1 In case of:

a) Failure of one Process

The working mode shall enter in a downgraded operating logic, which corresponds to Multi-Engine mode.

- 3.6.2 Once entering Safe mode, it shall prevent any change of operating mode and the ignore the actuation of precautionary shut down of EM, illustrated in §2.6.8.

Appendix B

Pixhawk FMU tuned parameters

In Table B.1 are reported most important modified parameters in the *Pixhawk* FMU. Several other modified parameters set actuators trim, maximum and minimum excursion, channel assignment, travel direction and sensors calibration. The full list of parameters with their meaning is retrievable at [56].

Parameter	Value
BAT1_N_CELLS	4S
BAT1_V_EMPTY	3.20 V
BAT1_V_CHARGED	4.10 V
BAT_CRIT_THR	15%
BAT_EMERGEN_THR	10%
BAT_LOW_THR	20%
CAL_AIR_TUBED_MM	4.0 mm
CAL_AIR_TUBELEN	0.055 m
COM_ARM_CHK_ESCS	0
COM_ARM_SWISBTN	1
COM_DISARM_LAND	-1
COM_DISARM_PREFLT	-1
COM_FLTMODE1	Manual
COM_FLTMODE2	Altitude
COM_FLTMODE3	Position
COM_FLTMODE4	Stabilized
EKF2_GPS_POS_X	0.144 m
EKF2_GPS_POS_Y	0.030 m
EKF2_GPS_POS_Z	-0.060 m
FW_AIRSPD_MAX	25.0 m/s
FW_AIRSPD_TRIM	14.0 m/s
FW_GND_SPD_MIN	8.0 m/s
FW_PSP_OFF	-6 deg
FW_LND_FLALT	1.0 m
FW_THR_CRUISE	80%
FW_T_THR_DAMP	1.0
MPC_XY_CRUISE	20 m/s
NAV_RCL_ACT	Land mode
PWM_SBUS_MODE	1
SDLOG_MISSION	All messages
SDLOG_PROFILE	27
SENS_BOARD_Y_OFF	3.442 deg
UAVCAN_ENABLE	Sensors Automatic Config
UAVCAN_NODE_ID	21

Tab. B.1: *Pixhawk 4* FMU modified parameters

Appendix C

Pixhawk FTI sensors

In tables C.1 and C.2 are reported the internal and external Holybro *Pixhawk 4* sensors employed as flight testing instrumentation with their working parameters.

Accelerometer - TDK ICM-20689 [57]	
Temperature range	-40 → 85 °C
Full scale range	±16g
Sensitivity	2048 LSB/g
Initial tolerance	±2%
Non-linearity	±0.5%
Cross-axis sensibility	±2%
Rate	up to 4000 Hz
Accelerometer - Bosch BMI055 [58]	
Temperature range	-40 → 85 °C
Full scale range	±16g
Sensitivity	128 LSB/g
Initial tolerance	±70mg
Non-linearity	±0.5%
Cross-axis sensibility	±1%
Rate	up to 2000 Hz
Gyroscope - TDK ICM-20689 [57]	
Temperature range	-40 → 85 °C
Full scale range	±2000 deg/s
Sensitivity	16.4 LSB/(deg/s)
Initial tolerance	±5%
Non-linearity	±0.1%
Cross-axis sensibility	±2%
Rate	up to 8000 Hz
Gyroscope - Bosch BMI055 [58]	
Temperature range	-40 → 85 °C
Full scale range	±2000 deg/s
Sensitivity	262.4 LSB/(deg/s)
Initial tolerance	±1%
Non-linearity	±0.05%
Cross-axis sensibility	±1%
Rate	up to 2000 Hz
Barometer - TE Connectivity MS5611 [59]	
Temperature range	-40 → 85 °C
Range	10 → 1200 mbar
Resolution	0.012 mbar
Accuracy	±1.5 mbar @ 750 mbar
Rate	up to 20 MHz

Tab. C.1: Internal FMU sensors [43]

Pitot-static - TE Connectivity MS4525DO [60]	
Temperature range	-25 → 105 °C
Max pressure	20.7 bar
Accuracy	±0.25%
Total error band	±1%
Update time	0.5 ms
Magnetometer - Isentek IST8303 [61]	
Temperature range	-20 → 85 °C
Full scale range	±16 G
Resolution	3 mG/LSB
Hysteresis	0.1%
Non-linearity	±1%
Rate	up to 200 Hz
GNSS - u-blox Neo-M8N [62]	
Channels	up to 72
Dynamic limit	≤ 4g
Altitude limit	50 000 m
Velocity limit	500 m/s
Velocity accuracy	0.05 m/s
Heading accuracy	0.3 deg
Horizontal accuracy	2.5 m
Max update rate	10 Hz
Sensitivity	-167 dBm

Tab. C.2: External FMU sensors [43]

Appendix D

Zubax Myxa ESC tuned parameters

In Table D.1 are reported most important modified parameters related with the *Zubax Myxa* ESC. The full list of parameters with their meaning is retrievable at [63].

Parameter	Value
BEC.CAN_PWR_ON	false
CTL.HARD_STOP	true
M.CURRENT_RAMP	150 A/s
M.EANGVEL_ACCEL	15 000 rad/s
M.EANGVEL_CTL_KP	0.006
M.EANGVEL_DECEL	10 000 rad/s
M.MAX_CURRENT	30 A
M.MAX_EANGVEL	12 000 RPM
M.MIN_EANGVEL	400 RPM
M.NUM_POLES	14
M.VOLTAGE_RAMP	50 V/s
UAVCAN.ESC_INDEX	0
UAVCAN.ESC_RCM	2
UAVCAN.ESC_REVRS	false
UAVCAN.NODE_ID	1 – 6

Tab. D.1: *Zubax Myxa* ESC modified parameters

Appendix E

Preliminary flight test activity planning

After the execution of the simulated flight test campaign, a real flight test mission was carried out. The in-flight test aimed to determine typical SSA for a real GA aircraft, and to compare its value with the one obtained with the computer flight simulator.

E.1 Test aircraft

Aircraft to be tested is Cruiser Aircraft *PS-28* registered F-HZCE (Figure E.2). It is a CS-VLA certified single-engine, full metal, low-wing, two-seat propeller driven aircraft for General Aviation training and private employment. In this specific version, engine adopted is a Rotax *912 ULS S2*, rated for 100 hp at 5800 RPM for a maximum of 5 minutes and 95 hp continuous power at 5500 RPM. It has a non-retractable landing gear and a large wing dihedral, namely 5.6 deg. This could have an influence in the test, enhancing a greater yaw-roll coupling. Table E.1 shows main parameters, while Figure E.1 reports aircraft 3-view layout.

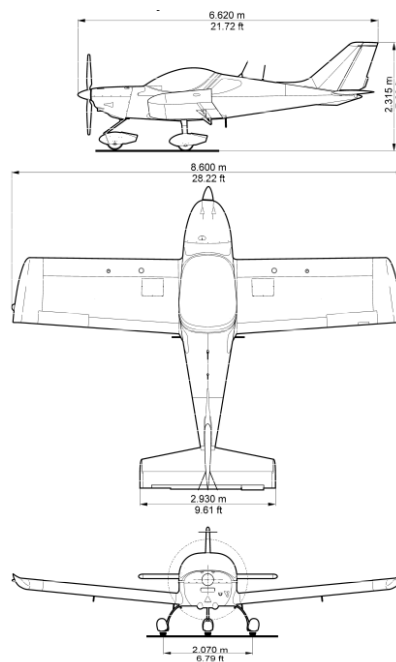


Fig. E.1: *PS-28* 3-view representation

Wing span	Length	Wing area	MTOM	Empty mass
8.60 m	6.62 m	12.3 m ²	600 kg	399 kg

Tab. E.1: *PS-28* main parameters (from POH)



Fig. E.2: *PS-28* test aircraft

E.1.1 Flight controls and landing gear

PS-28 exhibits control surfaces with standard configuration: two ailerons on the wings, rudder and elevator on the tail with mechanical linkages. Two trim tabs are installed, one on the horizontal tail plane and the other on the right aileron. Both are electrically operated and controlled from pilot stick. Wing flaps are of single-slotted type and electrically driven. They can be set in a continuous way from 0 deg up to 40 deg. Landing gear is tricycle with hydraulic disk brakes on main landing gear. Nose wheel is free to steer, but it is not controllable from the pilot. Ground control is possible through differential braking. Landing gear is non-retractable. There are no stability or control augmentation systems, nor autopilot systems.

E.1.2 Avionic and Systems

The aircraft is equipped with a Dynon *SkyView HDX* avionic suite. It comprehends: two EFIS Dynon *SV-D1000* screens, namely EFIS-1 and EFIS-2, one ADAHRS Dynon *SV-Adahrs-200* system (Air Data Attitude and Heading Reference System), one Dynon *SV-GPS-250* GNSS system, two backup batteries and backup airspeed indicator and altimeter. It is a complete glass-cockpit avionic suite, which provides the pilot a wide set of flight parameters and navigation aids, from reconstructed wind speed and direction, to terrain-avoidance indications and synthetic view.

An illustration of the system connection is shown in Figure E.3. EFIS-1 is in front of the pilot seat and arranged as PFD (Primary Flight Display), while EFIS-2 is in front of the passenger seat and arranged as MFD (Multi-Function Display) and directly interconnected with EMS (Engine Monitoring System). A PFD example view is reported in Figure E.4, taken from the user guide [35].

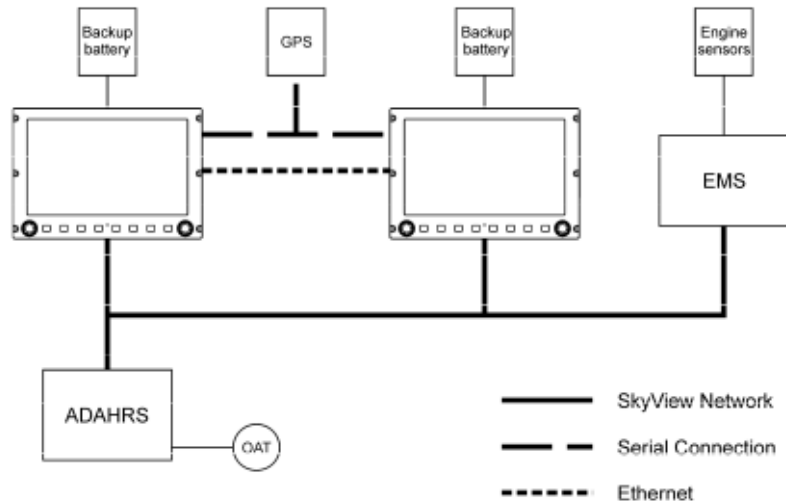


Fig. E.3: Dynon *SkyView HDX* system connections [35]



Fig. E.4: Dynon *SkyView HDX* PFD example view [35]

The avionic suite offers the possibility to record and export flight data which have been shown on the displays. Thanks to this feature, it is exploited as FTI. The system can store a hundred of parameters, recorded during the previous 15 hours of screen-on time, up to 16 Hz sample rate.

Avionic suite is then completed with a COM/NAV system Garmin *GNC 255A* and a transponder *TRIG TT21*. The Aviatik *WA037383* Pitot-static probe feeds ADAHRS and alternate instruments (analog altimeter and airspeed indicator). All onboard instruments are Day-VFR-certified.

The fuel pump system feeds the engine via an electric fuel pump to guarantee fuel supply in all flight attitudes. Fuel level is determined with one sensor in each tank. A fuel pressure sensor and a fuel-flow meter are installed too, with readings shown on PFD or MFD. When the measured fuel pressure is too low, an automatic alarm alerts the pilot with visual and aural messages.

Airspeed indicator reports speed in knots. Indicated airspeed is already corrected from

measured airspeed (MAS) to calibrated (CAS). Embedded airspeed conversion error should not exceed 2.3 kn within 3 minutes after calibration. The airplane is also equipped with a stall warning system, located on the left wing leading edge. When activated, a strong alarm rings inside the cabin, and a red alert appears on PFD.

ADAHRS embeds a magnetometer, which has to be calibrated. Last calibration prior to test activity was made in September 2020.

E.1.3 Engine and propeller

PS-28 is powered by the engine *Rotax 912 ULS S2*. Coupled with a reduction gear with 2.43:1 ratio, it drives a three-bladed, ground variable-pitch, composite *Sensenich 3B0R5R68C* propeller of 1.727 m diameter. *Rotax 912 ULS S2* is a four-cylinder, four-stroke horizontally opposed, normally aspirated engine with mixed water-air-cooling system, dual carburetor and dual electronic ignition system. In-cockpit controls include a throttle lever with a friction lock and carburetor heat lever. In Table E.2 main engine parameters are reported, while figures E.5 and E.6 depict its power curves [33].

Displacement	Compression ratio	Take-off performance	Max cont. performance
1352 cm ³	10.8 : 1	59.6 kW at 5800 RPM	58 kW at 5500 RPM

Tab. E.2: *Rotax 912 ULS S2* main parameters

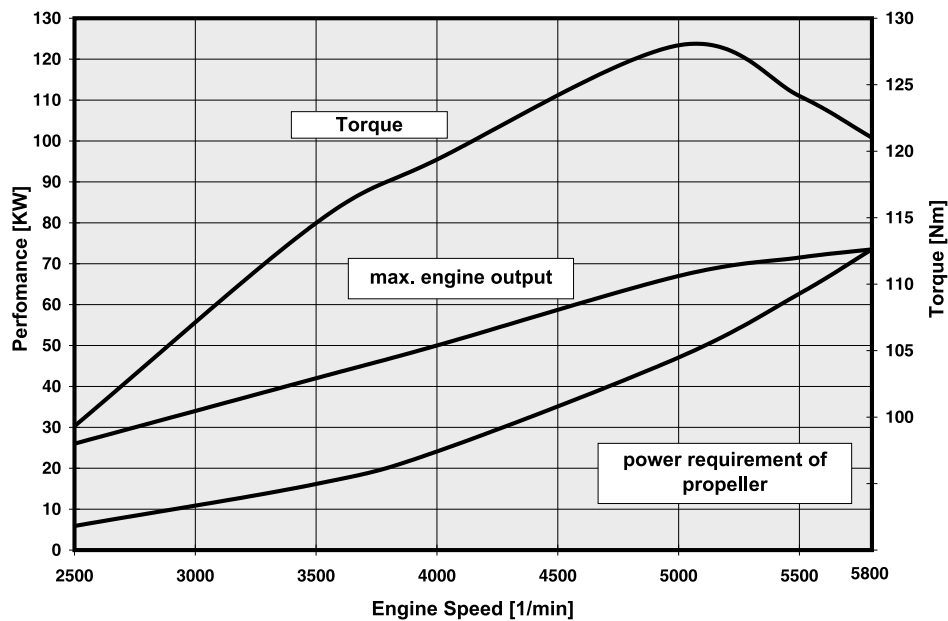


Fig. E.5: *Rotax 912 ULS S2* power curve in standard conditions [33]

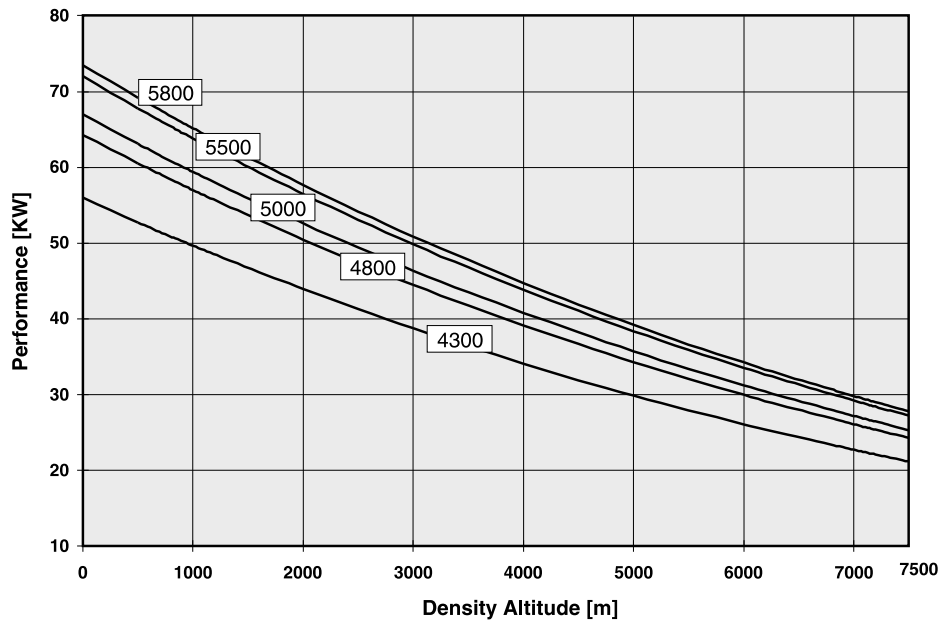


Fig. E.6: Rotax 912 ULS S2 power curve variation with altitude [33]

E.1.4 Mass and balance

PS-28 masses are reported in Table E.3. In Figure E.7 is reported a representation of the aircraft center of balance envelope.

MTOM	Max landing mass	Empty mass	Max fuel mass
600 kg	600 kg	399 kg	82 kg

Tab. E.3: Masses of PS-28

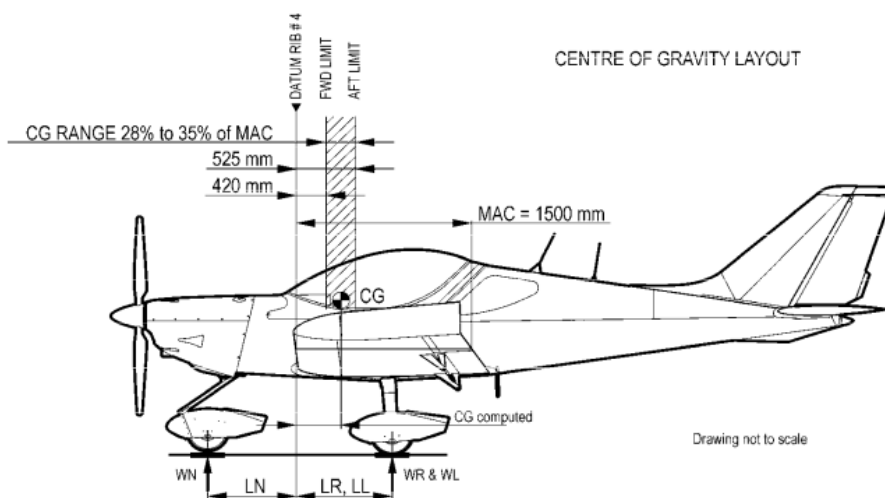


Fig. E.7: PS-28 center of balance representation [34]

All weights (including fuel, pilot and passenger) must be accounted for determination of

take-off mass and the real center of gravity (CG) location. The CG location must be located inside the mass and balance envelope. Lateral and vertical CG location are not checked and not of interest.

E.2 Test instrumentation

Experimental data are gathered via two sources: aircraft native instrumentation and a smartphone application. No additional instruments can be installed on-board, as every modification to the aircraft must be subjected to certification and approval process.

E.2.1 Aircraft native instrumentation

As presented in Section E.1.2, aircraft instrumentation is digital and gives the opportunity to record and download flight data on any USB storage device, also after flight completion and shutdown of the suite. Table E.4 enlists a collection of the main parameters that can be exported and are of interest for the analysis. The acquisition rate was 5 Hz, not modifiable by the pilot, being just editable from a technician. Anyway, this rate proved to be enough for the purpose.

INS	Air data	GNSS	Systems
Attitude	IAS	GPS time	Session time
Heading	CAS	GPS position	Engine RPM
Angular rates	TAS	Ground speed	Manifold pressure
Magnetic heading	OAT	Vertical speed	Barometer setting
Magnetic variation	Pressure altitude	Ground track	Wind estimation

Tab. E.4: Dynon *SkyView HDX* exportable parameters of interest

E.2.2 Smartphone application

A smartphone app is employed as back-up of aircraft native instrumentation. The very same app has already been validated in 2019-2020 experimental flight test campaign in Politecnico di Milano course of Flight Testing, in which some students successfully employed it for testing the performance of a Cessna 172.

Modern smartphones feature a great variety of sensors, also with high precision if related to their cost. Anyway, there are a lot of issues to be accounted for:

- the third-party application installed on the smartphone could crash in every moment, without forewarning, causing the loss of all the data;
- accelerometers and gyroscope sensors (MEMS) could be influenced by aircraft engine vibrations, magnetic or electro-magnetic interference;
- the way the smartphone is strapped to the aircraft influences accelerometers and gyroscopes: if handheld, data will be completely unreliable, while fixing it to the airframe could be not easy; additionally, the strapping orientation will influence data post-processing.

Analyzing these issues, smartphone with a recording app can be employed, but with reservation. GNSS measurement (position, altitude, speed) will always be considered reliable as GNSS accuracy is greater than possible in-cabin motion.

Smartphone employed in the trial is a Samsung *Galaxy S10 SM-G973F* with *Android 10* updated on October the 1st, 2020. The software chosen for data recording is *AndroSensor* v1.9.6.3 [36]. The software records parameters at the chosen time interval and exports a *.csv* file which can later be employed for data post processing. A downside of the chosen application is that there is no "event" button, hence the time instant of important events should be hand-written on the test card to recognize data related to a particular flight phase. Even if the acquisition rate could be faster, the chosen rate is 8 Hz, also because the smartphone app cannot match the same rate of the avionic suite.

In Table E.5 are depicted the sensors enforced with their output parameters and limitations.

Sensor	Parameters	Range	Resolution	Delay
GNSS	Position, altitude, speed	ND	ND	ND
Accelerometers	acceleration in (x, y, z) axis	78.5 ms^{-2}	0.00239 ms^{-2}	$2000 - 180\,000 \mu\text{s}$
Gyroscope	rotation around (x, y, z) axis	17.5 rads^{-1}	$0.000061 \text{ rads}^{-1}$	$2000 - 180\,000 \mu\text{s}$

Tab. E.5: *AndroSensors* parameter outputs

E.3 Test range

Flight test airfield is Albenga-Riviera international airport (ICAO: LIMG; IATA: ALL), headquarter of *Aeroclub di Savona e della Riviera Ligure*. Albenga airport is located in Liguria, 4.2 nm west of the shoreline. It has an elevation of 148 ft AMSL, and has an asphalt runway designated 09-27 and ICAO CAT 5 firefighting service. Runways have dimension 1429 x 45 m, are equipped with PAPI lights and contoured by a grass strip of 1549 x 150 m. VOR equipment is located inside the aerodrome. Standard downwind is located on the north side of the favorite runway, orientation 09 [64].

Aerodrome is open to both VFR and IFR flights. LIMG does not have a control tower, but an AFIS on frequency 123.85 MHz (Albenga Info) and its airspace is categorized as Golf. LIMG is inside Milan FIR (LIMM), whose frequency is 124.925 MHz. Low-level airspace between Albenga and France boundary is categorized as Golf as well, without particular restrictions.

LIMG tower emits hourly METAR bulletins and periodical NOTAMs, consulted before flying. Observations also from Cape Mele Italian Air Force Meteorological Base of the day of the test are here reported, with reference to locations and times of interest:

```
LIMG 081350Z 10006KT 9999 SCT018 SCT045 17/15 Q1025
LIMG 081450Z 10004KT 9999 VCSH SCT015 17/15 Q1025
LIMU 081355Z 09005KT 9999 BKN010 SCT023 19/16 Q1025 RMK BKN QUK 2 QUL 1
S VIS MAR 20 KM VIS MIN 9999=
LIMU 081455Z 09006KT 8000 SCT010 SCT015 17/16 Q1025 RMK BKN QUK 2 QUL 1
S VIS MAR 8 KM VIS MIN 8000=
```

The intended working zone is a couple of miles out of the shoreline, in front of the city of Loano. This is a Golf-class airspace with low traffic and no restrictions. Moreover, in this area wind is expected to be constant, without major updrafts or gusts. In Figure E.8 is reported the ICAO visual approach chart for LIMG zone, in which the sea area on which the test was carried out is highlighted with an orange dashed line.

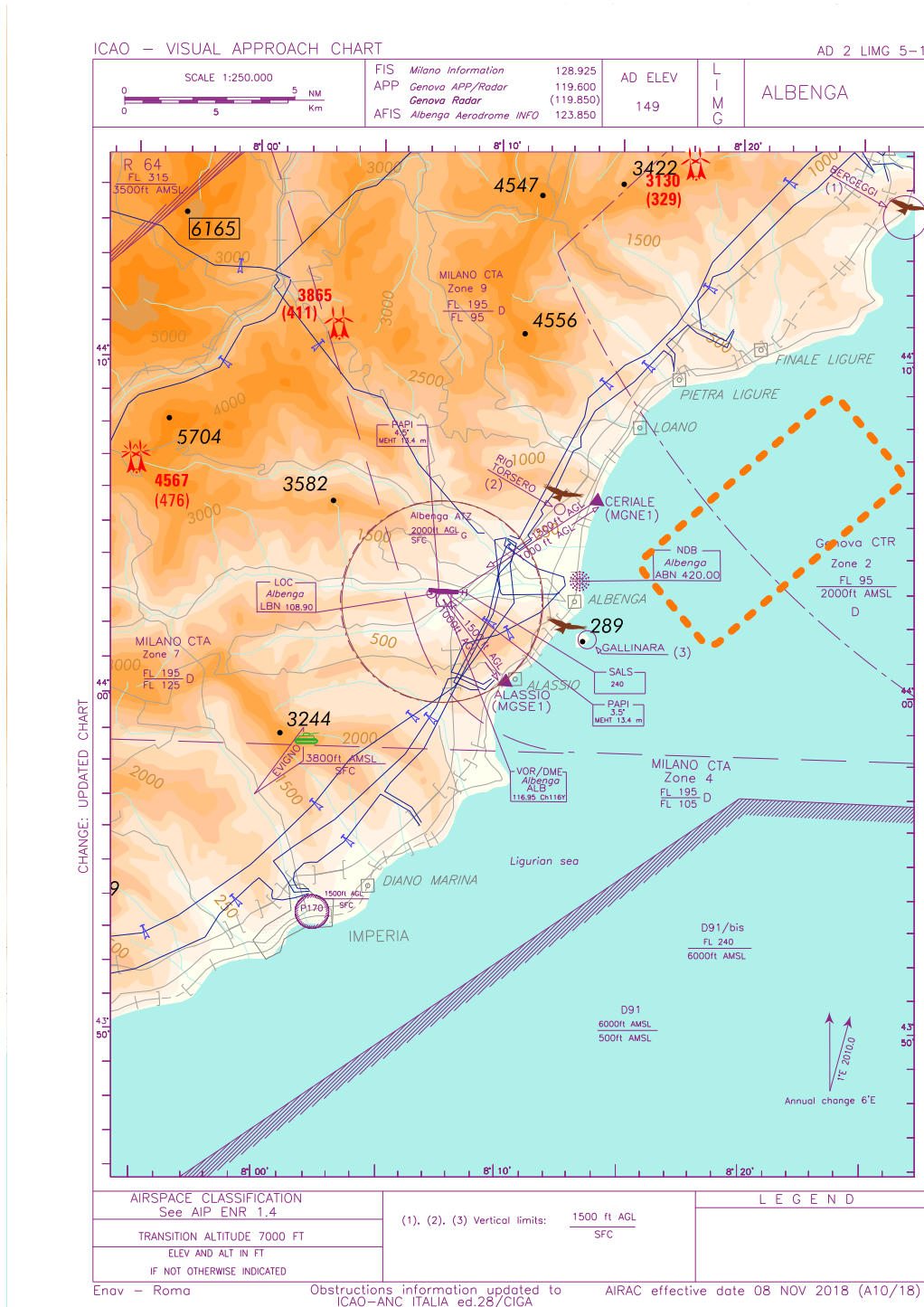


Fig. E.8: ICAO visual approach chart with test zone highlighted [64]

From the chart it is clear that no regulated zone is interested in the flight test, as long as altitude remains below 2000 ft QNH.

E.4 Limitations

E.4.1 Weather limitations

Flight test is intended to be delayed in case of bad weather: rain, low visibility or wind, responding to aircraft limitations and Visual Flight Rules (VFR) that must be always observed. *PS-28* has a maximum demonstrated crosswind velocity of 12 kn, and 24 kn for headwind. The performed test is sensible of turbulence, gust and wind, therefore calm air is to be sought as much as possible.

E.4.2 Aircraft limitations

Aircraft weight and balance limits have already been discussed, and can be summed with MTOM of 600 kg and center of gravity between 0.420 m and 0.525 m from reference datum.

Speed limitations need to be observed for the entire flight duration, both for low speeds dangers and for the risk of over-speed. Speed limitations are reported in Table E.6 in IAS.

V_{S1}	V_{NO}	V_A	V_{NE}
37 kn	108 kn	108 kn	138 kn

Tab. E.6: *PS-28* speed limitations

Aircraft load factor always needs to be included within limitations of minimum $-2g$ and maximum $+4g$. Test aircraft can be employed in non-aerobatic flight only, and maximum control surfaces excursion can be imposed up to 88 kn. Moreover, fuel pump is always needed for climbing or high bank attitude.

Engine limitations are reported in Table E.7.

Parameter	Limitation
Regime	< 5800 RPM
Oil pressure	< 7 bar
Oil temperature	< 130 °C
CHT	< 135 °C
Fuel pressure	< 0.4 bar
EGT	< 850 °C

Tab. E.7: *Rotax 912* limitations

E.5 Test objectives and schedule

The planned test flight aimed to investigate the relation between power setting and airspeed with yawing moment generated by propeller spinning and consequent induced SSA, bank angle and turn rate.

Pilot in command was Davide Pasquali, with Matteo Tombolini as FTE. Fuel quantity at take-off was determined prior to the flight, namely 72l, leading to a total take-off mass of

594 kg and a center of gravity located in the middle of its prescribed envelope. Position of CG was thus compliant with mass and balance envelope limitations. This information was also useful to predict the right stall speed. In fact, after weight and balance determination, stall speed in clean configuration can be corrected to retrieve the real stalling speed, enforcing:

$$V_{S1,\text{real}} = V_{S1,s} \sqrt{\frac{W}{W_s}}. \quad (\text{E.1})$$

Loading configuration of the trial is reported in Table E.8, while the planned mission schedule is presented in Table E.9.

Parameter	Value
FTE mass	66 kg
FTP mass	75 kg
Empty mass	399 kg
Baggage mass	2 kg
Fuel mass	52 kg
Take-off mass	594 kg
CG position at TO	476 mm
Planned used fuel	171
CG position at LND	480 mm
$V_{S1,\text{real}}$	36 kn

Tab. E.8: Pre-flight loading table

Activity	Duration	Fuel	Altitude
Pre-flight checks and taxi	5 min	11	GND
Take-off	2 min	11	0 – 300 ft AGL
Cruise to test range	2 min	11	300 ft AGL – 2000 ft QNH
Preliminary trials	8 min	21	2000 ft QNH
Beta testing	30 min	91	2000 ft QNH
Aerodrome approach	3 min	11	2000 – 1200 ft QNH
Landing	2 min	11	300 – 0 ft AGL
Taxi and post-flight checks	5 min	11	GND
Total	57 min	171	

Tab. E.9: Planned flight mission sequence

E.6 Flight test cards

Flight test cards employed in the flight test activity are reported in Figure E.9, related to preliminary test points for configuration selection, and Figure E.10, example of main trial for quantitative investigation of propeller effects. These templates are both related to constant speed FTT, whereas flight test cards of constant altitude trials are not reported, as they share the same structure.

ITEM	TEST	TIME
PS1	PreTest const. Speed 1 HW FRFR	
1.11	Cruising ALT 2000 ft QNH Clean configuration	
1.12	WIND: HDG <input type="text"/> SPEED <input type="text"/>	
1.13	Headwind , trim at 60 KIAS	
1.14	Rudder FREE Ailerons FREE Constant SPEED	
1.15	Full power QUALITY <input type="text"/>	
1.16	Descend to 2000 ft QNH Regain trim speed 60 KIAS Regain attitude	

Fig. E.9: Preliminary test flight test card (constant speed)

ITEM	TEST	TIME
MS1	Main Test constant Speed HW 1	
3.11	Cruising ALT 2000 ft QNH Test: HEAD WIND: HDG <input type="text"/> SPEED <input type="text"/>	
3.12	Trim at 100 KIAS <input type="text"/> MAP Trim Throttle: <input type="text"/> RPM Rudder <input type="text"/> Ailerons <input type="text"/> Constant SPEED	
3.13	Full power	
3.14	Regain attitude and trim spee 100 KIAS	
3.15	Throttle to IDLE: Begin descent	
3.16	Regain attitude	

Fig. E.10: Main test flight test card (constant speed)